Epoxy-Clay Nanocomposites for Structural Applications

Wei Ping Liu

A Thesis

In

The Department

of

Mechanical and Industrial Engineering

Submitted in Partial Fulfillment of the Requirements

for the Degree of Doctor of Philosophy at

Concordia University

Montreal, Quebec, Canada

October 2005

Your file Votre référence
ISBN: 978-0-494-16297-2
Our file Notre référence
ISBN: 978-0-494-16297-2

ABSTRACT

Epoxy-Clay Nanocomposites for Structural Applications

Wei Ping Liu, Ph. D.
Concordia University, 2005

High-performance epoxy-clay nanocomposites and hybrid epoxy nanocomposites modified with both organoclay and rubber were synthesized. The nanocomposites were characterized by optical microscopy, XRD, AFM, TEM and SEM. A new method to disperse organoclays into organic media, high pressure mixing (HPM), is proposed. TEM images show that organoclay agglomerates are broken down by the HPM method to form small particles consisting of 5~10 silicate layers. Adding organoclay into rubber-modified epoxies not only increases the degree of cure and T_g, but also changes the morphology of the rubber phase.

Water uptake behavior of nanocomposites has been systematically studied with Fickian and non-Fickian diffusion models. Diffusion models for nanocomposites were developed. The diffusivity in nanocomposites decreases with increasing clay loading and improving dispersion quality of organoclay. Hybrid nanocomposites can decrease the effect of rubber on water uptake of epoxy resins at high environmental temperature.

The fracture toughness of epoxy systems is greatly enhanced by adding organoclay and by improving dispersion quality of organoclay in epoxy resins. The increased toughness is explained in terms of a crack-pinning mechanism and increased fracture surface area. There is a superposition effect on toughness of hybrid epoxy nanocomposites modified with both rubber and organoclay.

ACKNOWLEDGEMENTS

I would first like to express my sincere gratitude to my thesis supervisors: Dr. Suong V. Hoa and Dr. Martin D. Pugh for their supervision, encouragement, and the financial support during the course of this research. Their effort and time in reviewing this thesis are gratefully acknowledged.

Special appreciation is also due to Dr. Ming Xie for his assistance with laboratory procedures and for his technical support.

I am grateful to Mr. Paul Ouellette and Mr. John Elliott who assisted me in preparing and running experiments.

I am also thankful to Mr. Heng Wang for help in conducting AFM tests.

The friendship and help provided by Dr. Qi Zhao, Dr. Lixin Wu, Mr. Khassan Mourtazov and Mr. Xu Yuan are also acknowledged.

Last, but not least, I express my sincere gratitude to my wife, Yi Jun, and my daughter, Jenny, for their patience, understanding, encouragement and supports.

DEDICATION

To My Parents

TABLE OF CONTENTS

LIST OF FIGURES ..... **xii**

LIST OF TABLES ..... **xxiv**

Chapter 1: Introduction **1**

1.1 Overview of the Project 2

1.1.1 Project Motivation 2

1.1.2 Challenges 3

1.1.3 Objectives 4

1.2 Content of the Thesis 4

Chapter 2: Background and Literature Review **8**

2.1 Clay and Organoclay 9

2.1.1 Montmorillonite 10

2.1.2 Organoclay 12

2.2 Epoxies 15

2.3 Synthesis of Nanocomposites 20

2.3.1 *In Situ* Polymerization 21

2.3.2 Solution Method 22

2.4 Formation Mechanism of Epoxy-Clay Nanocomposites 24

2.5 Characterization of Nanocomposites 26

2.5.1 X-Ray Diffraction (XRD) 26

2.5.2 Transmission Electron Microscopy (TEM) 28

2.6 Properties of Nanocomposites 29

2.6.1 Mechanical Properties 30

2.6.2 Barrier Properties 31

2.6.3 Thermal Properties 32

2.6.4 Flammability 33

Chapter 3: Dispersion of Organoclay in Organic Media 34

3.1 Introduction 35

3.2 Theoretical Background 37

3.2.1. Terminology in Clay Colloid Chemistry 37

3.2.2 Clay-Water System 38

3.2.3 Dispersion Methods 44

3.2.4 Viscosity of Suspension with Volume Concentration 46

3.3 Experimental 48

3.3.1 Materials 48

3.3.2 Dispersion Method 51

3.3.3 Physical Measurement 55

3.4 Results and Discussion 57

3.4.1 Organoclay in Organic Solvent 57

3.4.2 Dispersion of Organoclay in Epoxy Resins 70

3.4.3 Effects of Curing Agents on Organoclays in Suspensions 80

3.5 Summary 87

Chapter 4: Synthesis and Morphology of High-Performance Epoxy-Clay Nanocomposites 89

4.1 Introduction 90

4.2 Experimental 92

4.2.1 Materials 92

4.2.2 Synthesis of Nanocomposites/Filler Composites 94

4.2.3 Physical Measurement 94

4.3 Results and Discussion 95

4.3.1 Cure Kinetic Study 95

4.3.2 Manufacturing Processes 102

4.3.3 Morphology 104

4.3.4 Effect of Cure Temperature on Morphology 118

4.3.5 Formation Mechanism and Proposed Models 121

4.4 Summary 125

Chapter 5: Synthesis and Morphology of Hybrid Nanocomposites Modified with Organoclay and Rubber 126

5.1. Introduction 127

5.2 Experimental 129

5.2.1 Materials 129

5.2.2 Synthesis of Nanocomposites and Rubber-Modified Epoxy 130

5.2.3 Physical Measurement 131

5.3 Results and Discussion 132

5.3.1 Cure Kinetic Study 132

5.3.2 Rheological Properties 136

5.3.3 Effect of Curing Temperature on Formation of Rubber Phase 139

5.3.4 Degree of Cure and Glass Transition Temperature 142

5.3.5 Morphology 148

5.3.6 Formation Mechanism and Proposed Models 161

5.4 Summary 163

Chapter 6: Water Uptake of Epoxy-Clay Nanocomposites 165

6.1 Introduction 166

6.2 Diffusion Models 168

6.2.1 Fick's Law 169

6.2.2 Anomalous (Non-Fickian) Models 170

6.2.3 Models for Composites 174

6.2.4 Barrier Model 175

6.2.5 Model Development for Nanocomposites 176

6.3 Experimental Setup 189

6.3.1 Sample Preparation 189

6.3.2 Physical Measurement 189

6.4 Results and Discussion 190

6.4.1 Moisture Content in Clay and Organoclays 190

6.4.2 Water Uptake Behavior of Epoxy Resin Systems 192

6.4.3 Model Predictions 199

6.4.4 Effect of Interface on Water Uptake of Composites 204

6.4.5 Water Uptake of Nanocomposites with Different Methods 215

6.4.6 Water Uptake of Nanocomposites with Different Organoclays 223

6.4.7 Water Uptake of Nanocomposites with Different Matrices 227

6.4.8 Water Uptake of Hybrid Nanocomposites 229

6.5 Summary 236

Chapter 7: Fracture Toughness of Epoxy-Clay Nanocomposites 239

7.1 Introduction 240

7.2 Background 241

7.2.1 Fracture Toughness 241

7.2.2 Toughening Mechanisms 245

7.2.3 Fracture Surface Area Analysis 251

7.3 Experimental 261

7.3.1 Sample Preparation 261

7.3.2 Mechanical Measurement 262

7.4 Results and Discussion 264

7.4.1 Effect of Surface Modification of Clay on Toughness 264

7.4.2 Toughness of Nanocomposites with Different Dispersion Methods 273

7.4.3 Nanocomposites with Different Epoxy Systems 286

7.4.4 Fracture Toughness of Hybrid Nanocomposites 290

7.5 Summary 297

Chapter 8: Conclusions, Contribution and Future Work 300

8.1 Conclusions 300

8.1.1 Organoclay Suspensions with Different Dispersion Methods 300

8.1.2 Nanocomposites Based on TGDDM/DDS Epoxy System 301

8.1.3 Hybrid Nanocomposites Modified with Rubber and Organoclay 303

8. 2 Claims of Originality 304

8.3 Suggested Future Work 306

8.4 List of Publications 307

8.5 Patent 308

References 309

LIST OF FIGURES

Figure 2-1: Schematic illustration of clay-polymer structure 9

Figure 2-2: Idealized structure for montmorillonite [ref. 26] 11

Figure 2-3: Schematic microstructure of montmorillonite [ref. 27] 11

Figure 2-4: Cation exchange process between alkylammonium ions and cations initially intercalated between clay layers [ref. 28] 13

Figure 2-5: Synthesis reaction of diglycidylether of bisphenol A (DGEBA) 16

Figure 2-6: Cure reaction of epoxy resins cured with amines [ref. 38] 18

Figure 2-7: Cure reaction of epoxy resins cured with BF_3.MEA [ref. 38] 18

Figure 2-8: Flowchart presenting the different steps of the "*in situ* polymerization" approach 21

Figure 2-9: Schematic illustration of *in situ* polymerization 22

Figure 2-10: Flowchart presenting the different steps of the solution approach 23

Figure 2-11: Proposed homopolymerization mechanism of DGEBA catalyzed by alkylammonium ions [ref 45] 25

Figure 2-12: Principle of X-ray diffraction 27

Figure 2-13: X-ray diffraction patterns of $CH_3(CH_2)_{15}NH_3^+$- montmorillonite in different physical states [ref 17] 28

Figure 3-1: A principle scheme (Stern model) of the electrical double layer on the boundary clay face surface – aqueous solution [ref. 72] 39

Figure 3-2: Repulsive and attractive energy as a function of particle separation at three electrolyte concentrations [ref. 28] 42

Figure 3-3: Schematic representation of the electric potential between two plates, as compared with that for a single double layer [ref. 28] 43

Figure 3-4: Schematical representation of particle association in clay suspensions 44

Figure 3-5: Chemical structure of TGDDM 49

Figure 3-6: Chemical structure of DDS 49

Figure 3-7: M-110 EH XP Microfluidizer 53

Figure 3-8: Free swelling of organoclays in organic solvents at room temperature..... 59

Figure 3-9: Basal spacing of I.30E and 30B organoclays and their suspensions 60

Figure 3-10: Phase separation and sediment of I.30E/acetone suspensions made by the HPM at different process pressures, after three months at room temperature..... 62

Figure 3-11: Swelling factors of I.30E/acetone suspensions made by HPM with different process pressures..... 63

Figure 3-12: X-ray patterns of I.30E/acetone suspensions at different pressures..... 65

Figure 3-13: X-ray patterns of 30B/acetone suspensions at different pressures..... 66

Figure 3-14: Viscosity-shear rate curves of 5 wt % I.30E/acetone suspensions made by the HPM method at different pressures 68

Figure 3-15: Shear thinning index of 5 wt% I.30E/acetone suspensions with process pressure 68

Figure 3-16: Schematic graph of dispersion of I.30E organoclay by the HPM method 69

Figure 3-17: Free swelling of organoclays and Na-clay in epoxy resins at 135°C 70

Figure 3-18: XRD patterns of I.30E/DGEBA suspensions with different mixing methods 73

Figure 3-19: Viscosity-shear rate curves of I.30E/DGEBA suspensions made by the DM method at different clay loadings at 25 °C 75

Figure 3-20: Relative viscosity *versus* clay loading in DGEBA epoxy suspensions 77

Figure 3-21: Relative viscosity *versus* clay loading in TGDDM epoxy suspensions.... 78

Figure 3-22: Viscosity-shear rate curves of 6-phr organoclay/DGEBA systems with different mixing methods at 25°C 79

Figure 3-23: XRD patterns of DDS, I.30E and their combination with acetone 81

Figure 3-24: XRD patterns of DDS, 30B and their combination with acetone 82

Figure 3-25: XRD patterns of BF_3.MEA, I.30E and their combination with acetone... 83

Figure 3-26: FTIR curves of acetone, I.30E and the dry powder from the sediment in"I.30E+ BF_3.MEA +Acetone" 85

Figure 3-27: FTIR curves of BF_3.MEA and the viscous liquid from the sediment in"I.30E+ BF_3.MEA +Acetone" 86

Figure 4-1: Exothermal curves of homopolymerization of TGDDM resin in the presence and absence of organoclay 97

Figure 4-2: Exothermal peak temperature *versus* clay loading 99

Figure 4-3: Exothermal curves of cure reactions of the TGDDM/DDS system in the presence and absence of organoclay 102

Figure 4-4: SEM micrographs of fracture surface of HPM-A-3 nanocomposites..... 103

Figure 4-5: Optical micrograph of the filler composite at 6-phr clay loading..... 106

Figure 4-6: Optical micrograph of the nanocomposite made of I.30E by the DM method at 6-phr clay loading 106

Figure 4-7: Optical micrograph of the nanocomposite made of 30B organoclay by the DM method at 6-phr clay loading 106

Figure 4-8: Area percentages of agglomerates in nanocomposites and filler composites 107

Figure 4-9: Schematic graphs of the dispersion of organoclay and Na-montmorillonite 107

Figure 4-10: Optical micrograph of the nanocomposite made by the HPM method at 6-phr I.30E clay loading 108

Figure 4-11: SEM micrographs of fracture surfaces 110

Figure 4-12: TEM image of HPM-A-nanocomposite (HPM-A-6) at low magnification 111

Figure 4-13: TEM image of HPM-A-nanocomposite (HPM-A-6) at high magnification 112

Figure 4-14: TEM image of HPM-B-nanocomposite (HPM-B-3) at low magnification 113

Figure 4-15: TEM image of HPM-B-nanocomposite (HPM-B-3) at high magnification 114

Figure 4-16: XRD patterns of Na-montmorillonite and its composites made by the DM method 115

Figure 4-17: XRD curves of the TGDDM-DDS epoxy system and its nanocomposites made of I.30E organoclay by the DM method 116

Figure 4-18: XRD patterns of TGDDM/DDS and its nanocomposites by the HPM method 118

Figure 4-19: XRD patterns of HPM-A-6 nanocomposites at different stages 120

Figure 4-20: XRD patterns of HPM-B-6 nanocomposites at different stages 120

Figure 4-21: Schematic illustration of nanocomposites made by different methods... 124

Figure 5-1: Exothermal curves of homopolymerization of DGEBA with different modifiers 133

Figure 5-2: Exothermal cure curves of DGEBA/BF_3.MEA with different modifiers . 135

Figure 5-3: Viscosity-temperature curves of various uncured epoxy systems 137

Figure 5-4: Viscosity-shear rate curves of various uncured epoxy systems at 90°C... 138

Figure 5-5: DMA curves of rubber-modified epoxy and hybrid nanocomposites..... 139

Figure 5-6: Effect of cure temperature on T_gs of epoxy and rubber phases of modified epoxy (8C-20) 141

Figure 5-7: Effects of cure temperature on T_gs of epoxy and rubber phases of hybrid nanocomposites (8CI-20-6) 142

Figure 5-8: Degree of cure of rubber-modified epoxies with concentration of CTBN 143

Figure 5-9: Degree of cure of nanocomposites with clay loading 145

Figure 5-10: T_g of rubber-modified epoxies *versus* concentration of CTBN 146

Figure 5-11: T_g of nanocomposites *versus* clay loading 147

Figure 5-12: Micrographs of rubber-modified epoxies and nanocomposites 150

Figure 5-13: AFM micrographs of rubber-modified epoxy (8C-20) 151

Figure 5-14: AFM micrographs of hybrid nanocomposite (8CI-20-3)..... 152

Figure 5-15: AFM micrographs of hybrid nanocomposite (8CI-20-6)..... 153

Figure 5-16: SEM micrographs of fracture surfaces 155

Figure 5-17: TEM image of the nanocomposite (8I-6) at low magnification 156

Figure 5-18: TEM image of the nanocomposite (8I-6) at high magnification 157

Figure 5-19: XRD patterns of nanocomposites with different clay loadings 158

Figure 5-20: XRD patterns of hybrid nanocomposites with different clay loadings ... 159

Figure 5-21: XRD patterns of 8I-6 nanocomposites at different stages 160

Figure 5-22: XRD patterns of 8CI-20-6 nanocomposites cured at different temperatures 161

Figure 5-23: Schematic representation of phase separation scheme 163

Figure 6-1: Schematic drawings of an exfoliated and ordered nanocomposite (A), and its square representative volume element (RVE) (B) 177

Figure 6-2: Schematic drawings of diffusion of diffusing molecules parallel to the face of clay platelets 179

Figure 6-3: Schematic drawings of diffusion of diffusing molecules in the direction normal to the face of clay platelets 181

Figure 6-4: Schematic drawings of the 2-D and 3-D cases for diffusion of diffusing molecules in a nanocomposite at random orientation 183

Figure 6-5: Schematic drawing of diffusion of diffusing molecules in the direction parallel to the face of the clay platelets in intercalated nanocomposites 187

Figure 6-6: Weight loss of clay and organoclays over time at 120°C 191

Figure 6-7: Water absorption profiles of DGEBA/BF_3.MEA epoxy system at different temperatures 193

Figure 6-8: Water absorption profiles of TGDDM/DDS epoxy system at different temperatures 193

Figure 6-9: Diffusivity obtained with the Fickian law and LMD *versus* environmental temperature for DGEBA /BF_3.MEA and TGDDM/DDS 195

Figure 6-10: Diffusivity with time in DGEBA/BF_3.MEA system at different temperatures 197

Figure 6-11: Different model profiles of DGEBA/BF_3.MEA system at 80°C 198

Figure 6-12: Different model profiles of TGDDM/DDS system at 80°C 198

Figure 6-13: Ratio of longitudinal diffusivity (D_{11}) in an exfoliated and ordered nanocomposite to pure resin (D_m) *versus* volume fraction of clay, at different aspect ratios 200

Figure 6-14: Ratio of transverse diffusivity (D_{22}) in an exfoliated and ordered nanocomposite to pure resin (D_m) *versus* volume fraction of clay, at different aspect ratios 201

Figure 6-15: Ratio of diffusivity (D_n) in a randomly exfoliated nanocomposite to pure resin (D_m) *versus* volume fraction of clay, at different aspect ratios 202

Figure 6-16: Ratio of transverse diffusivity (D_{22}) in an intercalated and ordered nanocomposite to pure resin (D_m) *versus* volume fraction of clay, at different numbers of clay platelets in agglomerates 203

Figure 6-17: Ratio of diffusivity (D_n) in a randomly intercalated nanocomposite to pure resin (D_m) *versus* volume fraction of clay, at different numbers of clay platelets in agglomerates 204

Figure 6-18: Water absorption profiles of filler composites at 23°C 205

Figure 6-19: Ratio of diffusivity (D_c) in filler composites to pure resin (D_m), with clay loading with Fickian law 206

Figure 6-20: Equilibrium moisture content ($M_{c\infty}$) of filler composites with clay loading 207

Figure 6-21: Water absorption profiles of nanocomposites made by the DM method at 23°C 208

Figure 6-22: The equilibrium moisture content (M_∞) of nanocomposites made by DM method, as a function of clay loading 209

Figure 6-23: Ratio of diffusivity (D_n) in nanocomposites made by the DM method to pure resin (D_m), as a function of clay loading, by the Fickian law 210

Figure 6-24: Ratio of diffusivity (D_c) in filler composites to pure resin (D_m) with clay loading with LMD model 211

Figure 6-25: Ratio of diffusivity (D_n) in nanocomposites made by the DM method to pure resin (D_m), as a function of clay loading, by the LMD model 211

Figure 6-26: Ratio ($\alpha/\alpha+\gamma$) *versus* clay loading, for filler composites and nanocomposites made by the DM method 214

Figure 6-27: Water absorption profiles of HPM-E nanocomposites at 23°C 216

Figure 6-28: Water absorption profiles of HPM-A nanocomposites at 23°C 216

Figure 6-29: Ratio of maximum water uptake (M_{nm}) of HPM-E nanocomposites to pure resin ($M_{m\infty}$) *versus* clay loading, at different temperatures 217

Figure 6-30: Ratio of maximum water uptake (M_{nm}) of HPM-A nanocomposites to pure resin ($M_{m\infty}$) *versus* clay loading, at different temperatures 218

Figure 6-31: Ratio of diffusivity (D_n) obtained by Fickian law for HPM-E nanocomposites to pure resin (D_m) *versus* clay loading, at different temperatures 219

Figure 6-32: Ratio of diffusivity (D_n) obtained by Fickian law for HPM-A nanocomposites to pure resin (D_m) *versus* clay loading, at different temperatures 220

Figure 6-33: Ratio of diffusivity (D_n) obtained by LMD for HPM-A nanocomposite to pure resin (D_m) *versus* clay loading, at different temperatures 221

Figure 6-34: Maximum water uptakes of TGDDM/DDS and its nanocomposites made with different dispersion methods, at 6-phr clay loading for 5000 hours at 23°C 222

Figure 6-35: Diffusivities of TGDDM/DDS and its nanocomposites made with different dispersion methods, at 6-phr clay loading at 23°C 223

Figure 6-36: Maximum water uptakes of 30B and I.30E nanocomposites made by the DM method at 3-phr and 6-phr clay loading, for 5000 hours at 23°C 225

Figure 6-37: Diffusivities of 30B and I.30E nanocomposites made by the DM method at 3-phr and 6-phr clay loading, at 23°C 225

Figure 6-38: Maximum water uptakes of 30B and I.30E nanocomposites made by the HPM method at 1.5-phr and 3-phr clay loading, for 5000 hours at 23°C 226

Figure 6-39: Diffusivities of 30B and I.30E nanocomposites made by the HPM method at 1.5-phr and 3-phr clay loading, at 23°C 226

Figure 6-40: Water absorption profiles of I.30E/DGEBA/BF_3.MEA nanocomposites at 23°C 227

Figure 6-41: Ratio of maximum water uptake (M_{nm}) of 8I nanocomposites to pure resin ($M_{m\infty}$) *versus* clay loading, at different temperatures 228

Figure 6-42: Ratio of diffusivity (D_n) obtained by the LMD method for 8I nanocomposite to pure resin (D_m) *versus* clay loading, at different temperatures..... 229

Figure 6-43: Water absorption profiles of DGEBA/BF3.MEA pure epoxy (8F) and rubber-modified epoxy (8C-20), at different temperatures..... 230

Figure 6-44: Maximum water uptake (M_{rm}) of rubber-modified epoxies *versus* CTBN concentration, at different temperatures 231

Figures 6-45: Fickian, LMD and DTVD numerical fits for rubber-modified epoxy at 20-phr CTBN concentration, at different temperatures 232

Figure 6-46: Ratio of diffusivity (D_r) obtained by the LMD method for rubber-modified epoxies to pure resin (D_m) *versus* CTBN concentration, at different temperatures..... 233

Figure 6-47: Water absorption profiles of hybrid nanocomposites modified with CTBN rubber and I.30E organoclay, at 80°C..... 234

Figure 6-48: Maximum water uptake (M_{nm}) of hybrid nanocomposites *versus* clay loading, at different temperatures 235

Figure 6-49: Ratio of diffusivity (D_n) obtained by the LMD method for hybrid nanocomposites to pure resin (D_m) *versus* clay loading, at different temperatures..... 236

Figure 7-1: Three basic modes for crack propagation: Mode I, tensile opening model; Mode II, sliding or in-plane shear mode; Mode III, tearing or anti-plane shear mode... 243

Figure 7-2: Stress analysis near a sharp crack tip of an isotropic and elastic plate [ref. 144] 245

Figure 7-3: Schematic illustration of crack pinning [ref. 146] 247

Figure 7-4: Schematic drawing of pull-out of clay platelets..... 252

Figure 7-5: Schematic drawings of pull-out of clay platelets in the direction normal to the face of the clay platelets in an exfoliated nanocomposite 253

Figure 7-6: Schematic drawings of crack propagation and fracture modes of clay platelets in the completely random orientation in an exfoliated nanocomposite 256

Figure 7-7: Schematic drawing of pull-out of clay platelets in the direction normal to the face of the clay platelets in the intercalated nanocomposite 257

Figure 7-8: Schematic drawing of pull-out of clay platelets in the direction parallel to the face of the clay platelets in the intercalated nanocomposite 259

Figure 7-9: Schematic drawings of a cube representative volume element (RVE) and crack propagation and fracture mode in intercalated nanocomposite 261

Figure 7-10: Specimen dimensions of SENB. 263

Figure 7-11: K_{IC} of nanocomposites and filler composites made by the DM method. 265

Figure 7-12: G_{IC} of nanocomposites and filler composites made by the DM method. 265

Figure 7-13: Ratio K_{IC} (nanocomposite)/K_{IC} (matrix) *versus* ratio (d_p/D_s), for nanocomposites made by the DM method 267

Figure 7-14: SEM micrographs of TGDDM/DDS epoxy systems. 268

Figure 7-15: SEM micrographs of filler composite at 6-phr clay loading. 270

Figure 7-16: SEM micrographs of a nanocomposite made by the DM method. 272

Figure 7-17: K_{IC} of nanocomposites made by different methods. 275

Figure 7-18: G_{IC} of nanocomposites made by different methods. 275

Figure 7-19: Schematic illustration of rectangular obstacles. 277

Figure 7-20: Ratio K_{IC} (nanocomposite)/K_{IC} (matrix) *versus* ratio (ℓ/D_s) for nanocomposites made by the HPM method 277

Figure 7-21: SEM micrographs of HPM-E nanocomposite at 6-phr clay loading. 279

Figure 7-22: SEM micrographs of HPM-A nanocomposite at 6-phr clay loading..... 280

Figure 7-23: K_{IC} of nanocomposites with different methods at 6-phr clay loading..... 281

Figure 7-24: G_{IC} of nanocomposites with different methods at 6-phr clay loading 282

Figure 7-25: SEM micrographs of the GMM-2 nanocomposite at 6-phr clay loading 284

Figure 7-26: SEM micrographs of the GMM-4 nanocomposite at 6-phr clay loading 285

Figure 7-27: SEM micrographs of the GMM-6 nanocomposite at 6-phr clay loading 286

Figure 7-28: K_{IC} of nanocomposites based on different epoxy systems with the HPM method..... 288

Figure 7-29: G_{IC} of nanocomposites based on different epoxy systems with the HPM method..... 288

Figure 7-30: SEM micrograph of BF_3.MEA/DGEBA epoxy system..... 289

Figure 7-31: SEM micrograph of I.30E/BF_3.MEA/DGEBA nanocomposite at 6-phr clay loading..... 289

Figure 7-32: K_{IC} of rubber modified epoxies with concentration of CTBN..... 291

Figure 7-33: G_{IC} of rubber modified epoxies with concentration of CTBN..... 291

Figure 7-34: SEM micrographs of rubber modified epoxies..... 293

Figure 7-35: The critical stress intensity factor (K_{IC}) of nanocomposites with clay loading..... 295

Figure 7-36: The critical strain energy release rate (G_{IC}) of nanocomposites with clay loading..... 295

Figure 7-37: SEM micrographs of hybrid nanocomposites..... 297

LIST OF TABLES

Table 3-1: Typical properties of DGEBA and TGDDM epoxy resins 48

Table 3-2: Typical properties of curing agents 49

Table 3-3: Compositions and properties of clay and organoclays 50

Table 3-4: Typical dry particle sizes (micrometers) 51

Table 3-5: Sediment volumes (ml) of clay-acetone suspensions after three months at room temperature 64

Table 3-6: Basal spacing of suspensions with different mixing methods 73

Table 3-7: Maximum possible solid volume concentrations (φ_m) of suspensions 77

Table 4-1: Notation for nanocomposites and filler composites 93

Table 4-2: Structural parameters of nanocomposites 123

Table 5-1: Notation of nanocomposites and rubber-modified epoxies 130

Table 5-2: Degrees of cure and T_gs of nanocomposites and rubber-modified epoxies 144

Table 6-1: Basal spacing and volume reduction of clay and organoclays before and after drying 191

Table 6-2: Water uptake parameters of DGEBA /BF_3.MEA system 195

Table 6-3: Water uptake parameters of TGDDM/DDS system 196

Table 6-4: Water uptake parameters obtained by LMD for filler composites 212

Table 6-5: Water uptake parameters obtained by LMD for nanocomposites made by the DM method 213

Table 7-1: Predicted values of σ_c/σ_m as a function of d_p/D_s for particle-filled composites 248

Chapter 1

Introduction

Polymer-clay nanocomposite (PCN) is a multi-phase material in which clay particles are dispersed in the continuous polymeric matrix on a nanometer (10^{-9} m) scale. This new class of materials has attracted increasing interest from both scientific and industrial perspectives, because they show dramatic improvements in mechanical properties, barrier properties, thermal and flame resistance at lower clay loadings than their micro-scale counterparts [1-3]. This loading-to-performance ratio is known as the "nano-effect".

In advanced composites, the fiber phase provides most of the strength and stiffness of these composites. However, the matrix phase dominates many key properties, such as mechanical properties in hot/wet conditions, toughness, flame resistance and processing versatility, *etc.* New technologies for modifying polymeric matrices are being pursued in order to increase the applications of advanced composites. Recently, nanocomposite technology using clay particles as a nano-scale reinforcement offers an interesting alternative for modifying polymer matrices. It will be possible to combine nano-scale reinforcement and long-fiber composite technologies in the near future.

1.1 Overview of the Project

1.1.1 Project Motivation

Epoxy resins have been widely used as matrices of advanced composites in aerospace industries as well as in other structural applications, due to their good comprehensive properties such as relatively high strength and stiffness, thermal stability, good corrosion resistance, processing versatility, reasonable cost *etc* [4, 5]. However, there are some disadvantages of unmodified epoxy resins, which seriously limit their application. For example, highly crosslinked epoxy resin systems have high glass transition temperature but extreme brittleness, offering values of G_{IC} about 100 J/m^2 [6]. Application of these epoxy systems is limited to situations where the stress is relatively low and preferably static. The general way to improve fracture toughness is to add some modifier such as liquid rubbers [7] or engineering thermoplastics [8] and fillers [9] into epoxy resins. However, this typically results in one or more of the following problems: increase of cost, reduction of T_g, poorer processing versatility and mechanical properties under hot/wet conditions.

Moreover, these epoxy resins easily absorb moisture from high humidity environments, which lowers the glass transition temperature (T_g) greatly; typically, 1% absorbed water reduces the T_g by 20°C [6, 10]. This reduces the strength and stiffness of these resins, and those mechanical properties of advanced composites which are controlled by the matrix or matrix/fiber interface, especially at elevated temperature [11]. Thus the maximum service temperature of epoxy resins is greatly limited.

Recently, using clay as nano-scale reinforcement to modify epoxy resins offers an interesting alternative. Large improvements of mechanical and physical properties of epoxy-clay nanocomposites such as increases of modulus, strength and toughness [12], reduction of absorbed moisture [13] and residual stresses [14], and flammability resistance [15] at low clay content have been reported. However, most work has been on epoxies for coatings or non-structural epoxies; there is very limited work on epoxy-clay nanocomposites based on epoxy resins for structural applications. Therefore, the study and exploration of the potential properties of epoxy-clay nanocomposites for structural applications is the motivation of this thesis.

1.1.2 Challenges

Epoxy-clay nanocomposites are widely studied, and their formation mechanism and performances have been reported [16-20]. However, much is still unknown concerning the relationships between materials, synthesis, structure and properties of epoxy-clay nanocomposites, especially for structural epoxy resins. For example, exfoliated nanocomposites are the objective of most researchers, because they provide dramatic improvements in mechanical and physical properties. However, it is extremely difficult to synthesize completely exfoliated nanocomposites. Organoclays are not uniformly distributed, and agglomerates of organoclays are observed in epoxy resins. In Transmission Electron Microscopy (TEM) images of epoxy-clay nanocomposites in almost all published papers, few exfoliated platelets of clay are observed. As a result, the biggest challenge is how to exfoliate platelets of clay in epoxy resins. The scientific challenges encountered in this thesis can be summarized as follows:

- How to disperse organoclays in uncured epoxy resins?
- How to understand the formation of exfoliated nanocomposites?
- What is the morphology of hybrid nanocomposites with rubber and organoclay?
- How to understand and predict the improved properties of epoxy–clay nanocomposites?

1.1.3 Objectives

The objectives of this dissertation research are:

- To further explore the formation mechanism of epoxy-clay nanocomposites
- To analyze the relationships of materials, synthesis, structure and properties of epoxy-clay nanocomposites
- To use polymer-clay nanotechnology to improve epoxy resin systems for structural applications, such as matrices of advanced composites and structural adhesives in the aerospace industry.

1.2 Content of the Thesis

In this thesis a new method, high pressure mixing (HPM), is proposed to disperse organoclay into organic media. The synthesis of high performance epoxy-clay nanocomposites and hybrid nanocomposites with rubber and organoclay for structural applications is described. The effects of organoclay and dispersion methods on the morphology and properties of these epoxy-clay nanocomposites are investigated.

A general overview of epoxy-clay nanocomposites is given in Chapter 2. First, materials including clay, organoclay and epoxy resin systems are introduced; then synthesis processes and characterization of nanocomposites are described; finally, the physical and mechanical properties of nanocomposites are discussed.

Dispersion of organoclays in epoxy resins is studied in Chapter 3. Three dispersion methods: Direct Mixing (DM), High-Pressure Mixing (HPM), and Grinding Media Mill (GMM), are chosen to disperse organoclays into epoxy resins and other organic solvents. The dispersion quality of organoclays in these organic solvents and epoxy resins is characterized by rheological measurements, free swelling, sediment tests and X-ray diffraction (XRD). Effects of process pressures in the HPM method on dispersion quality of organoclays are investigated. The stability of organoclays in epoxy monomers and curing agents is investigated.

Synthesis of organoclay-modified high performance epoxy nanocomposites with different dispersion methods is presented in Chapter 4. The cure kinetics of epoxy systems in the presence of organoclays is studied by Differential Scanning Calorimeter (DSC). The morphology of high performance epoxy-clay nanocomposites is characterized by optical microscopy, XRD, TEM and Scanning Electron Microscopy (SEM). A formation mechanism and structural models of the nanocomposites are proposed.

Synthesis of hybrid-modified epoxy nanocomposites with organoclay and rubber is described in Chapter 5. The cure kinetics of a bi-functional epoxy system in the presence of organoclays and rubber is studied by DSC. The rheological properties of

various epoxy systems are measured. The effect of curing temperature on the formation of rubber phase is investigated by Dynamical Mechanical Analyzer (DMA), and the degrees of cure and T_g of all modified epoxies are measured. The morphology of hybrid-modified epoxy nanocomposites is characterized by microscopy, Atomic Force Microscopy (AFM), XRD, TEM and SEM. A formation mechanism and structural models of hybrid nanocomposites with organoclay and rubber are proposed.

Water uptake behavior of epoxy-clay nanocomposites is studied in Chapter 6. Models for the diffusivities of exfoliated and intercalated nanocomposites are developed. The equilibrium moisture content of nanocomposites is measured in specimens immersed in distilled water at different temperatures for 5000 hours. Diffusivities are determined by fitting Fick's Law, the Langmuir Model of Diffusion (LMD), and Diffusion with Time-Varying Diffusivity (DTVD) to the experimental data, employing a least-square approach. Diffusion models for nanocomposites are discussed and confirmed by experimental data on different kinds of nanocomposites. The effects of material, dispersion processes and morphology on water uptake behavior of nanocomposites are investigated.

Fracture toughness of epoxy-clay nanocomposites for structural applications is studied in Chapter 7. The toughening mechanisms of particle-filled and rubber-modified epoxies are reviewed. The critical stress intensity factor (K_{IC}) and critical strain energy release rate (G_{IC}) of nanocomposites, filler composites and rubber-modified epoxies are measured with single-edge-notch bending (SENB). The effects of material, surface modification, processes and morphologies on fracture toughness are discussed. Fracture surfaces of specimens are observed using SEM, to elucidate the toughening in the

materials. The crack pinning mechanism is applied to toughen exfoliated and intercalated nanocomposites.

In Chapter 8, conclusions are drawn based on dispersion of organoclay in epoxy systems: synthesis, characterization and properties of nanocomposites. Future experimental research work is proposed in order to transfer our current technology from the laboratory bench to the factory environment.

Chapter 2

Background and Literature Review

Clay has been used as a filler in polymers for many years, such as kaolin, bentonite and attapulgus [21]; however it plays little functional role, and mainly serves economic considerations. It was not until the early 1990's that clay received great attention from the polymer industry, when Toyota's researchers discovered the possibility of constructing a nanostructure with a polymer and an organoclay [22, 23].

In general, polymer-clay composites may be divided into the following three categories (shown in Figure 2-1) [1]:

Conventional composite, where the clay particles exist in their original aggregated states, without intercalation of polymer matrix into the galleries of clay;

Intercalated nanocomposite, where polymers are inserted into the galleries of clay;

Exfoliated (delaminated) nanocomposite, where individual 1 nm-thick layers of clay are dispersed in a continuous polymer matrix.

The exfoliated configuration is of particular interest, because it maximizes the interactions between polymers and clay. Thus, this configuration should result in maximum changes in mechanical and physical properties.

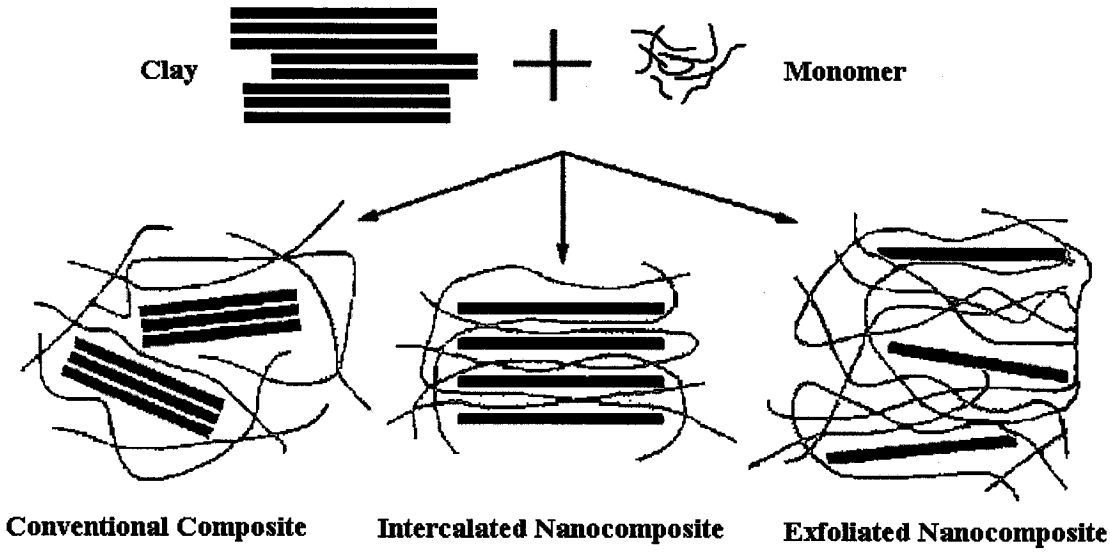

Figure 2-1: Schematic illustration of clay-polymer structure

The purpose of this chapter is to give an overview of epoxy-clay nanocomposites. First the materials, including clay, organoclay and epoxy resin systems, are introduced. Then different process methods available to synthesize epoxy-clay nanocomposites, the formation mechanisms of nanocomposites, and characterization methods of nanocomposites are described. Last, the physical and mechanical properties of nanocomposites are discussed.

2.1 Clay and Organoclay

Clays are categorized as either swelling or non-swelling; swelling clays are called smectites [24]. This study focuses on a natural clay of the smectite family, montmorillonite. Because of its ability to thicken by swelling, suitable layer charge density, and low cost, it is nowadays the most widely used clay as a nano-filler. The

terms "organoclay" or "nanoclay" refer to organically modified clay, and will be discussed in more detail in section 2.1.2.

2.1.1 Montmorillonite

Montmorillonite refers to all clay materials with an expanding lattice except vermiculite, formed by the weathering of eruptive rock materials such as tuffs and volcanic rocks; it can be found all over the world.

All clay materials consist of two basic structural units: silica tetrahedra (a silicon atom surrounded by four oxygen atoms), and alumina octahedra (a cation coordinated with six oxygens or hydroxyl units) [25]. Montmorillonite is a 3-layer crystal sheet (shown in Figure 2-2), consisting of two tetrahedral layers sandwiching an octahedral layer [26]. The chemical formula of montmorillonite is $(OH_2)_{12}AlSi_8O_{16}{\bullet}nH_2O$. Non-stoichiometric substitutions of Si^{4+} by Al^{3+} in the tetrahedral layer, and of Al^{3+} by Mg^{2+} in the octahedral layer, cause an excess of negative charges within the montmorillonite layers. These negative charges are counterbalanced by interlayer cations, such as Ca^{2+} and Na^{+}. The counter ions can be shared by two neighboring platelets, resulting in stacks of platelets that are tightly held together.

Montmorillonite often exists in a multi-scale organization in nature (shown in Figure 2-3). Each platelet is 9.6 Å thick, but 100~1000 times that in width; eight to ten platelets are associated by interlayer cations in primary particles, and larger irregular aggregates are mainly present in nature [27]. The sum of the single platelet (9.6 Å) and the interlayer represents the repeating unit of the multilayer material, the so called d-spacing or basal spacing, which can be calculated from X-ray diffraction patterns.

A single platelet of clay or a primary particle containing several platelets of clay has a higher aspect ratio (ratio of length to thickness) and larger special surface area (surface area per unit in weight) than an aggregate. When clay platelets are completely dispersed into individual platelets, the total surface area is calculated at $752m^2/g$ [28]. Compared with polymers, the platelets of montmorillonite have high in-plane strength and stiffness.

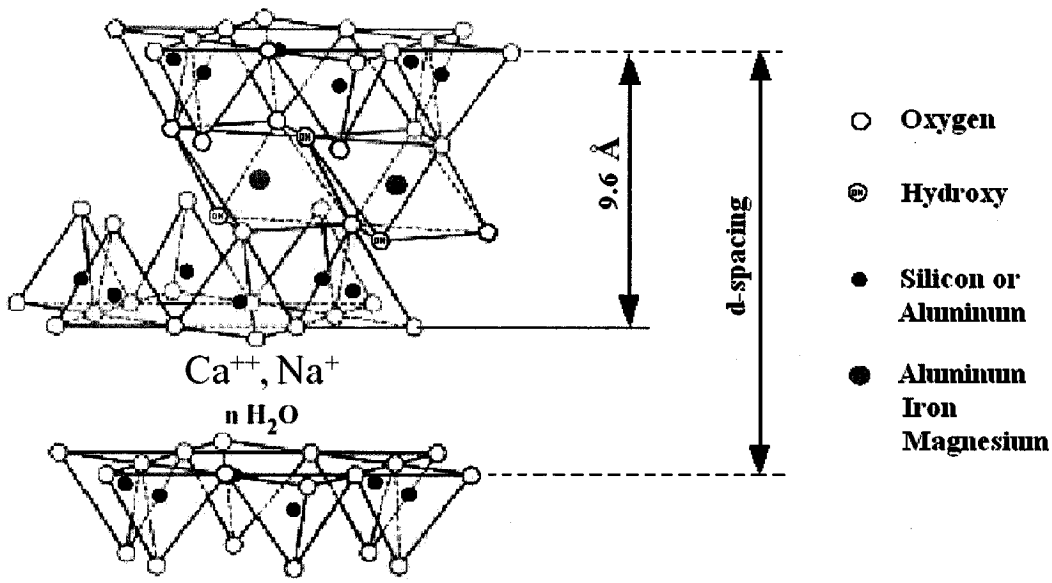

Figure 2-2: Idealized structure for montmorillonite [ref. 26]

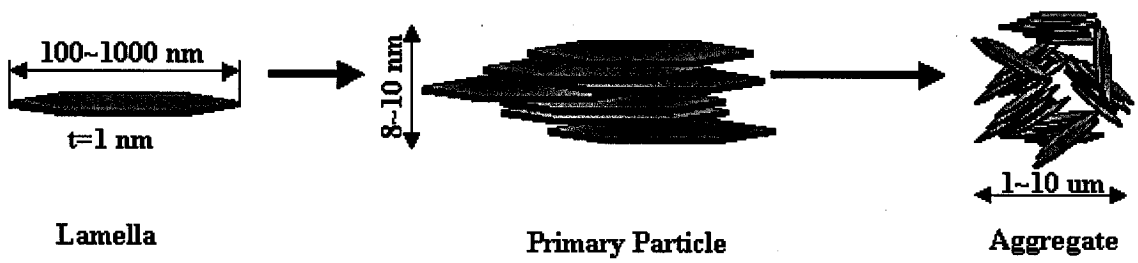

Figure 2-3: Schematic microstructure of montmorillonite [ref. 27]

2.1.2 Organoclay

Montmorillonite is naturally hydrophilic; the stacks of clay platelets are held tightly together by electrostatic forces. As a result, they are generally incompatible with most organic polymer matrices. A popular and relatively easy method of modifying the clay surface is ion exchanging with compatibilizing agents. The alkali cations of montmorillonite can be exchanged out of the clay, and be replaced with organophilic cations such as alkylammonium ions. The exchangeability of cations is $Na^+ < K^+ < Mg^{2+} < Ca^{2+} < NH_4^+$ [28]. For a given clay, the maximum proportion of cations that can be taken up is constant, known as the cation-exchange capacity (c.e.c.). Its unit is milliequivalents per gram (meq/g) or per 100 g (meq/100g). The c.e.c. of montmorillonite varies from 80 to 150 meq/100g [28].

In general, a molecule of a compatibilizing agent consists of one hydrophilic function and one organophilic function. Its role is to improve compatibility between polymers and clay, in order to disperse clay in polymers. The first compatibilizing agents used in the synthesis of nanocomposites (polyamide 6-clay hybrids) were amino acids [22]. Molecules of amino acids consist of a basic amino group ($-NH_2$) and an acidic carboxyl group (-COOH); in an acidic medium, a proton (H^+) is transferred from the –COOH group to the intramolecular $-NH_2$ group. A cation exchange is then possible between the $-NH_3^+$ and a cation (*i.e.* Na^+, K^+) in the clay, so that the clay becomes organophilic. The acid function has the ability to polymerize with ε-caprolactam intercalated between the layers. Thus, polymerization occurs in the

galleries of clay to exfoliate the clay platelets in the polymer matrix, and an exfoliated nanocomposite is formed.

Numerous other kinds of compatibilizing agents have been used in the synthesis of nanocomposites. The most popular are alkylammonium ions, because they can be exchanged easily with the ions between the layers. The basic formula of alkylammonium ions is $CH_3\ (CH_2)_n\text{-}NH_3^+$, where n is between 1 and 18. These ions are formed by putting primary alkylamines into an acidic medium to protonate the amine function. The cation exchange process of linear alkylammonium ions is described in Figure 2-4; the cationic ammonium associates with the negative charges of the clay sheets, and the carbon chains extend away from the clay layers, generally leading to an increased d-spacing of clay.

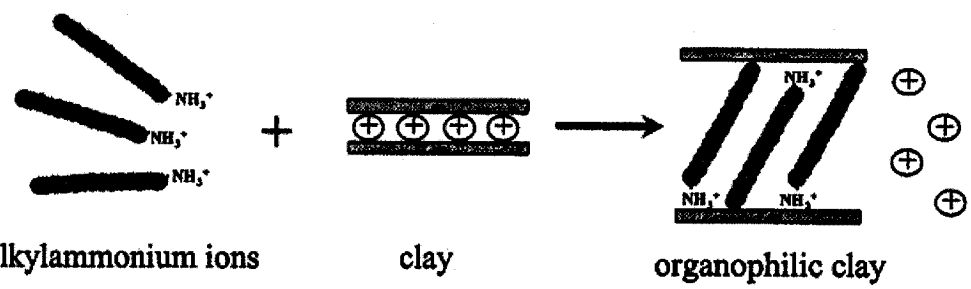

Figure 2-4: Cation exchange process between alkylammonium ions and cations initially intercalated between clay layers [ref. 28]

The chain length of the alkylammonium ions has a great influence on the d-spacing of clay, swelling in organic solvents, and the structure of nanocomposites. The d-spacing of organoclay increases in proportion to the chain length of the alkylammonium ions; Jordan first demonstrated that intergallery swelling in organic

solvents is significant as the modifying ion alkyl chains are based on more than 10 carbon atoms [29]. Lan, *et al.* reported that the basal spacings for a series of epoxy-solvated $CH_3(CH_2)_n$-NH_3^+ montmorillonites with n=4, 8, 10, 12, 16 and 18 increase in proportion to the chain length of the alkylammonium ions. Montmorillonites intercalated by long-chain (n>8) alkylammonium ions allow the formation of exfoliated nanocomposites, whereas clays intercalated by shorter alkylammonium cations tend to afford an intercalated nanocomposite configuration [17].

Organoclays modified with alkylammonium ions containing the same long chain but different head groups, such as $CH_3(CH_2)_{17}NH_3^+$, $CH_3(CH_2)_{17}N(CH_3)H_2^+$, $CH_3(CH_2)_{17}N(CH_3)_2H^+$ and $CH_3(CH_2)_{17}N(CH_3)_3^+$ have slightly increased d-spacing with molecule weight [18]. However, these organoclays have the same d-spacing in epoxy resins, indicating that the d-spacing of organoclays is controlled by the C_{18} long alkyl chain.

There are two major suppliers of organoclay for nanocomposites: *Southern Clay Products, Inc.* and *Nanocor, Inc.* *Nanocor's* products for epoxy resin are *Nanomer* I.30E and I.28E, which are alkylammonium ion surface-modified montmorillonites [30]. The former is designed to be easily dispersed into amine-cured epoxy resins to form nanocomposites; the latter is for anhydride-cured ones. *Southern Clay Products, Inc.* does not specify organoclays for epoxy resins; their products are *Cloisite* 10A, 15A, 20A, 25A, 30B and 93A [31].

One laboratory-purified, and two commercially available alkylammonium (octadecyl amine) exchanged montmorillonites from Nanocor, were studied to form

rubbery and glassy epoxy-clay nanocomposites [1, 32]. All of these nanocomposites are characterized by the absence of peaks in X-ray diffraction patterns, providing evidence that the d-spacing of clay platelets is increased in the epoxy curing process. It is noteworthy that commercially available organoclays prepared on an industrial scale afford nanocomposites with performance properties comparable with those purified in the laboratory, although there are differences in their platelet aspect ratio, layer charge density, and degree of exfoliation.

Two commercially available organoclays, *Nanomer I.30E (Nanocor)* and *Cloisite 30 B (Southern Clay Products)*, were selected for this study. The former is an octadecyl amine-modified montmorillonite; the latter contains two hydroxyls. They are widely used as reinforcements in epoxy-clay nanocomposites by other researchers [33-37], and they provide similar results as laboratory-purified organoclays [36, 37].

2.2 Epoxies

Epoxy resin is often applied to both prepolymers and cured resins; the former contains reactive epoxy groups, three-membered rings containing two carbons and an oxygen (shown in Figure 2-5), hence their name [6]. And the term "epoxy resin system" is often used for the system containing both epoxy prepolymers and curing agents.

The most common epoxy resin is based upon the condensation polymer formed from epichlorohydrin and bisphenol A, called diglycidylether of bisphenol A (DGEBA), and shown in Figure 2-5. This resin is a bi-functional epoxy available in various chain

lengths, depending on the amounts of reactants present and other reaction conditions, with commercial examples being Epon-826, 828 (*Shell*), DER317, 324, and 332 (*Dow Chemicals*). The presence of glycidyl units in these resins enhances the processability, but reduces thermal resistance. Higher T_g and improvement in thermal and mechanical properties can be achieved by either introducing thermally stable rigid rings in the backbone, or by increasing cross-link density, such as in a multi-functional epoxy resin, tetraglycidyl 4,4'-diamino-diphenyl methane (TGDDM), which has four reactive epoxy groups per molecule.

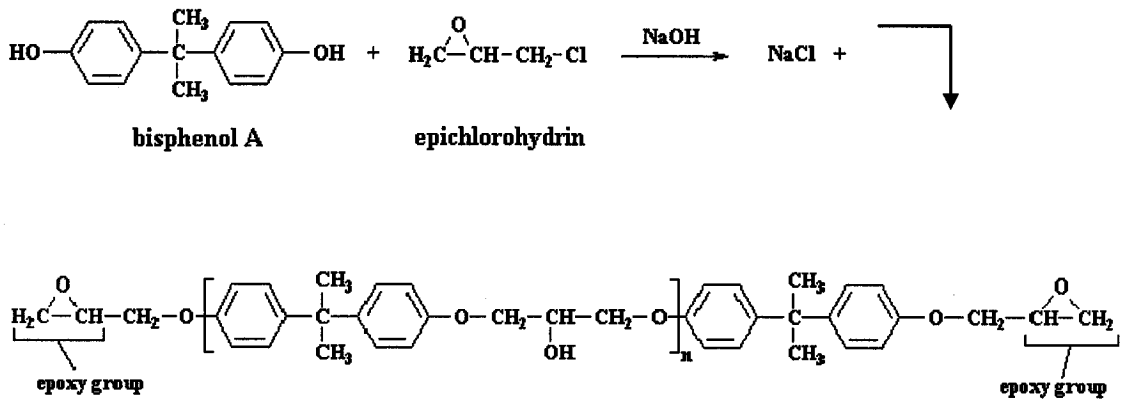

Figure 2-5: Synthesis reaction of diglycidylether of bisphenol A (DGEBA)

In order to achieve optimum performance by cross-linking epoxy resins into a three-dimensional and infusible thermoset network, it is necessary to use curing agents (hardeners), either reactive or catalytic. A catalytic curing agent such as Lewis acids functions as an initiator for homopolymerization of epoxy resins, whereas the reactive type acts as a co-monomer in the polymerization process. The choice of curing agent depends on the processing method, curing conditions (*i.e.* curing temperature and time),

physical and chemical properties desired, toxicological and environmental limitations, and cost. The properties of cured epoxy systems are greatly dependent on the nature of the curing agents used. Some cured epoxies are rubbery at room temperature; others may be glassy when the same epoxy resin is cured by different curing agents, even with similar chemical structure. In general, cured epoxy systems have higher T_g and thermal stability, as the curing agents used contain thermally stable rigid rings in the backbone, or provide higher cross-link density.

A variety of curing agents containing active hydrogen atoms, such as aliphatic or aromatic amines, polyamides, anhydrides, dicyandiamide, *etc.* have been used in composites and adhesives. Amines are the most common curing agents, because they offer good reactivity with the epoxy groups and exist in a wide variety. One amino group reacts with two epoxy groups (shown in Figure 2-6); the primary amino group is more reactive than the secondary towards epoxy. At the gel point, most of the primary amino groups (95%), but only some of the secondary (28%), are consumed [38].

Lewis acids (*e.g.*, boron trihalides) also react easily with the epoxy group to initiate the curing reaction (shown in Figure 2-7) [38]. Boron trifluoride monoethylamine (BF_3.MEA) is the Lewis acid most widely used in advanced composites. BF_3.MEA does not initiate a curing reaction at lower temperatures (< 92°C), but enhances epoxy group reactivity at higher temperatures [39]. This feature makes BF_3.MEA widely used, either alone as a curing agent for manufacturing processes which need a long time at room temperature, or with other cure agents, in order to enhance crosslink density of the matrices in advanced composites.

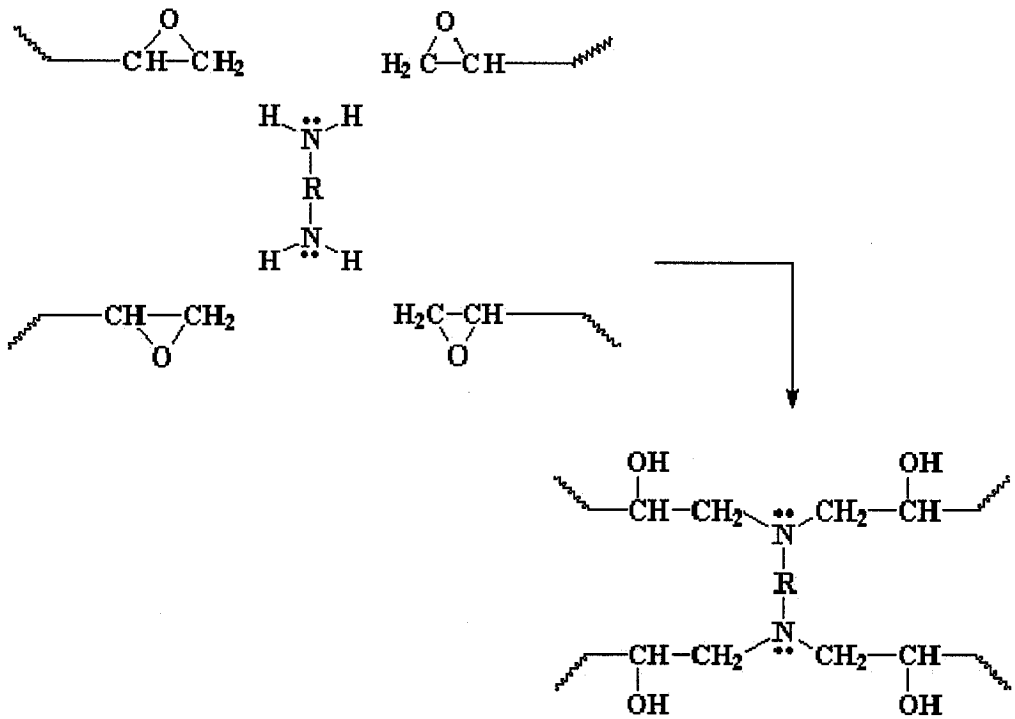

Figure 2-6: Cure reaction of epoxy resins cured with amines [ref. 38]

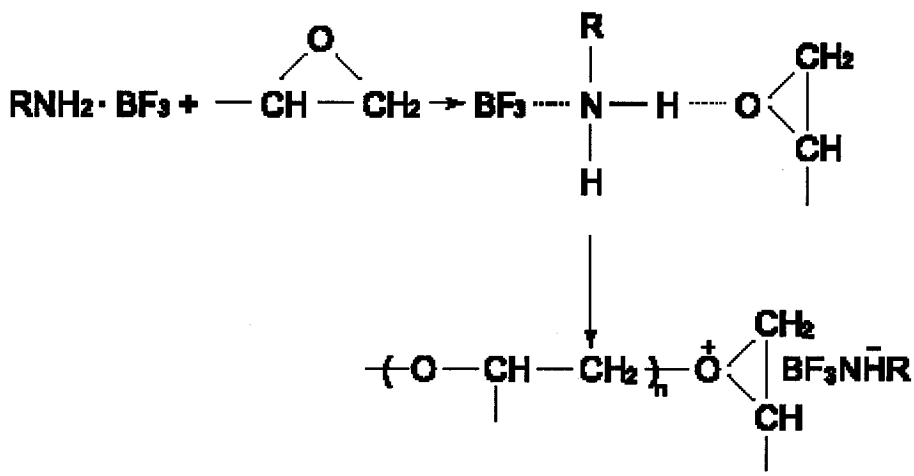

Figure 2-7: Cure reaction of epoxy resins cured with BF_3.MEA [ref. 38]

Epoxy resin systems are widely used in the aerospace industry and other structural applications, and are divided into two categories according to curing and service temperatures. One group is cured at medium temperature (120~150°C), and can be used at 80~100°C for civil airplanes and helicopters; the other is cured at high temperature (177°C), and can be used at 130~150°C for military aircraft, or composite parts of civil airplanes and helicopters near the engines. The former group mainly consists of DGEBA epoxy resins cured with aromatic amines, dicyandiamide, urea formaldehyde, or BF_3.MEA, and modified with liquid reactive rubbers. The latter mainly consists of multi-functional epoxy resins such as TGDDM, and aromatic amine curing agents such as diaminodiphenyl sulphone (DDS), modified with thermoplastics.

Epoxy resin systems for structural applications are usually very brittle, due to their high crosslink density. Thus, they have to be modified prior to using them. Among all the approaches that have been considered and adopted in an attempt to alleviate the brittle characteristics of epoxy resins, rubber-modification is possibly the most successful. Strong improvement in fracture surface work and fracture energy can be achieved by adding 5 to 15% carboxyl-terminated butadiene acrylonitrile (CTBN) rubber. However, the use of rubber as a toughening agent results in reduced elastic modulus, high temperature properties, and poorer creep resistance of epoxy resins. Therefore, this technology is only used for epoxy resin systems cured at medium temperature. For high modulus and high T_g epoxy resins such as TGDDM-DDS, modification with thermoplastics not only provides a higher level of toughness enhancement than that provided by rubber [40], but also retains the comparatively high modulus and Tg values,

regarded as highly advantageous [41]. Therefore, in most cases, this kind of epoxy is only modified by thermoplastics under consideration for high temperature applications.

Epoxy-clay nanocomposites have been extensively studied [16-20], because the reactants of epoxy systems have suitable polarity so that they can diffuse into the galleries of clay, and form an exfoliated nanocomposite upon polymerization. However, so far dramatic improvement of properties is usually only reported for rubbery state epoxy resins [12, 42]; in glassy epoxies, the benefit of epoxy-clay nanocomposites is not obviously greater than that of most particulate-filled systems.

Most researchers select DGEBA epoxy resins cured with aliphatic amines with different carbon chain lengths to synthesize epoxy-clay nanocomposites. These epoxy systems have low T_g and mechanical properties; thus they are only used for coatings or other non-structural applications. In this study, two types of epoxy resin systems for structural applications are chosen: one is a DGEBA epoxy resin cured with BF_3.MEA, and modified with CTBN liquid reactive rubber; the other is a multi-functional epoxy resin, TGDDM, cured with an aromatic amine curing agent, DDS. Both are widely used as matrices of advanced composites and structural adhesives in the aerospace industry and other structural applications.

2.3 Synthesis of Nanocomposites

Three routes have been developed to form polymer-clay nanocomposites: *In situ* Polymerization; Solution; and Melt intercalation. The last process is important only for thermoplastics, and will not be discussed here.

2.3.1 *In Situ* Polymerization

In situ polymerization was the first method used to form polyamide 6-clay nanocomposites [22]; nowadays, it is the conventional process for synthesizing thermoset-clay nanocomposites. The strategy is described schematically in Figure 2-8.

First, the organoclay is swollen by the monomer; this step requires a certain amount of time, which depends on the polarity of the monomer molecules, the surface treatment of the organoclay, and the swelling temperature. Then, the reaction is initiated; for epoxies, a curing agent is added to initiate the polymerization.

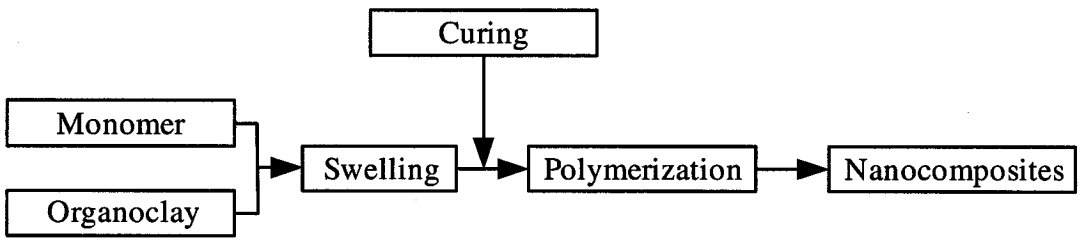

Figure 2-8: Flowchart presenting the different steps of the "*in situ* polymerization" approach

The driving force of the *in situ* polymerization method is linked to the polarity of the monomer molecules. During the swelling phase, the high surface energy of the clay attracts polar monomer molecules, so that they diffuse between the clay layers (see Figure 2-9). When a certain equilibrium is reached, the diffusion stops and the clay is swollen by the monomer to an extent corresponding to a perpendicular orientation of the alkylammonium ions. Then the monomer starts to react with the curing agent to initiate polymerization; this reaction lowers the overall polarity of the intercalated molecules, and

displaces the thermodynamic equilibrium so that more polar molecules are driven between the clay layers. As this mechanism occurs, the organic molecules can eventually exfoliate the clay.

Uncured epoxy resins and curing agents are small molecules, which have a suitable polarity to easily diffuse into the galleries of organoclay. As a result, the *in situ* polymerization method is widely used to synthesize epoxy-clay nanocomposites. In order to break down the clay agglomerates and accelerate clay swelling, mechanical stirring or ultrasonic tooling are used during the mixing process.

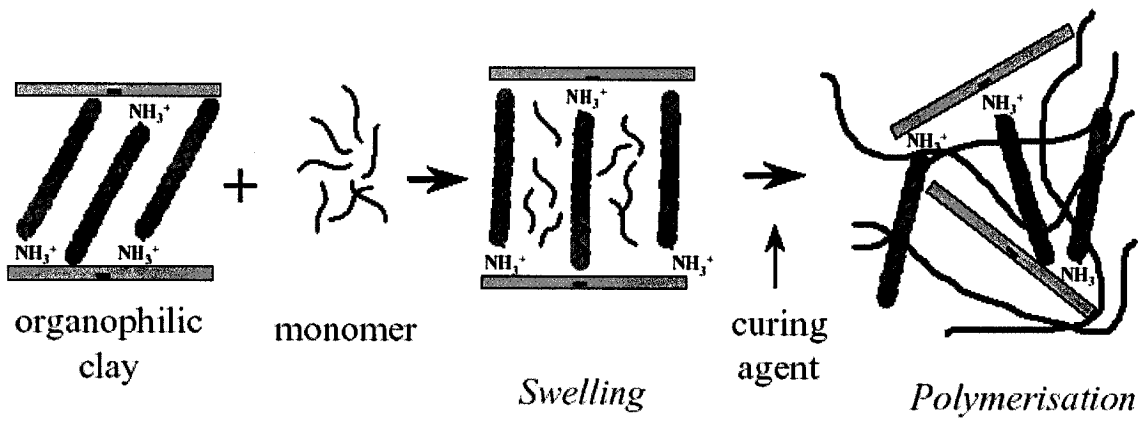

Figure 2-9: Schematic illustration of *in situ* polymerization

2.3.2 Solution Method

Polar solvents can be used to synthesize polymer-clay nanocomposites. The strategy is similar to the one used in the *in situ* polymerization approach.

Figure 2-10 describes the different steps of synthesis of nanocomposites using the solution method. First, the organoclay is dispersed by mechanical stirring, and the

polymer is dissolved in a polar solvent such as acetone, toluene or N, N-dimethylformamide. Then the suspension of organoclay is added to the polymeric solution, and the polymer is intercalated between the clay layers. The last step consists in removing the solvent by evaporation, usually under vacuum. This strategy can be used to synthesize epoxy–clay nanocomposites, but the large amount of solvent required is a major disadvantage.

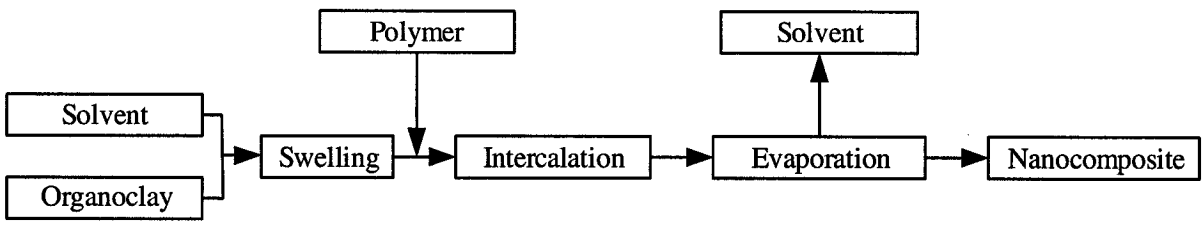

Figure 2-10: Flowchart presenting the different steps of the solution approach

In order to achieve uniform dispersion of exfoliated clays, all components must be compatible. In the first step, the interactions between organoclays and solvents are the key parameters which govern the dispersion of the platelets, and thus determine the final properties of nanocomposites. However, the swelling of organoclays in organic solvents is not yet clearly understood.

Usuki, A. *et al.* [43] reported in their patent that it is necessary to use N, N-dimethylformamide as a swelling solvent to exfoliate $CH_3(CH_2)_{11}COOH^+$ -montmorillonite in the DGEBA epoxy resin cured with DDS.

Chen, *et al.* [36] used acetone, chloroform, tetrahydrofuran, toluene and N, N-dimethylformamide to help the layered silicate particles disperse in an epoxy-amine

system, especially for high clay loading (>10%). Among these solvents, acetone seems better than the others because of its good compatibility, low boiling point and relatively low toxicity.

More recently, Chen and Tolle [44] reported that fully exfoliated layer silicate epoxies were obtained with a combination of high–shear mixing in the presence of acetone and ultrasonication. Homogeneous and random dispersion of individual silicate layers was observed with TEM. However, the TEM images showed aggregation of organoclays in the nanocomposite through processing without solvent assistance.

2.4 Formation Mechanism of Epoxy-Clay Nanocomposites

The formation mechanism of exfoliated epoxy-clay nanocomposites has been widely studied. However, much is still unknown, and some results are contradictory concerning the formation of exfoliated epoxy-clay nanocomposites.

The term "exfoliated nanocomposite" was defined above. However, it is often assumed by many researchers that a nanocomposite is exfoliated as the peak (001) in X-ray diffraction patterns of the nanocomposite disappears.

Exfoliating clay platelets in a polymer requires a driving force, to overcome the attractive electric force between the negatively charged silicate layers and the gallery cations; one way to achieve this effect is to use the energy of intra-gallery self-polymerization. The research group at Michigan State University has studied the self-polymerization of epoxy resin in organophilic smectite clays, due to the presence of alkylammonium ions [45]. The proposed mechanism is described in Figure 2-11,

wherein the dissociation of the alkylammonium cations in the clay galleries generates protons that attack the epoxy ring, causing acid-catalyzed ring-opening homopolymerization. The self-polymerization of epoxy resin in the gallery of organoclays due to the presence of the alkylammonium ions results in polymerization being faster intra-gallery than extra-gallery; thus exfoliated nanocomposites form.

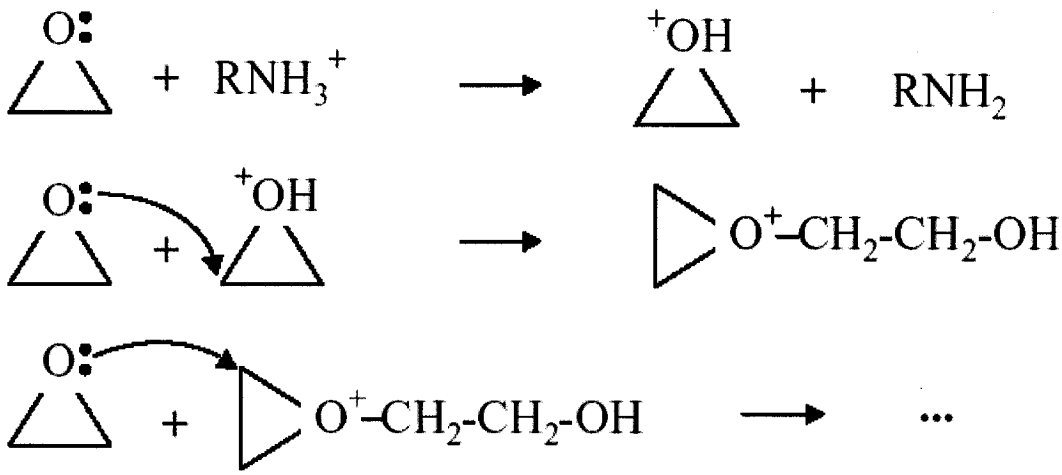

Figure 2-11: Proposed homopolymerization mechanism of DGEBA catalyzed by alkylammonium ions [ref 45]

Another major discovery by the research group at Michigan State University is that a balance is required between intragallery and extragallery polymerization, in order to exfoliate the clay in an epoxy matrix [17]. If the curing temperature is too low, and thus the rates of epoxy and hardener intercalation are too low, then extragallery polymerization will be faster than intragallery, and intercalated nanocomposites form. Intercalated nanocomposites also form if extragallery curing is favored by curing at high temperature. Thus, it is important to select curing conditions that balance the intra- and extragallery polymerization rates. Short alkylammonium exchange ions on the gallery

surfaces make intragallery diffusion more restrictive, and it becomes more difficult to achieve the curing conditions needed to balance the rates of intra-and extragallery polymerization.

This group claimed that they synthesized exfoliated monolithic clay nanocomposites, and thus greatly improved the strength and modulus of the rubbery epoxy matrix [12, 42] and other rubbers such as polyurethane [46] and silicone rubber [47]. However, nanocomposites do not show a monolithic structure, as they describe. The agglomerates of clay were observed at lower magnification, although epoxy resins were indeed observed between the platelets of organoclays with TEM at higher magnification. To our knowledge, a few publications report agglomerates of organoclays in epoxy systems [19, 20, 33, 37], but very few papers work on breaking down the agglomerates.

2.5 Characterization of Nanocomposites

There are two main methods of characterizing the structure of polymer-clay nanocomposites: X-ray diffraction (XRD) and transmission electron microscopy (TEM).

2.5.1 X-Ray Diffraction (XRD)

Wide-angle X-ray diffraction (WXRD) is a very popular, and the most straightforward, method to characterize nanocomposites. Sample preparation is relatively easy, and the X-ray analysis can be performed within a few minutes. It quantifies the spacing of galleries between adjacent layers, and thus proves the widening

of the basal spacing as polymer molecules intercalate between the galleries [48]. The basal spacing can be calculated according to the Bragg equation (shown in Figure 2-12):

$$2d\sin\theta = n\lambda \tag{2-1}$$

Where d is the basal spacing, θ is the X-ray incidence angle, λ is the wavelength of X-rays, and n is integers, 1, 2, 3...

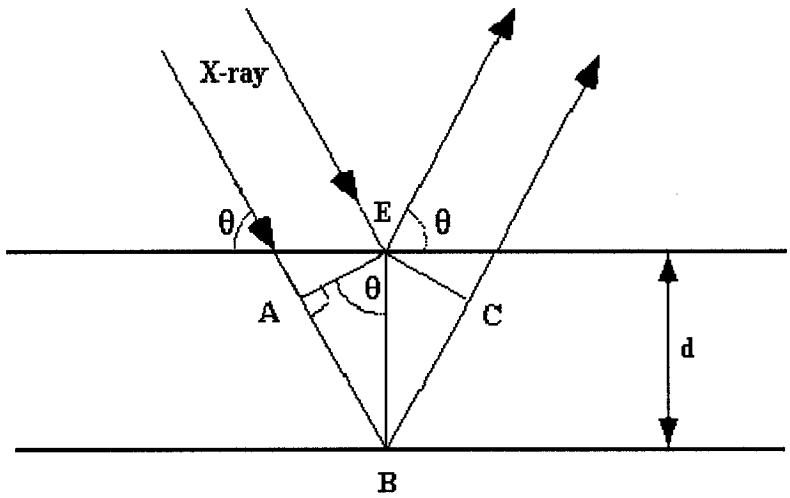

Figure 2-12: Principle of X-ray diffraction

Figure 2-13 shows typical X-ray patterns of epoxy-clay composite materials formed by polymerizing a DGEBA resin with a stoichiometric amount of mPDA as the curing agent in different physical states [17]. The basal spacing of clay can be calculated from X-ray patterns.

However, WXRD can only be used to prove the formation of intercalated nanocomposites with d-spacing less than 4 nm, the resolution limit of typical instruments.

Some researchers consider the complete disappearance of WXRD peaks as a proof of complete or almost complete exfoliation of nanocomposites; but this supposition is not adequate, and needs to be further confirmed by TEM.

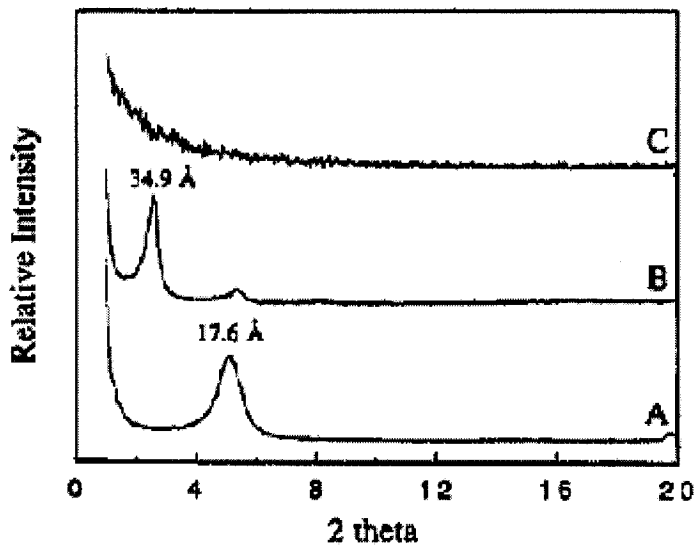

Figure 2-13: X-ray diffraction patterns of $CH_3(CH_2)_{15}NH_3^+$- montmorillonite in different physical states [ref 17]

(A) pristine clay, (B) 5 wt% clay in Epon-828 suspension, and (C) exfoliated clay (5 wt%) in mPDA-cured epoxy nanocomposites

2.5.2 Transmission Electron Microscopy (TEM)

Transmission electron microscopy is a powerful technique for studying structures at and below the nanometer scale; it allows precise observation of nanostructures, with an

exceptional resolution (about 0.2 nm) [49, 50]. Therefore, this technique is widely used in characterizing polymer nanocomposites.

If the specimen is thin enough to form an image in the TEM, it can be assumed that the primary electrons that enter the top of the specimen emerge from the bottom. Regions of the specimen which are thicker or of higher density will scatter the electron beam more strongly, and will appear darker in the image (fewer and fewer electrons transmitted). This phenomenon, known as "mass-thickness contrast", is used to observe the repartition of clay layers in nanocomposite structures. The clay has a higher density than the polymer (about 2.7 and 1.1, respectively); therefore, the clay layers appear darker than the polymer. If the specimen is too thick, the polymer appears darker, and this reduces the contrast with the clay.

Transmission electron microscopy is a necessary complement to X-ray diffraction. TEM gives a direct measure of the spatial distribution of the layers, but it requires substantial skills in specimen preparation and analysis. Therefore it can be used to confirm XRD results about the organization of clay layers in nanocomposites.

2.6 Properties of Nanocomposites

In conventional composites, an improvement of modulus is normally achieved; however this benefit is usually accompanied by sacrificing other properties, such as strength or toughness. Polymer nanocomposites with a relatively low amount of clay provide the possibility of modifying drastically not only mechanical, but also some

physical, properties; but so far such dramatic improvements only occur in polymers whose T_g is near or below room temperature.

2.6.1 Mechanical Properties

Dramatic improvements in tensile strength and tensile modulus of exfoliated nanocomposite structure on polyamide 6-clay hybrids were first reported by Toyota researchers; the tensile strength of polyamide 6 was increased by 55%, and the modulus by 90%, by adding only 4wt% of organoclay [23]. Lan and Pinnavaia [12] reported more than a ten-fold increase in strength and modulus in a rubbery epoxy matrix (Tg ~ -40°C) with only 15wt% (7.5 vol%) of organoclay; the reinforcement effect is dependent on the extent of organoclay separation. The benefit for exfoliated nanocomposites is substantially greater than for intercalated.

The compression behavior of glassy epoxy-clay nanocomposites, based on DGEBA epoxy resin cured with Jeffamine D-230, was studied by Massam and Pinnavaia [1, 32]; the compressive yield strength and modulus of exfoliated nanocomposites were increased by 17 and 27%, respectively, with a clay loading of 10 wt%. Kornmann, *et al.* [51] also conducted compression experiments on nanocomposites based on a similar epoxy system, and obtained the same improvement of compressive yield strength with clay content for exfoliated nanocomposites.

Although an exfoliated nanocomposite structure brings out a substantial increase in modulus for polyamide 6-clay nanocomposite, the fracture energy G_{IC}, unfortunately, is lowered more than 10 times with the addition of only 4 wt% of organoclay [52]. It is thought that the reduction in the extent of plastic deformation in the constrained polymer

matrix increases the brittleness of the nanocomposite; however, increased fracture toughness by adding organoclay into epoxy resin systems is reported by many researchers [33, 53-60]. Kornmann, *et al.* [55] showed a 112% increase in fracture toughness of TGDDM-DDS matrix reinforced by 4.2 vol% organoclay. To the knowledge of the author, very few papers discuss fracture toughness of epoxy-clay nanocomposites where organoclay agglomerates are broken down.

Although the toughening mechanism for epoxy-clay nanocomposites is not clear, most researchers believe that it is mainly attributed to the morphology of epoxy-clay nanocomposites: epoxy resins are intercalated into the galleries of organoclays, and organoclays are agglomerated on a micron scale in epoxy systems. Compared with thermoplastics, epoxy resins are easily improved in toughness by nanotechnology, because they have very low fracture toughness to begin with, two orders of magnitude lower than thermoplastics [6].

2.6.2 Barrier Properties

The substantial decrease of permeability brought about by a nanocomposite structure is also a major advantage of polymer-clay nanocomposites. It was first reported by the Toyota researchers that their polyamide 6 clay hybrid had a rate of water absorption 40% lower compared with the pristine polymer [22, 61].

Later, Messersmith, *et al.* [62] observed a dramatic decrease up to 80%of water permeability with their poly (ε-caprolactam) layered silicate nanocomposite with only 5 vol% of clay.

This impressive decrease of permeability is attributed to the large aspect ratio of the clay layers, which should increase the tortuosity of the path of water and gas molecules as they diffuse into the nanocomposite [63]. Measurements of the permeability of polyimide-clay hybrids, using clays with different aspect ratios, tend to confirm this idea [64].

However, until now there are no reports about great improvements in water uptake behavior for epoxy resins with nanotechnology. Some contradictive results were reported for epoxy-clay nanocomposites [65-68]. The main reason may be that there are discrepancies in the raw materials such as organoclays and epoxy resins, and dispersion methods used by different researchers.

2.6.3 Thermal Properties

Toyota researchers also showed that their new material has an improved thermal stability [23]; the heat distortion temperature of their nanocomposite was 87°C higher than that of unfilled polyamide 6, extending the use of this polymer to under-the-hood structural parts in the engine compartment. This property was combined with a reduction of the thermal expansion coefficient of up to 45%. They thought that the improvement of heat distortion temperature increases with the length and content of silicate layers, and is attributed to the presence of a constrained region in the nanocomposite.

However, epoxy-organoclay nanocomposites do not show this great increase in T_g and heat distortion temperature. While increased T_gs were reported in some cases of epoxy-clay nanocomposites [14, 69, 70], others have found a constant or slightly

decreased T_gs [33, 53, 55]. Messersmith and Giannelis [69] found that glassy epoxy-exfoliated clay nanocomposites formed from epoxy-philic exchange forms of montmorillonite exhibit a broadened T_g at slightly higher temperature than the unmodified polymer.

2.6.4 Flammability

Polymer-clay nanocomposites exhibit very low flammability; the peak heat release rate during combustion of polyamide 6-clay nanocomposite is reduced by 63% at only 5 wt% of clay [71]. Moreover, the nanocomposite structure appears to enhance the performance of the char by reinforcing the char layer; this means that nanocomposite parts conserve their shape during combustion. After ignition for two hours at 1000°C, it is still possible to distinguish the shape that the epoxy-clay nanocomposites samples had prior to ignition.

J. W. Gilman, *et al.* [72] investigated the flammability of intercalated epoxy-clay nanocomposites of different epoxy-hardener systems: DGEBA cured with MDA and DGEBA cured with BDMA. The results show that both the peak and average heat release rates (HRR) are significantly improved for these nanocomposites with 6 wt% organoclay: 40% reduction in peak HRR, average HRR and average mass loss rates (MLR). The heat of combustion, soot and carbon monoxide yields are unchanged.

Chapter 3

Dispersion of Organoclay in Organic Media

Exfoliated nanocomposites are studied by many researchers because they can provide dramatic improvements in mechanical and physical properties. To achieve the desired morphology, it is of first importance to break down the large stacks of clay platelets into single layers, or tactoids of a small number of layers, in the epoxy systems.

In this chapter, clay colloid chemistry is reviewed. Dispersion methods of particles in liquids are discussed; three dispersion methods: Direct Mixing (DM), High-Pressure Mixing (HPM) and Grinding Media Mill (GMM), are used to disperse organoclays into epoxy resins and other organic solvents. Free swelling of organoclays in organic solvents and epoxy resins is studied, and a swelling factor is used to describe the volume increase of organoclays in organic media. Effects of process pressures in the HPM method on dispersion quality of organoclays are investigated. The dispersion of organoclays in these organic media is characterized by rheological measurement, sediment tests, X-ray diffraction and microscopy. The effects of curing agents on organoclays are investigated.

3.1 Introduction

Organoclays are used for many applications, such as absorbing organic pollution in ground water [73], polymer-clay nanocomposites [1-3], coatings and paints, due to their ability to swell and form thixotropic gels in organic media [28, 74]. However, the interactions between organoclays and organic media are not well characterized and understood [75]. True dispersion of organoclay particles in organic solvents, like montmorillonite in water, is very seldom observed, so that the main process is loosening particle/particle contacts [76].

Uncured epoxy resins and curing agents are small molecules which have a suitable polarity to easily diffuse into the galleries of organoclay. As a result, the *in situ* polymerization method is widely used to synthesize epoxy-clay nanocomposites. However, it seems very difficult to uniformly disperse organoclays in epoxy resins, although they have good compatibility with each other, with conventional mixing methods and mechanical stirring and then ultrasonic tooling are used during the mixing process. Epoxy resins were observed in the galleries of organoclays with TEM at higher magnification, but, organoclay agglomerates on a micron scale were observed at lower magnification.

Yasmin *et al.* [77, 78] used a three-roll mill machine as a means of applying shearing forces to disperse I.28E and 30B organoclays, respectively, into an epoxy matrix based on the DGEBA epoxy resin cured with an anhydride hardener. Improved distributions of organoclay particles in the epoxy matrix were observed. The dispersion of 30B organoclay with this method is better than that of I.28 E. The basal spacing of

30B organoclay in the cured epoxy system is 8 nm at 5 wt% clay loading, and 5 nm at 10 wt% clay loading; the maximum number of platelets of organoclays in an agglomerate is 16. On the other hand, I.28E nanocomposites prepared under identical conditions showed only ordered intercalates with an average basal spacing of 3.5 nm, regardless of clay content. However, the drawback of the three-roll mill method is that it breaks the clay platelets, reducing their initial aspect ratio from 200~1000 to 90~120, due to the high shear forces applied to the high viscosity state of the DGEBA resin at low temperature.

Knudson, *et al.* [79] reported in their patent that a clay mineral may be intercalated with a polymer by mixing a dispersion of a polymer in a liquid carrier, and a dispersion of a clay mineral in a liquid carrier, to form a dispersion mixture. The latter was produced by the Manton-Gaulin homogenizer at a pressure of about 4500 psi (31 MPa).

More recently, Chen and Tolle [44] reported that fully exfoliated layer silicate epoxies were obtained by high–shear mixing in the presence of acetone, and ultrasonication; homogeneous and random dispersion of individual silicate layers was observed with TEM. However, the TEM images showed the aggregation of organoclays in the nanocomposite through the processing without solvent assistance. They did not mention the machine used to produce the high–shear forces for dispersion, or any properties of the nanocomposite.

The author and his supervisors realized the importance of aggregation of organoclays, and thus proposed a new method, high-pressure mixing (HPM), to disperse organoclays in epoxy resins [80, 81]. A patent application for this method has been submitted [82].

So far no method for evaluating dispersion of organoclays in uncured epoxy resins is widely accepted. The glass slide test and the sedimentation test are recommended by *Nancor* [30], but these methods cannot give quantitative results. XRD is widely used to measure the basal spacing of organoclays during dispersion and curing processing [12, 17], but it does not reflect changes in the size of agglomerates. Melt rheology has been investigated and discussed as a method to characterize thermoplastic–clay nanocomposites [83]; pronounced shear thinning behavior has been found to be a characteristic feature of exfoliated nanocomposites.

The purpose of this chapter is to study how to break down agglomerates of organoclays in epoxy resins, and to understand the influences on the dispersion of organoclays, such as basal spacing and particle size in epoxy resin systems.

3.2 Theoretical Background

3.2.1. Terminology in Clay Colloid Chemistry

A colloid solution or sol is a homogeneous dispersion of very small particles (10^{-9}~10^{-6} m). The dimensions of the particles in the solution are such that they do not settle within a reasonable time. As the particles become larger (>10^{-6} m) and settle comparatively rapidly, the dispersion is called **a suspension** [28].

The turbid-looking suspension finally separates into a bottom sediment and a clear, particle-free supernatant liquid. This phenomenon is called **flocculation** or **coagulation.**

Flocculation is the process whereby small particles clump together like a bunch of grapes (or flocs), but do not fuse into new particles. In flocculation, there is no reduction of surface, and the small particles retain their identity; only their kinetic independence is lost. Flocs move as a single unit. Adding a little salt into a clay colloid can precipitate flocculation; upon removal of salt and stirring, it is usually possible to restore the original dispersion of individual particles. This restoration of the sol is called **deflocculation** or **peptization**.

3.2.2 Clay-Water System

The swelling of montmorillonite in water has been considered as a model of colloids for many years, due to its high swelling capacity and its ability to form stable suspensions. In order to analyze the behaviour of organoclay in epoxy resins, the clay-water system is reviewed.

3.2.2.1 Electric Double Layer

In montmorillonite, the negative charges are distributed on the surface of platelets, due to non-stoichiometric substitutions of Si^{4+} for Al^{3+} in the tetrahedral, and of Al^{3+} for Mg^{2+} in the octahedral sheets. In clay-water systems, a double layer is made up by the negative surface charge and the balancing cation charge (shown in Figure 3-1 A). However, these cations are not uniformly distributed throughout the dispersion medium, and diffuse away from the surface of platelets to the bulk solution, where their concentration is low (shown in Figure 3-1 B). The concentration of anions, on the contrary, decreases towards the surface. This diffuse character of the counter-ion atmosphere was proposed by Gouy [84] and Chapman [85]; their theory predicts an

approximate exponential decay of electrical potential φ of the solution with distance x from the plane surface, as shown in Figure 3-1 A.

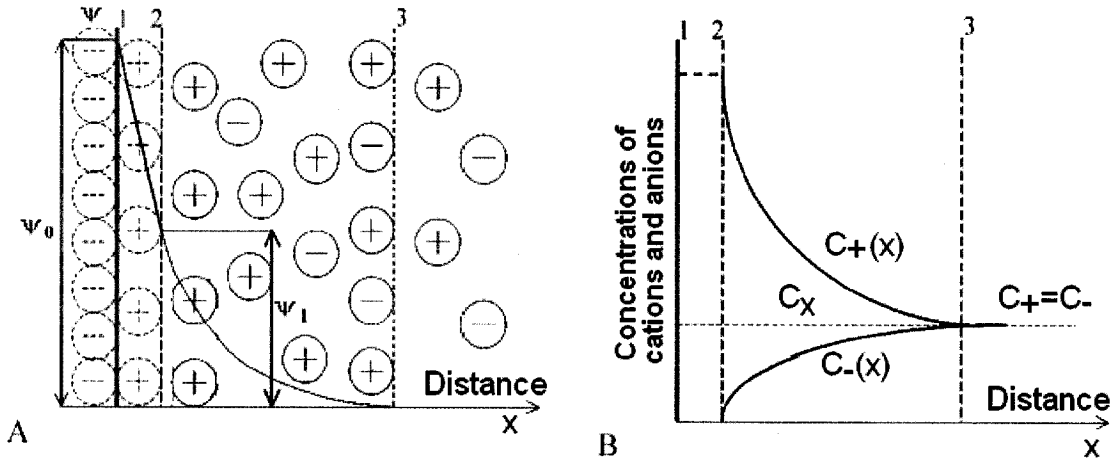

Figure 3-1: A principle scheme (Stern model) of the electrical double layer on the boundary clay face surface – aqueous solution [ref. 72]

A - cation and electrical potential distribution near a charged surface.

B - cation (C_+) and anion (C_-) concentration as a function of a distance from the surface.

ψ_o = surface potential; ψ_1 = Stern potential;

1 - Clay surface; 2 – Stern plane; 3- Boundary between a diffuse layer and free solution.

Stern conceived of the double-layer theory based on the Gouy-Chapman model [86]. Counter-ions with associated water molecules in a closely packed layer approach and tightly bind to the clay surface, with an adjacent diffuse layer extending into the solution. The Stern water layer is estimated at about 0.4 nm for montmorillonite. Increasing the valence of counter-ions and electrolyte concentration decreases the thickness of the diffuse ion layer and the potential.

3.2.2.2 Stability of Clay Suspension

A theoretical analysis of the interaction between colloidal particles was developed by Derjaguin and Landau [87] and Verwey and Overbeek [88], known as the DLVO theory. According to this theory, this interaction is determined by a combination of inter-particle double layer repulsion energy (V_R) and Van der Waals attractive energy (V_A).

Interparticle Double Layer Repulsion

The amount of work required to carry out these changes, and to bring particles from infinite separation to a given distance, is the repulsive energy or repulsive potential. The repulsive potential V_R between two clay platelets can be computed from the diffuse double layer theory as [89, 90]:

$$V_R = \frac{64K\rho T}{\chi}\left(\tanh\frac{ze\psi_s}{4KT}\right)^2 e^{-\kappa H} \qquad (3\text{-}1)$$

where ρ is the concentration of electrolyte (molarity x 10^{-3}x6.02x10^{23}) ions/cm^3, K is the Boltzmann constant, T is absolute temperature, ψ_s is the Stern layer potential, H is the distance between the centres of two particles, e is the electron charge, Z is the valence of the counter-ions, ε is the dielectric constant of the solvent, and X is the thickness of the diffuse ion layer, the reciprocal Debye length (κ).

$$\frac{1}{X} = \kappa = \sqrt{\frac{2e^2\rho Z^2}{\varepsilon KT}} \qquad (3\text{-}2)$$

The repulsive potential decreases exponentially with increasing particle separation, and the range of repulsion is considerably reduced with electrolyte concentration. Figure 3-2 shows repulsive potential as a function of particle separation at three electrolyte concentrations.

Van der Waals Attractive Forces

There are three types of recognised intermolecular attraction: dipole-dipole interaction; induced dipole-dipole interaction; and attractive forces between non-polar molecules (London dispersion forces). The attractive energy between two semi-infinite flat plates may be expressed by the following equation [28, 90]:

$$V_A = -\frac{A}{12\pi}\left(\frac{1}{H^2} + \frac{1}{(H+2t)^2} - \frac{1}{(H+t)^2}\right) \qquad (3\text{-}3)$$

where A is the Hamaker constant; t is the thickness of the clay platelet, and H is the distance between the centres of two particles. The Hamaker constant depends on the nature of both the particles and dispersion medium.

The attractive energy remains practically the same with varying concentrations of the electrolyte, as shown in Figure 3-2.

Total Interaction Energy

The net or total interaction energy (V_T) is the sum of the repulsive potential (V_R) and attractive potential (V_A).

$$V_T = V_R + V_A \qquad (3\text{-}4)$$

According to the DLVO theory, colloidal particles spontaneously flocculate as the Van der Waals attractive force overcomes the repulsive forces.

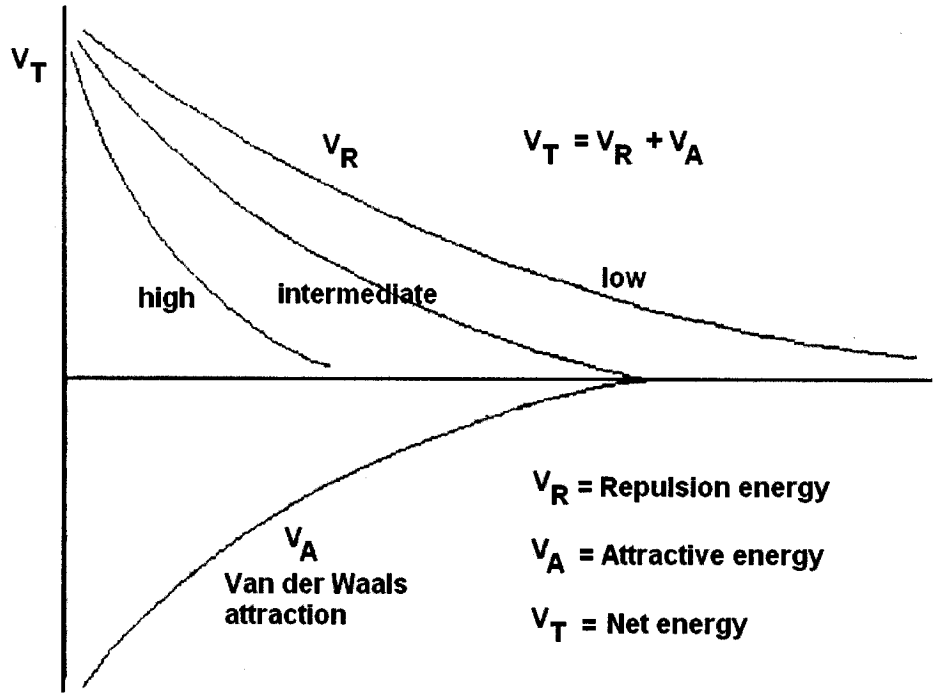

Figure 3-2: Repulsive and attractive energy as a function of particle separation at three electrolyte concentrations [ref. 28]

Interactions of Clay Particles

As two clay particles approach each other in suspension due to Brownian motion, their diffuse double layers begin to interfere and overlap over a certain distance, as shown in Figure 3-3. This results in a higher cation concentration in the mid-plane than in the bulk water solution, and an increase of the free energy of the system. If the clay particles are confined, an osmotic pressure is generated. In case the particles are free to move, the distance between particles increases to an extent such that the pressure is in equilibrium. This distance depends on the thickness of each diffuse ion layer.

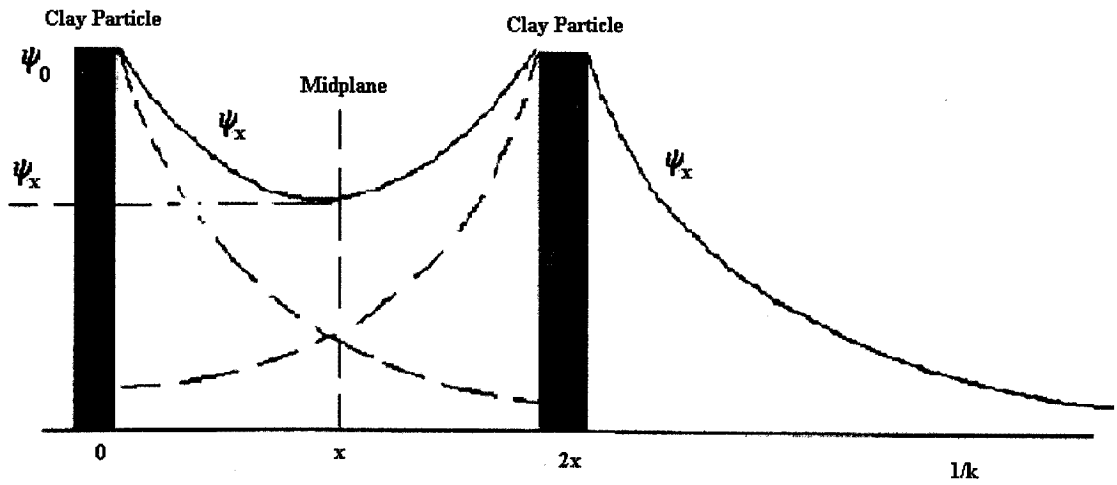

Figure 3-3: Schematic representation of the electric potential between two plates, as compared with that for a single double layer [ref. 28]

3.2.2.3 Particle Association in Clay Suspension

When a suspension of clay platelets flocculates, three different basic modes of particle association may occur (Figure 3-4) [28]: (b) face-to-face (FF); (c) edge-to-face (EF); and (d) edge-to-edge (EE) aggregation. (FF) association merely leads to thicker and larger tactoids, whereas (EF) and (EE) lead to three-dimensional "house of cards" structures. Aggregation can be described by the (FF) association, whereas the continuous gel-like structure is a consequence of (EF) and (EE) associations. A combination of these basic modes is present in clay suspensions, as shown in Figure 3-4 (e), (f) and (g).

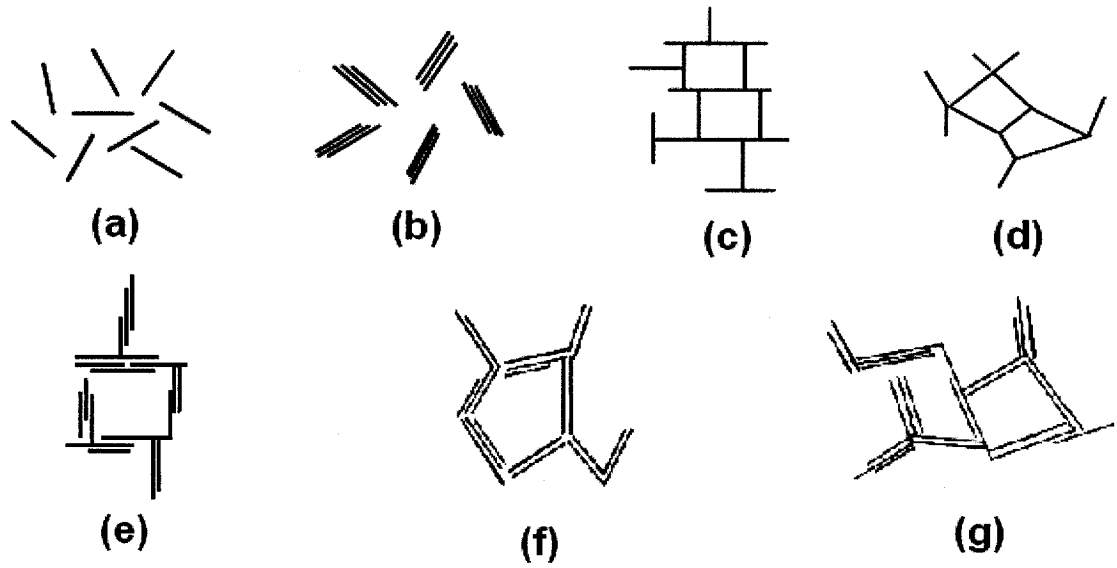

Figure 3-4: Schematical representation of particle association in clay suspensions

(a) Dispersed and deflocculated; (b) Aggregated but deflocculated; (c) Edge-face flocculated but not aggregated; (d) Edge-edge flocculated but not aggregated; (e) Edge-face flocculated and aggregated; (f) Edge-edge flocculated and aggregated; (g) Edge-face and edge-edge flocculated and aggregated [ref. 28]

3.2.3 Dispersion Methods

Three methods are frequently used to disperse a powder in a liquid: dispersion by hydrodynamic shear, particle-collision technology and ultrasonics. Forming a dispersion can be described as a process consisting of three steps [91]: (1) wetting the particle surface, (2) breaking up agglomerated particle clusters into primary particles, and (3) stabilizing the dispersed particles against reagglomeration. The effectiveness of a dispersion process depends on: (1) particle reduction, aided by wetting of the solid particles, (2) the nature of the particle surface and the dispersion medium, and (3) the stabilization of the dispersed particles by adsorption of the dispersant [92].

Shear, realized either by stirring or as contractile flow, has a duplicate effect on dispersion: it may disrupt aggregates, and it may bring particles together, inducing coagulation. Thus, the final particle size is the outcome of two countering processes.

A grinding mill is the oldest and most widely used particle-collision technology, and has higher efficiency in dispersion than stirring [92, 93]. In a grinding mill, the material (a liquid, slurry or powder) to be processed is combined with media such as ceramic beads; as the mill rotates, the beads grind the material into smaller and smaller particles. Limitations of grinding mills include: contamination of the product by the grinding media; lack of control of the amount of energy applied; very long processing times required to achieve small particles; and high support requirements (cleaning, setting up and extracting the media).

An alternative to particle-collision technology is homogenizer valves, which push fluids through a variable geometry spring-loaded valve [91, 92]. Homogenizers offer simplicity of operation and reliable service (at pressures typically below 10,000 psi (68.9MPa)). They work for applications requiring high-volume throughput at low pressures, such as milk homogenization at 2,000 psi (13.8MPa) to 3,000 psi (20.7MPa). The main drawbacks are limited particle size reduction, and the fact that the spring-actuated valve controls the orifice size in response to the size of the particles passing through. This creates two potential problems: particle size is allowed to vary, and the process pressure is limited.

A relatively new method of particle-collision technology is to use a Microfluidizer to reduce particles into uniform sub-micron sizes, and disperse them uniformly in a liquid

[94, 95]. The basic principle is bombarding a colloid system or fluid stream against itself inside an interaction chamber of fixed geometry, at very high energy. Characteristics of this method include: smaller and more uniform particle size distribution; faster processing; better control of the amount of energy applied; much higher energy (up to 40,000 psi (275.8MPa) sustained); little or no contamination of product being produced; and a highly repeatable process from run to run.

Dispersion by ultrasonics may result in pronounced deaggregation [91, 92]. This method is quite easy to apply, but the principles are not too clear. Ultrasonics has been found not only to disperse aggregates, but to enhance reaggregation. Limitations of ultrasonics include: very long processing times required to achieve small particles; small batches; high power required; changes of the dispersion medium, such as curing of epoxy resin at high power; and wide distribution of particle size.

3.2.4 Viscosity of Suspension with Volume Concentration

Many equations have been proposed for estimating the viscosity of a Newtonian liquid containing spherical particles. Einstein derived this theoretical equation between the relative viscosity of a suspension and the amount of dispersed solid [96]:

$$\eta_r = 1 + 2.5\varphi \tag{3-5}$$

where η_r is the relative viscosity, the ratio of suspension viscosity (η_s) to viscosity of medium(η_m); and φ is the volume concentration. This formula is valid for solid spheres which are far enough apart not to influence each other.

As the particles, such as plates, in many clay suspensions are anisometric, constants larger than 2.5 apply. Theoretical expressions for the proportionality constant can be derived as platelets are idealized as ellipsoids of revolution, or as discs. For large thin discs with a small height to diameter ratio λ, Simha proposed the following equation [97]:

$$\eta_r = 1 + (32/15\pi)(1/\lambda)\varphi \tag{3-6}$$

Therefore, from Equation 3-6, the aspect ratio of organoclay can be obtained. However, this equation is only valid for dilute suspensions.

One of the simplest one-parameter equations up to moderate concentration is the one based on the work of Maron and Pierce [98]:

$$\eta_r = \left(1 - \frac{\varphi}{\varphi_m}\right)^{-2} \tag{3-7}$$

where φ_m is the maximum possible solid volume concentration, the value of φ at which the suspension viscosity become infinitely large.

The relationship between the volume concentration (φ) of organoclay and clay parts per hundred of resin by weight (W_c) commonly used in polymer nanotechnology processing is the following:

$$\varphi = \frac{W_c/\rho_c}{W_c/\rho_c + 100/\rho_e} \tag{3-8}$$

where ρ_c and ρ_e are the densities of organoclay and epoxy resin, respectively.

3.3 Experimental

3.3.1 Materials

3.3.1.1 Epoxy Resin System

Two types of epoxy resins were chosen in this study: bifunctional and multifunctional. The former is the diglycidyl ether of bisphenol A (DGEBA), Epon 828 (***Shell Chemicals***). Its chemical structure is presented in Figure 2-5 in Chapter 2. The latter is N,N,N',N'-tetraglycidyl-4,4'-diaminodiphenylmethane (TGDDM), Araldite MY720 (***Vantico***). The chemical structure of TGDDM is shown in Figure 3-5. Typical properties of Epon 828 and MY720 are listed in Table 3-1 [99, 100].

Table 3-1: Typical properties of DGEBA and TGDDM epoxy resins

Item	Property	
	Epon 828 (DGEBA)	**MY 720 (TGDDM)**
Visual Appearance	Clear liquid	Clear, dark brown semi-solid
Epoxy Equivalent, g/eq.	185~192	116~134
Viscosity, (cps)	11,000~15,000 (25 °C)	8,000~18,000 (50 °C)
Density at 25 °C, g/cm^3	1.16	1.15~1.18

3.3.1.2 Curing Agents

Two kinds of curing agents are selected in this study: an aromatic amine, and a Lewis acid. The aromatic curing agent is 4,4'-diaminodiphenyl sulphone, Aradur

976-1(*Vantico*); its chemical structure is shown in Figure 3-6.

The Lewis acid, boron trifluoride monoethylamine (BF_3.MEA, $BF_3.NH_2CH_2CH_3$), (*Sigma-Aldrich Fine Chemicals*) is a catalytic curing agent. The typical properties of these curing agents are listed in Table 3-2 [89, 90].

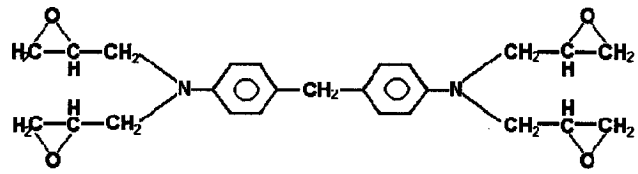

Figure 3-5: Chemical structure of TGDDM

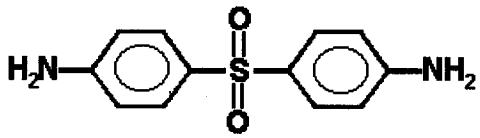

Figure 3-6: Chemical structure of DDS

Table 3-2: Typical properties of curing agents

Item	**Properties**	
	976-1 (DDS)	**BF_3.MEA**
Visual Appearance	Off-white powder	White crystalline powder
Purity, %	>99	>95
H+ active Equivalent, g/eq.	63	/
Melting Point, °C	174~178	85~89

3.3.1.3 Clay and Organoclay

A natural montmorillonite and two commercially available organoclays, I.30E and 30B, were chosen for this study [30, 31]. Each type of clay differs from the others in the nature of the exchanged ions in the galleries. Their compositions and properties are listed in Table 3-3, and their size distributions in Table 3-4.

Table 3-3: Compositions and properties of clay and organoclays

Product / Item	Cloisite Na^+	Nanomer I.30E	Cloisite 30B
Simplified Name	Na-clay	I.30E	30B
Description	Natural montmorillonite	Octadecyl amine modified montmorillonite	Ternary ammonium salt modified montmorillonite
Organic Modifier	None	$CH_3(CH_2)_{17}NH_3^+$	MT2EtOH*
Modifier Concentration	0	100 meq/100g clay	90 meq/100g clay
Moisture Content %	<2	<2	<2
Weight Loss on Ignition, wt %	7	30	28
Basal spacing (d_{001}) nm	1.17	2.25	1.74
Density, g/cm^3	2.86	1.82	1.98
Supplier	*Southern Clay Products*	*Nanocor*	*Southern Clay Products*

* MT2EtOH: methyl tallow, bis-2-hydroxyethyl, quaternary; with chemical structure:

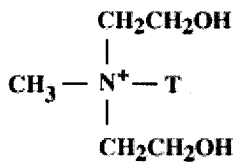

where T is Tallow (~65 % C18; ~30% C16; ~5% C14).

Table 3-4: Typical dry particle sizes (micrometers) [30, 31]

Clay	Mean Dry Particle Size	10% less than (by volume)	50% less than (by volume)	90% less than (by volume)
I.30E	8~10	/	/	/
30B	/	2	6	13
Na-clay	/	2	6	13

3.3.2 Dispersion Method

3.3.2.1 Direct Mixing (DM) Method

An organoclay was directly added into an epoxy resin with mechanical stirring and sonication; this method is widely used to disperse organoclays in epoxy resins by other researchers [12-20, 32, 33, 36, 37, 45-47, 51-60]. Dispersion process parameters

mainly include mixing temperature and time, speed and time of stirring, and power of ultrasonic tooling.

The detailed procedures and process parameters of the DM method in this work were decided according to both viscosity-temperature curves and DSC results. First, an organoclay was dried at 120°C for more than 2 hrs before mixing, in order to remove water molecules in the organoclay. The DGEBA (or TGDDM) epoxy resin was slowly heated to 80 °C (or 120 °C) to approach low viscosity; then the desired amount of hot clay was added into the resin while stirring. The suspension was held at 80°C for DGEBA (or 120 °C for TGDDM) and stirred at 1000 rpm for 2 hrs, and then degassed in a vacuum oven at 90 °C (or 130~135 °C) for 30 min, followed by sonication at 80°C for 1 hr. At higher clay loadings, a foam of tiny bubbles appeared during degassing, and was removed.

3.3.2.2 High-Pressure Mixing (HPM) Method

An organoclay powder was dispersed in an organic medium with the M-110 EH XP Microfluidizer (shown in Figure 3-7 A). Because the process pressure used to disperse organoclays in organic media is up to 15,000 psi (103.4 MPa), this dispersion method is called a high-pressure mixing (HPM) method. The concentration of organoclay, process pressure and run times were selected as parameters to form different dispersion efficiencies.

The basic principle of this machine is based on particle-collision technology: the bombardment of a colloid system or fluid stream against itself inside an interaction

chamber of fixed geometry, at very high energy. The size of particles is reduced by: crushing forces of the particles hitting themselves; crushing forces of the particles against the wall of the chamber; shear forces on the particles within the interaction chamber; and cavitational forces due to extreme pressure changes in the material stream.

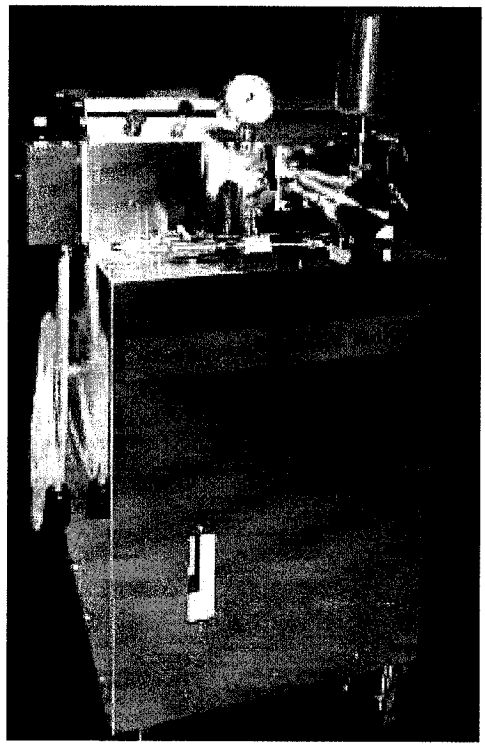

(A) Photo of M-110 EH XP Microfluidizer

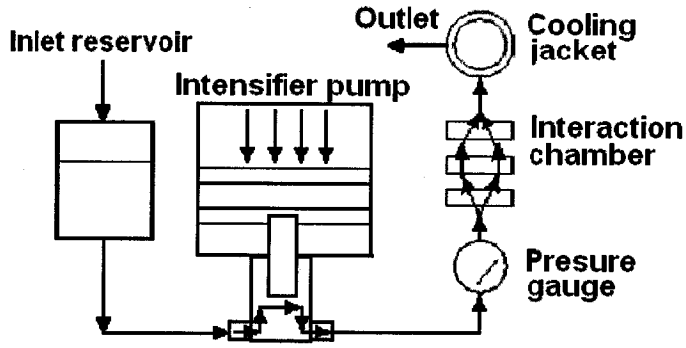

(B) Principle of operation

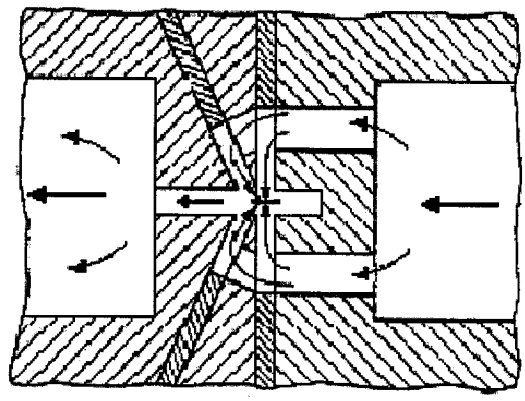

(C) A partial cross-section of the interaction chamber

Figure 3-7: M-110 EH XP Microfluidizer

As shown in Figure 3-7 B, particle-collision technology pressurizes a fluid stream, develops high-velocity stream(s), and then smashes these against each other within the interaction chamber (shown in Figure 3-7 C). Breaking the stream in two and

redirecting the streams to impinge upon themselves doubles the relative velocity with which particles impact each other. The geometry of the jet paths within the interaction chamber remains constant. Therefore all particles experience similar forces, and the smallest size and the most uniform size distribution of any high-performance mixing process are achieved.

Added to the force of this impact are the cavitational forces created by the sudden increase in velocity within the interaction chamber. This sudden increase in velocity results in a sudden decrease of pressure in the channels, creating cavitation. There are also shear forces acting within the passages at very high speeds.

Due to the high viscosity of epoxy resins at room temperature, it is impossible to directly disperse organoclays in epoxy resins with the Microfluidizer. As a result, two dispersion routes were used: one is that organoclays were first dispersed in acetone, to form a suspension with the HPM method, and then the suspension was added into the epoxy resin; the other is that an epoxy resin was first diluted with acetone, and then an organoclay was dispersed in the epoxy solution with the HPM method.

The exact concentration of clay was measured by drying the solution for 8 hrs at 100°C. The desired amount of paste was added to the epoxy resin (DGEBA or TGDDM), and the mixture was mixed by hand at room temperature. When the epoxy resin was visibly dispersed, the mixture was mechanically stirred at 1000 rpm in a fume hood at room temperature for 30 min, followed by slow heating to 80 °C for DGEBA, or 120 °C for TGDDM, where it was held for 1 hr. Finally, the mixture was degassed under vacuum at 95 °C for DGEBA, or 135 °C for TGDDM, for 30 minutes.

3.3.2.3 Grinding Media Mill (GMM) Method

A grinding mill was also selected, in order to compare dispersion efficiencies with the HPM method. In a grinding mill, organoclay powder in acetone is combined with grinding media, 0.5mm ceramic beads. As the mill rotates at about 500 rpm, the beads grind the organoclays into smaller and smaller particles. The ratio of acetone, grinding balls and organoclays is 5:5:1 by weight. During milling, acetone is always complemented to counteract evaporation. Due to limitations of grinding mills, such as contamination of the product by the grinding media, lack of control of the amount of energy applied, and very long processing times required to achieve small particles, the GMM method was only used as a reference to disperse the I.30E organoclay in acetone, and then the suspension was added into the TGDDM/DDS system to manufacture nanocomposites. Grinding time was varied as a parameter to demonstrate different dispersion efficiencies. The measurement of exact clay loadings, and the mixing procedures between the organoclay suspension and the TGDDM resin, were the same as those in the HPM method.

3.3.3 Physical Measurement

Free swelling testing: 1 g organoclay was slowly added into a graduated tube containing 20 ml of epoxy resins, organic solvents and curing agents, without any mixing. The sediment volume of swollen organoclay was measured after 48 hrs. This process is denoted as "free swelling". The swelling factor S is defined by the following equation:

$$S = \frac{(V_s - V_c)}{V_c} \tag{3-9}$$

Where V_s is the volume of clay after swelling, and V_c is that of dry clay.

Due to their high viscosity at room temperature, DGEBA/TGDDM epoxy resins were preheated to 130 °C. Solid curing agents, BF_3.MEA and DDS, were dissolved with acetone.

X-ray diffraction (XRD) analysis was performed on a Max 3100 X-ray Generator with Cu radiation (40KV, 20mA). Diffraction was performed from 2° to 12° at a scan rate of 0.96°/min, with a step size of 0.02°. The diffracted beam was monochromated before detection. The clay powder, clay-acetone paste and clay-epoxy samples were placed on a sample holder; a smooth surface was obtained by pressing and scraping the clay with a glass slide. In order to reduce evaporation of acetone and avoid damaging the machine, liquid samples were covered with a thin packaging film.

Fourier Transform Infrared Spectroscopy (FTIR) analysis was preformed on a Thermol Nicolet 670 FT-IR.

Rheological measurement was performed on a Brookfield CAP2000+ viscometer for organoclay/epoxy suspensions using cone and plate geometry, and a Brookfield Digital viscometer Model DV-II+ and Thermosel Accessory for organoclay/acetone suspensions using coaxial cylinder geometry. The software used is Capcalc V.20. After the desired temperature was achieved, another 5 minutes was allowed to reach temperature balance between the sample and spindle.

Sediment measurement: An organoclay suspension was slowly added into a 10ml graduated tube. The sediment volume of swollen organoclay was measured after 3 months.

3.4 Results and Discussion

3.4.1 Organoclay in Organic Solvent

3.4.1.1 Free Swelling

As an organoclay is slowly added into a solvent without any mixing, two phases are present in the test tubes after several hours. One is a slurry composed of organoclay and solvent; the other phase is only pure solvent, without organoclay. The free swelling factor, S, defined in Equation 3-9, is used to describe this property.

Slabaugh, *et al.* [103] described this swelling as a two-step process: (i) solvents first diffuse into the galleries of organoclays, and cover the platelets inside and outside, without increasing the basal spacing; and (ii) the organic ions are dissolved, and Van der Waals interactions existing between the ammonium ions are destroyed. In order to swell organoclays, solvents must be compatible with the dual characters of the organoclay, *i.e.*, polar from the hydroxyl groups present on the edges of the platelets, and dispersible due to exchanged ion alkyl chains. The swelling behavior of three types of organoclays (including 30B) was examined in many organic solvents, with different solubility parameters and surface tensions [104]. Jordan [29] and Burgentzle, *et al.* [102] report that any clear relationship between the swelling factor and the surface tension of

the solvent, γ, or the solubility parameter δ, cannot be deduced, and that the swelling factor and the basal spacing of organoclay are independent parameters.

The emphasis in this thesis is to ascertain the effect of process pressures on the swelling factor and the basal spacing of organoclays, using the HPM method. As a result, only acetone and ethyl alcohol were selected as solvents, since they have been widely used in epoxy resins and are able to swell organoclays.

The swelling factors of I.30E and 30B organoclays in acetone and ethyl alcohol at room temperature after 48 hours of free swelling are shown in Figure 3-8. The swelling factors of 30B organoclay in acetone and ethyl alcohol are 2.12 and 1.43, respectively; that is, the volumes of 30B slurry are increased by 2.14 and 1.43 times the initial volume of the organoclay powder. These swelling factors are larger than those reported by Burgentzle, *et al.* [102]; this may be due to the fact that they measured the swelling factors of the organoclay after 24 hours, and swelling had not reached the maximum state. However, the I.30E organoclay has lower swelling factors than 30B, in either acetone or ethyl alcohol, only 0.61 and 0.57. The swelling factors of Na-clay in acetone and ethyl alcohol were also measured as references; unmodified clay exhibits very little swelling in organic media.

The basal spacing of the organoclays in acetone and ethyl alcohol was examined by X-ray diffraction (XRD) after 48 hours of free swelling. The basal spacing of I.30E organoclay in the slurry was confirmed to increase from 2.25 to 3.45 nm in acetone, and to 3.57 nm in ethyl alcohol (shown in Figure 3-9); that is, basal spacing increases by 53% and 58%, respectively, values close to the respective swelling factors. This indicates

that the organic solvents were intercalated into the galleries of organoclay, and that the swelling volume of I.30 E in acetone or ethyl alcohol is mainly attributed to increased basal spacing. In the same way, the basal spacing of 30 B organoclay in the slurry was also confirmed to increase from 1.74 to 3.64 nm in acetone, and to 3.54 nm in ethyl alcohol; that is, basal spacing increases by 109% and 103%, respectively, which are smaller than the swelling factors, 2.12 and 1.43, respectively. This indicates that the swelling volume of 30B in acetone and ethyl alcohol is partly attributed to the increase of basal spacing, although the organic solvents were also intercalated into the galleries of organoclay.

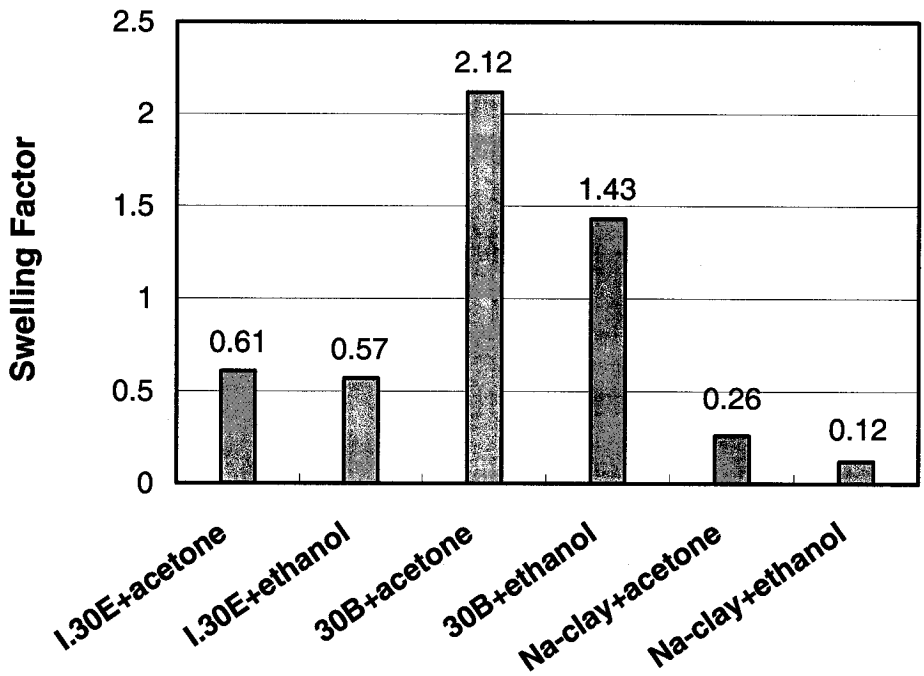

Figure 3-8: Free swelling of organoclays in organic solvents at room temperature

The macroscopic swelling can be explained by the nature of the chemical interactions developed between solvents and exchanged organoclay surfaces. I.30E has

long alkyl chains on the surface of clay platelets, which result in weak Van der Waals actions between the organoclay with solvents. During free swelling, the particles of I.30E organoclay are so large that the gravity forces break the links between the organoclay with solvents. As the individual particles of I.30E organoclay reach the lower part of the tube, they are able to slide and roll past each other, due to their mutual repulsion, and thus they reach the lowest position in the tube, producing rather closely packed, dense sediments. On the other hand, 30B contains two hydroxyl groups (-OH), which are able to form hydrogen bonding with acetone and ethyl alcohol, and between particles. In suspensions, the haphazardly formed voluminous flocs settle as such, and pile up at the bottom of the tube to form a voluminous sediment, with large void spacing in and between the agglomerates. As the particles are nearly spherical, the flocs and the sediment may have a string-of-beads character.

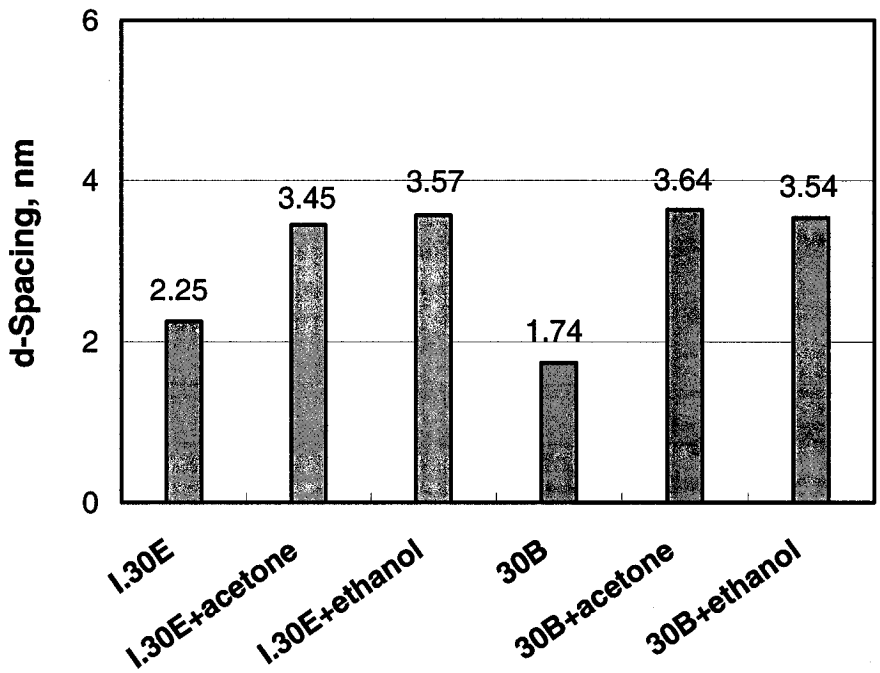

Figure 3-9: Basal spacing of I.30E and 30B organoclays and their suspensions

The swelling factor of both organoclays, I.30 E and 30B, in acetone is larger than in ethyl alcohol. Also, acetone has a lower boiling point than ethyl alcohol, so that selecting acetone as a solvent benefits the manufacturing processes of nanocomposites.

3.4.1.2 Dispersion of Organoclay in Acetone with the HPM Method

Organoclay suspensions in acetone were formed by the HPM method with different types of organoclays, process pressures and clay loadings. These suspensions were characterized by optical microscopy, sediment testing, viscosity measurement and XRD.

The suspensions made by the HPM method were inspected with optical microscopy after they were further diluted with acetone. The size and quantity of agglomerates decreased considerably, compared to the original state. Most agglomerates of I.30E organoclay are less than 1μm; the maximum diameter observed is only 1~2μm. These remnant agglomerates may be attributed to impurities or unmodified clay in the commercial product. For 30B organoclay, all agglomerates are less than 1μm.

Phase separation and sedimentation of these suspensions stored in sealed containers were observed during storage, and recorded after three months at room temperature. Figure 3-10 shows the phase separation and sediment of the suspensions containing 5% I.30E organoclay in acetone. The samples were prepared as follows: first, the organoclay was added into acetone, and mixed by hand with a glass bar; the result is called sample 1. After the mixture was added into the Microfluidizer machine and processed at pressure of 5000±500 psi (34.5±3.5 MPa), the result is called sample 2. Other samples (from number 3 to 6) were obtained using the same procedure as sample 2, but at different pressures.

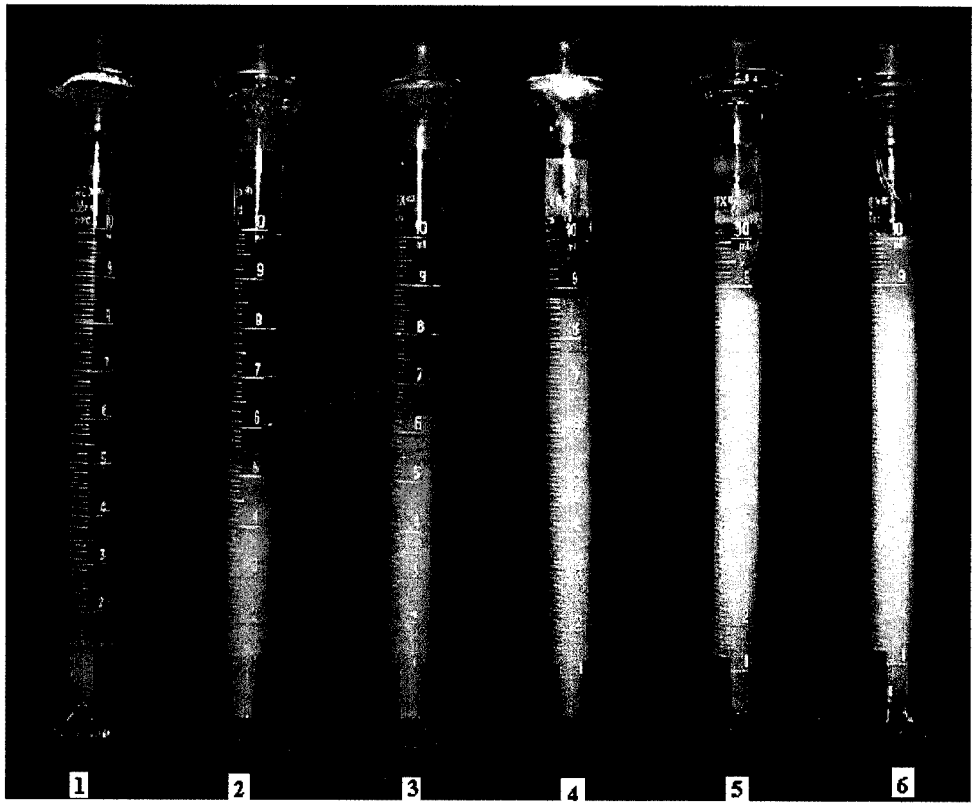

Figure 3-10: Phase separation and sediment of I.30E/acetone suspensions made by the HPM at different process pressures, after three months at room temperature

(1) 0; (2) 5 kpsi (34.5 MPa); (3) 10 kpsi (68.9 MPa);
(4) 15 kpsi (103.4 MPa); (5) 20 kpsi (137.8 MPa); (6) 25 kpsi.(172.3 MPa)

The sediment in sample 1 was observed right after the mixture was poured into a graduated tube. The height of sediment gradually increased with time, and the liquid above the sediment became clear instead of turbid. After several hours, two phases were present in the test tube; this mixing method is similar to free swelling. However, the suspensions (samples 2 to 6) made with the HPM method showed different behavior. At first, the suspensions are not fluid, but paste-like. The clear, free-particle supernatant liquid appeared above the suspension after several days, and true sediment like sample 1 was not observed during storage. The volume of supernatant liquid phase decreased

with increased process pressure. The swelling factors of theses suspensions were calculated, and shown to increase with process pressure, as shown in Figure 3-11.

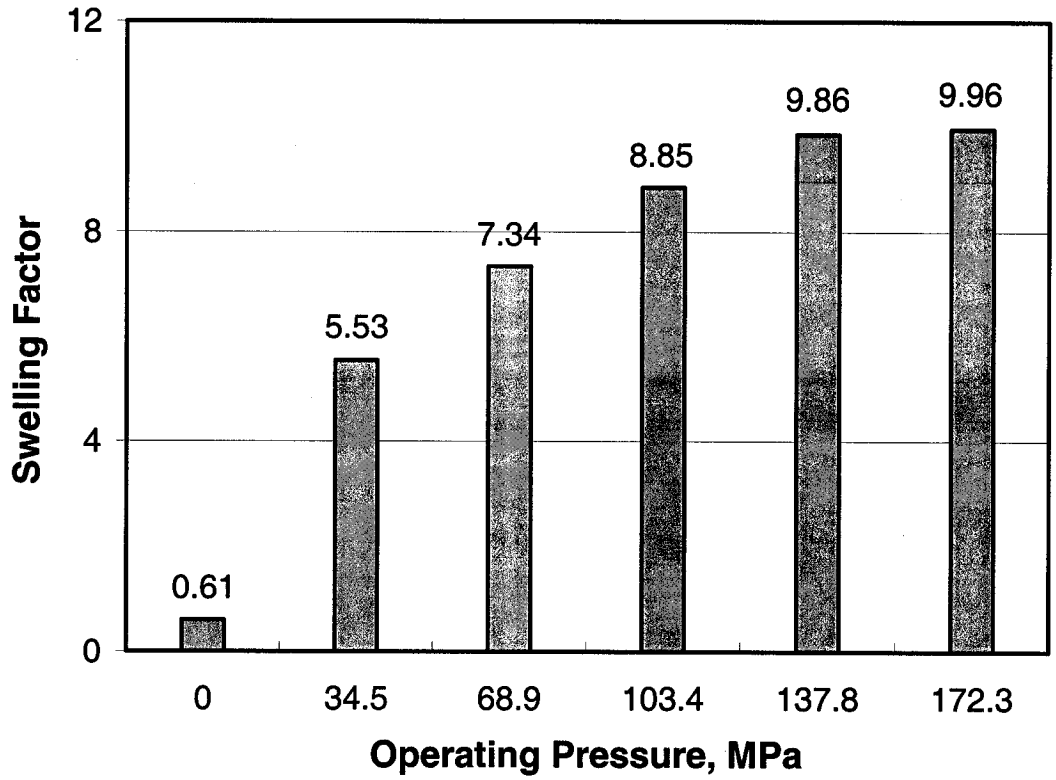

Figure 3-11: Swelling factors of I.30E/acetone suspensions made by HPM with different process pressures

I.30E/acetone suspensions at high clay loading were also prepared and tested, as shown in Table 3-5; the volume of the supernatant liquid phase decreased with increasing clay loading. Beyond a clay loading of 10% and process pressure of 15 kpsi (103.4 MPa), no phase separation was observed in the suspensions stored in the sealed container. It is necessary to point out that the two phases occur at whatever level of process pressure or clay loading, if the suspensions do not fill the container, due to the fact that acetone evaporates from suspensions, and then coacervates on the top surface of the suspensions.

In the same way, 30B organoclay was dispersed in acetone with the HPM method, as shown in Table 3-5. Due to the higher swelling factor of 30B in acetone, it is necessary to select a lower clay loading, 2.5 wt%, to observe phase separation; at clay loading of 10 wt%, the suspensions look like solids. Like free swelling, the HPM method produces a higher swelling factor for 30B organoclay than I.30E, at the same clay loading and process pressure.

Table 3-5: Sediment volumes (ml) of clay-acetone suspensions after three months at room temperature

		Pressure					
Clay Type	**Clay Loading**	**0**	**5 kpsi (34.5 MPa)**	**10 kpsi (68.9 MPa)**	**15 kpsi (103.4 MPa)**	**20 kpsi (137.8 MPa)**	**25 kpsi (172.3 MPa)**
I.30E	**5 %**	1.6	5.5	7.3	8.8	9.8	9.9
I.30E	**10 %**	3.1	8.5	9.8	10	10	10
I.30E	**15 %**	4.8	10	10	10	10	10
30B	**2.5 %**	2.3	7.5	8.9	9.8	9.9	10
30B	**5 %**	4.1	9.3	9.8	9.9	10	10
30B	**10 %**	7.2	10	10	10	10	10

Suspensions made with different process pressures were examined by X-ray diffraction (XRD), as shown in Figures 3-12 and 3-13. Unexpectedly, the basal spacing of the organoclays in suspension did not obviously increase with increased process

pressure, for either clay I.30E or 30B; the suspensions have the same basal spacing as that of free swelling, upon changes of process pressure or clay loading. The same results were obtained for suspensions made by the GMM method. As a result, the basal spacing of organoclays in organic media is not dependent on external action, but more on the interactions between the organoclay and organic media. According to the theory of colloidal stability, an organoclay may swell to the equilibrium value of the basal spacing, as it is added into an organic medium. External action may accelerate organoclay achieving the final basal spacing. Even if the basal spacing of the organoclay exceeds the equilibrium value due to external action, it returns to the equilibrium value as the external action is removed.

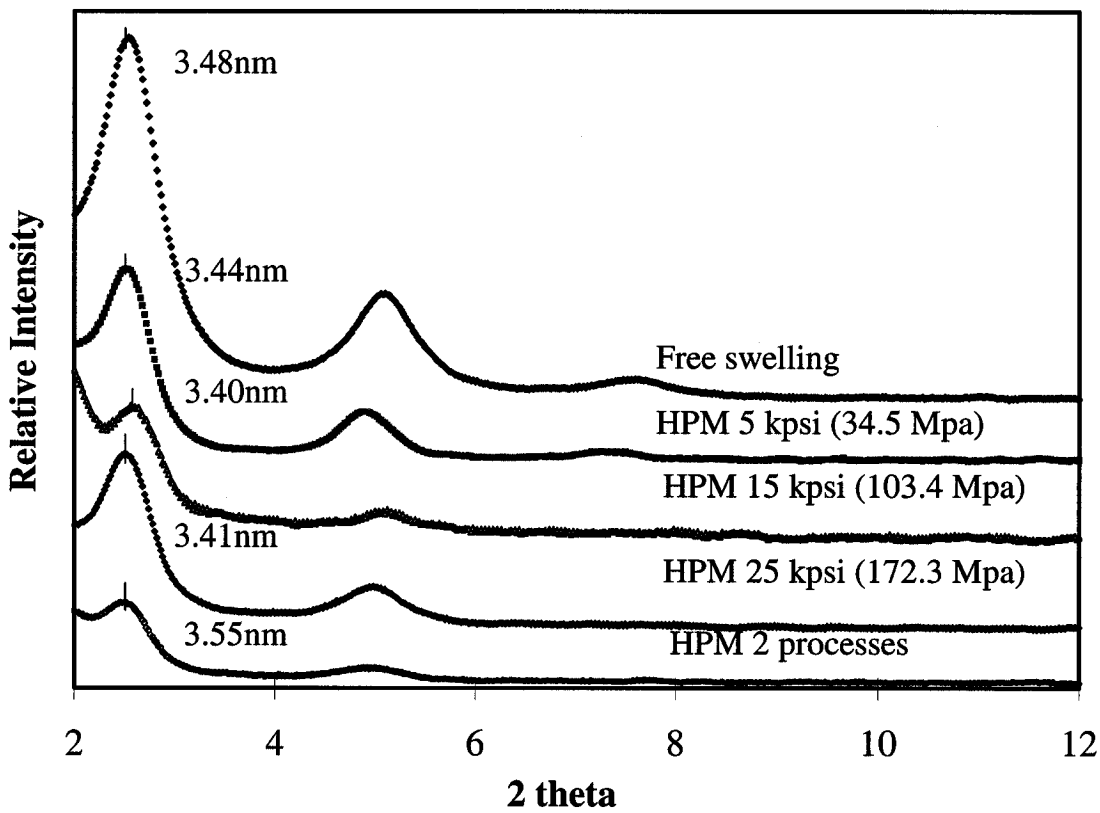

Figure 3-12: X-ray patterns of I.30E/acetone suspensions at different pressures

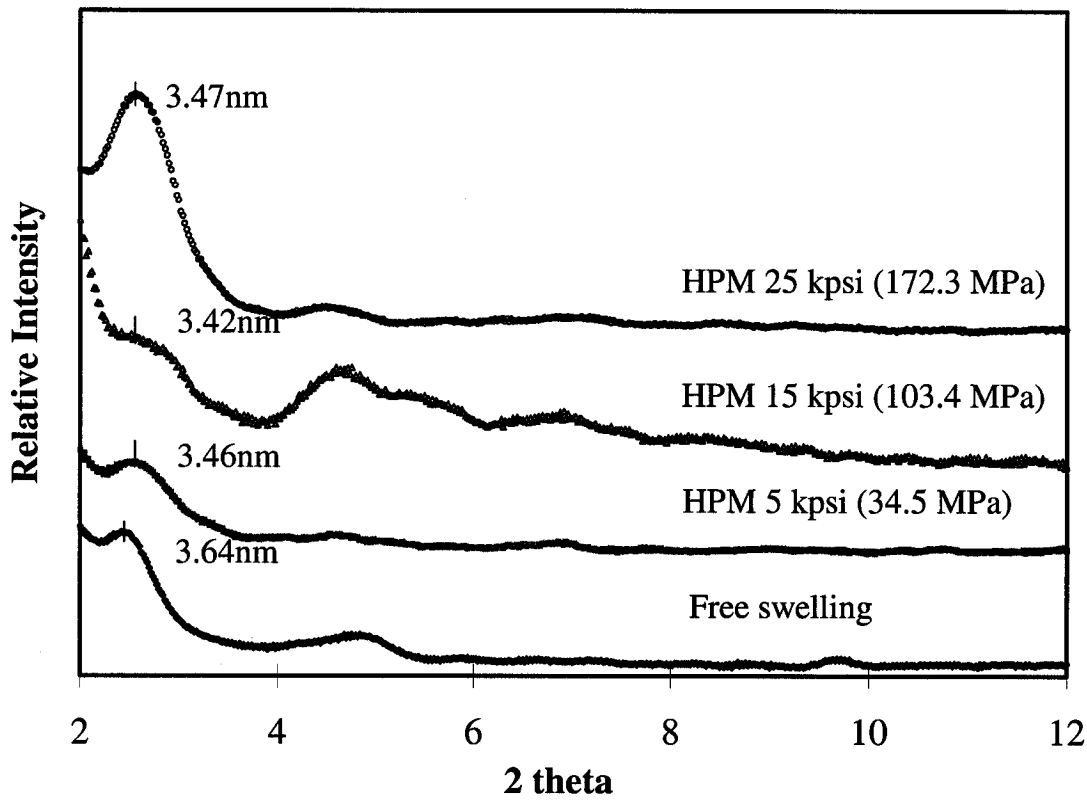

Figure 3-13: X-ray patterns of 30B/acetone suspensions at different pressures

If the ammonium ions in the gallery of I.30E organoclay are able to re-orient from their initial monolayer, bilayers or paraffin-like orientation to a vertical orientation relative to the clay surfaces, due to the fact that the organic ions are solvated, the basal spacing follows the relationship [18]:

$$d_{001} = 1.27(n-1) + d_A + r_M \quad (\text{Å}) \tag{3-10}$$

where (n-1) is the number of the methylene groups in the onium ion chain, d_A is the basal spacing of NH_4^+-montmorillonite (12.8 Å), r_M is the van der Waals radius of the methyl end group (3.0 Å), and 1.27 Å is the contribution due to the $-CH_2-$ chain segments when

the chain adopts an all-trans configuration. For I.30E organoclay ***n*** is equal to 18, and thus the basal spacing calculated with Equation 3-10 is 37.4 Å, very close to the basal spacing measured with XRD. This means that the ammonium ions in the gallery of I.30E organoclay may be vertical to the surfaces of clay platelets.

I.30E suspensions made by the HPM method behave like pastes, displaying higher viscosity and more shear-thinning flow behavior with increasing process pressure. Viscosities of the suspensions at 5 wt% clay loading with different pressures were measured using coaxial cylinder geometry, as shown in Figure 3-14. At low shear rate, the viscosity of the suspension at higher process pressure is much larger than those at lower pressure. As the shear rate increases, the difference in the viscosities of suspensions between different process pressures decreases noticeably. This shear-thinning flow behavior may be expressed as a shear thinning index, the ratio of the viscosity at 1 rpm to 10 rpm. Figure 3-15 shows that the shear thinning index increases with process pressure. As a result, the higher the process pressure, the stronger the shear-thinning flow behavior of I. 30E organoclay suspensions.

The size and distribution of organoclay particles were further examined with microscopy, TEM and SEM after they were added to the epoxy system and the epoxy system was cured. TEM results (in Chapters 4 and 5) show that particle size decreased about 10,000 fold. This indicates that the agglomerates of organoclays may be broken down to very small particles or clay platelets, and that the face-edge and edge-edge card-house structure may be formed, as shown in Figure 3-16.

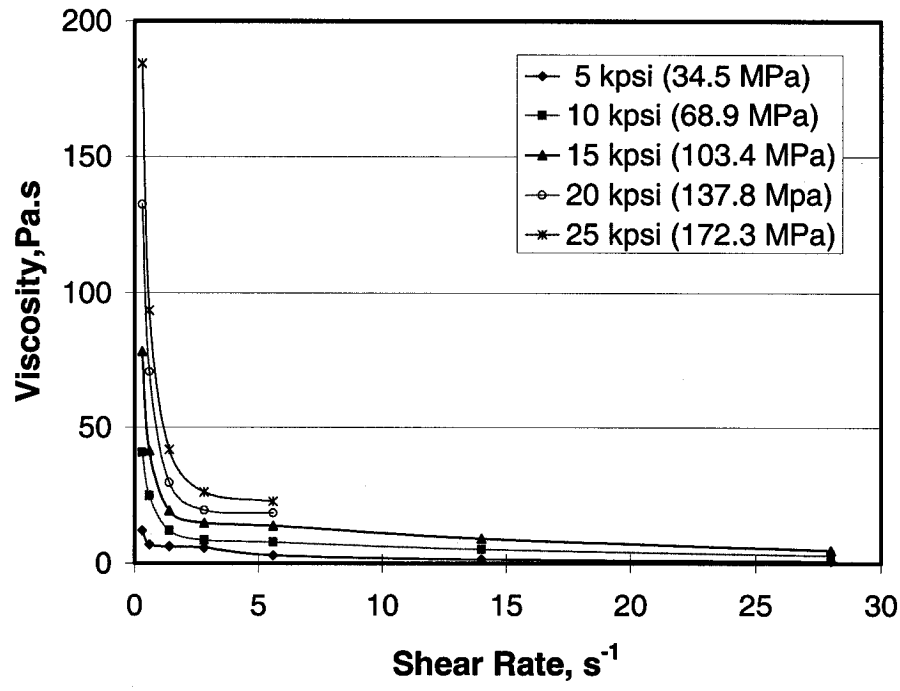

Figure 3-14: Viscosity-shear rate curves of 5 wt % I.30E/acetone suspensions made by the HPM method at different pressures

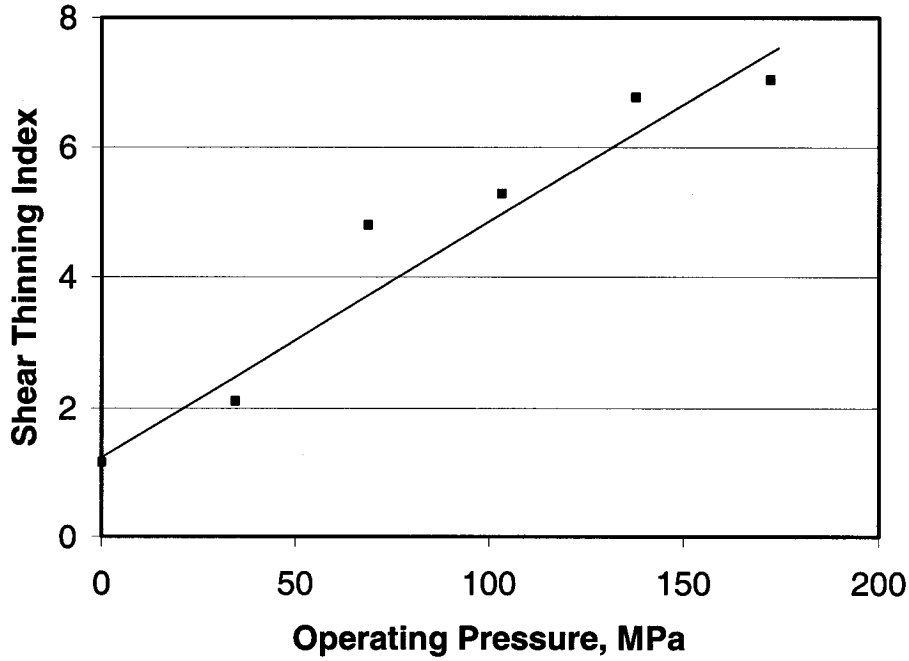

Figure 3-15: Shear thinning index of 5 wt% I.30E/acetone suspensions with process pressure

TEM results show that the diameter of organoclay platelets remains at 500~700 nm for I.30E, and 400~600 nm for 30B. This indicates that the HPM method does not break the clay platelets as much as using a three-roll mill machine, reported by Yasmin [77, 78]. After I.30E and 30B organoclays were passed through the Microfluidizer with acetone at high pressure, the organoclay suspensions were dried to return them to the powder state. These powders have the same XRD patterns and FT-IR curves as the originals; there are no obviously new strong peaks in the FT-IR curve of liquid phases separated from the organoclay/acetone suspensions, compared with that of acetone. This indicates that the modifiers of the organoclays were not washed out by the high shear forces during the HPM process.

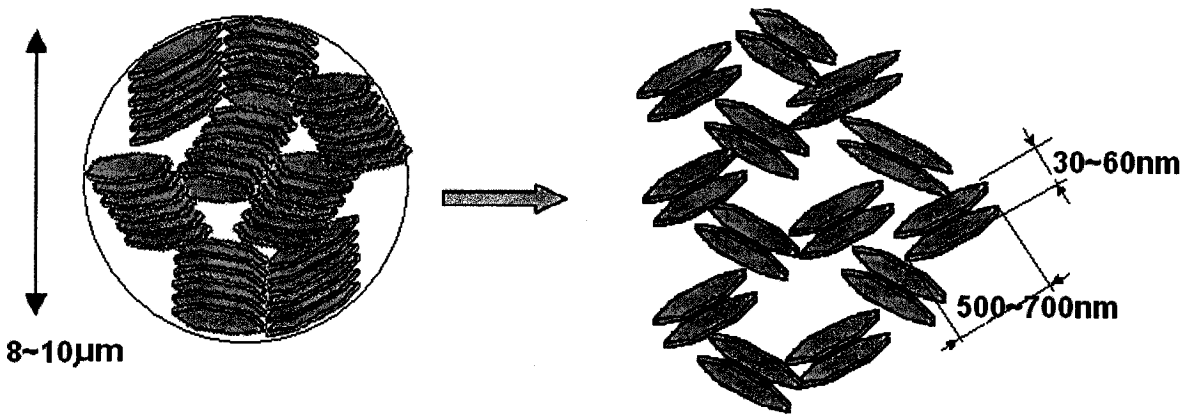

Figure 3-16: Schematic graph of dispersion of I.30E organoclay by the HPM method

3.4.2 Dispersion of Organoclay in Epoxy Resins

3.4.2.1 Swelling and Sedimentation of Organoclays in Epoxy Resins

The free swelling of organoclays and Na-clay in epoxy resins was also observed, as the epoxy resins (DGEBA and TGDDM) were heated to low viscosity at 130 °C. When added into the epoxy resins without any mixing, Na-clay was quickly wetted by the epoxy resins, and settled to the bottom of test tubes after several hours, due to the fact that Na-clay has higher surface energy (about 45 mJ/m^2) and density (about 2.86 Mg/m^3) than the epoxy resins (30~35 $mJ/m^2$and about 1.1~1.2 Mg/m^3) [105], when the epoxy resins are in a lower viscosity state. The free swelling factors are also very small, about 0.08 in DGEBA and 0.09 in TGDDM epoxy resin, respectively, as shown in Figure 3-17.

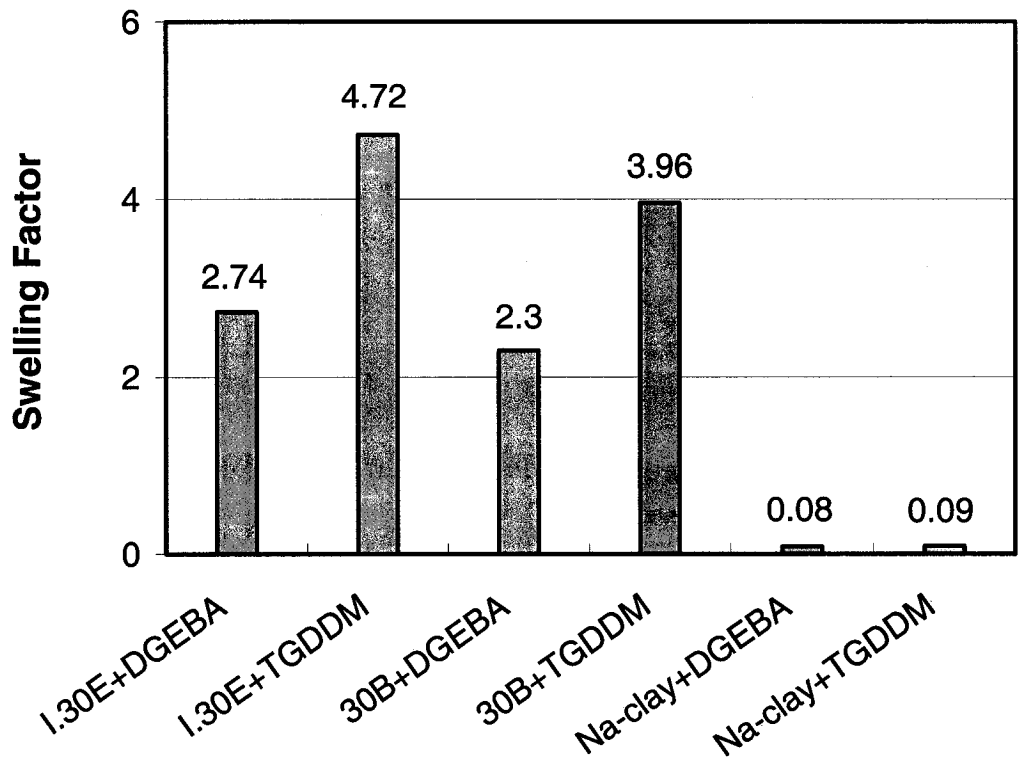

Figure 3-17: Free swelling of organoclays and Na-clay in epoxy resins at 135°C

On the other hand, I.30E and 30B organoclays are wetted very slowly in epoxy resins at 130°C, due to their surface energies (30~35 mJ/m^2) [102] being to those of the epoxy resins. They sink slowly, and their volumes gradually increase. After 48 hrs of free swelling, the swelling factors of I.30E organoclay in DGEBA and TGDDM are 2.72 and 4.72, respectively. However, 30B organoclay has lower swelling factors than I.30E, in either DGEBA or TGDDM, being only 2.30 and 2.96, respectively. The swelling factor of organoclays in TGDDM is larger than in DGEBA, for both I.30 E and 30B organoclay; this may be attributed to the fact that TGDDM resin has higher viscosity than DGEBA.

Suspensions of organoclays in epoxy resins formed by the DM method were carefully examined right after they were prepared. Two types of test methods recommended by Nanocor for determining the quality of dispersion were used: the glass slide test and the sedimentation test. No agglomerates were seen by holding two slides containing a drop of mixture between them up to the light and looking through them. No sediment was observed when the suspensions were held at 135°C for 20 min, but two phases were present when the suspensions were held at this temperature for more than 48 hours. The agglomerates were observed under an optical microscope after the mixture was diluted with acetone; they were similar to those observed in cured samples. These results show that the glass slide test is not effective to evaluate dispersion in this system. The sample in the sedimentation test should also be held in the low viscosity state of epoxy resins for a long time.

The same measurements were performed for suspensions made by the HPM method. No phase separation or sediments were observed in these suspensions under conditions identical to those with the DM method. Suspensions were inspected with optical microscopy after they were further diluted with acetone; the size and quantity of agglomerates in the epoxy resins are almost the same as those observed in acetone with the HPM method. That is, most of the agglomerates of the I. 30E organoclay are less than 1μm, and the maximum diameter observed is only 1~2μm. For the 30B organoclay, all agglomerates are less than 1μm.

3.4.2.2 Basal Spacing of Organoclays in Epoxy Resins with XRD

The basal spacing of the organoclays in the epoxy resins was examined with X-ray diffraction (XRD) after free swelling and mixing with both DM and HPM methods. Figure 3-18 shows the XRD patterns of I.30E/DGEBA suspensions with different mixing methods. In Figure 3-18, the prominent peak in every curve is absent, but there is a shoulder, which may correspond to the basal spacing of I.30E organoclay in DGEBA. Thus, these suspensions have the same basal spacing, about 3.37 nm, although they were made by different mixing methods. Similar results were obtained for I.30E/TGDDM, 30B/DGEBA and 30B/TGDDM systems, as shown in Table 3-6.

According to the DLVO theory, the following factors may influence the basal spacing of an organoclay in an epoxy resin: the dielectric constant of the epoxy resin; concentrations of impurities in the epoxy resin, such as water, organic solvents or NaCl; and temperature.

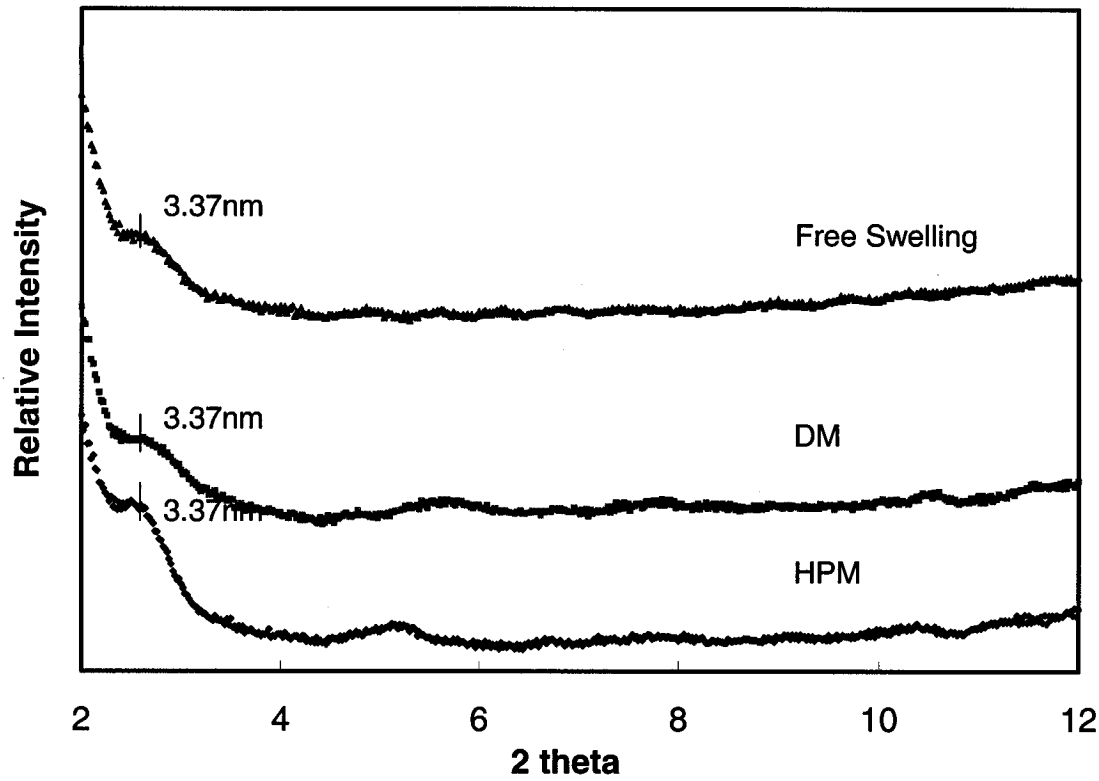

Figure 3-18: XRD patterns of I.30E/DGEBA suspensions with different mixing methods

Table 3-6: Basal spacing of suspensions with different mixing methods

Materials	Dispersion Method		
	Free Swelling	DM	HPM
I. 30E + DGEBA	3.37 nm	3.37 nm	3.37 nm
I.30E + TGDDM	3.37 nm	3.37 nm	3.37 nm
30B + DGEBA	3.37 nm	3.37 nm	3.34 nm
30B + TGDDM	3.20 nm	3.27 nm	3.27 nm

The larger the thickness of the double layer, the higher the dielectric constant of the medium, according to Equation 3-2. Due to the increased double layer, the range of the repulsive force is increased according to Equation 3-1, but the attractive forces do not change, according to Equation 3-3. This explains why I.30E and 30B organoclays in acetone and ethyl alcohol have larger basal spacing than in epoxy resins. This is due to the fact that acetone and ethyl alcohol have higher dielectric constants, 21 and 24 respectively, compared to epoxy resins (about 4).

Another reason is the concentration of NaCl. According to Equation 3-2, the concentration of electrolyte considerably reduces the range of repulsion. Because NaCl is a by-product of the synthesis reaction of epoxy resins, as shown in Figure 2-6 in Chapter 2, the NaCl content may influence the basal spacing of organoclays in epoxy resins.

The effect of temperature on the basal spacing of organoclays is very complicated and uncertain, though the thickness of the double layer increases with rising temperature according to Equation 3-2. Benson, *et al.* [96] reported that the basal spacing of I.30E organoclay in DGEBA epoxy is 14 nm at 90°C, but only 4.2 nm at 80°C.

3.4.2.3 Rheological Properties

In general, the rheological properties of the suspensions depend on the following factors: (1) the viscosity of the fluid medium; (2) the content of solid particles; (3) the size and shape of particles; and (4) the forces of interaction between the particles.

The rheological properties of the suspensions were measured with a Brookfield CAP2000+ viscometer, using cone and plate geometry. Figure 3-19 shows the viscosity-shear rate curves of I.30E/DGEBA suspensions made by the DM method at different clay loadings at 25 °C. The DGEBA epoxy resin and I.30E/DGEBA suspensions made by the DM method have little decrease in viscosity with shear rate. Similar results were obtained for I.30E/TGDDM, 30B/DGEBA and 30B/TGDDM suspensions. Therefore, they are considered as Newtonian fluids and particle interactions may be neglected as building a relationship between viscosity and clay loading.

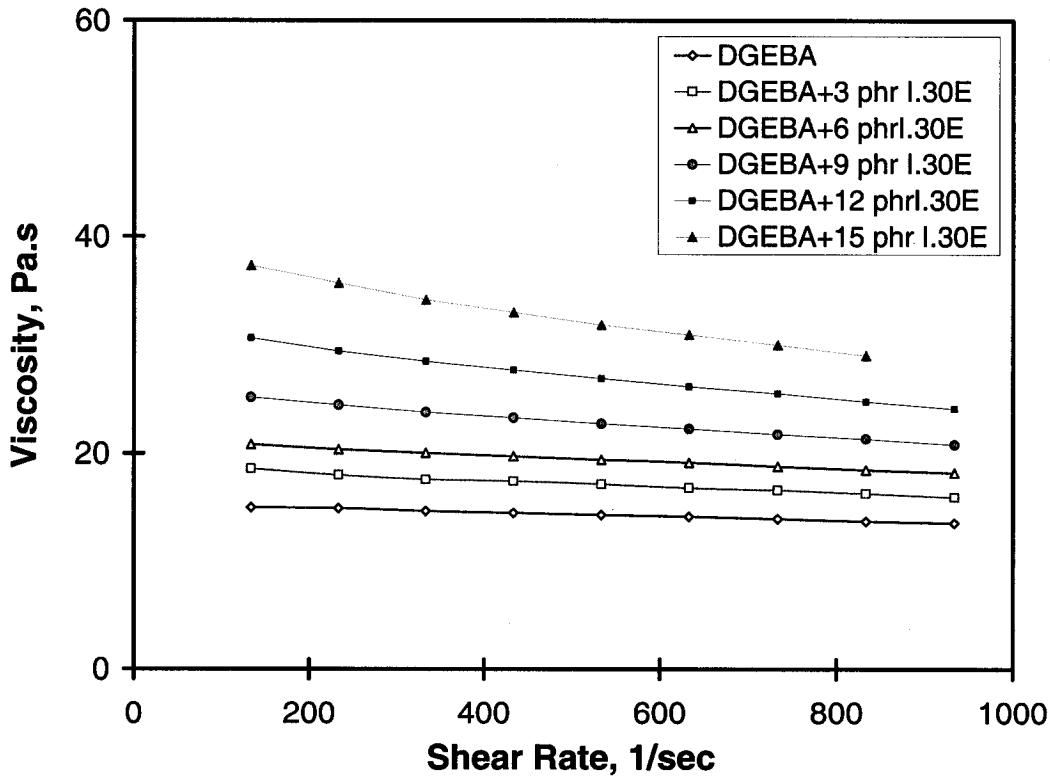

Figure 3-19: Viscosity-shear rate curves of I.30E/DGEBA suspensions made by the DM method at different clay loadings at 25 °C

Figures 3-20 and 3-21 show the relative viscosity (η_s/η_m) *versus* clay loading of suspensions of DGEBA and TGDDM epoxy resins, respectively. The relative viscosity increases with the clay loading; the Maron and Pierce equation (3-7) describes these changes of suspensions. Maximum possible solid volume concentrations (φ_m) were determined for these suspensions, as shown in Table 3-7.

If the volume concentration is calculated without considering swelling of organoclay in epoxy resins according to equation 3-8, the maximum volume concentrations φ_m are very low. However, the value of φ_m is generally accepted as about 0.60, without interactions both between the particles in suspension, and between the particles and the medium; the lower the value of φ_m, the stronger the interactions. The volume of swollen organoclays (φ_s) may be calculated from the following equation:

$$\varphi_s = \frac{d_s}{d_o}\varphi \qquad (3\text{-}12)$$

where d_s and d_o are the basal spacing of the original powder state and after swelling, respectively. Using this new concept of volume concentration, the results from the Maron and Pierce equation (3-7) are the same, but the value of φ_m is enlarged, as shown in Table 3-7.

Organoclay/epoxy suspensions may be examined with XRD, as mentioned above; the results are exhibited in Figure 3-18 and Table 3-6. However, the prominent peaks in the XRD curves in Figure 3-18 are absent, and there is only a shoulder in each curve; it is not yet determined whether the shoulder corresponds to the (001) or the (002) peak.

Table 3-7: Maximum possible solid volume concentrations (φ_m) of suspensions

Materials	Original State		After Swelling		Ideal State	
	Basal Spacing	φ_m	Basal Spacing	φ_m	Max. possible Basal Spacing	φ_m
DGEBA+I.30E	2.25 nm	0.28	3.37 nm	0.41	5.06 nm	0.62
DGEBA+30B	1.74 nm	0.27	3.37 nm	0.52	4.01 nm	0.62
TGDDM+I.30E	2.25 nm	0.21	3.37 nm	0.31	6.85 nm	0.62
TGDDM+30B	1.74 nm	0.15	3.27 nm	0.28	7.50 nm	0.62

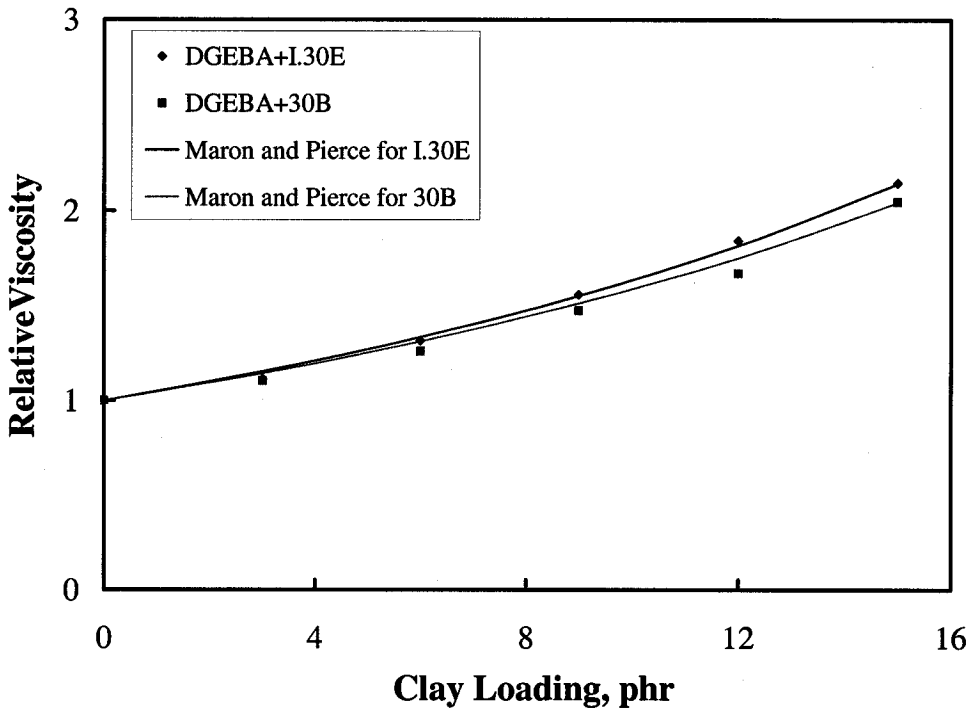

Figure 3-20: Relative viscosity *versus* clay loading in DGEBA epoxy suspensions

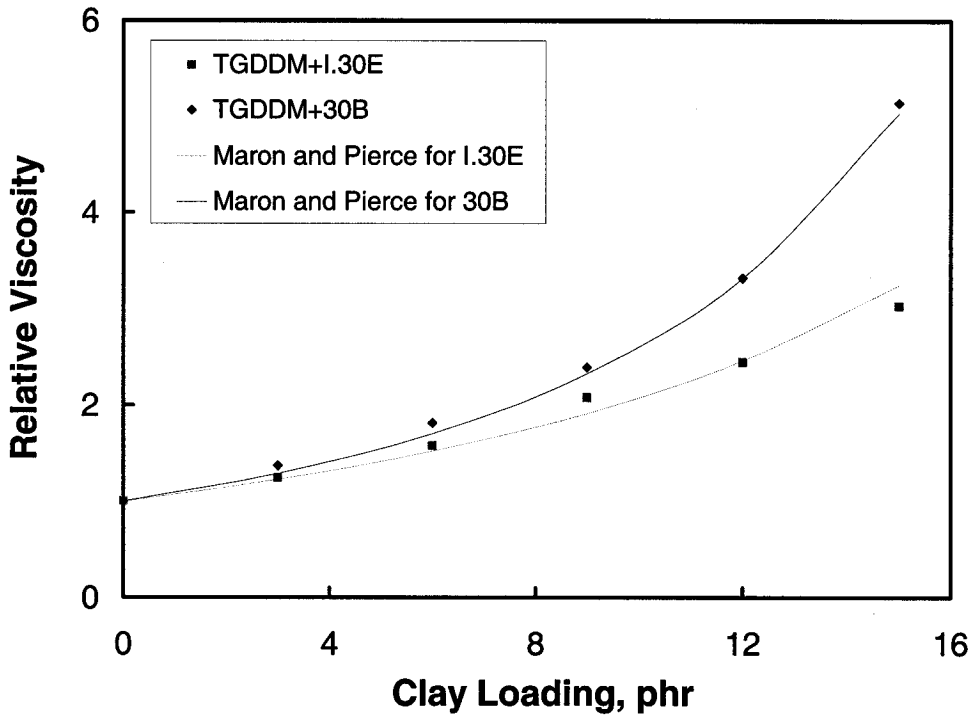

Figure 3-21: Relative viscosity *versus* clay loading in TGDDM epoxy suspensions

Viscosity analysis can predict the maximum possible basal spacing of organoclay. Poslinski, *et al.* [106] reported that the average diameter of glass beads was 15 microns, and the value of φ_m determined by liquid displacement experimental experiments was 0.62 for the Maron and Pierce equation. Assuming that the value of φ_m is also 0.62 for organoclays in epoxy resins, which are in an ideal state, that is, without interactions between the particles and the epoxy resins, the maximum possible basal spacing of these organoclays may be obtained, as shown in Table 3-7.

The rheological properties of suspensions made by the HPM method were also studied. Figure 3-22 shows viscosity-shear rate curves of I.30E/DGEBA suspensions made by both DM and HPM methods at 6-phr clay loadings at 25 °C. The suspensions made by the HPM method have higher viscosity and much stronger shear-thinning

behavior than those by the DM method. Thus, the HPM suspensions have higher yield stresses and relative viscosities than the DM suspensions; this is attributed to the fact that the particles were broken down to form very small anisometric platelets, and strong interactions between particles and epoxy resins. Similar results were obtained for these organoclays in TGDDM systems.

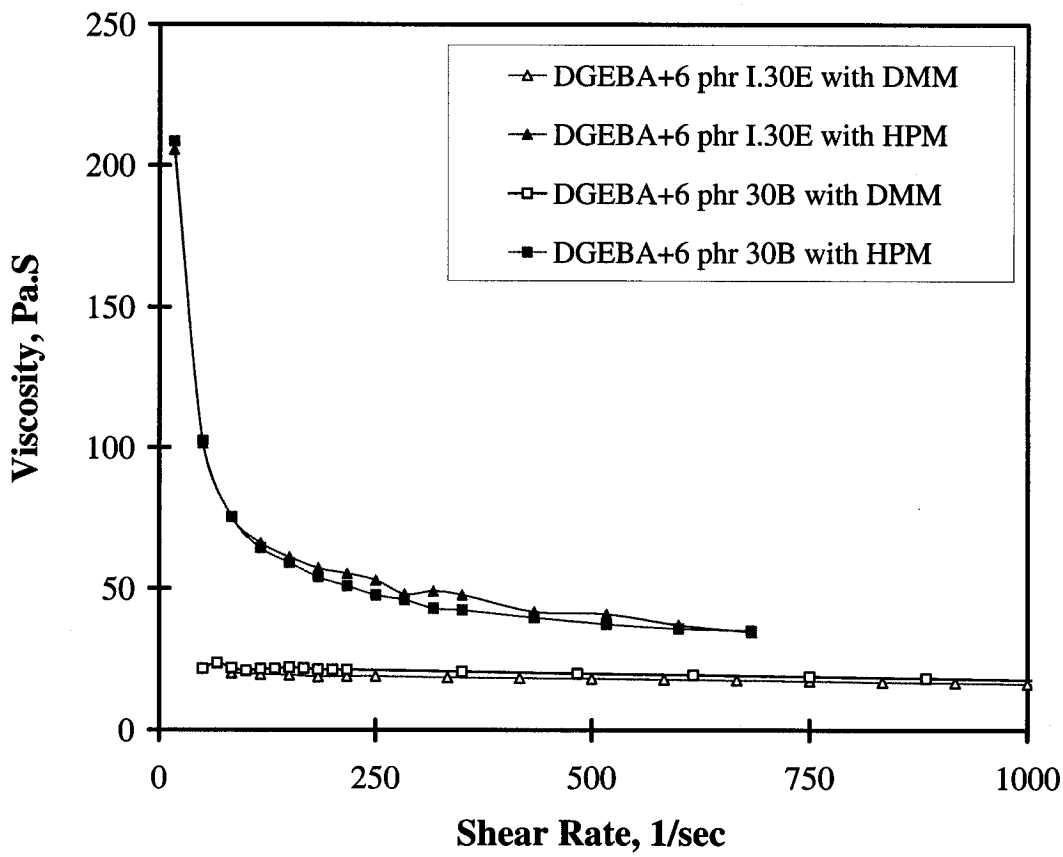

Figure 3-22: Viscosity-shear rate curves of 6-phr organoclay/DGEBA systems with different mixing methods at 25°C

3.4.3 Effects of Curing Agents on Organoclays in Suspensions

Due to the solid state of the curing agents, DDS and BF_3.MEA, interactions between the curing agents and the organoclays were studied using a medium to dissolve the curing agents. The curing agents were dissolved in acetone, and then the organoclays were slowly added into the solutions. Like free swelling of the organoclays in acetone, two phases were present in the test tubes after several hours; but the colour of the solvent above the sediments of organoclays is buff (light yellow) for DDS, and puce(deep red to dark)for BF_3.MEA.

The basal spacing of the organoclays in sediments was examined by XRD after several days of free swelling. Figure 3-23 shows the XRD patterns of DDS, I.30E and their combination with and without acetone. The curve of "I.30E+Acetone" was introduced above, and indicates that the basal spacing of the I.30E organoclay increased from 2.25 to 3.47 nm in acetone. After removing acetone from the organoclay, the basal spacing returned to the initial position, as shown in the curve of "Dry I.30E". The DDS curing agent has a peak corresponding to 0.77 nm, and a shoulder corresponding to 3.10 nm. The basal spacing of the organoclay increases slightly, from 3.47 to 3.58 nm, in the presence of DDS, as seen by comparing the curves of "I.30E+Acetone" and "I.30E+DDS+Acetone". It is clear that DDS has entered into the galleries of the organoclays. After washing the sediments of the organoclay several times with acetone, and then removing acetone from the sediments, the sediments were re-examined by XRD, as shown in the curve of "I.30E+DDS". This curve shows a prominent peak

corresponding to basal spacing at 3.09 nm, indicating that the DDS curing agent still remains in the galleries of the organoclay.

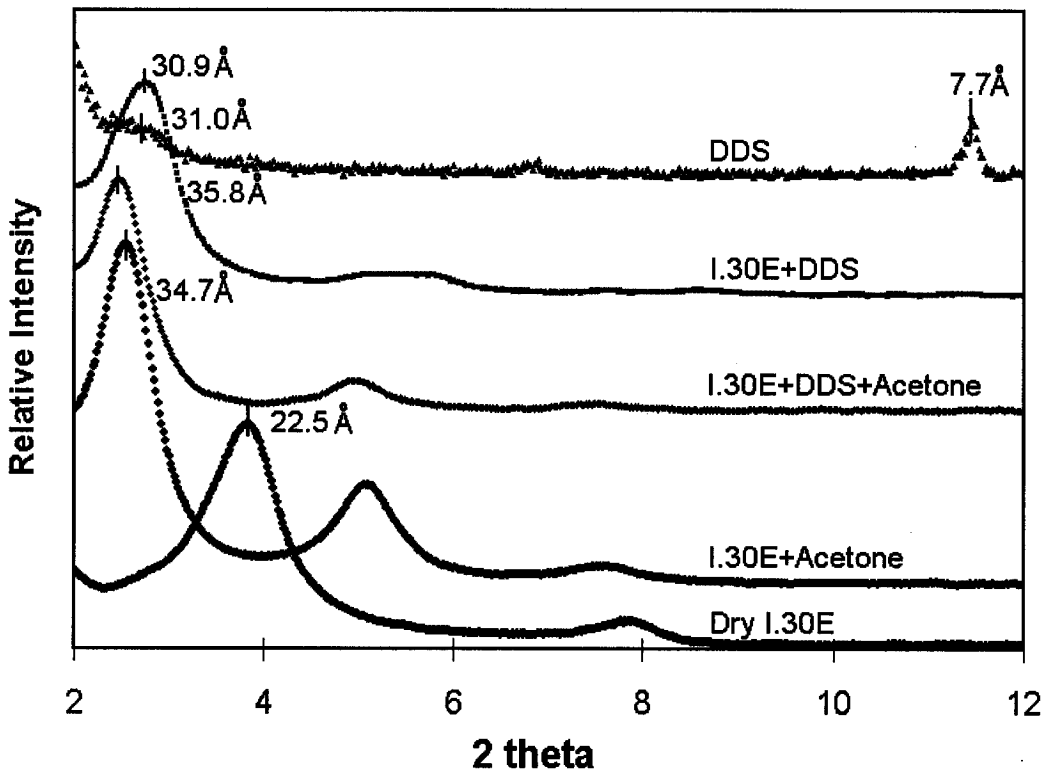

Figure 3-23: XRD patterns of DDS, I.30E and their combination with acetone

In the same way, the changes in basal spacing of the 30B organoclay in DDS solution was examined by XRD, as shown in Figure 3-24. The basal spacing of the 30B organoclay increases from 3.64 to 3.91 nm in the presence of DDS, as seen by comparing the curves of "30B+Acetone" and "30B+DDS+Acetone". The curve of "30B+DDS" shows a prominent peak corresponding to a basal spacing of 3.25 nm. These results indicate that the DDS curing agents has a stronger influence on expanding the basal spacing of the 30B organoclay than I.30E.

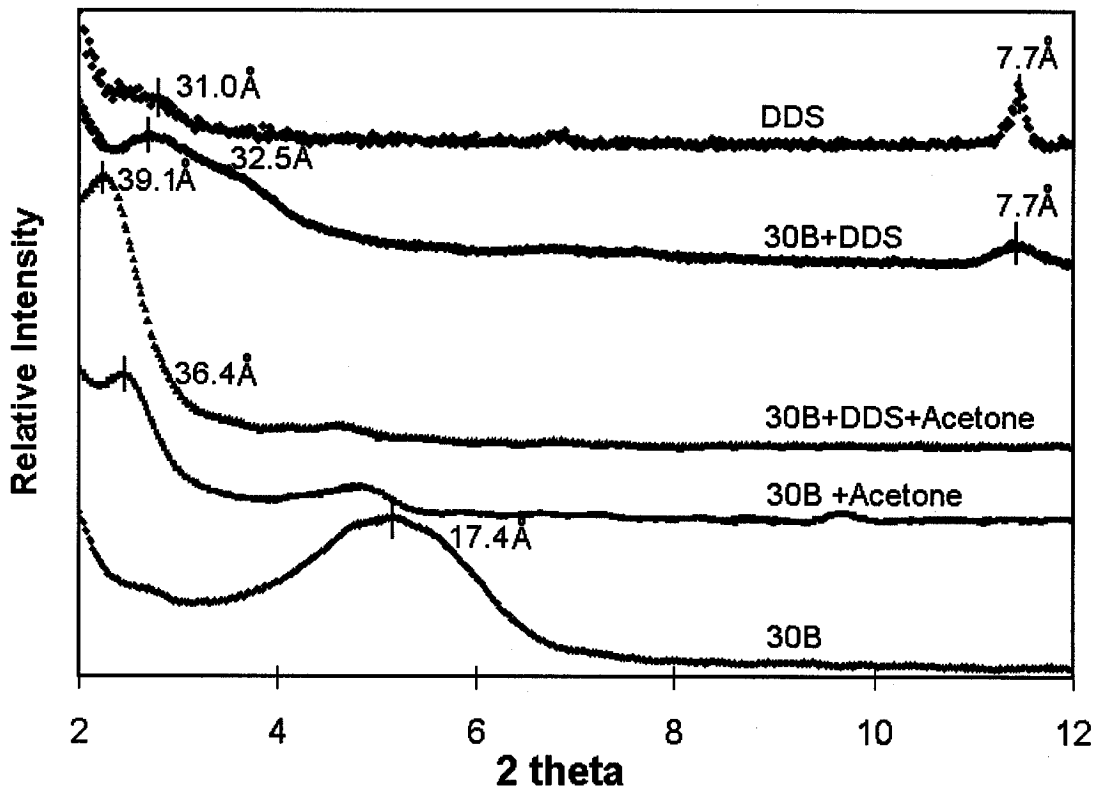

Figure 3-24: XRD patterns of DDS, 30B and their combination with acetone

On the other hand, the BF_3.MEA curing agent has a negative influence on expanding the basal spacing of the I.30E organoclay. Figure 3-25 shows the XRD patterns of BF_3.MEA, I.30E and their combination with and without acetone. The BF_3.MEA curing agent has a peak corresponding to 0.92nm. As the BF_3.MEA curing agent is added into the I.30E suspension, the basal spacing of the organoclay decreases from 3.47 to 1.65 and 1.32 nm; After washing the sediments of the organoclay several times with acetone, and then removing acetone from the sediments, the sediments were re-examined with XRD, as shown in the curve of "I.30E+BF_3.MEA", which shows a prominent peak corresponding to basal spacing at 1.32 nm.

If the ammonium ions in the gallery of I.30E organoclay are replaced by the monoethylamine (MEA) of BF_3.MEA as a following reaction:

$$CH_3(CH_2)_{17}NH_3^+ + CH_3CH_2NH_2 \longrightarrow CH_3(CH_2)_{17}NH_2 + CH_3CH_2NH_3^+$$

the basal spacing is calculated to be about 1.71nm according to Equation 3-11, which is very close to the basal spacing of the organoclay measured by XRD, because the organic ions are solvated, and a vertical orientation relative to the clay surfaces,

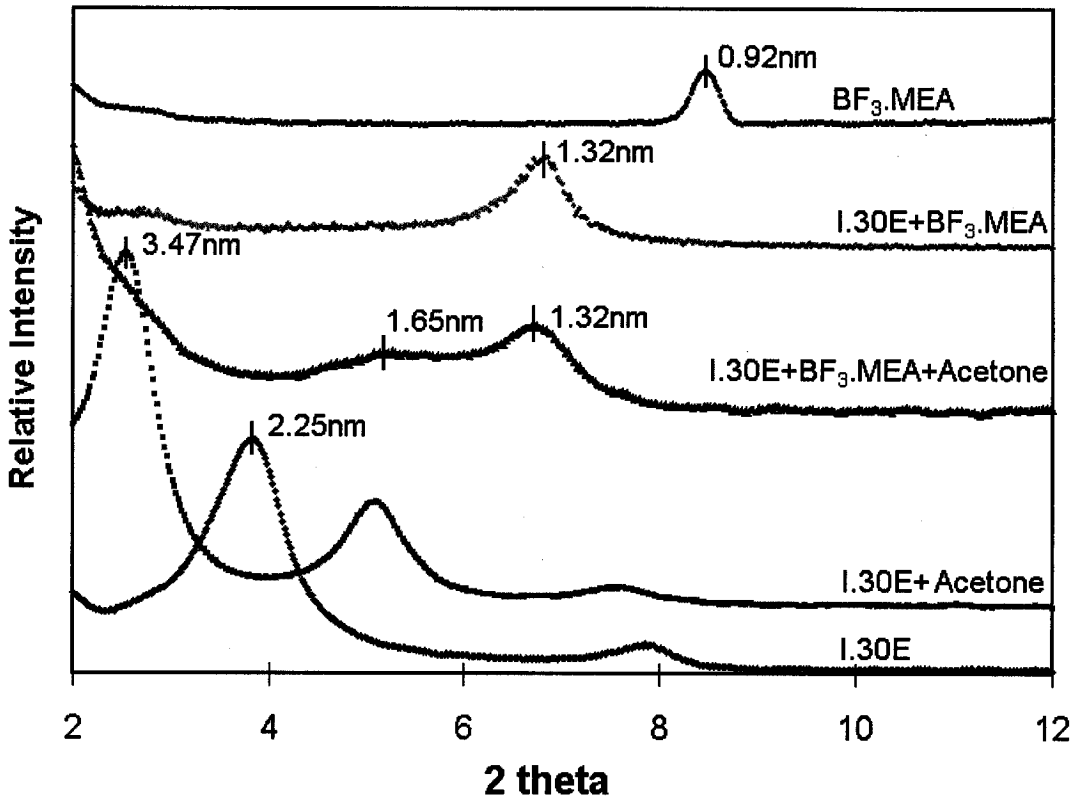

Figure 3-25: XRD patterns of BF_3.MEA, I.30E and their combination with acetone

After free swelling of the I.30E organoclay in BF_3.MEA solution for several days, chemical changes of the organoclay were analyzed by FT-IR. At first, the two phases of "I.30E+ BF_3.MEA +Acetone" were separated; then the sediment was washed with

acetone several times, and dried at 110 °C. The dry powder was tested with FT-IR, and compared with that of I.30E. On the other hand, the liquid phase was heated to 60 °C and vacuumed to remove acetone. The viscous liquid obtained was tested with FT-IR, and compared with the BF_3.MEA/acetone solution.

Figure 3-26 shows the FTIR curves of acetone, I.30E and the dry powder from the sediment in "I.30E+BF_3.MEA+Acetone". There are prominent peaks at 2922 and 2850 cm^{-1}, corresponding to symmetric and asymmetric stretching vibrations of alkyl (-CH_2-), respectively [107-109]. Clearly I.30E contains long alkyl chains; however, the two peaks disappear in the FT-IR curve of the dry powder. This indicates that the long alkyl chains are excluded from the galleries of I.30E organoclay. Compared with the curve of I.30E, the new peaks in the curve of dry powder are the same as those in acetone, showing that acetone was not completely removed from the sediment.

Figure 3-27 shows the FTIR curves of BF_3.MEA and the viscous liquid from the sediment in"I.30E+BF_3.MEA+Acetone". The peaks at 1217 and 949 cm^{-1} are caused by BF asymmetric and symmetric stretching in BF_3 [107, 110]; the peak at 1021 cm^{-1} is caused by BF_4^-. These BF peaks remain in the curve of the viscous liquid. As expected, the two peaks which disappear in the curve of the dry powder are present in that of the viscous liquid, confirming that the long alkyl chains are expelled from the galleries of the organoclay. Although this result was unexpected, the effect of BF_3.MEA on the organoclay should be considered, because BF_3.MEA is widely used in the matrices of composites and structural adhesives, as a curing agent alone or with other curing agents.

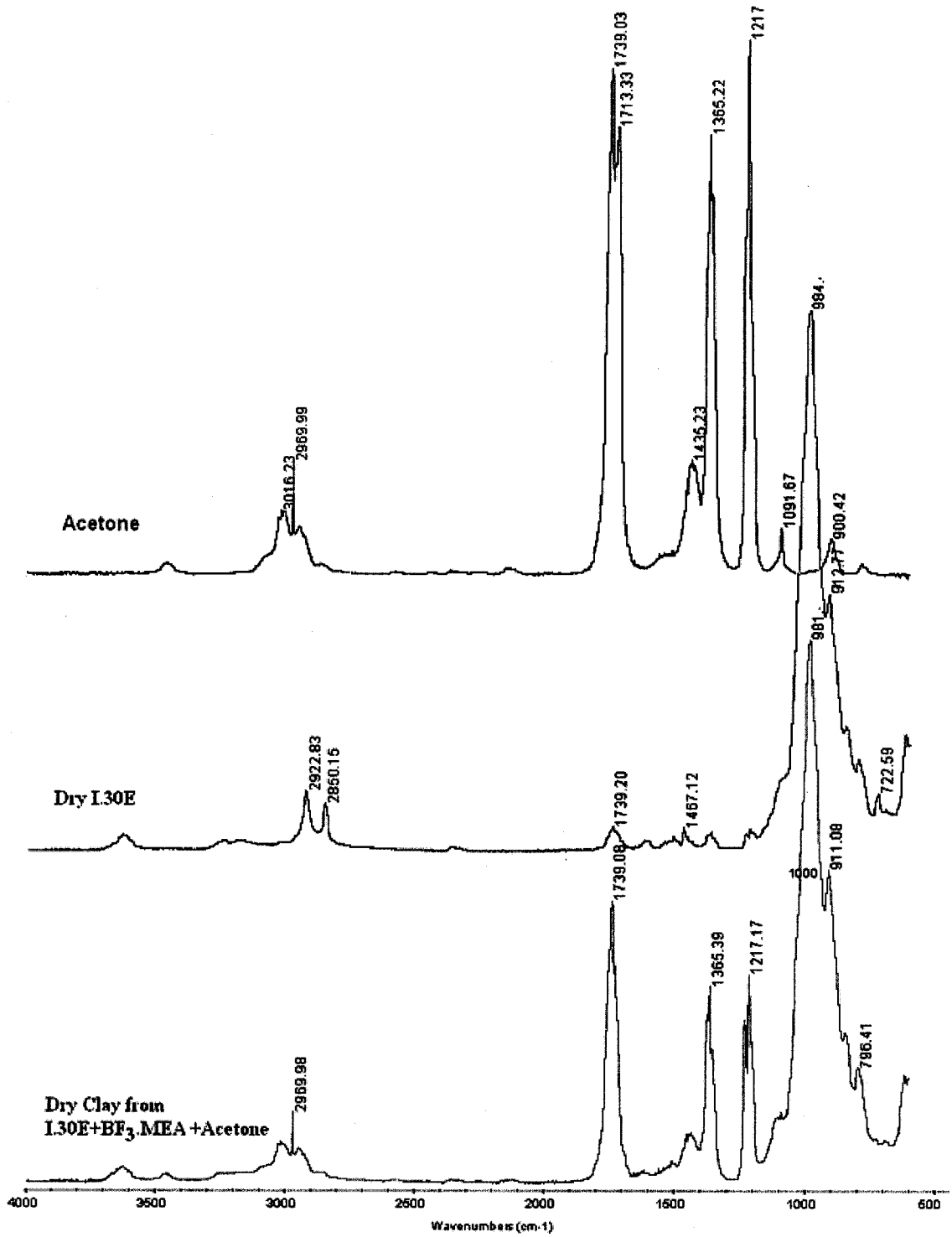

Figure 3-26: FTIR curves of acetone, I.30E and the dry powder from the sediment in"I.30E+ BF_3.MEA +Acetone"

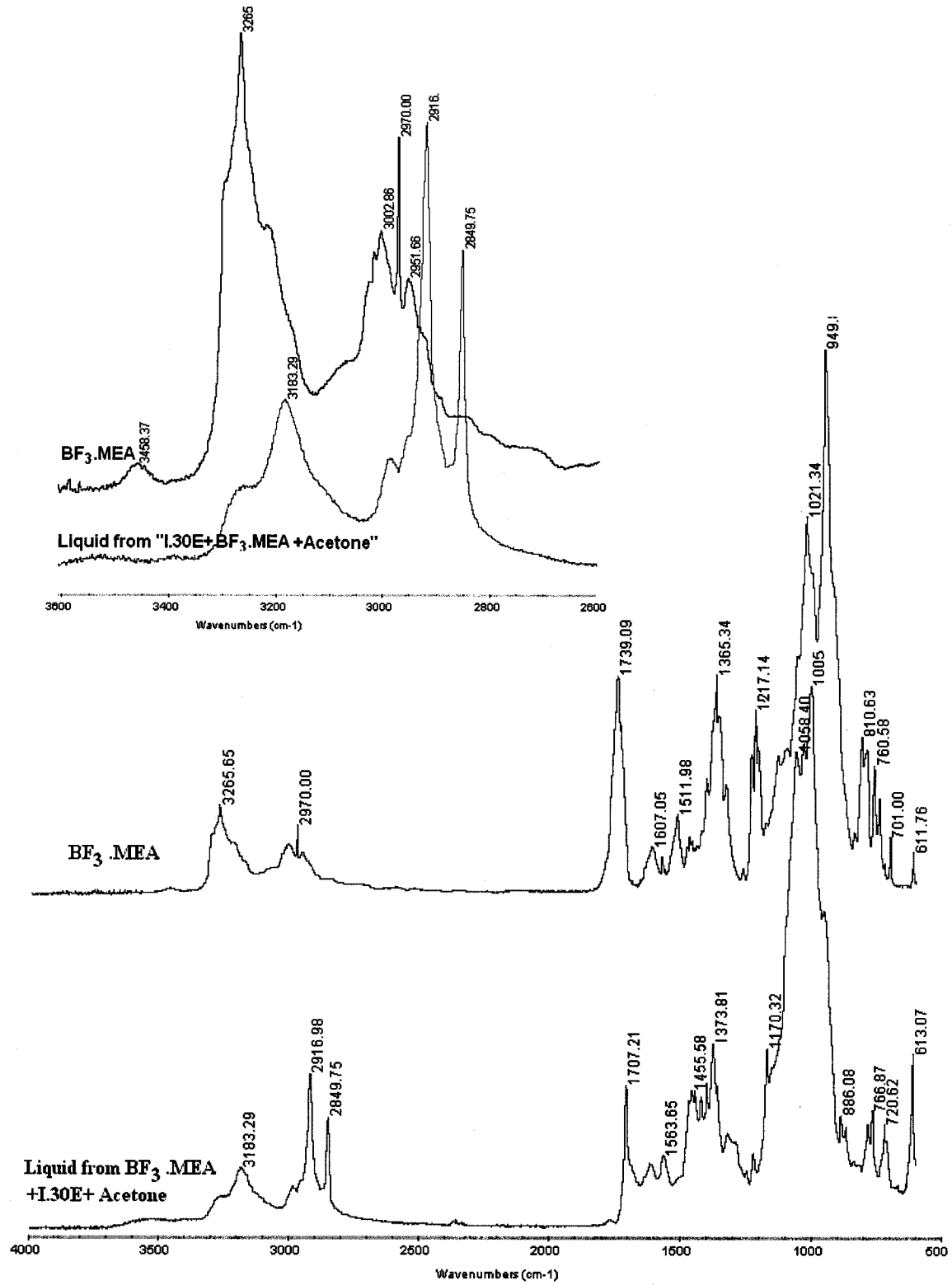

Figure 3-27: FTIR curves of BF_3.MEA and the viscous liquid from the sediment in"I.30E+ BF_3.MEA +Acetone"

Chemical changes of I.30E and 30B organoclays in DDS solution were also examined by FT-IR analysis. There are no obvious new strong peaks in liquid phases, and the peaks corresponding to alkyl chains still remain in the sediment phases. Therefore, the modifiers of the organoclays are not replaced or repelled out of the galleries of the organoclays.

3.5 Summary

The swelling factor and basal spacing of organoclays are two independent parameters. As organoclays are dispersed in acetone by the HPM method, the agglomerates of organoclays are broken down into very small particles, and the swelling factor, viscosity and shear–thinning behaviour of organoclay suspensions greatly increase with process pressure; however, the basal spacing of organoclay in suspensions does not change with process pressure. The experimental results show that high shear forces in the HPM method do not break the clay platelets, or wash out the modifiers from the surfaces of organoclays.

Organoclays still remain as very small particles in epoxy resins after suspensions made by the HPM method were mixed with epoxy resins by stirring. Suspensions made by the HPM method have higher viscosity and much stronger shear-thinning behavior than those from the DM method. However, the basal spacing of organoclays in epoxy resins is independent of the dispersion method.

As I.30E organoclay is added to BF_3.MEA/acetone solution, the ammonium ions in the galleries of I.30E organoclay may be replaced by the monoethylamine (MEA) of

BF_3.MEA, and the long alkyl chains are expelled out of the galleries of the organoclay. This results in reducing the basal spacing of organoclay; however, the DDS curing agent increases the basal spacing of I.30 E and 30B organoclays.

Chapter 4

Synthesis and Morphology of High-Performance Epoxy-Clay Nanocomposites

TGDDM epoxy resin cured with DDS is a typical high-performance epoxy system, widely used as the matrix for fiber-reinforced composites and adhesives in structural applications. However, this resin system is very brittle, and has a high equilibrium content of water absorption.

The synthesis of organoclay-modified, high-performance epoxy nanocomposites are described in this chapter by dispersing organoclays in the TGDDM epoxy by the DM, GMM and HPM methods discussed in Chapter 3. The influence of organoclays and dispersal methods on the homopolymerization of TGDDM and the cure reaction of TGDDM/DDS system has been studied by Differential Scanning Calorimeter (DSC). The catalytic effect of organoclays on the morphology of nanocomposites is discussed. The morphology of high-performance epoxy-clay nanocomposites is characterized by optical microscopy, X-ray diffraction (XRD), Transmission Electron Microscopy (TEM) and Scanning Electron Microscopy (SEM). The influence of cure temperatures on the morphology of nanocomposites is investigated. Finally, a formation mechanism of the exfoliated nanocomposites, and structural models of the nanocomposites made in this chapter, are proposed.

4.1 Introduction

A high-performance epoxy system – tetraglycidyl-4,4'-diaminodiphenylmethane (TGDDM) epoxy resin and 4,4'-diaminodiphenyl sulphone (DDS) hardener – is widely used as the matrix for advanced composites in military and civilian aircraft, due to its good properties such as excellent adhesion to fiber, relatively high strength and stiffness at room and elevated temperatures, processing versatility and reasonable cost, *etc.* [4]. Commercially available prepreg resins such as Narmco 5208, Fiberite 934 and Hercules 3501 all primarily consist of a TGDDM-DDS epoxy system [5, 6]; the latter two systems also contain boron trifluoride catalysts. However, this resin system is very brittle, with values of G_{IC} about 100 J/m^2, and has a high equilibrium content of water absorption, up to 7% [10].

The main approach to toughening high crosslink density epoxy systems, such as the TGDDM/DDS epoxy resin system, is to use thermoplastic polymers such as polyethersulphone [111] or polyetherimide [112]. Because of both high modulus and high T_g values of these thermoplastics, large concentrations of thermoplastics generally have a minor effect on these particularly important parameters. This represents a significant advantage over rubber modification, where reductions in both high modulus and high T_g values can occur. However, adding thermoplastics offers only double or threefold increase in fracture toughness with concentrations of thermoplastics up to 30 ~ 40 -phr [38, 112].

Recently, nanocomposite technology using organoclay particles as nano-scale reinforcement offers an interesting alternative for modifying epoxy resin systems.

However, very limited study has been done on epoxy-clay nanocomposites based on high-performance epoxy resins for structural applications. Kornmann, *et al.* [55] first synthesized high-performance epoxy–clay nanocomposites, based on the TGDDM/DDS epoxy resin system with mechanical stirring; they used mainly chemical means to achieve improvements in this resin system. They modified the synthetic sodium fluorohectorite, Somasif, ME-100 by means of interlayer cation exchange with different surface modifiers: octadecylamine (ODA), 1-methtyl-2-norstearyl-3-stearinoacid-amidoethyl-dihydro-imidazolinium methosulfate (W75), hydroxyethyl-dihydro-imidazolinium chloride (HEODI), and ricinyl-dihydro-imidazolinium chloride (RDI). Several aggregates of layered silicate in all systems were observed by SEM. The d-spacing of organoclays in the epoxy matrix varies from 25 Å in the phase separate composite based on W75, to 40 Å for nanocomposites based the ODA and HEODI. A large d-spacing of 75 Å is observed in nanocomposites based on RDI.

Becker, *et al.* [114] synthesized epoxy-clay nanocomposites based on different epoxy resins cured with diethyltoluene diamine (DETDA): bifunctional DGEBA, trifunctional triglycidyl p-amino phenol (TGAP), and tetrafunctional TGDDM. I.30 E organoclay was dispersed in these epoxy resins with mechanical stirring; large particulate phases were observed in nanocomposites by optical microscopy. XRD results show that d-spacing of the organoclay in the DGEBA-based system is larger than that in the higher functionality systems; however, improvement in fracture toughness of the higher functionality systems is larger than those achieved in the bifunctional DGEBA resin system.

Usuki, *et al.* [43] reported in their patent that a nanocomposite based on DGEBA epoxy resin (Epicoat -828) cured with DDS was synthesized with montmorillonite modified with $[H_3N(CH_2)_{11}\text{-}COOH]^+$ ion. However, it was necessary to use *N,N*-dimethyformamide as a swelling solvent to achieve exfoliation (d_{001}=50 Å) in the epoxy matrix. The impact resistance and heat distortion temperature of the epoxy resin system were enhanced from 0.91 J/m^2 to 1.08 J/m^2 and 193 °C to 207 °C, respectively.

The objective of this chapter is to explore the formation mechanism of exfoliated nanocomposites based on the high-performance epoxy system. Besides the chemical mechanism, a mechanical one was a main means to achieve exfoliation of nanocomposites. The effect of materials, process parameters and dispersion methods on the morphology of nanocomposites is examined.

4.2 Experimental

4.2.1 Materials

Commercially available I.30E is the main organoclay discussed in this chapter. A natural montmorillonite (Na-clay) and another commercially available organoclay (30B) are chosen as references, in order to compare the effects of different surface modifications, and confirm results validated for another organoclay. The epoxy resin system is N,N,N',N'-tetraglycidyl-4,4'-diaminodiphenylmethane (TGDDM) cured with 4,4'-diaminodiphenyl sulphone (DDS); the recommended formulation of TGDDM/DDS is 100/44 parts by weight. The chemical structures and properties of these materials were introduced in Chapter 3.

The HPM method was chosen to disperse the organoclays into a TGDDM/DDS epoxy system. The DM and GMM methods were also used as references, in order to compare experimental data with different methods and with other researchers. The concentrations of various materials and dispersion methods corresponding to the notation of nanocomposites and filler composites are shown in Table 4-1.

Table 4-1: Notation for nanocomposites and filler composites

Designation/Name	Concentration of Various Materials	Dispersion Method
TD Pure resin system	100-phr TGDDM+44-phr DDS	
N-x Filler Composites	100-phr TGDDM+44-phr DDS +"x"-phr Na-clay "x" is 3, 6, 9, 12, or 15-phr- clay loading	DM
E-x Nanocomposites	100-phr TGDDM+44-phr DDS +"x"-phr I.30E "x" is 3, 6, 9, 12, or 15-phr- clay loading	DM
B-x Nanocomposites	100-phr TGDDM+44-phr DDS +"x"-phr 30 B "x" is 3, 6 or 9-phr- clay loading	DM
GMM-x Nanocomposites	100-phr TGDDM+44-phr DDS +6-phr I.30E "x" is 2, 4 or 6 hr-grinding time	GMM
HPM-A-x Nanocomposites	100-phr TGDDM+44-phr DDS +"x"-phr I.30E "x" is 1.5, 3, 4.5, 6 or 7.5-phr- clay loading	HPM (disperse I.30E in acetone)
HPM-E-x Nanocomposites	100-phr TGDDM+44-phr DDS +"x"-phr I.30E "x" is 1.5, 3, 4.5, 6 or 7.5-phr - clay loading	HPM (disperse I.30E in epoxy solution)
HPM-B-x Nanocomposites	100-phr TGDDM+44-phr DDS +"x"-phr 30B "x" is 0.75, 1.5, 2.25 or 3-phr - clay loading	HPM (disperse 30B in acetone)

4.2.2 Synthesis of Nanocomposites/Filler Composites

The 44-phr DDS hardener was dried at 135 °C for 1 hr prior to use. Suspensions of resin and clay prepared by DM, GMM and HPM methods described in Chapter 3 were heated slowly to 135~140 °C while stirring. The hot DDS was added into the resin/clay suspension, and then the mixtures were mechanically stirred at 1000 rpm for 15 minutes, and subsequently degassed at 135~140 °C for 30~ 45 min. During degassing, a foam of tiny bubbles appeared and was removed.

Mixtures by the DM method were sonicated at 80 °C for 30 min., and then poured into rubber molds. Mixtures by the GMM and HPM methods were directly poured into rubber molds. All materials for mechanical and hydrothermal properties were cured at 135 °C/1 hr + 150 °C/1.5 hrs and 177 °C/2 hrs; the post-cure treatment was 200 °C/8 hrs in nitrogen atmosphere.

4.2.3 Physical Measurement

Cure kinetic analysis was performed on a TA 983 Differential Scanning Calorimeter (DSC) model 2010 at a desired heating rate in nitrogen atmosphere.

X-ray diffraction (XRD) analysis was performed on the same machine and under the same testing conditions described in Chapter 3. The 25.4 × 25.4 mm square samples of modified epoxies were cut from 3 mm thick plates, and their bottom surface was polished with $600^{\#}$ grit sandpaper. The polished surface was tested.

Optical micrographs were obtained using an Olympus BH2-UMA Microscope. The distribution, average sizes and area percentages of the agglomerates in the matrix were measured using Clemex Image Analysis System Software. The samples were cut from nanocomposites and filler composites, and their surfaces were polished.

Scanning electron microscope (SEM) images were obtained on a JEOL JSM-840A. SEM was performed on the fracture surfaces, after coating with a thin layer of Au/Pd.

Transmission Electron Microscopy (TEM) images were obtained on a JEOL JEM-2000. TEM samples were cut from nanocomposite blocks using an ultramicrotome (Reichert Ultra Cut AV), equipped with a diamond knife at ambient temperature. The specimens are about 100 nm in thickness.

4.3 Results and Discussion

4.3.1 Cure Kinetic Study

This chapter is concerned only with the high-performance epoxy TGDDM; however, important results about the effect of organoclay on homopolymerization of epoxy resins were obtained by other researchers [45], based on DGEBA epoxy. Therefore, the influence of organoclays and dispersion methods on the homopolymerization of TGDDM and DGEBA epoxy resins is discussed in this section.

4.3.1.1 Effect of Organoclays on Homopolymerization of Epoxy Resins

The influence of organoclays and dispersion methods on the homopolymerization of epoxy resins was studied by DSC. Samples were prepared by both DM and HPM

methods. I.30E and 30B organoclays were dispersed into DGEBA epoxy resin by the DM method at 80 °C for 0.5 hr, respectively, but at 120 °C for TGDDM epoxy resin. A sample of the mixture was taken, cooled in air, and then analyzed with DSC. Pure TGDDM and the samples from the HPM method were also heated to the same temperature for 0.5 hr, in order to have the same heat history as the samples prepared by the DM method. Acetone in the samples from the HPM method was completely evaporated.

Figure 4-1 shows the exothermal curves of homopolymerization of TGDDM resin in the presence and absence of the organoclay. In the curve of pure TGDDM (curve 1), the temperature corresponding to the peak is about 285 °C at 2.5 °C /min heating rate. Upon adding 6-phr I.30E organoclay to TGDDM epoxy by the DM method, two peaks appear in the exothermal curve (curve 2). Lan and Pinnavaia [45] assumed that the appearance of two peaks is attributed to two different epoxy polymerization processes on the presence of the organoclay. The lower temperature peak is assigned to the polymerization of pre-intercalated epoxy monomers in the clay galleries, where the concentrations of acidic onium protons is high; the higher temperature peak is due to the polymerization of extra-gallery monomers. If this assumption is correct, similar behavior should also be observed in samples made using the HPM method, since epoxy monomers should also exist inside and outside the galleries of organoclay, as the organoclay agglomerates were broken down with the HPM method. As a result, there should also be two peaks in the exothermal curve with the HPM method. However, only one peak appears in curve 3 of Figure 4-1; the peak becomes thin and high as dispersion of organoclay in the epoxy improves.

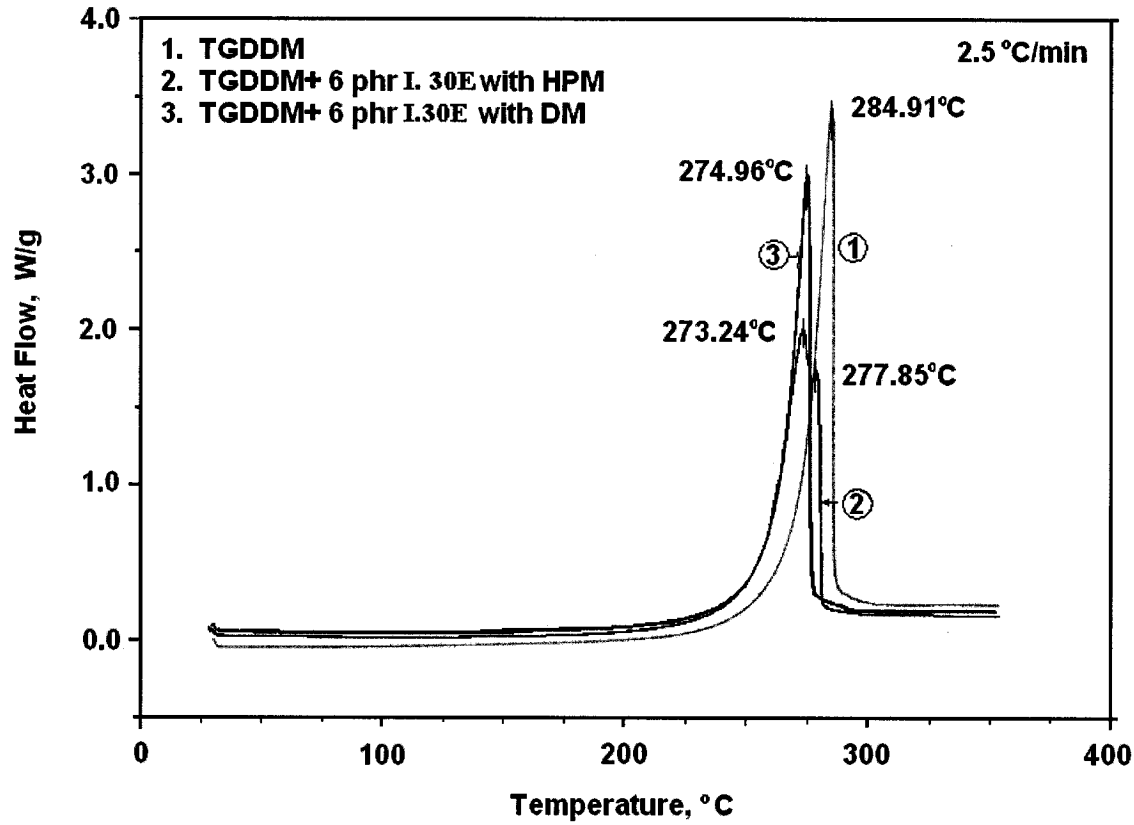

Figure 4-1: Exothermal curves of homopolymerization of TGDDM resin in the presence and absence of organoclay

DSC measurements were also conducted on three other systems: DGEBA/I.30E, DGEBA/30B and TGDDM/30B. DGEBA/I.30E involves the same resin and clay materials that Lan and Pinnavaia used [45]. Two peaks were observed in samples made by the DM method, but only one in samples made by the HPM method. Therefore, the appearance of two peaks may not be attributed to intergallery *vs.* extragallery polymerization; it may rather be due to the difference in reaction rates of materials in the vicinity of the clay clusters, and materials far away from these clusters. The "*vicinity of*

the clay clusters" includes the epoxy both inside and outside of the clay sheets. If the size of the clusters and the distance between them are large, then the difference in reaction rates is clearer. In systems with a poorer distribution of particles, the material in the vicinity of the clusters and that far away may have different properties, and two peaks in the DSC curve may be observed. In systems with finer distribution, the size of the clusters is small and the distance between them is smaller; hence the material in the vicinity of the clusters and that at a distance from them may not differ significantly in properties. Thus the difference in the reaction rates may not be significant, and thus there is only one peak in the DSC curve.

A large catalytic effect of organoclay modified with alkyl ammonium ions (I.30E) on the self-polymerization of DGEBA was obtained (shown in Figure 4-2), similar to that reported by others [45, 114]. Adding 3 -phr I.30E organoclay decreased the first peak temperature by almost 170 °C at 10 °C/min heating rate; any further addition of organoclay has no significant influence on the first peak. A cure mechanism for DGEBA epoxy resin in the galleries of organoclay due to acidic onium ions is proposed and described in Chapter 2; according to this mechanism, the alkyl ammonium ion generates protons through dissociation, which further catalyze the opening of the epoxy rings.

However, these alkyl ammonium ions have little catalytic influence on TGDDM epoxy resin, resulting in a decrease of the peak temperature by only 15 °C at 10 °C/min heating rate at 15-phr clay loading, as shown in Figure 4-2, similar to that reported by others [55, 114]. Compared with DGEBA resin (peak at 375°C in Figure 4-2), TGDDM

epoxy resin (peak at 319°C) is readily self-polymerized in the absence of catalysts. The homopolymerization of TGDDM is due to decomposition of TGDDM molecules to form small molecules containing hydroxyl groups, which catalyze the opening of epoxy rings [103]. But the temperature where alkyl ammonium ions catalyze the opening of the epoxy rings in DGEBA is about 80 °C lower than the decomposition temperature of TGDDM. The alkyl ammonium ions should catalyze the opening of the epoxy rings of TGDDM resin at least at the same temperature as DGEBA resin, because TGDDM contains more epoxy groups. What weakens this catalytic effect? Explaining this phenomenon distracts from the research objectives of this thesis; therefore, further chemical analysis was not performed.

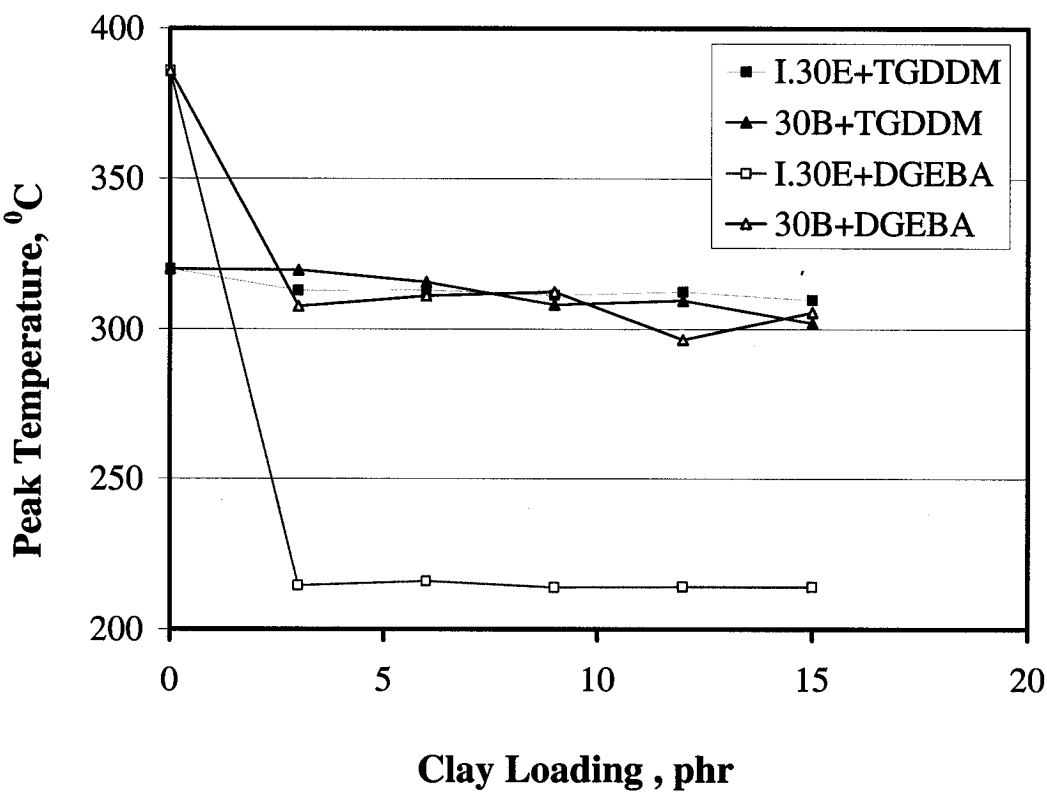

Figure 4-2: Exothermal peak temperature *versus* clay loading

It is important that this weaker catalytic effect does not provide a situation where the intergallery reaction is much faster than extragallery; however, the exfoliation of clay layers in epoxy-clay nanocomposites is attributed to this type of catalysis, according to research results of others [17]. Thus it would be difficult to form fully exfoliated nanocomposites with the combination of I.30E organoclay and TGDDM epoxy resin, if only chemical mechanisms are involved.

A catalytic effect of 30B organoclay on the self-polymerization of DGEBA and TGDDM epoxy resins was also obtained (shown in Figure 4-2). Compared with I.30E organoclay, 30B has less influence on the self-polymerization of DGEBA. The addition of 3 -phr 30B organoclay decreases the first peak temperature by almost 70 °C at 10 °C/min heating rate; any further addition of organoclay also has no significant influence on the first peak. On the other hand, 30B organoclay has the same effect as I. 30E on the homopolymerization of TGDDM; the peak temperature slightly decreases with clay loading, by up to 19 °C at 15-phr clay loading at 10 °C/min heating rate.

From Figure 4-2, it is clear that 30B has the same catalytic influence on both DGEBA and TGDDM epoxy resins. This catalysis may be attributed to the presence of OH groups in the molecular structure of surface modifiers. It is well known that hydroxyl groups are able to catalyze epoxy in the opening polymerization of the epoxy rings, *via* hydrogen bonding and hydrogen transfer. This catalysis effect of hydroxyl-substituted surface modifier on the polymerization of epoxy resins is also reported by Brown, *et al.* [115].

4.3.1.2 Effect of Organoclay on Cure Reaction of the TGDDM/DDS System

After dispersing organoclays in TGDDM resin, DDS curing agent was added to the suspensions, and then the mixture was stirred for another 15 minutes at 135~ 140 °C, in order to dissolve the curing agent. Then a sample was taken from the mixture, quenched in air and analyzed by DSC.

Figure 4-3 presents the exothermal peaks of TGDDM/DDS in the presence of organoclays. In the curve of the pure TGDDM/DDS system, the temperature corresponding to the peak is about 243 °C at 10 °C /min heating rate. Upon adding 10-phr organoclays into the TGDDM/DDS epoxy system, onset temperatures decrease about 4 °C for both organoclays; the exothermal peaks shift downwards 4 °C for I.30E, and 8°C for 30B, respectively. This indicates that the organoclays can accelerate the cure reaction, and thus provide a situation where the intergallery reaction is faster than extragallery; but the difference in reaction rates is not great. Therefore, it may result in a small increase in the d-spacing of organoclay layers with increasing curing temperature.

Because 30B organoclay shifts the exothermal peak downwards more than I.30E, 30B should have larger d-spacing than I.30E in nanocomposites at the same curing conditions.

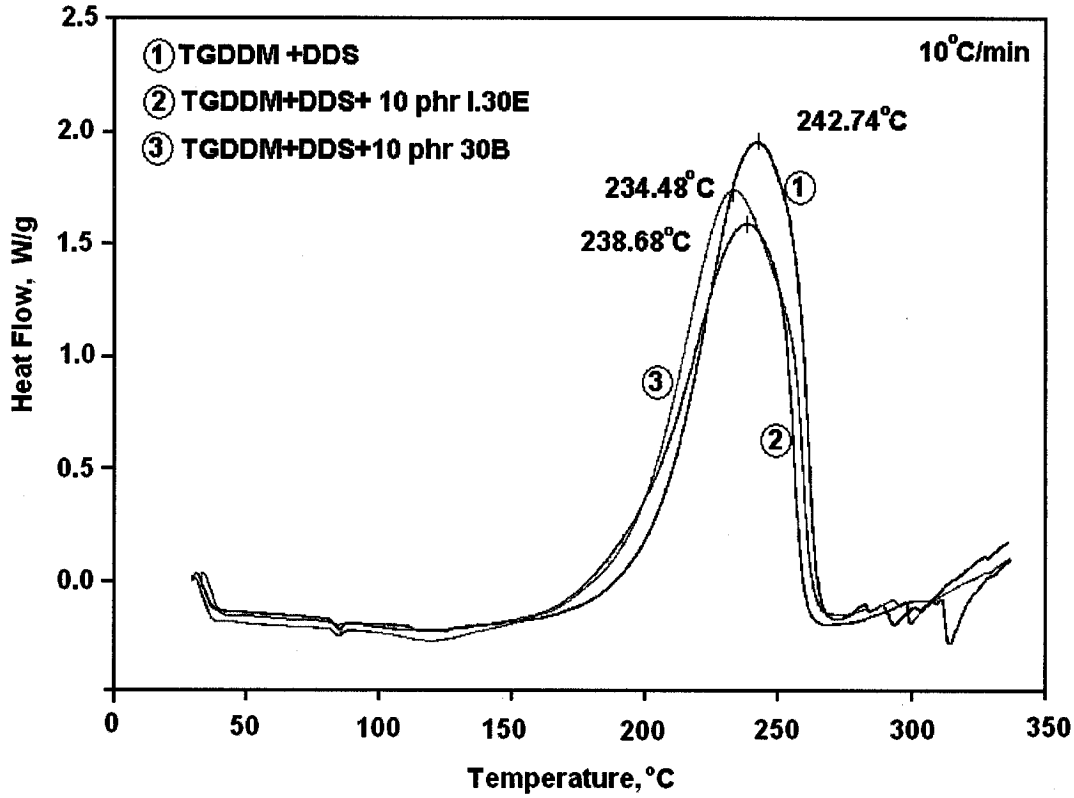

Figure 4-3: Exothermal curves of cure reactions of the TGDDM/DDS system in the presence and absence of organoclay

4.3.2 Manufacturing Processes

A wide range of nanocomposites made of I.30E (E-x series in Table 4-1) and filler composites (N-x series) were synthesized by the DM method. As described in Chapter 3, the addition of I.30E organoclay and Na-clay into TGDDM epoxy resin by the DM method, respectively, results in small increases in viscosity, and has little influence on shear thinning behavior. Therefore, the manufacture of nanocomposites and filler composites by the DM method is the same as that of a pure TGDDM/DDS resin system, except for using sonication at 80 °C for 30 min in order to improve dispersion of clay. However, as the clay loading exceeds 15-phr, it is difficult to dissolve the solid curing

agent, DDS, in the clay/TGDDM suspensions. For 30B organoclay, only two clay loadings of nanocomposites (B-x series) were synthesized, by the same manufacturing process as for I.30E; the main reason is that adding 30B organoclay into TGDDM epoxy resin results in strong shear thinning behavior, due to forming a web of hydrogen bonds between the epoxy and hydroxyl groups of the modifier in the organoclay.

Whether mixed with HPM-E or HPM-A, the suspension of I.30E organoclay and TGDDM resin also shows the same effect on flow behavior: increased viscosity and shear-thinning. However, this results in some problems, such as decreased solubility of solid DDS in TGDDM, high void content, and violent exothermic polymerization in manufacturing samples of nanocomposites at high clay loadings. Therefore, when the same manufacturing process as above was used, only nanocomposites containing 1.5 and 3-phr organoclay were synthesized; the latter contained some micro-voids (about 3 μm in diameter) which can be observed at high magnification (shown in Figure 4-4).

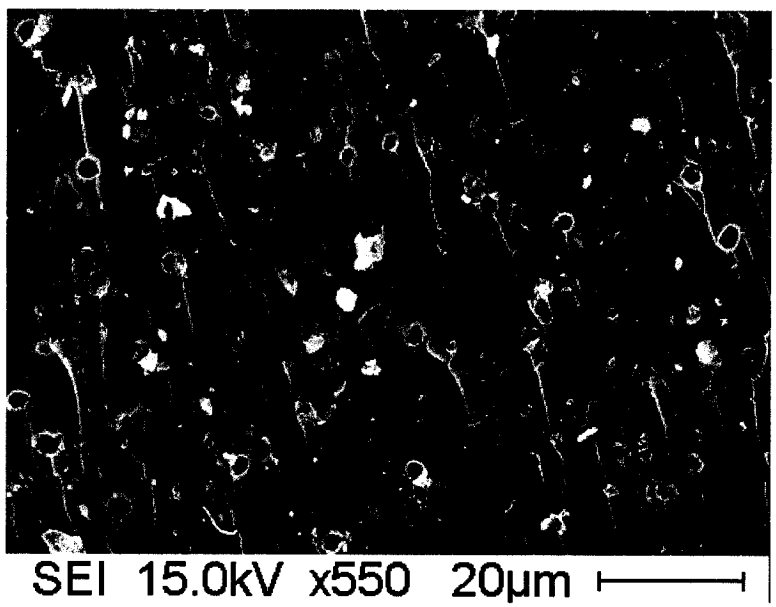

Figure 4-4: SEM micrographs of fracture surface of HPM-A-3 nanocomposites

In order to synthesize nanocomposites with high clay loading, two main modifications were made during the manufacture of specimens, compared to the process above. One involves the vacuum-stirring equipment used to degas; air bubbles in suspensions disappear very fast when stirring under vacuum. The other is removing the sonication procedure; sonication is useful to improve the dispersion of nanoclay in epoxy resin, and reduce air bubbles at the interface between clay platelets and resin molecules; but it results in a rapid increase in viscosity after adding the curing agent. In the case of small levels of clay loading (up to 3%), sonication was possible due to the lower viscosity of the mixture; in the case of higher clay loadings, the viscosity of the mixture is already large, which inhibits the use of sonication. As a result, this modified process can only manufacture specimens of nanocomposites up to 7.5-phr clay loading for I.30E, and 3-phr for 30B, respectively.

4.3.3 Morphology

4.3.3.1 Microstructural Observation by Optical Microscopy

The morphology of these cured systems was first investigated using optical microscopy. The filler composites contained many agglomerates of Na-montmorillonite clay (shown in Figure 4-5A); most of them are transparent, and have a clear interface with the resin due to their crystal structure. The distribution of agglomerates in the filler composites is shown in Figure 4-5B; the average size of agglomerates is 5.9 μm at 6-phr clay loading.

Like the filler composites, the nanocomposites made of I.30E and 30B organoclays by the DM method also contained many agglomerates, with average diameter of about

7.1 and 4.9 μm, respectively (shown in Figures 4-6 and 4-7), similar to reports by others [19,20,33,37,53-55]. Furthermore, the size of agglomerates in nanocomposites made of I.30E organoclay is larger than that in nanocomposites made of 30B organoclay at the same clay loading. However, there are no obvious changes in size or quantity of agglomerates in nanocomposites due to modifying parameters such as stirring rate, temperature and time of mixing, or curing parameters.

The mean diameters and area percentages of agglomerates in the nanocomposites and filler composites were measured using an optical microscope and Clemex Image Analysis System Software. The mean diameter of agglomerates in nanocomposites made of I.30E organoclay gradually increases from 6.3 to 8.3 μm, with increasing clay loading from 3-phr to 15-phr, which is larger than in filler composites at the same clay loading (from 5.9 to 7 μm). Furthermore, nanocomposites made with DMM have about twice the area of agglomerates as filler composites at the same clay loading (shown in Figure 4-8). This may be explained by the fact that Na-montmorillonite clay was only dispersed by shear forces during mixing, while I.30E organoclay has two competing processes: break-up and intercalation by resin and hardener. The former decreases the size of agglomerates, but the latter increases their size. This is schematically described in Figure 4-9, where this intercalation of organoclay with the resin system is confirmed by X-ray diffraction and TEM results.

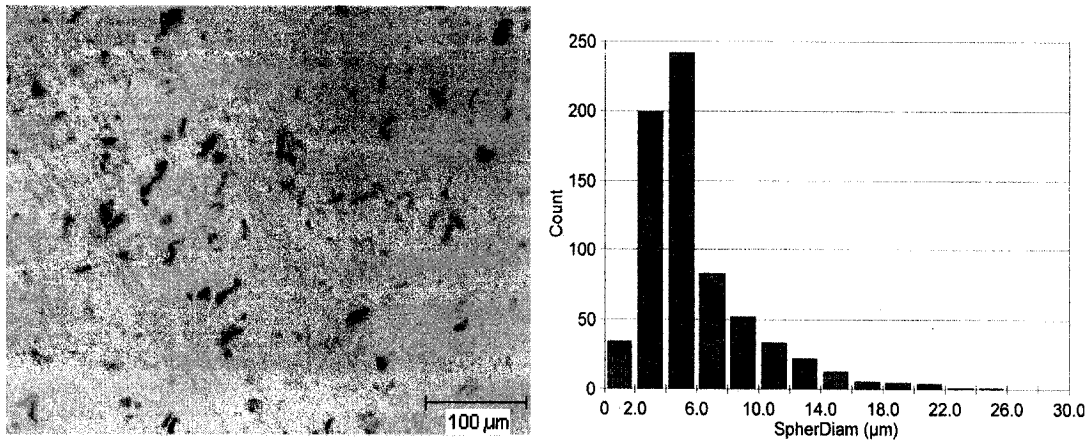

Figure 4-5: Optical micrograph of the filler composite at 6-phr clay loading

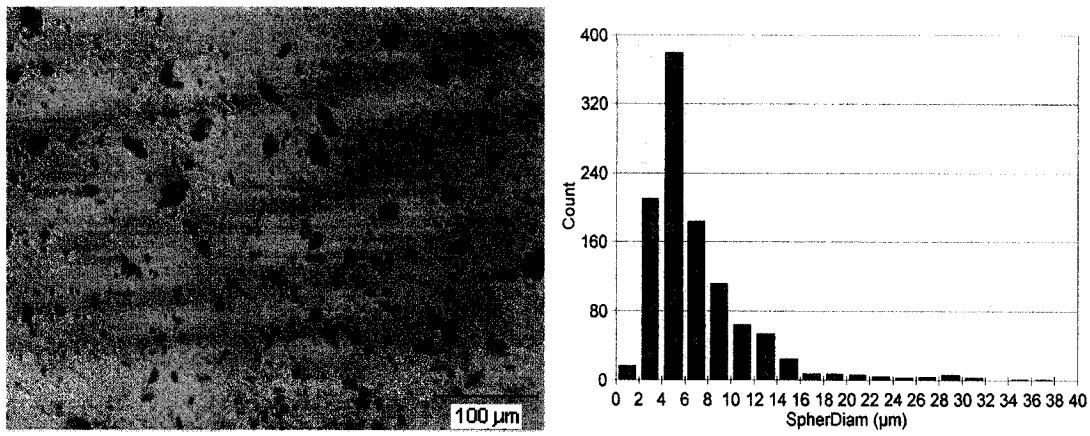

Figure 4-6: Optical micrograph of the nanocomposite made of I.30E by the DM method at 6-phr clay loading

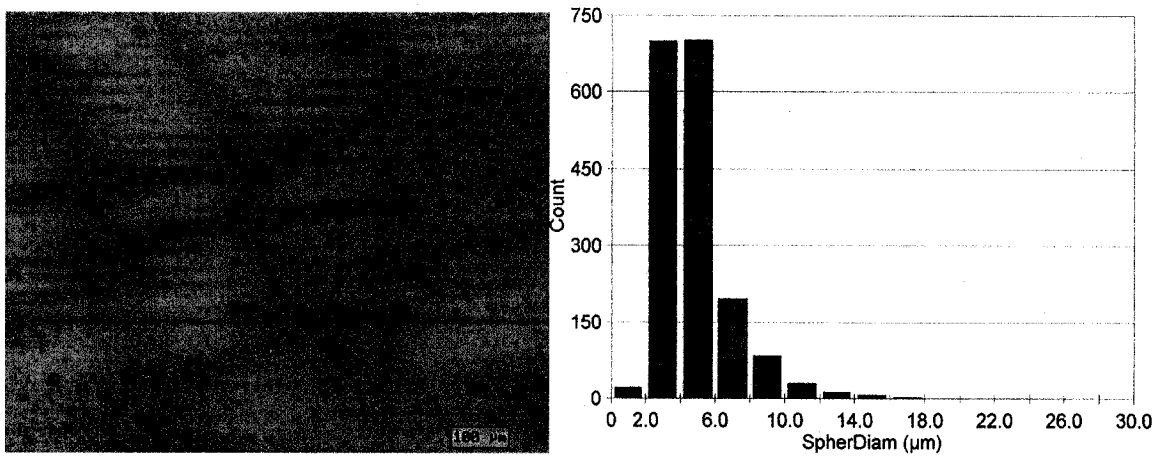

Figure 4-7: Optical micrograph of the nanocomposite made of 30B organoclay by the DM method at 6-phr clay loading

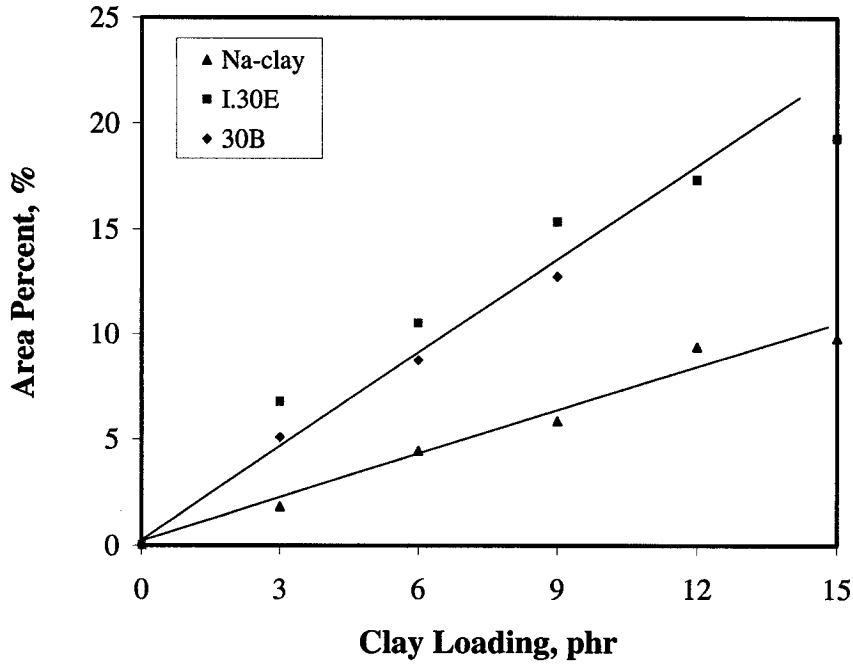

Figure 4-8: Area percentages of agglomerates in nanocomposites and filler composites

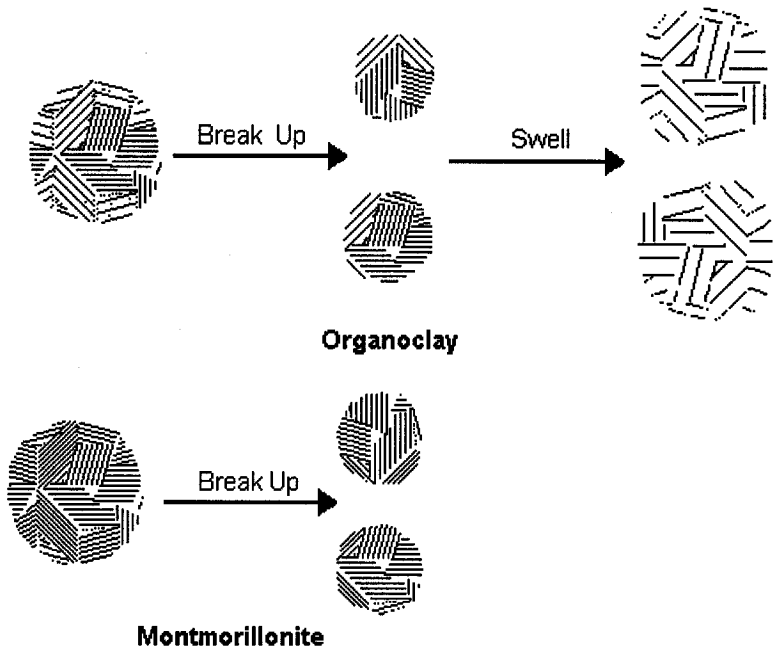

Figure 4-9: Schematic graphs of the dispersion of organoclay and Na-montmorillonite

A micrograph of the nanocomposite made with HPM-A at 6-phr clay loading is shown in Figure 4-10. The maximum size of agglomerates greatly decreases to 1~2 μm, and distribution of organoclay in the epoxy system is improved. These remnant agglomerates may be attributed to impurities or unmodified clay in the commercial products. Thus, this indicates that big agglomerates in nanocomposites mainly come from poor dispersion, and that these agglomerates may be broken down by the HPM method.

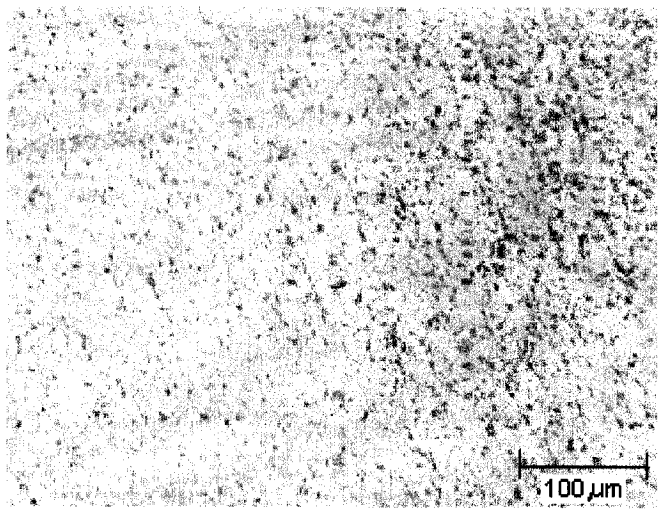

Figure 4-10: Optical micrograph of the nanocomposite made by the HPM method at 6-phr I.30E clay loading

4.3.3.2 Fracture Surface Observation with SEM

The fracture surfaces of these materials were examined by SEM, as shown in Figure 4-11. Figure 4-11 A shows the fracture surface of filler composite at 6-phr clay loading (N-6); agglomerates are visible in different sizes, with a maximum diameter of

about 20 μm. Figures 4-11 B and C exhibit the fracture surfaces of nanocomposites made of I.30E (E-6) and 30B (B-6) by the DM method at 6-phr clay loading, respectively. Agglomerates are also visible in both nanocomposites; larger in E-6, with a maximum diameter of about 30 μm, and smaller in B-6, with a maximum diameter of only about 10 μm. This indicates that 30B organoclay is more uniformly dispersed in TGDDM/DDS than I.30E organoclay; these results are consistent with those obtained by optical microscopy.

As I.30E organoclay was dispersed in TGDDM/DDS by the HPM-A method (HPM-A-6), no agglomerates were observed on the fracture surface, as shown in Figure 4-11 D. The same result was observed in nanocomposites made by the HPM-E method, and that made of 30B by the HPM method.

Even though the number and size of agglomerates were greatly reduced by dispersing I.30E in the epoxy system by GMM for two hours, some agglomerates are still visible on the fracture surface, with a diameter of about 10 μm (shown in Figure 4-11 E). As grinding time increases, the size of agglomerates further decreases to 6 μm, but the number increases, due to different batches and lack of control of the amount of energy applied, as shown in Figure 4-11 F. Thus agglomerates in organoclays can be broken down by both HPM and GMM methods, and nanocomposites made by the HPM method have more uniform distribution of organoclays than those by the GMM method.

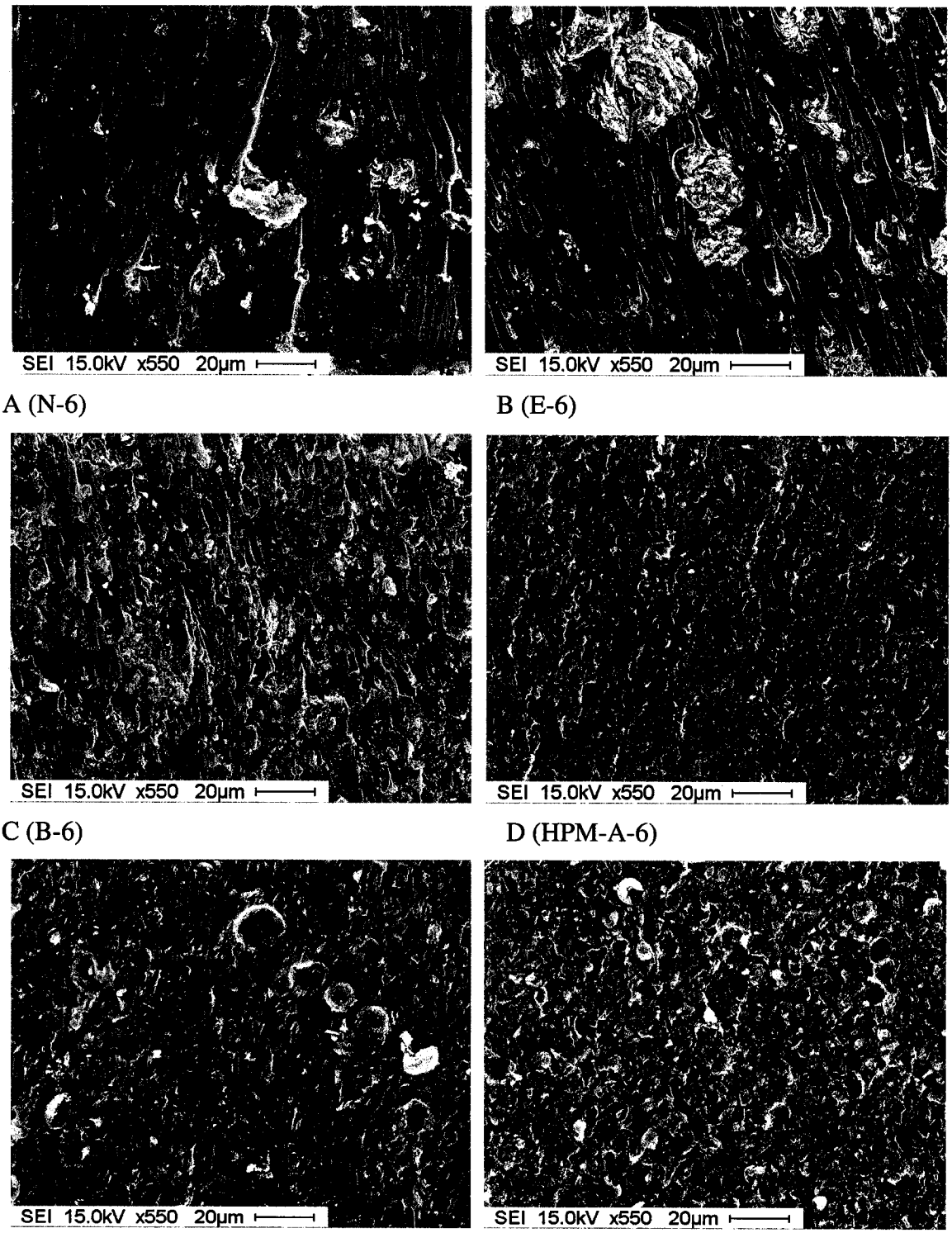

A (N-6) B (E-6)

C (B-6) D (HPM-A-6)

E (GMM-2) F (GMM-6)

Figure 4-11: SEM micrographs of fracture surfaces

4.3.3.3 Microstructure Observation by TEM

The nanocomposite made by HPM-A at 6-phr clay loading (HPM-A-6) was examined by TEM at low magnification (shown in Figure 4-12). In Figure 4-12, the dark lines are silicate layers of organoclay, and the white area in the vicinity of the clay layers is formed due to cutting. Figure 4-12 shows that agglomerates of organoclay are broken down to form small particles consisting of several clay platelets; particles of organoclay are uniformly distributed in the epoxy resin system. The dimensions of most particles range from 500~700 nm in length, and 30~60 nm in thickness.

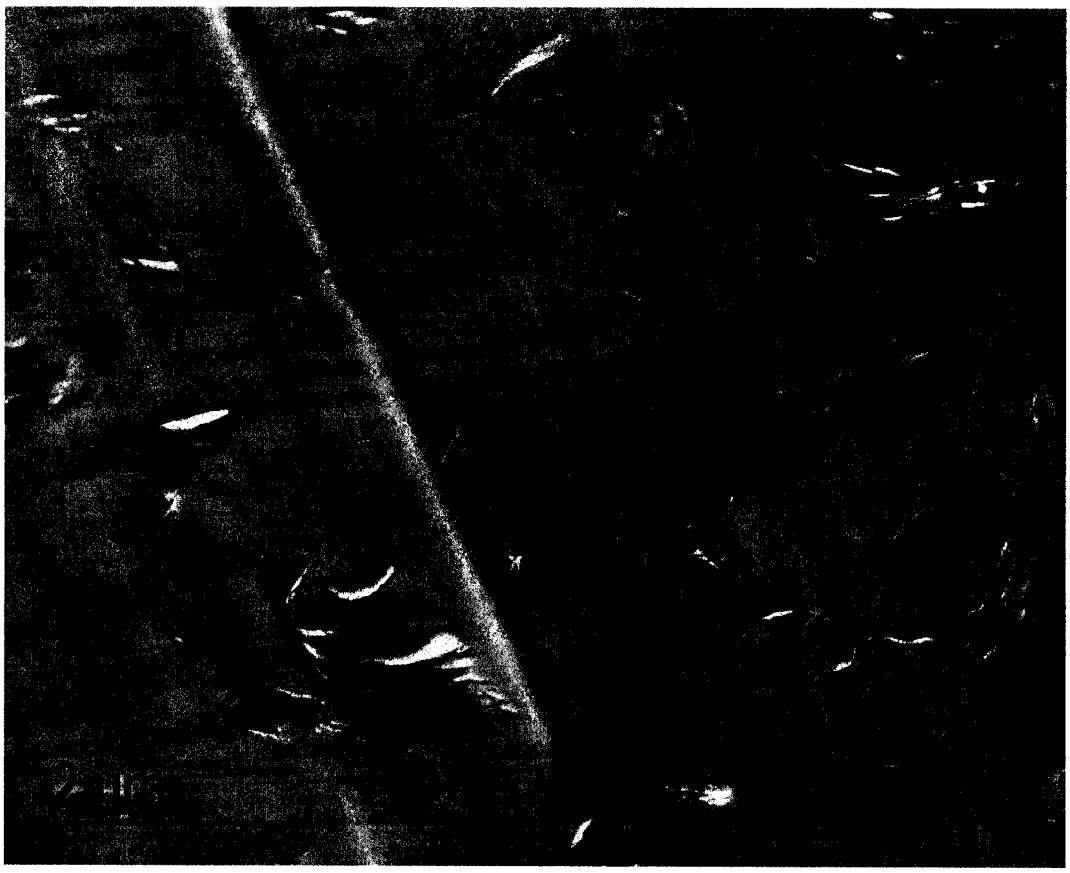

X10, 000

Figure 4-12: TEM image of HPM-A-nanocomposite (HPM-A-6) at low magnification

A single particle in the HPM-A-6 nanocomposite was further examined by TEM at high magnification (shown in Figure 4-13). In the nanocomposite, the clay packet consists of 5 or 6 silicate layers of organoclay, not in parallel arrangement. The thickness of the clay packet is about 31 nm, and the average d-spacing of organoclay in the packet is estimated to be 6 nm, varying from 3.5 nm to 13 nm. However, the layer thickness is larger than 1 nm, and this indicates that the cross-section is not perpendicular to clay platelets. Therefore, the estimated d-spacing should be slightly larger than the factual value. This d-spacing is larger than that (about 4 nm) reported by Kornmann, *et al.* [54] with similar materials but a different manufacturing process.

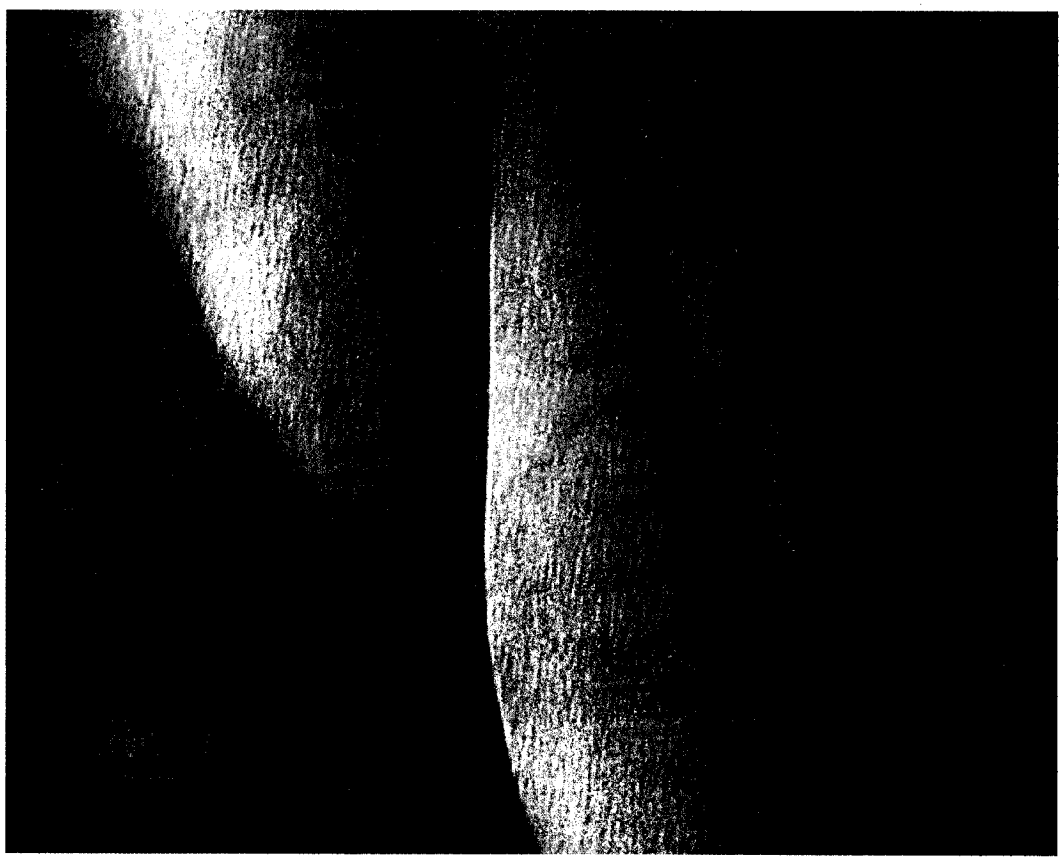

X250, 000

Figure 4-13: TEM image of HPM-A-nanocomposite (HPM-A-6) at high magnification

The nanocomposite made by HPM-B at 3-phr clay loading (HPM-B-3) was also examined by TEM at low magnification (shown in Figure 4-14). Figure 4-14 shows that the agglomerates of 30 B organoclay are also broken down to form small particles, consisting of several clay platelets, and that the HPM-B-3 nanocomposite has more uniform distribution of clay particles in the epoxy resin system than HPM-A-6. The dimensions of most particles range from 300~500 nm in length, and 30~60 nm in thickness.

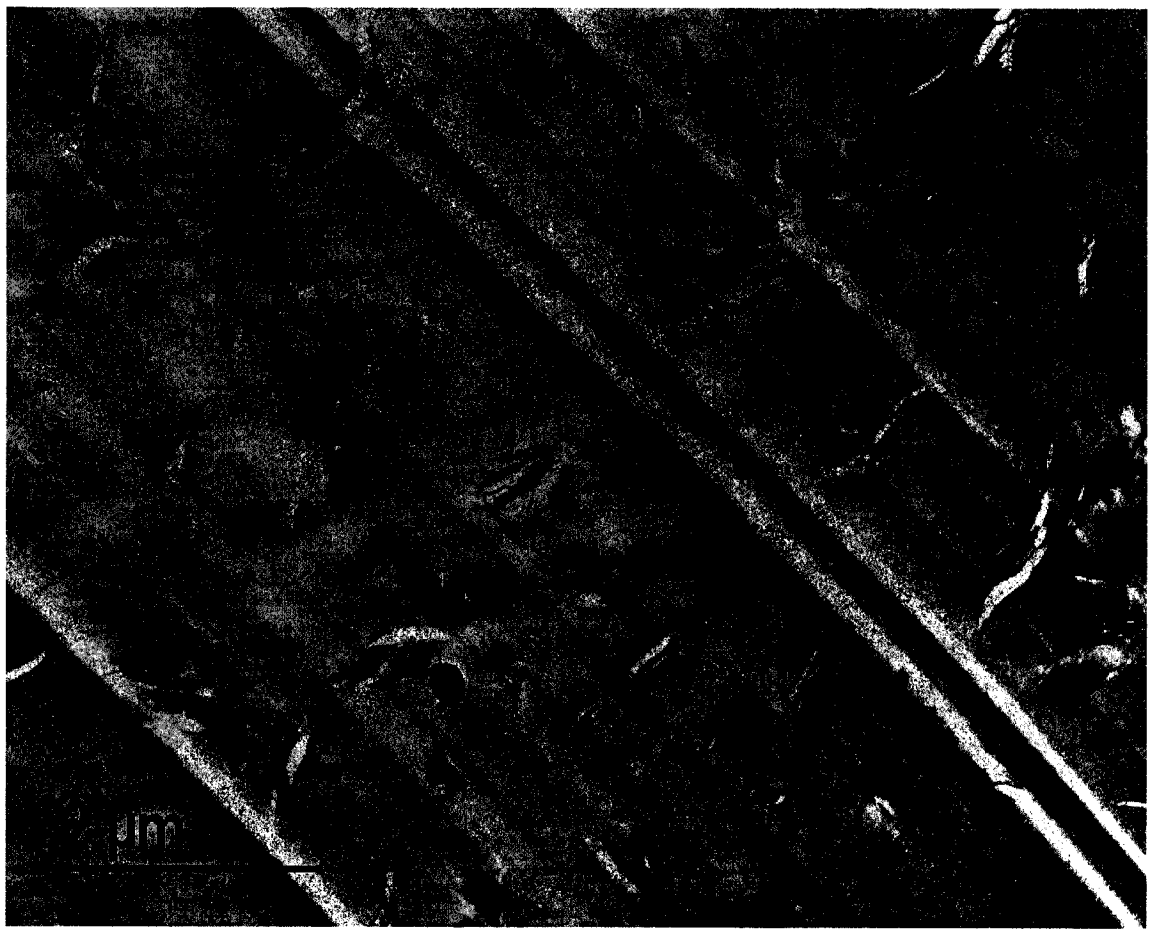

X10, 000

Figure 4-14: TEM image of HPM-B-nanocomposite (HPM-B-3) at low magnification

A single particle in the HPM-B-3 nanocomposite was further examined by TEM at high magnification (shown in Figure 4-15). In the nanocomposite, the clay packet consists of 8 or 9 silicate layers of organoclay, in nearly parallel arrangement. The thickness of the clay packet is about 54 nm, and the average d-spacing of organoclay in the packet is estimated to be 7 nm, varying from 3.5 to 11 nm. The d-spacing of the HPM-B-3 nanocomposite is larger than that of HPM-A-6.

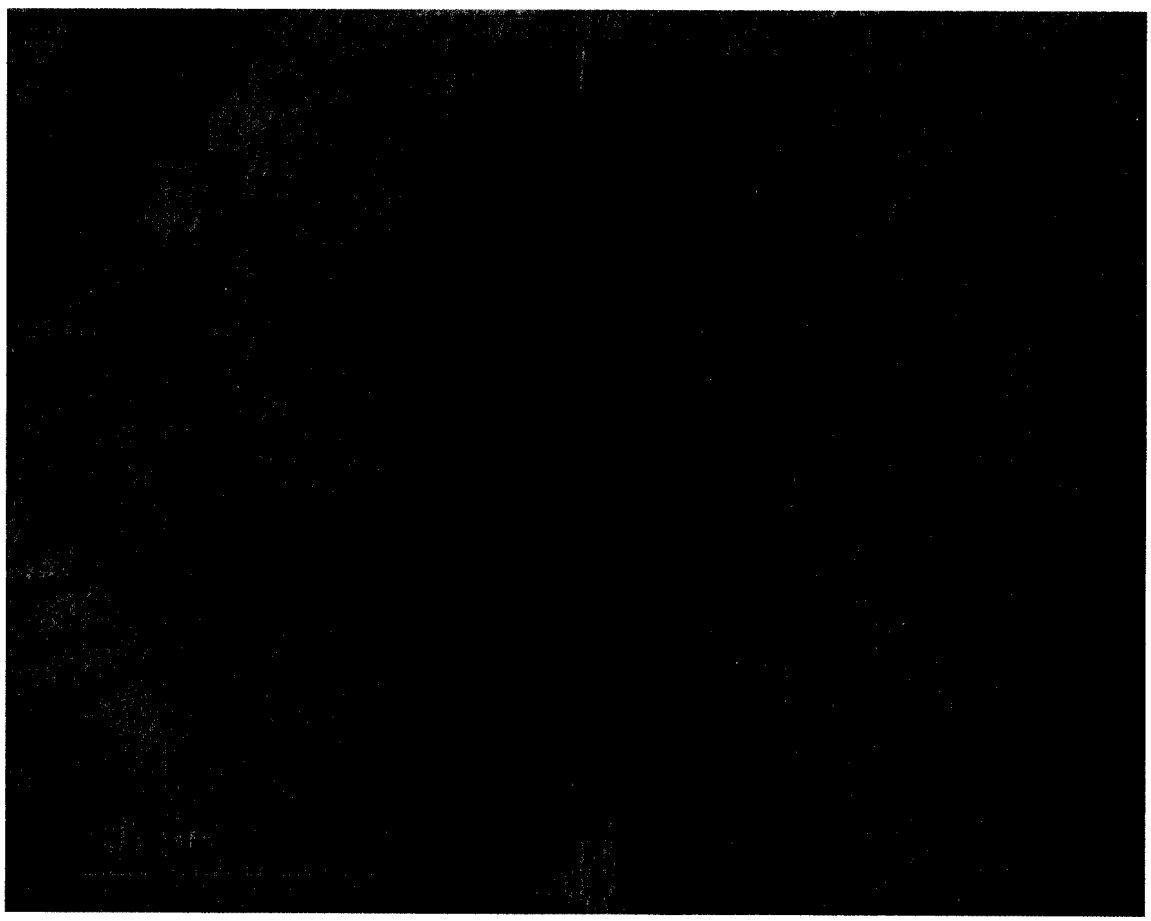

X250, 000

Figure 4-15: TEM image of HPM-B-nanocomposite (HPM-B-3) at high magnification

4.3.3.4 X-ray Diffraction Pattern of Nanocomposites

X-ray diffraction (XRD) was used to determine the microstructure of the clay in the nanocomposites and filler composites; Figure 4-16 presents XRD curves of Na-montmorillonite and its composites at different clay loadings. In the curve for clay powder without epoxy, a prominent peak corresponding to the basal spacing of Na-montmorillonite occurs at 1.22 nm. For all filler composites, prominent peaks appear; this indicates that XRD can detect basal spacing, even at low clay loading, if it is within the measurable range of the XRD machine. In Figure 4-16, the basal spacing of some filler composites is larger than that of Na-montmorillonite. This may be attributed to the fact that a small quantity of hardener or resin was forced into the galleries of the clay.

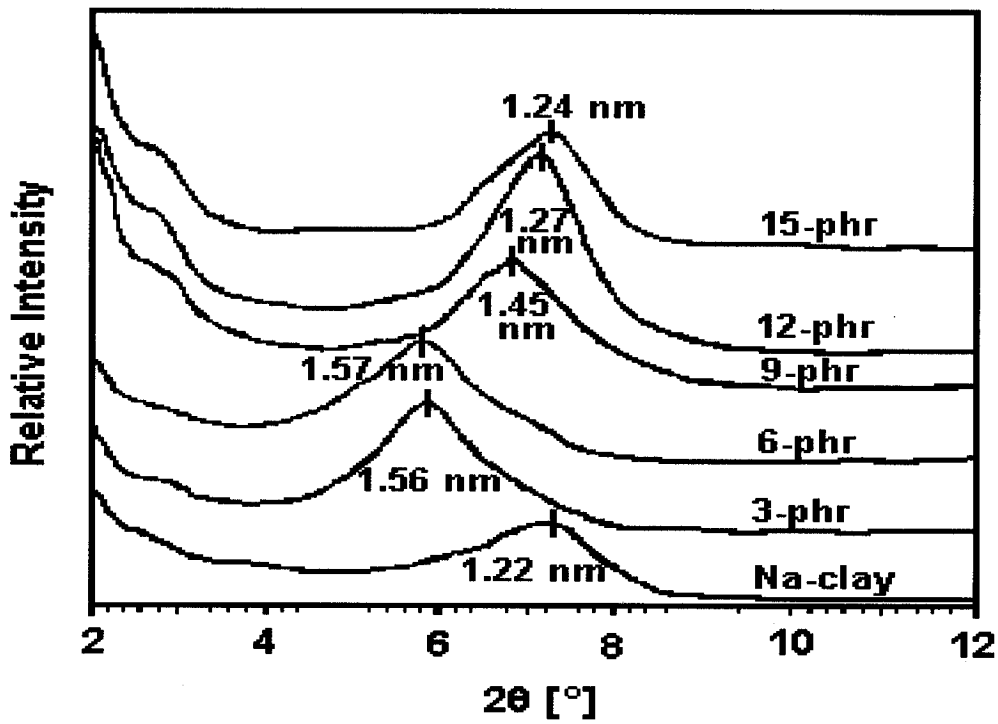

Figure 4-16: XRD patterns of Na-montmorillonite and its composites made by the DM method

The XRD curves of the TGDDM-DDS epoxy system and its nanocomposites made of I.30E organoclay by the DM method are shown in Figure 4-17. In contrast to the filler composites, prominent peaks are absent in the curves for the nanocomposites, which indicates that the basal spacing of organoclay may be more than 4 nm (corresponding to $\leq 2^{\circ}$ in 2 theta, which is out of the range of the machine). The remnant shoulder and small peak in some curves may be attributed to a combination of the (001) signals of a smaller basal spacing, and the (002) signals of a larger basal spacing, according to previous TEM results and the XRD results of HPM-A-6, to be discussed below. Therefore, the basal spacing of organoclay in the nanocomposite made of I.30E organoclay by the DM method increases to more than 4 nm; these results are similar to those reported by others [55, 114].

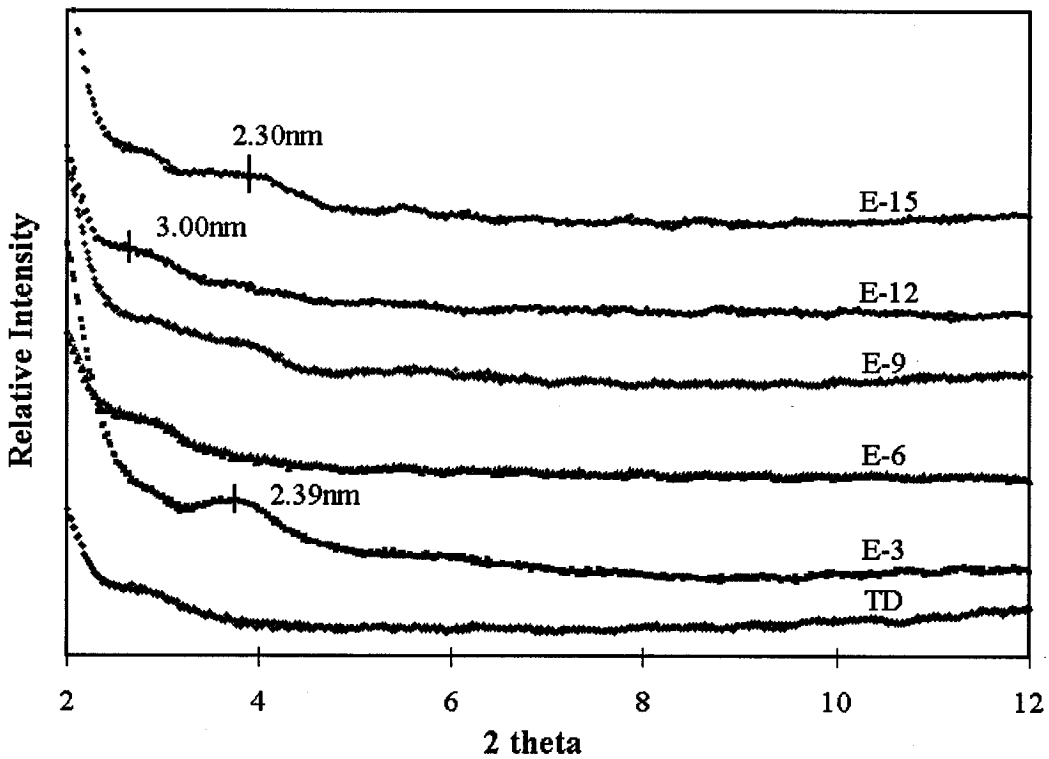

Figure 4-17: XRD curves of the TGDDM-DDS epoxy system and its nanocomposites made of I.30E organoclay by the DM method

The same results were obtained from nanocomposites made of 30B organoclay by the DM method. Although the basal spacing of the organoclay could not be measured from the XRD results, due to limitations of the equipment, it is confirmed that the clay is intercalated with the epoxy system by the DM method.

The XRD curves of TGDDM/DDS and its nanocomposites formed by the HPM method are shown in Figure 4-18. In the curve of the HPM-A-6 nanocomposite, the first peak (001) of the organoclay is absent, but the second peak (002) appears at around 3^{o} (corresponding to about 3.21 nm). The basal spacing is estimated to be 6.42 nm; this is consistent with data obtained by TEM. As shown in Figure 4-18, the other nanocomposites have similar XRD curves, with second peaks appearing around 3^{o}. Consequently, the XRD results disclose that the basal spacing of most organoclay platelets in the epoxy system expands to about 6.4 nm. Whether the HPM-E or HPM-A method is used, nanocomposites at the same clay loading have almost the same XRD curve, implying either that the dispersion difference between these two methods has no effect on the morphology of nanocomposites, or that the difference in the morphology of the nanocomposites was not measurable due to the limitations of the equipment.

Similar results were obtained for nanocomposites made of 30B organoclay by the HPM method, and I.30E organoclay by the GMM method, showing that no significant changes in XRD curves were observed whether the DM, GMM or HPM method was used. This indicates that the basal spacing of nanocomposites is dependent on the chemical properties of materials, and independent of the mixing process.

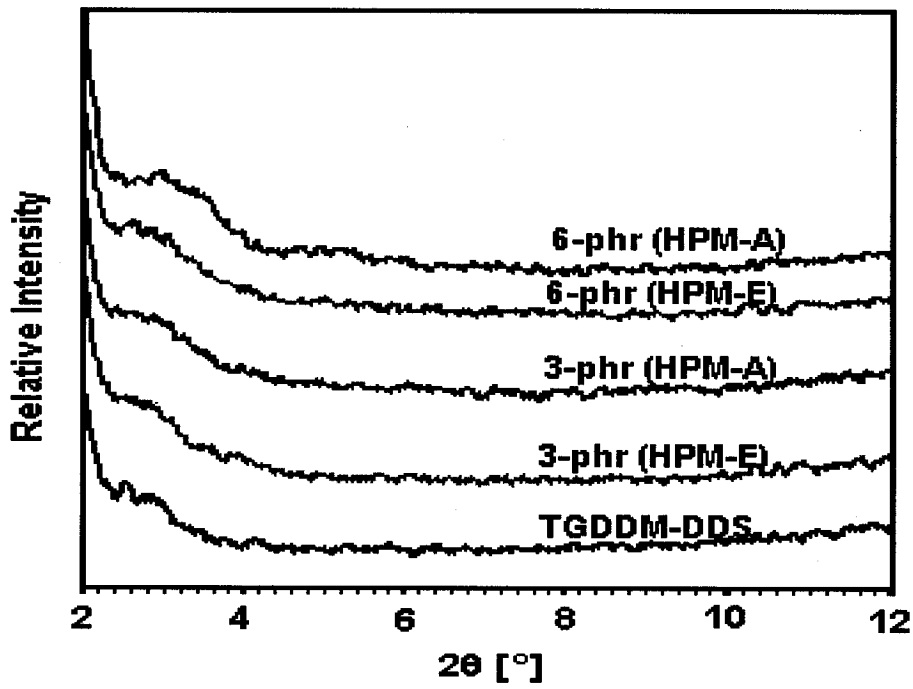

Figure 4-18: XRD patterns of TGDDM/DDS and its nanocomposites by the HPM method

4.3.4 Effect of Cure Temperature on Morphology

To understand the changes in basal spacing of organoclay during manufacturing the HPM-A-6 nanocomposite, samples at different stages were tested, as shown in Figure 4-19. From the previous result in Chapter 3, the basal spacing of I.30E was measured to be 2.25 nm. After the organoclay is dispersed in acetone by the high-pressure mixing machine, the basal spacing of organoclay increases from 2.25 to 3.40 nm. After mixing the clay suspension with the TGDDM resin, the basal spacing further increases to 3.81 nm, as shown in Figure 4-19; this indicates that the epoxy resin was intercalated into the organoclay. As the curing agent DDS is added into the organoclay/epoxy suspension with mechanical stirring, the first peak (001) disappears, but the second peak (002) shifts

slightly, from 1.92 to 1.97 nm; the basal spacing is estimated to be 3.94 nm. Finally, the samples were cured at three different temperatures, 125 °C, 150 °C and 175 °C, respectively. All first peaks (001) are absent, and the second peaks (002) appear at 2.90, 3.21 and 3.29 nm, respectively; therefore, the basal spacing of organoclay slightly increases from 5.8 nm to 6.58 nm upon increasing the cure temperature, consistent with what is expected according to the cure kinetic study above.

The same study was performed with nanocomposites made of 6-phr 30B, though the nanocomposite contains many voids, as shown in Figure 4-20. The basal spacing of 30B was measured at 1.74 nm. After the organoclay is dispersed in acetone by the HPM-A method, the basal spacing of organoclay increases from 1.74 to 3.42 nm. Upon mixing the clay suspension with the TGDDM resin, the basal spacing further increases to 3.72 nm, as shown in Figure 4-20. This indicates that the epoxy resin is intercalated into the organoclay. As the curing agent DDS is added into the organoclay/epoxy suspension with mechanical stirring, the first peak (001) disappears, but the second peak (002) shifts slightly, from 1.78 to 1.95 nm. The basal spacing is estimated to be 3.90 nm. Finally, the samples were cured at three different temperatures, 125 °C, 150 °C and 175 °C, respectively. All first peaks (001) are absent, and the second peaks (002) appear at 1.97, 3.04 and 3.27 nm, respectively. Therefore, the basal spacing of organoclay changes from 3.94 nm to 6.54 nm upon increasing the cure temperature. The change of the basal spacing with temperature in 30B nanocomposites is larger than in I.30E; thus, these results are also consistent with what is expected according to the cure kinetic study above.

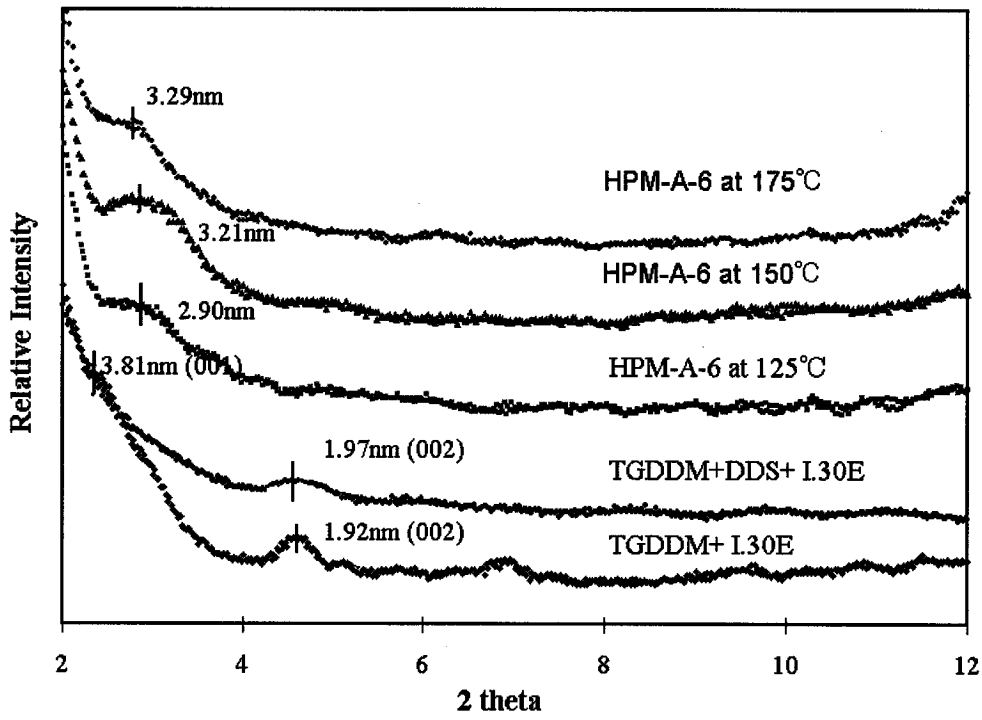

Figure 4-19: XRD patterns of HPM-A-6 nanocomposites at different stages

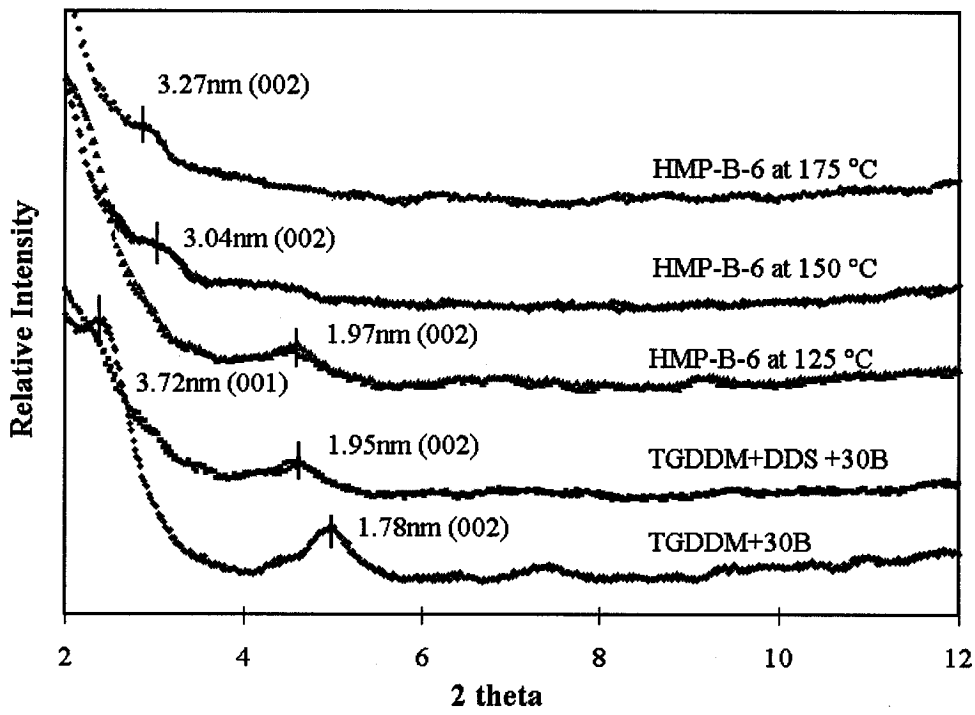

Figure 4-20: XRD patterns of HPM-B-6 nanocomposites at different stages

4.3.5 Formation Mechanism and Proposed Models

According to the above experimental results and those in Chapter 3, the formation mechanism of the nanocomposites is explained as follows:

As an organoclay is added into TGDDM epoxy resin at low viscosity, the epoxy molecules diffuse into the galleries of the organoclay, and thus expand the basal spacing of organoclay from 2.25 to 3.37 nm. Mechanical means such as stirring, ultrasonic, high shear force, collision, *etc.* may accelerate this process, but do not change the equilibrium value of basal spacing; this value is dependent on interactions between ammonium ions and epoxy resin molecules. Adding curing agent DDS to the epoxy-clay suspension results in a little increase in the basal spacing of organoclay; upon initiating the cure reaction, the basal spacing increases only 1~3 nm, because alkylammonium ions have a weak catalytic effect on the TGDDM/DDS system, which cannot provide a situation where the intergallery reaction rate is much faster than extragallery. Therefore, these materials only form a nanocomposite with 5~7 nm basal spacing.

Agglomerates of organoclay may be broken down by mechanical means in organic solvents or epoxy resins. By the DM method the size of agglomerates can only be reduced to several microns. The organoclays on the outside surface of agglomerates should have the same basal spacing as in the HPM-A-6 nanocomposite, but inside agglomerates should have smaller basal spacing, because not enough curing agent (DDS) is diffused into the galleries during the short process time. Therefore, a typical intercalated nanocomposite was synthesized with the DM method.

By the HPM method, agglomerates of organoclays can be broken down by a Microfluidizer machine to form tactoids of a small number of layers in organic solvents or epoxy resins. However, these small tactoids may be brought together, inducing coagulation, during later procedures such as mixing with the curing agent, evaporating solvents, or curing the resin system. Thus, the final particle size is the outcome of two processes of opposite effect. The tactoids of organoclay in nanocomposites consist of 5 ~ 10 silicate layers, and are uniformly distributed in the epoxy system. The shape of tactoids looks like discs, whose diameter is equal to that of clay layers, with a thickness of 30~60 nm. Therefore, this is a real nanocomposite, although the clay layers are not fully exfoliated. Fully exfoliated nanocomposites are only applicable for few special materials with chemical mechanism, but the HPM method can synthesize nanocomposites of a wide class of materials using mechanical mechanism.

The results obtained by the GMM method fall between those of the DM and HPM methods; the shape of some agglomerates is still spherical, and the maximum diameter is several microns.

In order to analyse the mechanical and physical properties of these nanocomposites, the following schematic illustrations (Figures 4-21) and parameters (shown in Table 4-2) are proposed according to the above experimental data.

Table 4-2: Structural parameters of nanocomposites

Nanocomposite	Organoclay	Dispersion Method	Shape and Size	Basal Spacing
E-x	I.30E	DM	Spherical, Aver. Diameter: 7 μm Max. Diameter: 30 μm	More than 4 nm
B-x	30B	DM	Spherical, Aver. Diameter: 5 μm Max. Diameter: 20 μm	More than 4 nm
GMM-x	I.30E	GMM	Spherical and Disc Max. Diameter: 10 μm	More than 4 nm
HPM-A, HPM-E	I.30E	HPM	Disc Diameter: 600nm Thickness: 45nm	About 6 nm
HPM-B	30B	HPM	Disc Diameter: 400nm Thickness: 45nm	About 7 nm

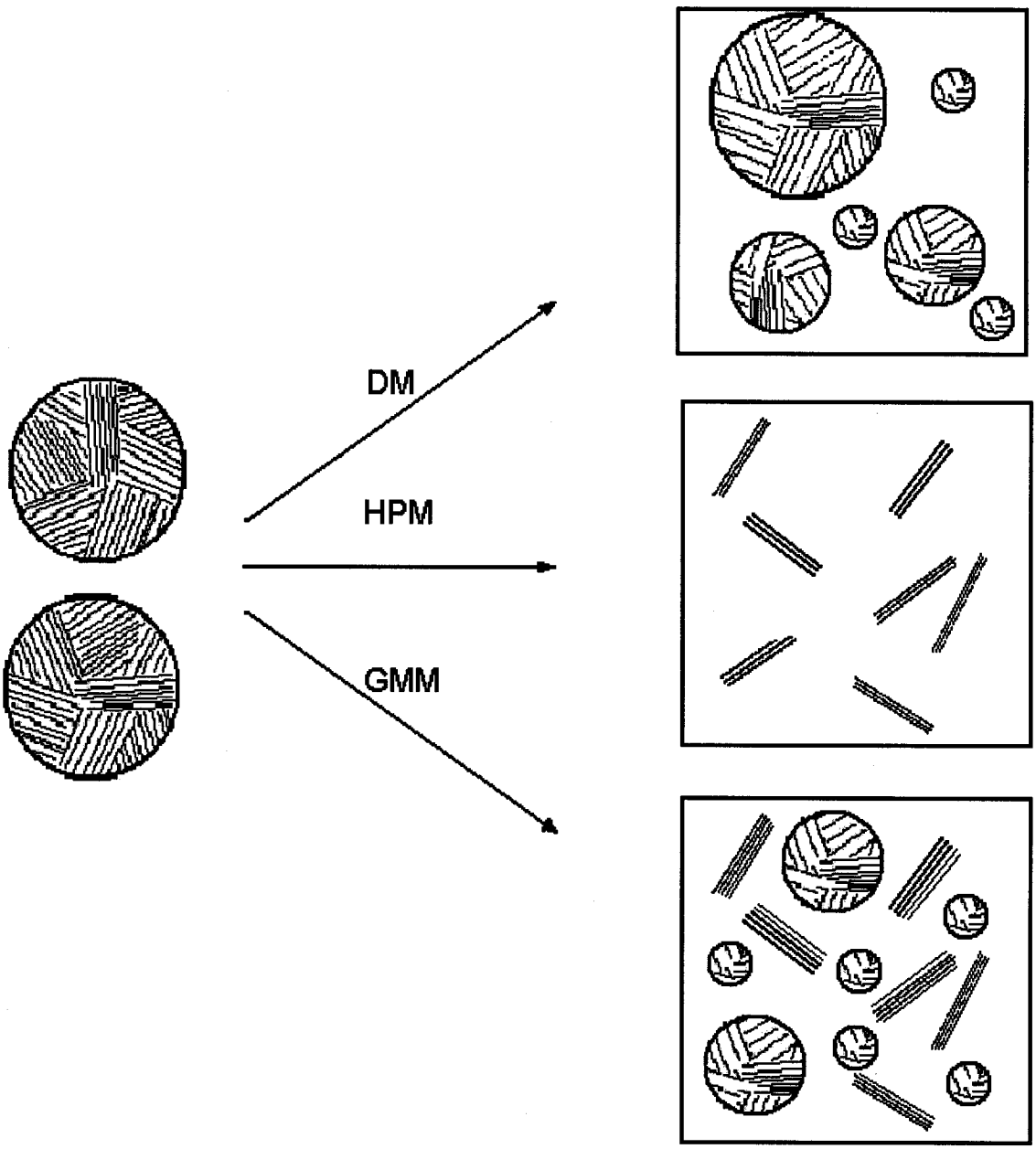

Figure 4-21: Schematic illustration of nanocomposites made by different methods

4.4 Summary

By the conventional mixing method, a typical intercalated nanocomposite was synthesized. The organoclay exists in the high-performance epoxy matrix in the form of agglomerates, whose size is on a micro-scale, although basal spacing is increased to 5~7 nm. However, these agglomerates may be broken down to tactoids which consist of 5 ~ 10 silicate layers, and are uniformly distributed in the epoxy system, by the HPM method. The shape of tactoids looks like discs, whose diameter is equal to that of clay layers, with a thickness of 30~60 nm. Therefore, real nanocomposites were synthesized by the HPM method.

Chapter 5

Synthesis and Morphology of Hybrid Nanocomposites Modified with Organoclay and Rubber

This chapter deals with the synthesis of hybrid epoxy nanocomposites modified with carboxyl-terminated butadiene acrylonitrile (CTBN) rubber and organoclay, after an organoclay was dispersed in the DGEBA epoxy resin by the HPM method. The effects of the organoclay and the rubber on the homopolymerization of DGEBA epoxy resin, and the curing of a DGEBA/BF_3.MEA system, were studied by DSC. The rheological properties of various epoxy resin systems were measured in order to determine the effect of the organoclay on the process properties of the epoxy system. The effect of curing temperature on the formation of the rubber phase was investigated by DMA; the degree of cure and T_g of all modified epoxies were measured. The morphology of nanocomposites was characterized by optical microscopy, XRD, Atomic Force Microscopy (AFM), TEM and SEM. The influence of cure temperatures on the morphology of nanocomposites was investigated. Finally, a formation mechanism for the exfoliated nanocomposites, and structural models of the nanocomposites made in this chapter, are proposed.

5.1. Introduction

One of the most successful approaches to enhancing the fracture toughness of epoxy resins is to incorporate a reactive liquid rubber into the materials [6]. In this method, it is critically important to form a two-phase morphology, with rubber particles dispersed in and bonded to the crosslinked epoxy matrix, to enhance toughness and minimize the decrease of other important properties, such as modulus and T_g. The rubbers most widely studied and employed are butadiene-acrylonitrile copolymers, with functional end groups such as carboxyl (CTBN), amine (ATBN) or epoxy (ETBN). These groups can form chemical bonds with the epoxy resin, to provide a good interface between the dispersed rubber phase and matrix.

Various factors influencing morphology have been widely studied. Increasing the quantity of rubber in the system results in increased volume fraction and sizes of the rubber phases, but the rubber concentration should not exceed about 20% by weight to be effective in enhancing toughness. The type of curing agent plays an important role in forming the two-phase morphology of rubber-modified epoxies. Cure agents with a highly reactive nature are relatively inefficient in enhancing toughness, because only a small quantity of rubber is separated from the epoxy phase [116]. However, highly reactive agents are generally required for many commercial applications, for economic considerations. A decrease in the molecular weight of the starting epoxy resin, which corresponds to an increased cross-linking density, decreases substantially the toughness of rubber-modified epoxies [117]. Resins with higher cross-linking density exhibit a very small improvement in fracture toughness with rubber modification.

Incorporating fillers such as silica, glass micro-spheres, calcium carbonate and alumina trihydrate into polymers, to enhance fracture toughness, has also been reported [8, 118]. The major advantage is that they simultaneously increase toughness and modulus. However, fillers are less efficient at enhancing toughness than rubber modification. The feasibility of adding both fillers and rubbers to epoxy resins has been examined; the results show that the G_{IC} and modulus of a CTBN-glass bead hybrid epoxy increase by 55% and 7%, respectively, at 15-phr CTBN and 35-phr glass beads, over the CTBN-modified epoxy [119, 120].

Recently, nanocomposite technology using organoclay as nanoscale reinforcement offers an interesting alternative for modifying epoxy resins. Like fillers, it can simultaneously improve toughness and modulus of resins, but it provides higher efficiency than fillers [55]. And organoclay at low clay loading dramatically increases the strength, modulus and fracture strain of rubbers at the same time [12, 42, 46, and 47]. Therefore, it is logical to design hybrid-modified epoxies with organoclay and rubber. However, the synthesis of hybrid epoxy nanocomposites modified with rubber and organoclay has not been reported.

Piperidine is a curing agent, mainly used to study toughening mechanisms in rubber-modified epoxies because of its relative high efficiency in enhancing toughness. However, it is so extremely toxic that it is difficult to ensure safety during the process of manufacturing nanocomposites with it.

Unlike piperidine, Boron trifluoride monoethylamine (BF_3.MEA) is a less toxic solid, widely used with other cure agents in the matrices of composites [4, 6, and 38].

BF_3.MEA is a latent catalyst, which does not initiate cure reaction of epoxy groups until curing temperature reaches about 80~90°C. Because of the higher reactive nature of BF_3.MEA, epoxies cured with this hardener have high crosslinking density and glass transition temperature (T_g), but low fracture toughness. To the best of the author's knowledge, epoxy nanocomposites cured with BF_3.MEA have not yet been reported.

The objective of this chapter is to explore the formation of hybrid epoxy nanocomposites modified with rubber and organoclay. The mechanical means of achieving exfoliation of nanocomposites was validated; the effects of materials and process parameters on the morphology of nanocomposites were examined.

5.2 Experimental

5.2.1 Materials

The epoxy resin system is the diglycidyl ether of bisphenol A (DGEBA) cured with boron trifluoride monoethylamine (BF_3.MEA). The recommended formulation of DGEBA/BF_3.MEA is 100/3 parts by weight. One commercially available organoclay (I.30.E) was dispersed in a DGEBA/acetone solution by the HPM method; the properties of these materials and the HPM method are introduced in Chapter 3. The reactive liquid rubber is Hycar CTBN 1300×8 (*Noveon Inc.*). The notation of nanocomposites and rubber-modified epoxy with different materials is shown in Table 5-1.

Table 5-1: Notation of nanocomposites and rubber-modified epoxies

Designation	Concentration of Various Materials
8F	Pure resin system: 100-phr Epon 828+ 3-phr BF_3.MEA
8C-x	100-phr Epon 828+ 3-phr BF_3.MEA +"x"-phr CTBN "x" is 5, 10, 15, or 20-phr - concentration of CTBN
8I-x	100-phr Epon 828+ 3-phr BF_3.MEA +"x"-phr I.30E "x" is 1.5, 3, 4.5, or 6-phr - clay loading
8CI-20-x	100-phr Epon 828+ 3-phr BF_3.MEA +20-phr CTBN +"x"-phr I.30E "x" is 1.5, 3, 4.5, or 6-phr - clay loading

5.2.2 Synthesis of Nanocomposites and Rubber-Modified Epoxy

1 part by weight of dry I.30 E clay, and 10 parts of Epon 828 epoxy resin, were mixed and mechanically stirred at room temperature for 30 min, and then the mixture was diluted with 5 parts of acetone. The solution was passed through the M-110 EH XP Microfluidizer at 15,000 psi to form a pasty mixture containing about 70% wt of organoclay and resin; after drying the paste under vacuum for 8 hrs at 100°C, the exact concentrations of organoclay and resin were measured.

The desired amounts of paste and CTBN rubber were added to DGEBA epoxy resin, and the mixture was mechanically stirred at 1000 rpm in a fume hood at room temperature for 30 min, followed by slow heating to 60°C, where it was held and stirred slowly for 2 hrs in order to support some chemical reaction between CTBN and DGEBA. Finally, the mixture was degassed under vacuum at 60~65°C for 30 minutes.

The 3-phr BF_3.MEA hardener was completely dissolved in acetone prior to use. The BF_3.MEA solution was added into the above mixture, and then the mixture was mechanically stirred at 1000 rpm in a fume hood at room temperature for 2 hrs, followed by slow heating to 60°C where it was held for 1 hr, and subsequently degassed at 60~70°C for 1 hr, and 90°C for 20 min. During degassing, a foam of tiny bubbles appeared and was removed. The mixture was poured into rubber molds. All materials for mechanical and hydrothermal properties were cured at 115°C/1 hr + 125°C/8 hrs. The post cure treatment was 175°C /4 hrs in nitrogen atmosphere.

5.2.3 Physical Measurement

XRD patterns, optical micrographs, SEM and TEM images were obtained on the same machine under the same testing conditions described in Chapter 4.

Dynamic mechanical properties of nanocomposites and rubber-modified epoxies were with a TA 983 Dynamical Mechanical Analyzer (DMA) in fixed frequency mode at 1 Hz with 0.3 mm oscillation amplitude, and from -100 °C to 225 °C at 2 °C/min nitrogen atmosphere. The sample size is 50 × 12.7 × 3.2 mm.

Viscosity-temperature curves, and viscosity-shear rates at lower rates, were measured with a Brookfield Digital Viscometer Model DV-II+ and a Thermosel Accessory, using coaxial cylinder geometry. Two spindles were used during measurements: SC4-18 for lower viscosities (<100 Pa.s), and SC4-31 for high viscosities (from 100 to 2000 Pa.s). When the set temperature was attained, another 10 minutes was allowed to reach temperature balance between the sample and the spindle.

Cure kinetic measurements were performed on the same machine and under the same testing conditions described in Chapter 4. The degree of cure (α) is calculated by the following expression:

$$\alpha(\%) = \left[\frac{\Delta H_{total} - \Delta H_{residual}}{\Delta H_{total}} \right] * 100 \qquad (5\text{-}1)$$

where ΔH_{total} corresponds to the total heat of reaction, and $\Delta H_{residual}$ to the residual heat of the specimen.

Atomic Force Microscope (AFM) images were obtained on a NanoScope IIIa, Multimode AFM machine, Digital Instrument Company, using the TappingMode™ test mode and tapping mode etched silicon probe (TESP).

5.3 Results and Discussion

5.3.1 Cure Kinetic Study

The influence of the I.30 E organoclay on the homopolymerization of DGEBA is introduced in Chapter 4. Further study of the influence of both I.30E organoclay and CTBN rubber on the homopolymerization of DGEBA, and the cure reaction of the DGEBA/ BF_3.MEA system, was performed with DSC.

5.3.1.1 Effect of Organoclay and Rubber on Homopolymerization of DGEBA Epoxy

In order to minimize the effects of temperature, all samples were mixed and degassed at room temperature, and BF_3.MEA curing agent was completely dissolved in acetone prior to use. The organoclay was dispersed in epoxy solution by the HPM method.

Figure 5-1 shows the exothermal curves of homopolymerization of DGEBA in the presence of different modifiers at 2.5°C/min heating rate. The results show that all systems were very stable, as the temperature was less than 100℃ whether DGEBA epoxy resin was mixed with I.30 E or CTBN. This observation provides the possibility of dispersing the organoclay in the epoxy at 80~100 °C with low viscosity.

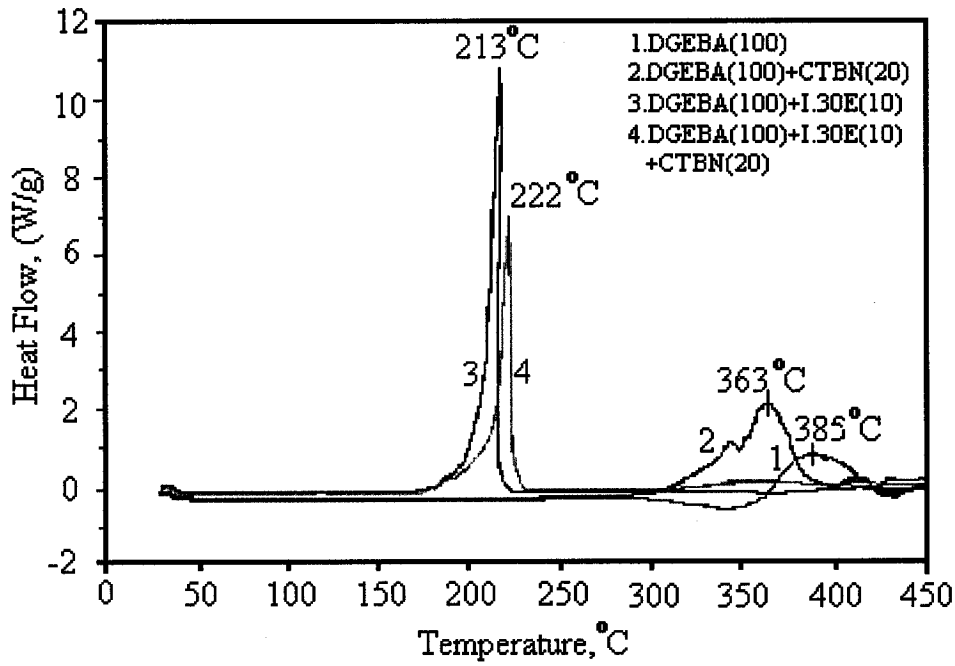

Figure 5-1: Exothermal curves of homopolymerization of DGEBA with different modifiers

In the curve of pure DGEBA (curve 1), the peak intensity is lowest and the temperature corresponding to the peak is highest, about 385°C; this indicates that it is difficult to self-polymerize DGEBA in the absence of catalysts. Upon adding 20-phr CTBN into DGEBA, the peak (curve 2) is shifted downwards about 22°C, and intensity increases slightly; this indicates that the epoxy group of DGEBA reacts more easily with the functional groups (-COOH) of CTBN than with itself.

Upon adding 10-phr I.30E organoclay into DGEBA, or the mixture containing 20-phr CTBN and 100-phr DGEBA, respectively, the peaks are shifted downwards by more than 150°C, and the intensities increase greatly (curves 3 and 4). This finding is discussed in the previous chapter, and is attributed to the acidity of the surface modifier, which catalyzes the epoxy ring opening. However, this catalytic effect decreases in the presence of 20-phr CTBN rubber.

5.3.1.2 Effect of Organoclay and Rubber on Cure Reaction of DGEBA/ BF_3.MEA

On the other hand, the organoclay and CTBN exert insignificant influence on the cure reaction of a DGEBA/BF_3.MEA system (shown in Figure 5-2). Only one peak and two shoulders appear in the exothermal curve of the DGEBA/BF_3.MEA system (curve 1). The temperatures corresponding to onset and peak of cure are 90°C and 171°C, respectively, and the cure rate is slow when the temperature is less than 135°C. Thus the cure cycle recommended for this system is 125°C for 1 hr, and then 175°C for 2 hrs.

Compared with BF_3.MEA catalyst, organoclay initiates homopolymerization of DGEBA epoxy resin at a higher temperature, about 165°C, but ends it at a lower

temperature, about 220°C (curve 3 in Figure 5-1). As a result, the I.30E organoclay has two countering actions on the cure reaction of DGEBA/BF_3.MEA: one retards the cure reaction and decreases the cure rate before 165°C, and thus forces the exothermal peaks upwards by 9°C (curve 2 in Figure 5-2); the other accelerates the reaction after this temperature, and results in disappearance of the second shoulder. The former provides a situation where the intergallery reaction is slower than extragallery, so that the basal spacing of organoclay layers does not increase, but rather reduces during the curing process, as long as the curing temperature is below 165°C. The latter will enhance the degree of cure of epoxy systems; this was confirmed later by measuring the degree of cure of epoxy systems with or without the organoclay.

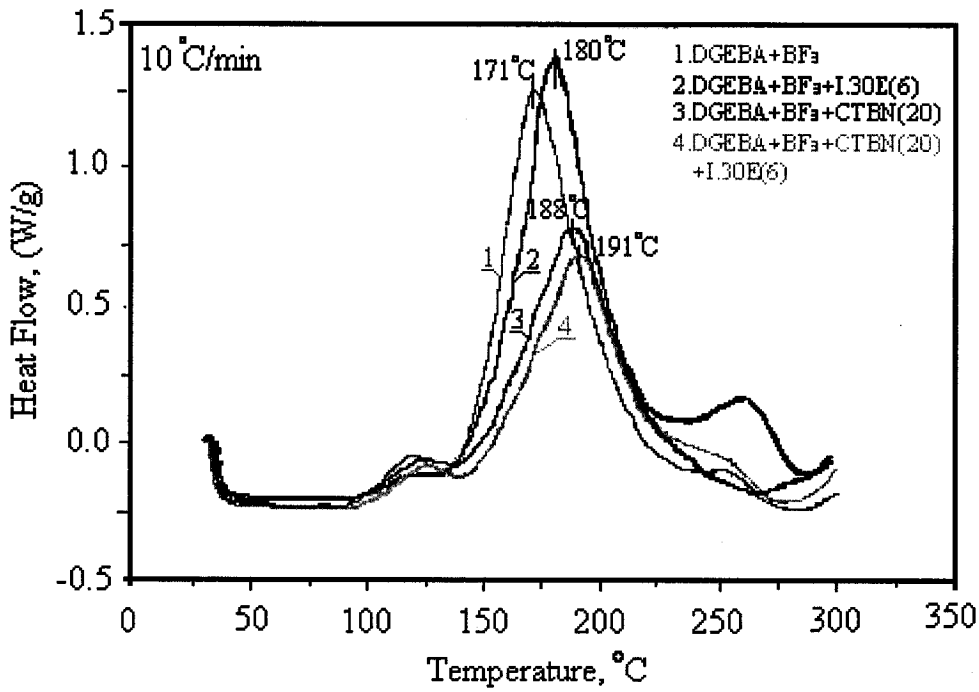

Figure 5-2: Exothermal cure curves of DGEBA/BF_3.MEA with different modifiers

CTBN retards the cure reactions of the DGEBA/BF_3.MEA and DGEBA/BF_3.MEA/I.30E systems during the entire temperature range, due to the higher content of CTBN and lower reactivity with epoxy groups (curves 3 and 4 in Figure 5-2). Unlike organoclay, it intensifies the second shoulders, which results in diminishing the degree of cure. However, adding CTBN reduces the difference of peak temperatures of DGEBA/BF_3.MEA and DGEBA/BF_3.MEA/I.30E from 9°C to 3°C, and thus may reduce the difference in reaction rates between outside and inside the galleries of the organoclay.

5.3.2 Rheological Properties

Viscosities of matrix at different temperatures are important data for determining a cure cycle of advanced composites. The viscosities of different material systems were measured with a Brookfield Digital Viscometer Model DV-II+ and a Thermosel Accessory, using coaxial cylinder geometry (shown in Figure 5-3). Due to the limitation of the equipment, shear rate can only change in a very small range. Although these viscosities were measured with the minimum shear rate, the minimum value of shear rate gradually increases with temperature (from 0.1 to 10 S^{-1}).

As shown in Figure 5-3, viscosity of all material systems falls quickly with increasing temperature. DGEBA has the lowest viscosity at the same temperature of all materials tested. As temperature rises to 75°C, DGEBA enters a low viscosity range (less than 1 Pa.s), and reaches the lowest viscosity, 0.13 Pa.s at 140°C. Therefore, the low viscosity range is chosen to disperse organoclays, in order that the epoxy resin can diffuse into the galleries of clay.

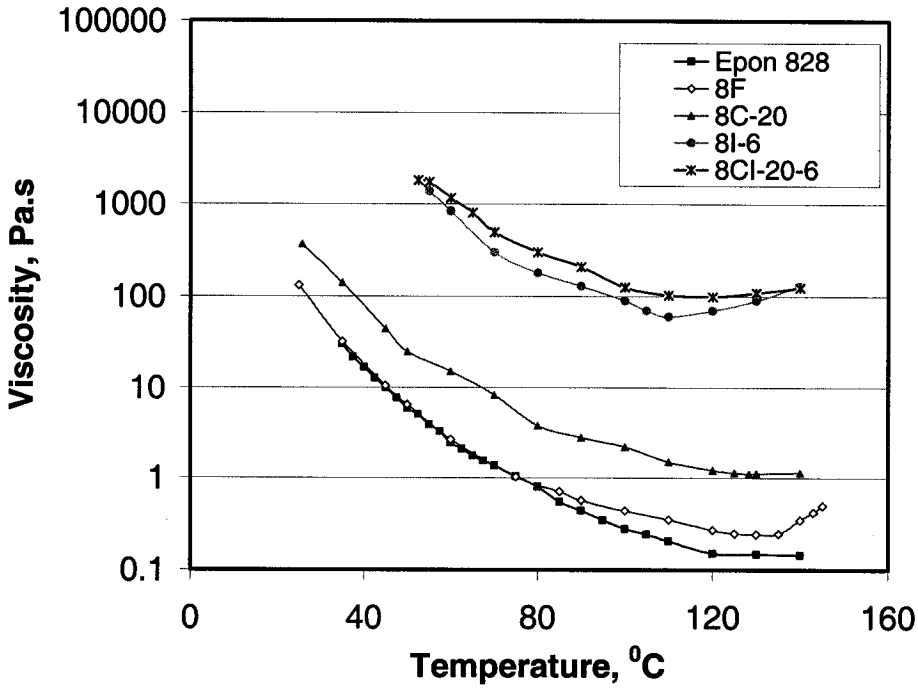

Figure 5-3: Viscosity-temperature curves of various uncured epoxy systems

Adding 3-phr BF_3.MEA into 100-phr DGEBA (8F) has an insignificant influence on the viscosity of resin until 80°C, where the cure reaction is initiated. As temperature rises to 135°C, the DGEBA/BF_3.MEA system (8F) reaches its lowest viscosity, and then viscosity quickly increases due to the cure reaction. The DGEBA epoxy resin and DGEBA/BF_3.MEA systems (8F) exhibit Newtonian behaviours; that is, their viscosities do not change with increasing shear rate at 90 °C, as shown in Figure 5-4.

Further addition of 20-phr CTBN into the DGEBA/BF_3.MEA system (8C-20) results in increased viscosity, but the increase of viscosity is weakened beyond 135°C because CTBN retards the cure reaction (Figure 5-3). The weak shear thinning behavior of the uncured 8C-20 system is observed in Figure 5-4.

On the other hand, adding 6-phr I.30E organoclay into the DGEBA/BF_3.MEA system (8I-6) not only greatly enhances viscosity (Figure 5-3), but also shows strong shear thinning behavior (Figure 5-4); the viscosity of the 8I-6 system quickly increases after 100°C. These behaviors were further strengthened with increased clay loading, and result in a high void content in specimens at high clay loadings. Therefore, the experimental conditions allow manufacturing nanocomposite specimens only up to 6-phr clay loading for I.30E.

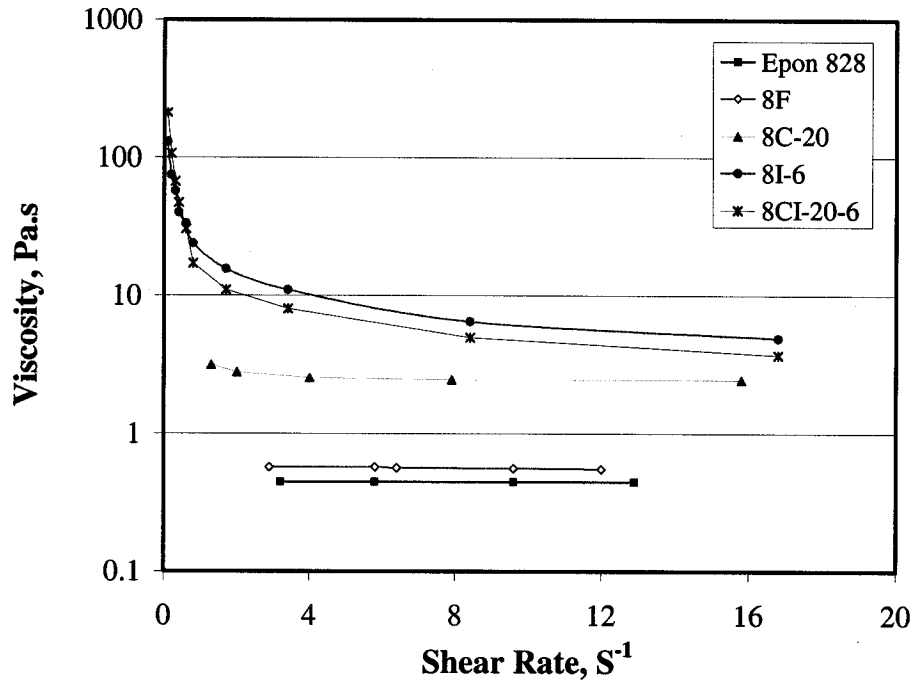

Figure 5-4: Viscosity-shear rate curves of various uncured epoxy systems at 90°C

Upon adding 20-phr CTBN into the uncured 8I-6 system, viscosity and shear thinning behavior of the new system (8CI-20-6) were only slightly changed, but increased viscosity after 100°C was weakened, helping the manufacturing of the samples.

5.3.3 Effect of Curing Temperature on Formation of Rubber Phase

It is now universally recognized that it is critically important to form a two-phase morphology with rubber particles dispersed in, and bonded to, the crosslinked epoxy matrix, to enhance toughness and minimize the decrease of other important properties such as modulus and T_g. The cure temperature is the key factor affecting the morphology of rubber-modified epoxies, but its effect is somewhat unpredictable [6]. Increasing cure temperature promotes both epoxy/rubber compatibility and cure rate, which tends to retard the phase separation process, and results in relatively small values of rubber volume fraction and particle size; on the other hand, increased temperature also results in reduced viscosity, which tends to enhance the phase separation process, and has the reverse effect on the morphology described above.

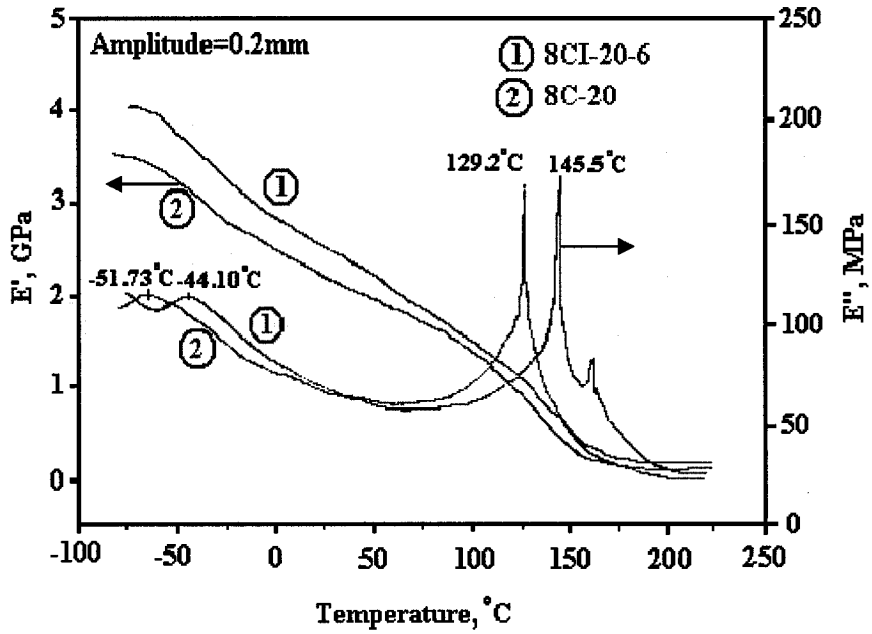

Figure 5-5: DMA curves of rubber-modified epoxy and hybrid nanocomposites

The common method for characterizing two-phase morphology is to test the T_g of modified epoxies. Figure 5-5 presents DMA curves of modified epoxy with 20-phr CTBN (8C-20), and hybrid epoxy nanocomposite with 6-phr organoclay and 20-phr CTBN (8CI-20-6). Like rubber-modified epoxy, the hybrid epoxy nanocomposite also contains two peaks in loss modulus, corresponding to the epoxy phase and rubber phase respectively.

5.3.3.1 Rubber-Modified Epoxy

Modified epoxies containing 20-phr CTBN were cured at different temperatures, from 95°C to 155°C. The glass transition temperatures (T_g) of these epoxies were measured by DMA. When the cure temperature is less than 140°C, there are two T_gs in the DMA curves, one for the epoxy phase and one for the rubber phase (shown in Figure 5-6). The reduction in T_g of the epoxy phase is due to the plasticizing effects of the dissolved rubber. Thus, DMA results indicate that the phase separation process becomes difficult, and more rubber is dissolved in the epoxy phase in the DGEBA/BF_3.MEA system with increasing cure temperature.

When cured at 155°C, the rubber phase of the modified epoxy completely disappears; this conclusion was confirmed by optical microscopy. However, the change of morphological characteristics is relatively small when the cure temperature varies from 110°C to 140°C.

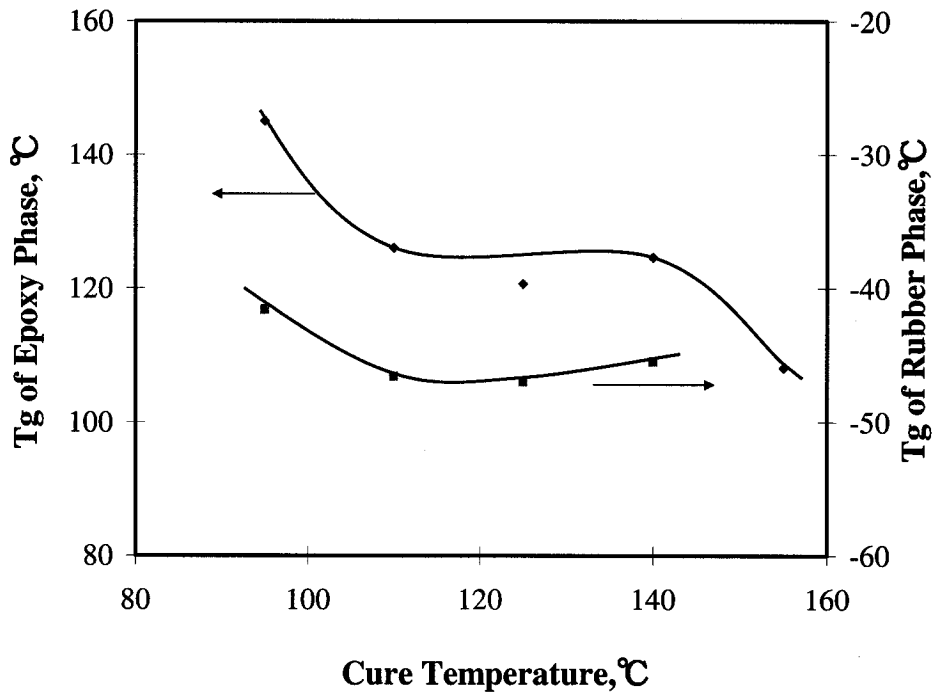

Figure 5-6: Effect of cure temperature on T_gs of epoxy and rubber phases of modified epoxy (8C-20)

5.3.3.2 Hybrid Nanocomposites

The effects of cure temperature on the two-phase structure of hybrid epoxy nanocomposites (8CI-20-6) were studied. These nanocomposites were cured at different temperatures, from 95°C to 155°C. When the cure temperature is less than 140°C, there are two T_g's in the DMA curves (shown in Figure 5-7). The change in morphological characteristics is again relatively small as the cure temperature changes from 110°C to 140°C; when the nanocomposite is cured at 155°C, the separate rubber phase completely disappears. The reduction in T_g of the epoxy phase is due to the plasticizing effects of the dissolved rubber, indicating that the phase separation process becomes more difficult, and that rubber dissolved in the epoxy phase increases with increasing cure temperature. These results are similar to rubber-modified epoxies with

the same CTBN content, but the T_g of the epoxy phase in the nanocomposites is higher than that in rubber-modified epoxies at the same cure temperature.

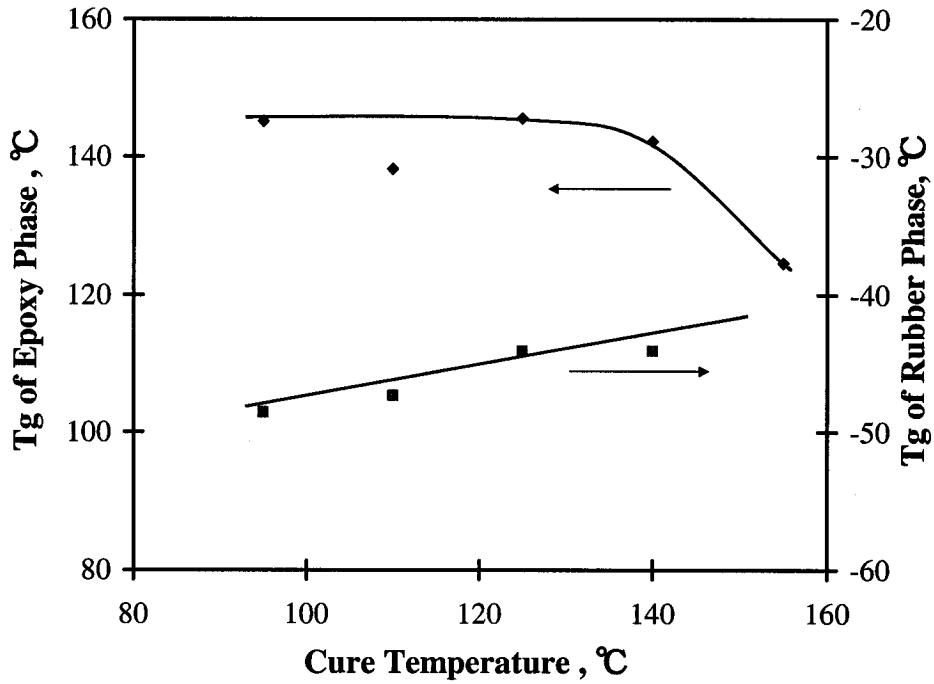

Figure 5-7: Effects of cure temperature on T_gs of epoxy and rubber phases of hybrid nanocomposites (8CI-20-6)

5.3.4 Degree of Cure and Glass Transition Temperature

All systems listed in Table 5-1 were cured at 115°C/1 hr + 125°C/8 hrs, and then postcured at 175°C/4 hrs in nitrogen atmosphere. The degrees of cure and glass transition temperatures (Tg) of these nanocomposites and rubber-modified epoxies are listed in Table 5-2.

5.3.4.1 Effect of Organoclay and CTBN on Degree of Cure

As shown in Table 5-2, adding 5-phr CTBN into DGEBA/BF_3.MEA decreases the degree of cure by almost 8.5%. Any further addition of organoclay has no significant influence on the degree of cure, as shown in Figure 5-8.

On the other hand, the organoclay has an insignificant influence on the degree of cure of the DGEBA/BF_3.MEA system (shown in Figure 5-9). However, adding the organoclay into the rubber-modified epoxy system enhances the degree of cure by about 5% at 6-phr clay loading. The influence of the organoclay and the rubber on the degree of cure are in good agreement with the above cure kinetics study results.

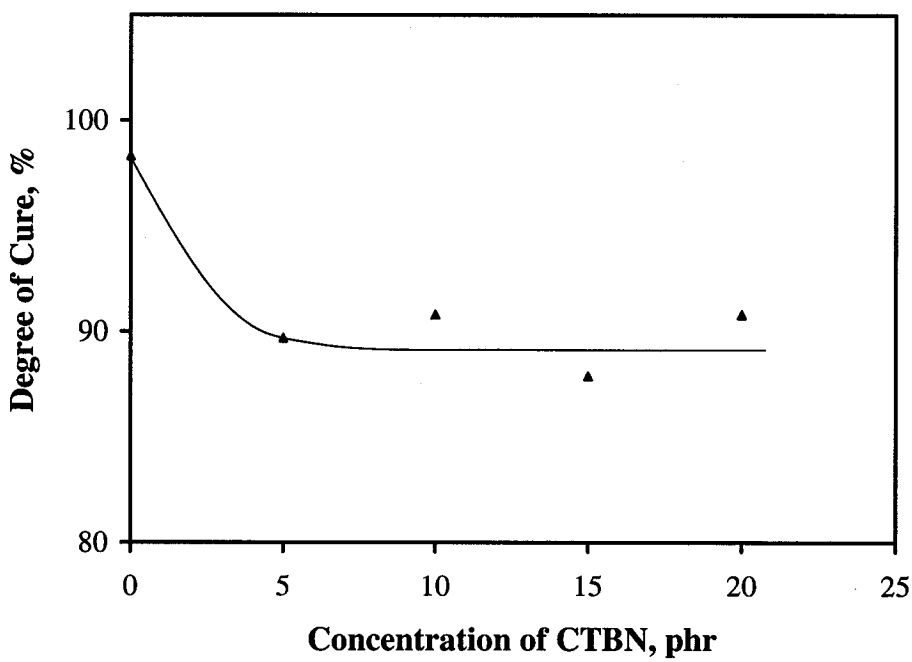

Figure 5-8: Degree of cure of rubber-modified epoxies with concentration of CTBN

Table 5-2: Degrees of cure and T_gs of nanocomposites and rubber-modified epoxies

Designation	T_g of Epoxy Phase, °C		T_g of Rubber Phase, °C	Cure Degree %
	DMA	DSC		
8F	182.5	150.8	/	98.3
8C-5	133.9	145.7	/	89.7
8C-10	130.5	138.2	/	90.8
8C-15	131.0	133.2	-46.9	87.9
8C-20	129.2	129.7	-51.7	90.8
8I-1.5	169.2	154.9	/	98.1
8C-10	187.8	165.8	/	98.9
8C-15	166.1	167.3	/	97.3
8C-20	172.9	168.4	/	97.8
8CI-20-1.5	133.3	133.2	-42.8	93.3
8CI-20-3	150.0	139.0	-47.5	95.4
8CI-20-4.5	150.3	140.4	-48.3	94.5
8CI-20-6	143.0	133.4	-47.0	95.3

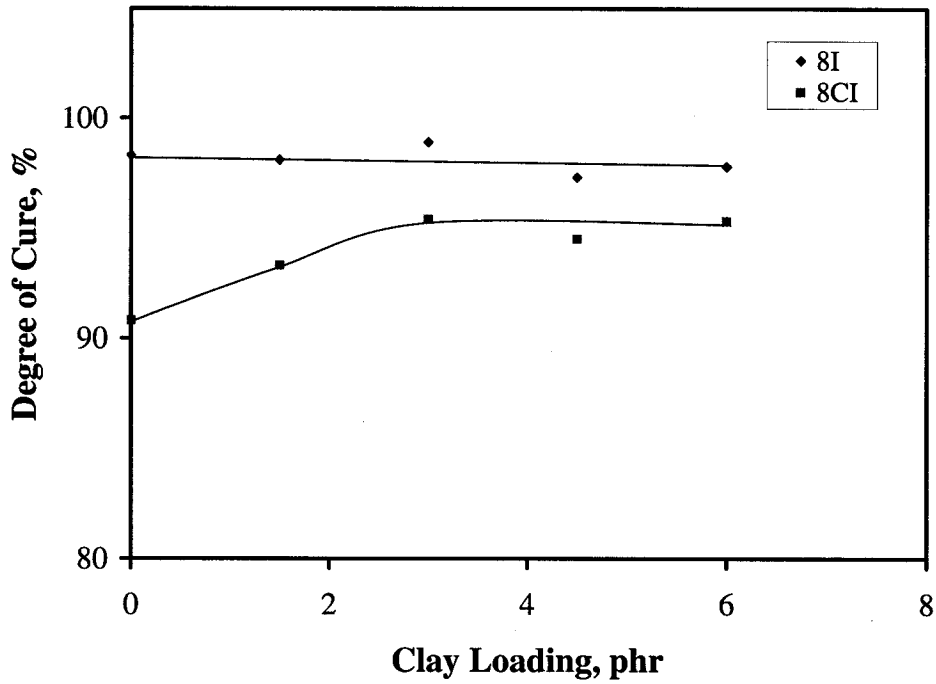

Figure 5-9: Degree of cure of nanocomposites with clay loading

5.3.4.2 Effect of Organoclay and CTBN on Glass Transition Temperature

The glass transition temperatures (T_g) of all systems were measured by both DMA and DSC, in order to compare experimental data with other researchers. DMA examines property changes of materials with mechanical vibration, and is used by researchers in nanocomposites, whereas DSC measures changes of specific heat, and is commonly used by researchers in rubber-modified epoxies.

Upon adding 5-phr CTBN into DGEBA/BF_3.MEA, the T_g of the epoxy phase is reduced by about 48.5°C (shown in Figure 5-10), and the T_g of the rubber phase is undetectable by DMA (Table 5-2). This may be because CTBN completely dissolves in

the epoxy phase, due to the high cure rate and relatively good compatibility. Upon increasing CTBN content, the T_g of the epoxy phase decreases slightly, and the T_g of the rubber phase is detected at 15-phr concentration of CTBN.

The T_g of the epoxy phase in Figure 5-10 has a similar trend to the degree of cure with the concentration of CTBN in Figure 5-8; this indicates that the decrease in T_g of the epoxy phase is not only due to dissolving rubber in the epoxy phase, but also due to the reduction of the degree of cure.

Only one T_g can be detected for all rubber-modified epoxies with DSC; it decreases linearly with increasing concentrations of CTBN within the order of 20°C at 20-phr CTBN.

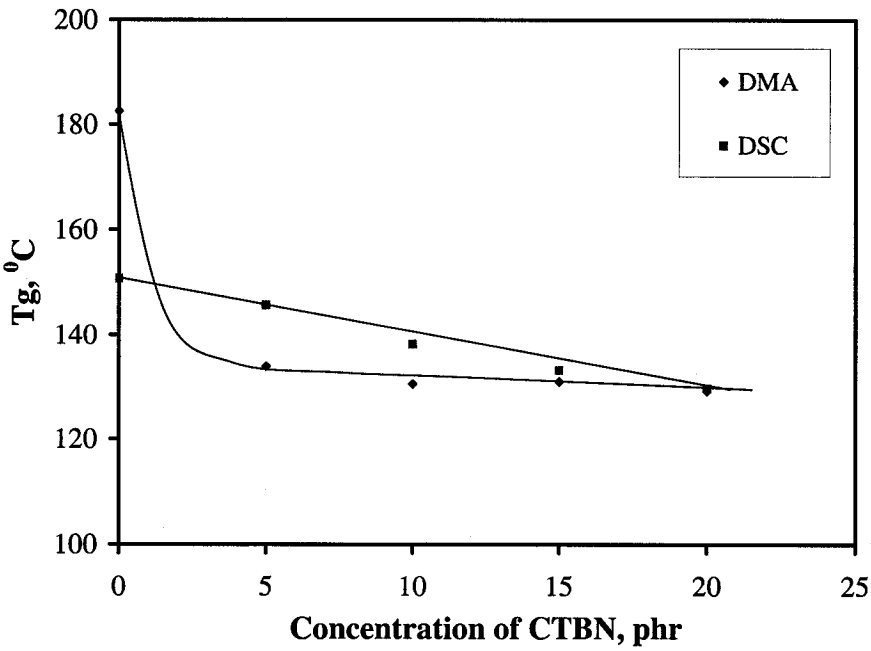

Figure 5-10: T_g of rubber-modified epoxies *versus* concentration of CTBN

On the other hand, as measured by DMA, the T_g of nanocomposites without CTBN (8I series) decreases with increasing clay loading (shown in Figure 5-11). The reduction in T_g is on the order of 10°C for the nanocomposite at 6-phr clay loading.

Contrary to the DMA results, the T_g measured by DSC for the same materials increases with clay loading, by 18°C for the nanocomposite at 6-phr clay loading.

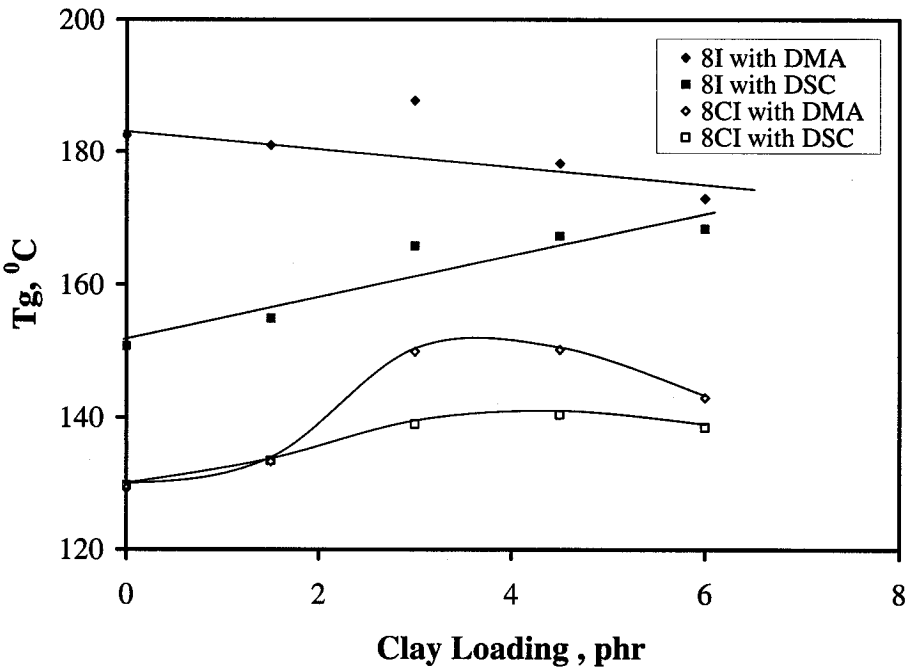

Figure 5-11: T_g of nanocomposites *versus* clay loading

Compared with nanocomposites without CTBN (8I series), hybrid nanocomposites (8CI series) have lower T_g's due to the presence of CTBN, but the Tg increases with increased clay loading to 4.5-phr, with either DMA or DSC. The maximum enhancement with DMA is 21°C at 4.5-phr clay loading. The changes of T_g for nanocomposites seem similar to those of degree of cure (shown in Figure 5-9); this indicates that adding organoclay into pristine epoxy reduces the degree of cure, and thus

T_g; conversely, adding organoclay into rubber-modified epoxies increases the degree of cure and T_g.

5.3.5 Morphology

5.3.5.1 Microstructure Observation with Optical Microscopy

The morphology of rubber-modified epoxies and nanocomposites was first examined using optical microscopy, as shown in Figure 5-12. A few spherical particles of rubber phase are observed in the rubber-modified epoxy at 5-phr CTBN (8C-5, Figure 5-12 A), though the T_g of the rubber in this material was not detected with DMA. As the content of CTBN increases to 20-phr, the number of spherical particles greatly increases (shown in Figure 5-12 B).

The nanocomposite at 4.5-phr clay loading (8I-4.5) was also examined (shown in Figures 5-12C); few agglomerates of organoclay were observed. Three hybrid nanocomposites with different clay loadings were examined (shown in Figure 5-12 D, E, and F); at low clay loading, the rubber phase still shows spherical particles, but linear rods form with increasing clay loading.

5.3.5.2 Microstructure Observation with AFM

AFM is a powerful tool for investigating rubber-modified epoxies and hybrid nanocomposites on a micro, and in some cases even a nano, scale. Figure 5-13 A is an AFM micrograph of the two-phase structure of rubber-modified epoxy (8C-20), where the rubber spheres (of diameter 4~5μm) are dispersed in the continuous epoxy matrix (25×25 μm). To further observe microstructure, two higher magnification micrographs

(1 μ×1 μ) from the epoxy phase and the interface region between rubber and epoxy phases were made (shown in Figure 5-13 B and C). In Figure 5-13B (1 μ×1 μ), a two–phase microstructure, consisting of a bright matrix and relatively dark interstitial regions, is observed; the size of the bright nodules is from 100 to 200 nm. However, the size of nodules in the rubber phase is larger than in the epoxy phase, and the interface between rubber and epoxy is indistinct, as shown in Figure 5-13 C.

The rubber particles of the hybrid nanocomposites at 3-phr clay loading (8CI-20-3) were also observed (shown in Figure 5-14 A, 30 μ×30 μ). The diameter of rubber particles is 7~10 μm, larger than in rubber-modified epoxy. The two higher magnification micrographs (4 μ×4 μ) and (1 μ×1 μ) from the interface region between rubber and epoxy phases were also examined (shown in Figures 5-14 B and C, respectively); the rubber phase nodules seem oriented, and the interface is clear in Figures 5-14 B and C.

Upon increasing the clay loading to 6-phr, the rubber phase cannot be determined from the micrograph in Figure 5-15 A (8CI-20-6), although the two-phase system of this hybrid nanocomposite is confirmed by DMA results. However, in higher magnification micrographs (Figures 5-15 B and C), the size of nodules in the epoxy phase is about 200~300 nm, larger than in the rubber-modified epoxy observed in Figure 5-13 B. The dark interstitial regions are wider, and seem continuous, as shown in Figure 5-15C; however, no agglomerates of organoclay were observed in hybrid nanocomposites, whether at 3-phr or 6-phr.

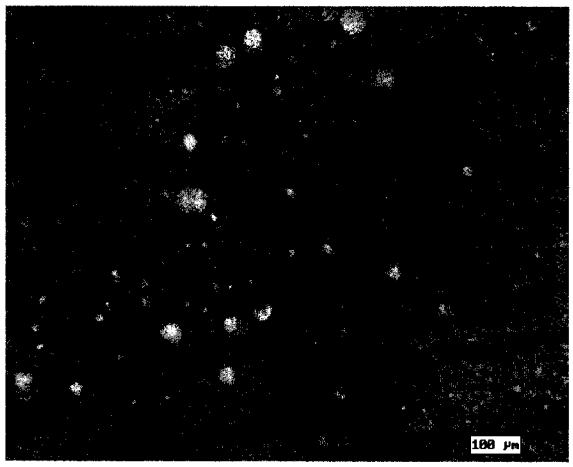

A (8C-5)

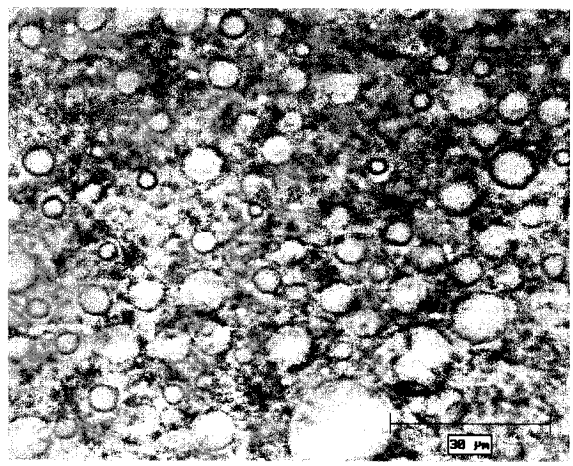

B (8C-20)

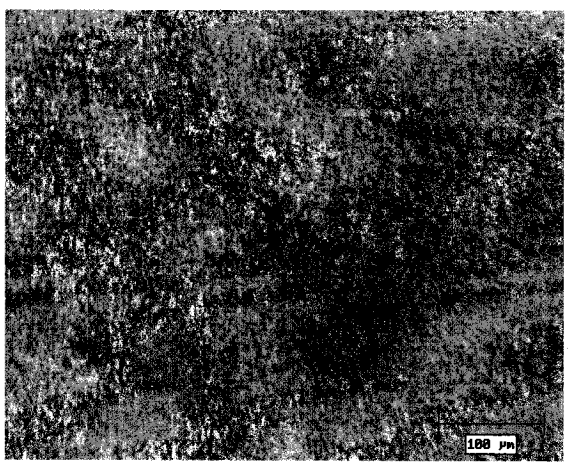

C (8I-4.5)

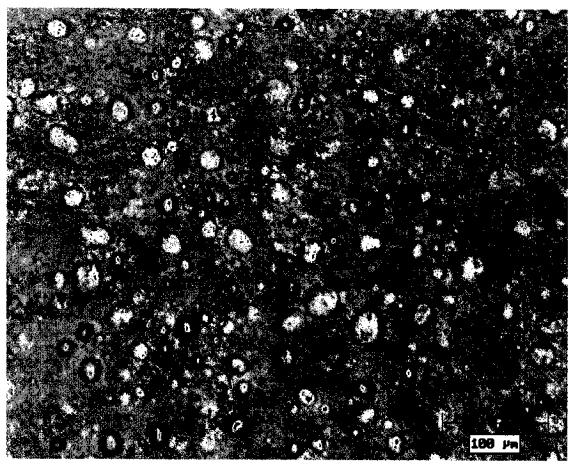

D (8CI-20-3)

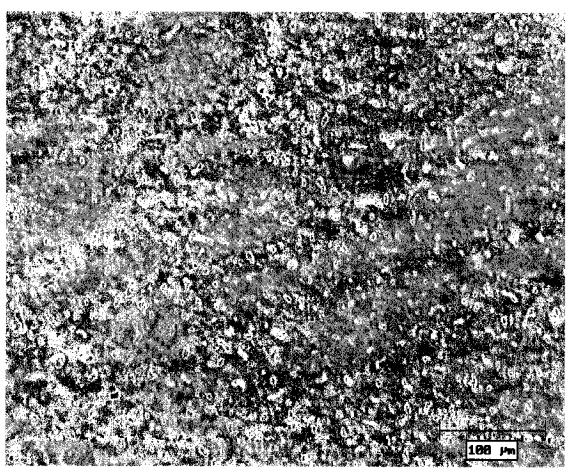

E (8CI-20-4.5)

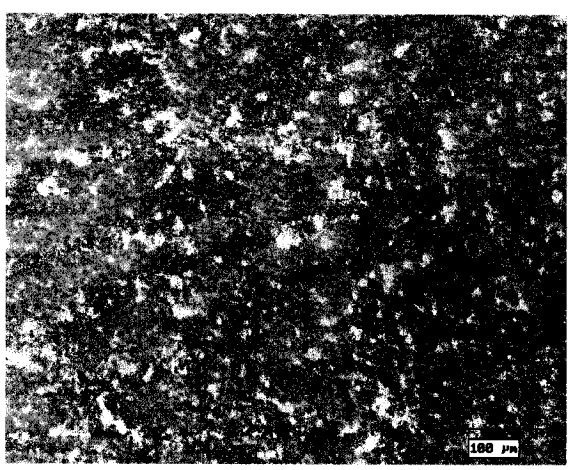

F (8CI-20-6)

Figure 5-12: Micrographs of rubber-modified epoxies and nanocomposites

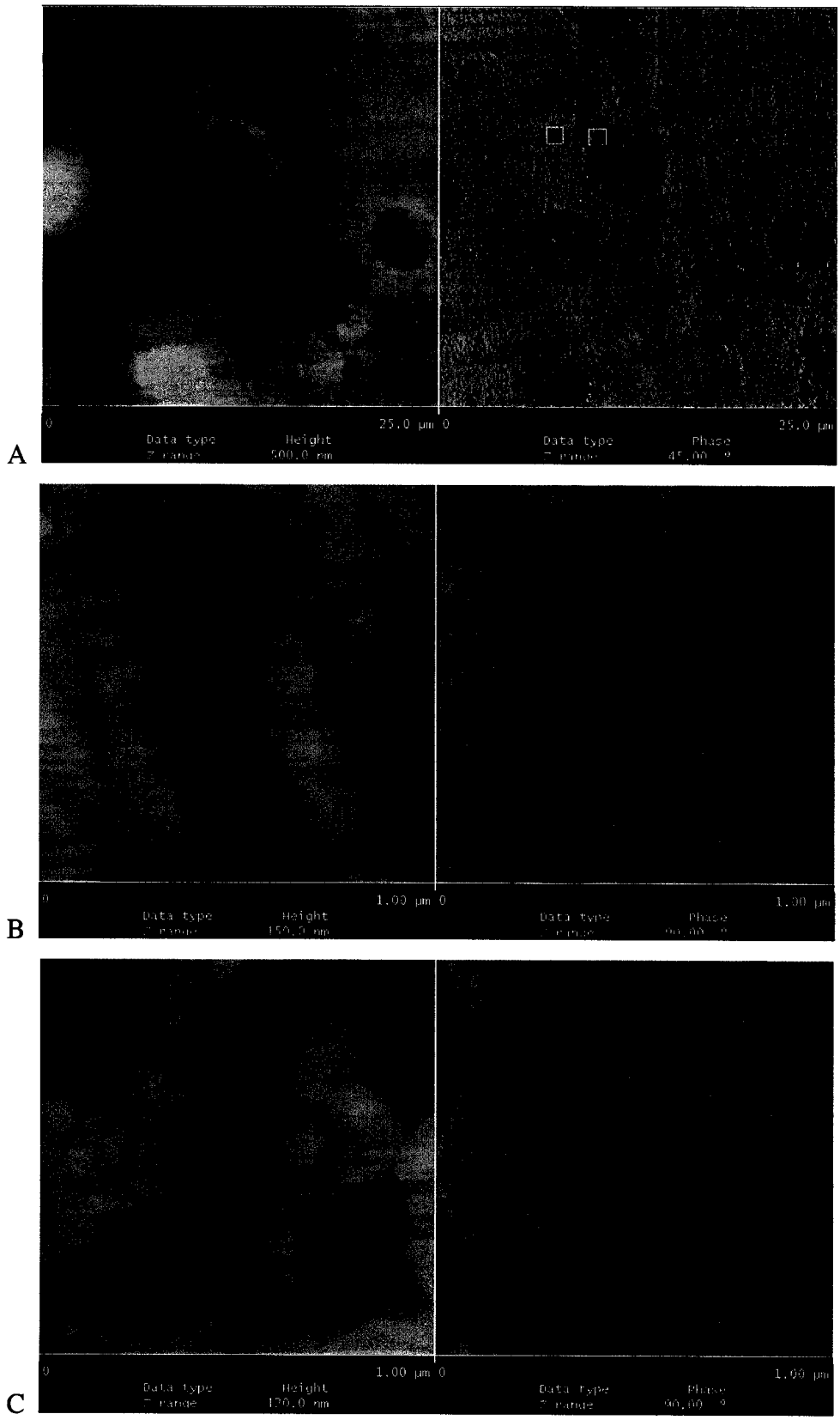

Figure 5-13: AFM micrographs of rubber-modified epoxy (8C-20)

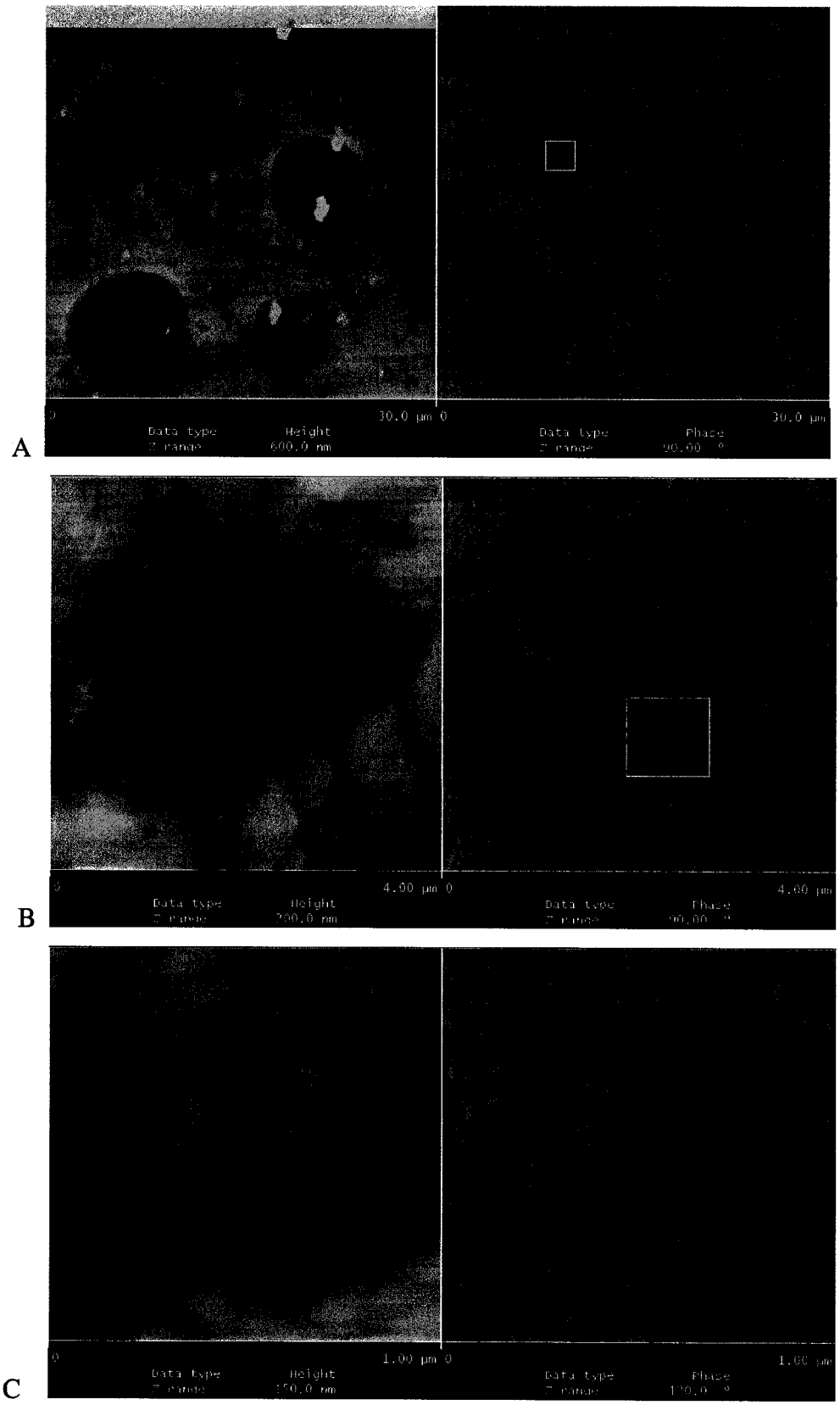

Figure 5-14: AFM micrographs of hybrid nanocomposite (8CI-20-3)

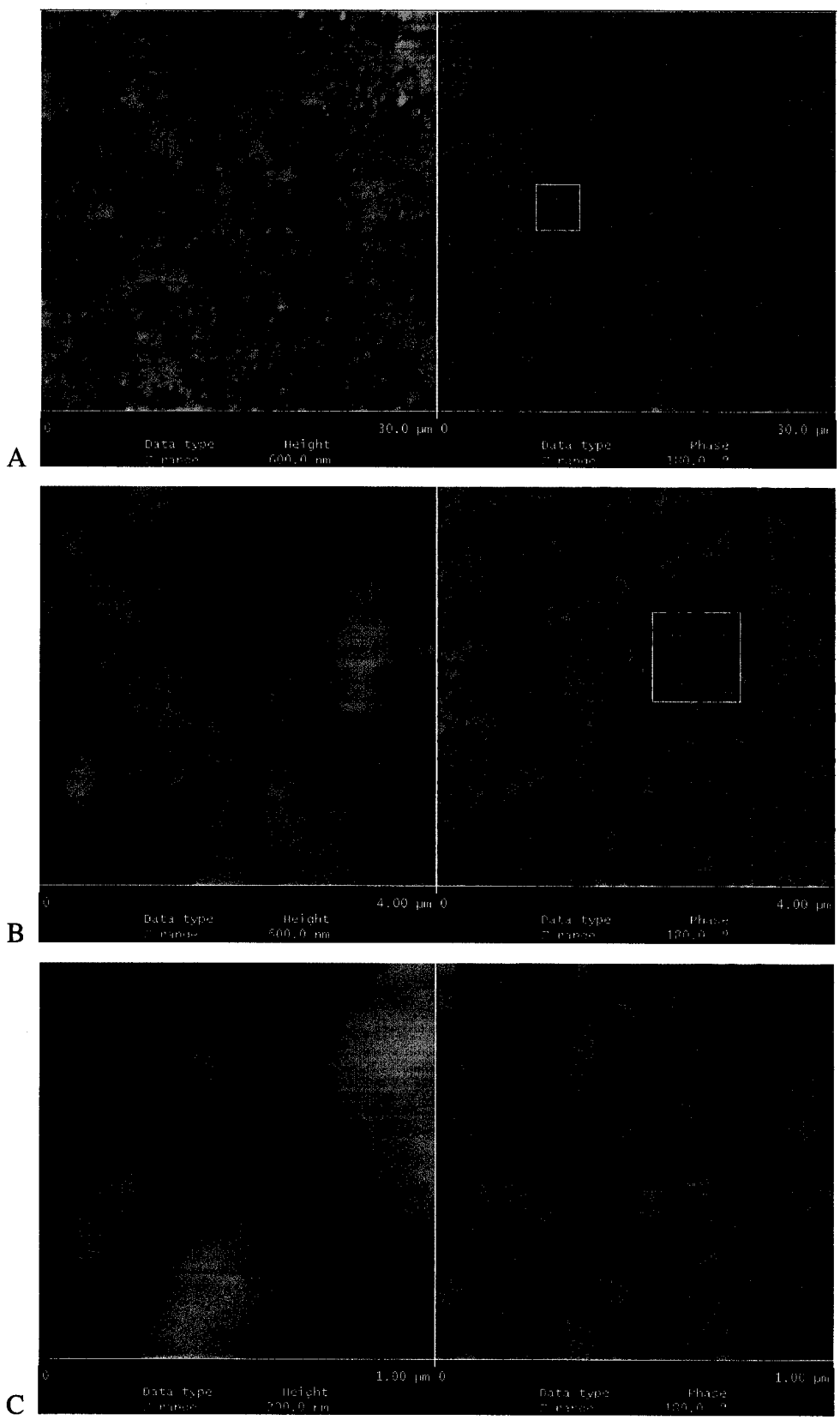

Figure 5-15: AFM micrographs of hybrid nanocomposite (8CI-20-6)

5.3.5.3 Fracture Surface Observation by SEM

The fracture surfaces of these materials were examined with SEM, as shown in Figure 5-16. The pristine resin sample (8F) SEM micrographs show that the fracture surfaces are smooth and featureless surfaces of a homogenous material. Figures 5-16 B, C and D show the fracture surfaces of the modified epoxy at 5, 15 and 20-phr CTBN rubber contents, respectively. A two–phase microstructure is visible, with rubber spheres dispersed in the continuous epoxy phase. For the rubber-modified 5-phr CTBN (8C-5) in Figure 5-16B, a few spherical particles of rubber phase are observed, with a size of about 10 μm. At higher concentrations of CTBN, the number of spherical particles greatly increases, and the diameter is about 4~5 μm. In hybrid nanocomposites at 3-phr clay loading (8CI-20-3), rubber particles are also observed (shown in Figure 5-16 E). The diameter of rubber particles is 14~20 μm, larger than those seen by the AFM. Upon increasing clay loading to 6-phr, the fracture surfaces exhibit a strong three-dimensional appearance (Figure 5-16 F); however, no rubber particles are found. These results are in good agreement with those obtained by AFM and optical microscopy.

Therefore, organoclay not only enhances the degree of cure of rubber-modified epoxies, but also changes the morphology of these materials. Changes in both the degree of cure and morphology result in increased T_g and modified mechanical performance.

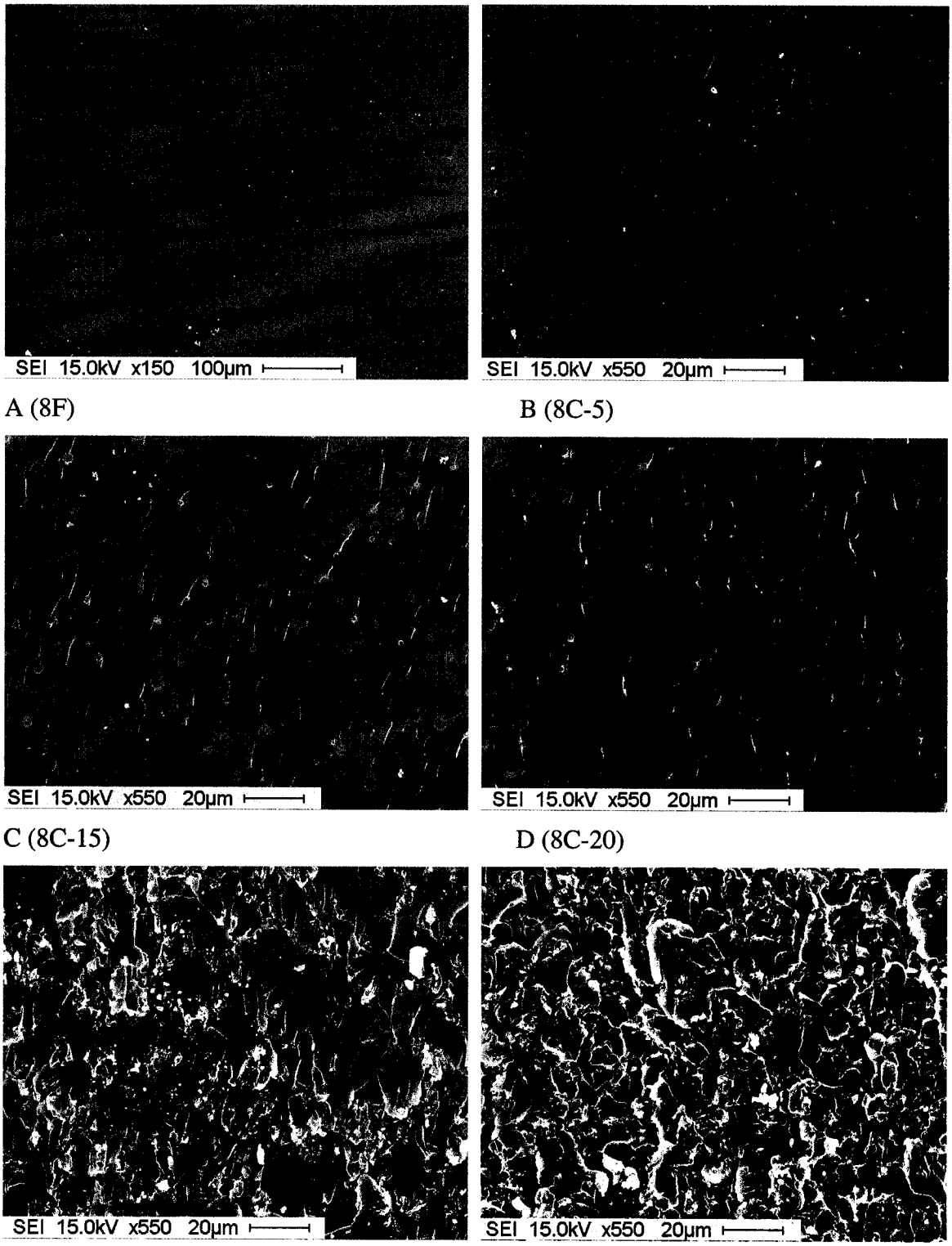

A (8F) B (8C-5)

C (8C-15) D (8C-20)

E (8CI-20-3) F (8CI-20-6)

Figure 5-16: SEM micrographs of fracture surfaces.

5.3.5.4 Microstructure Observation with TEM

The nanocomposite made with HPM-E at 6-phr clay loading (8I-6) was examined by TEM at low magnification (shown in Figures 5-17). In Figure 5-17, the dark lines are silicate layers of organoclay, and the white areas in the vicinity of the clay layers are sectioning artifacts. Figure 5-17 shows that agglomerates of organoclay are also broken down to form small particles consisting of several clay platelets, uniformly distributed in the epoxy resin system; most particles range from 500~700 nm in length, and 30~60 nm in thickness. These results are the same as with the nanocomposite based on the TGDDM/DDS system.

X 10, 000

Figure 5-17: TEM image of the nanocomposite (8I-6) at low magnification

A particle in the 8I-6 nanocomposite was further examined by TEM at high magnification (shown in Figure 5-18). In the nanocomposite, the clay packet consists of 6 or 7 silicate layers of organoclay, in nearly parallel arrangement. The thickness of the clay packet is about 18.6 nm, and the average basal spacing of organoclay in the packet is estimated at 3.1 nm.

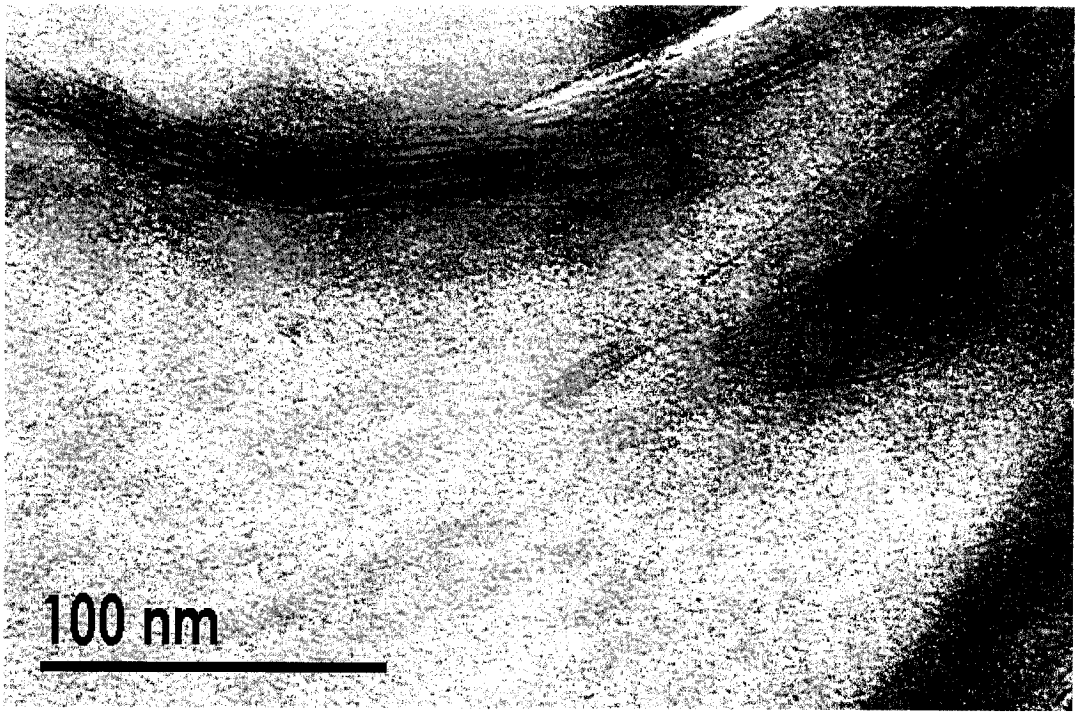

X250, 000

Figure 5-18: TEM image of the nanocomposite (8I-6) at high magnification

5.3.5.5 X-ray Diffraction Pattern of Nanocomposites

X-ray diffraction (XRD) was used to determine the basal spacing of organoclay in the nanocomposites. The XRD curves of the DGEBA/BF_3.MEA epoxy system and its nanocomposites, made of I.30E organoclay by the HPM-E method, are shown in Figure 5-19. In the curve for the nanocomposite at 6-phr clay loading (8I-6), a prominent peak

corresponding to the basal spacing of the organoclay occurs at 2.91 nm, which is slightly smaller than that (3.1 nm) observed with TEM. With increasing clay loading, the prominent peaks shift slightly, and the basal spacing decreases from 3.13 to 2.91 nm. This indicates that nanocomposites made of I.30E and DGEBA/BF_3.MEA are intercalated according to the basal spacing of organoclay.

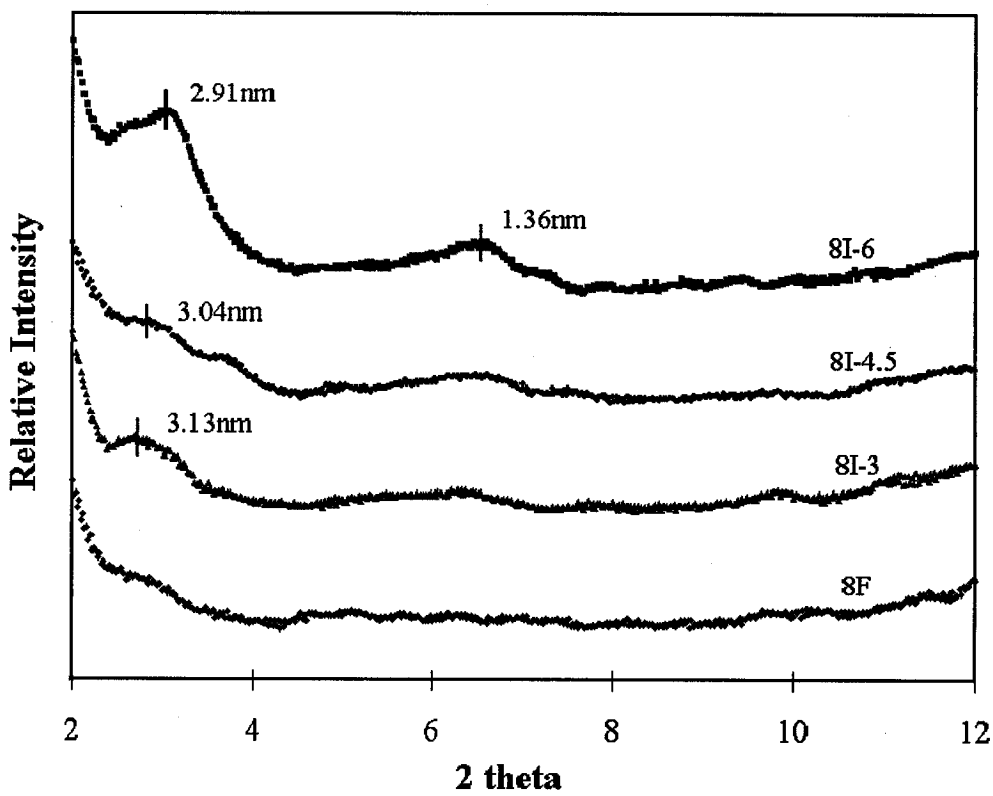

Figure 5-19: XRD patterns of nanocomposites with different clay loadings

Hybrid modified epoxy nanocomposites containing 3-phr and 6-phr organoclay were also tested, as shown in Figure 5-20. In the curve for the hybrid nanocomposite at 6-phr clay loading (8CI-20-6), a prominent peak corresponding to basal spacing occurs at 3.27 nm, slightly larger than that that of the nanocomposite (8I-6). This result is consistent with the prediction from the cure kinetic study.

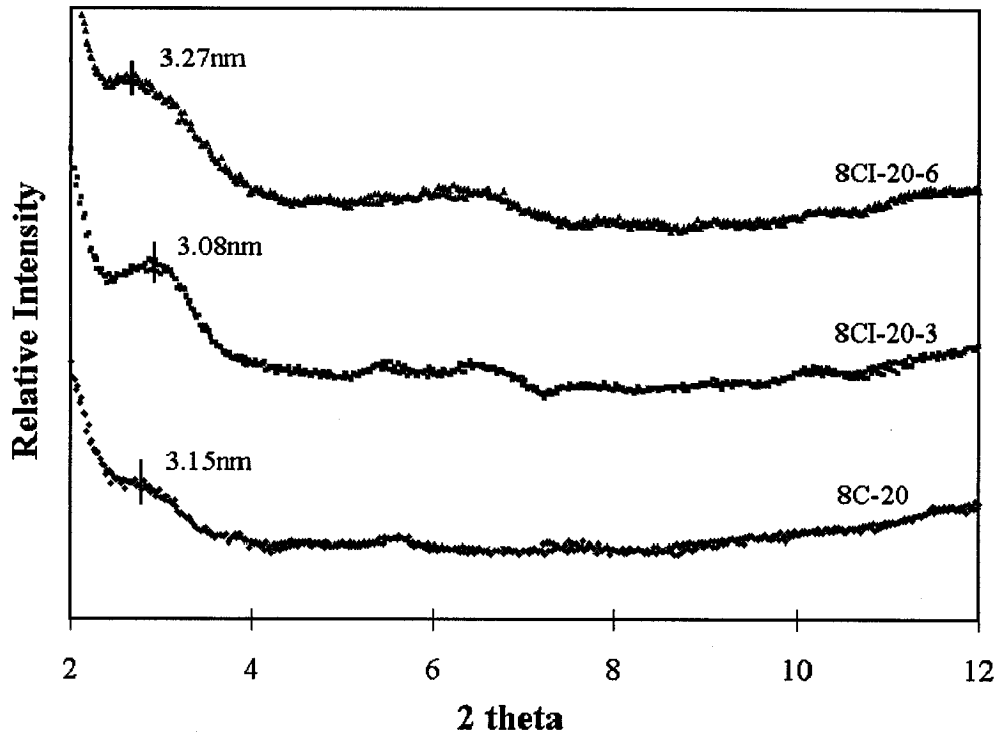

Figure 5-20: XRD patterns of hybrid nanocomposites with different clay loadings

To understand the changes in basal spacing of organoclay during manufacturing, samples of different stages were tested, as shown in Figure 5-21. From the previous result in Chapter 3, the basal spacing of I.30E was measured at 2.25 nm. After the organoclay was dispersed in the DGEBA (Epon 828)-acetone solution by the high-pressure mixing machine, the basal spacing of organoclay increases from 2.25 to 3.57 nm, as shown in Figure 5-21. This indicates that the epoxy resin was intercalated into the organoclay. As the curing agent BF_3.MEA is added into the organoclay/epoxy suspension with mechanical stirring, the basal spacing of the organoclay decreases from 3.52 to 3.09 nm, perhaps due to the fact that some alkylammonium ions were replaced by monoethylamine (MEA) from BF_3.MEA, as discussed in Chapter 3. The samples were cured at three different temperatures: 125°C, 150°C and 175°C, respectively.

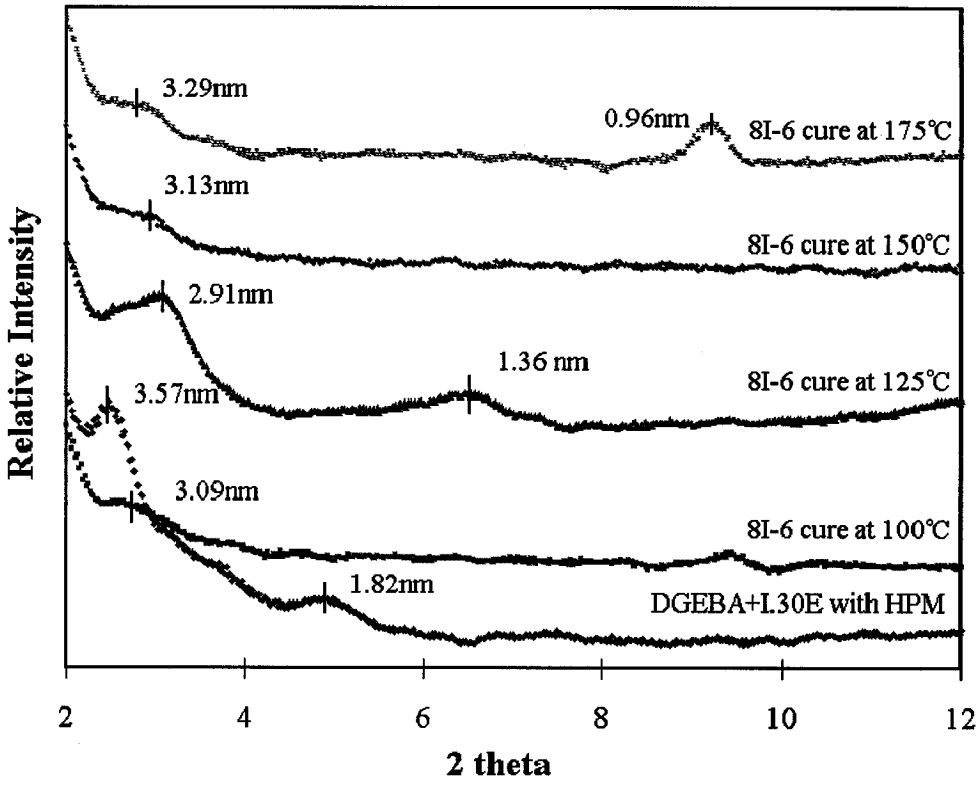

Figure 5-21: XRD patterns of 8I-6 nanocomposites at different stages

The basal spacing of organoclay slightly increases with cure temperature, as shown in Figure 5-21; this is opposite to what is expected according to the cure kinetics study. For this DGEBA/BF_3.MEA/I.30E system, the intergallery reaction is slower than extragallery. On increasing curing temperature, the difference between outside and inside reaction rates increases, and thus the basal spacing should be reduced. This result may be due to more alkylammonium ions further substituted by the monoethylamine (MEA) of BF_3.MEA at 125°C. At 125°C, the resin system has a slower cure reaction, and needs more than one hour to gel; during this stage of low viscosity at 125°C, the substitution process is accelerated. However, the resin system has a faster cure reaction,

and only needs a few minutes to gel at 175 °C. Therefore, there was not enough time for the substitution.

Similar results were obtained for hybrid modified epoxy nanocomposites containing 20-phr CTBN and 6-phr organoclay (8CI-20-6) cured at different temperatures, as shown in Figure 5-22.

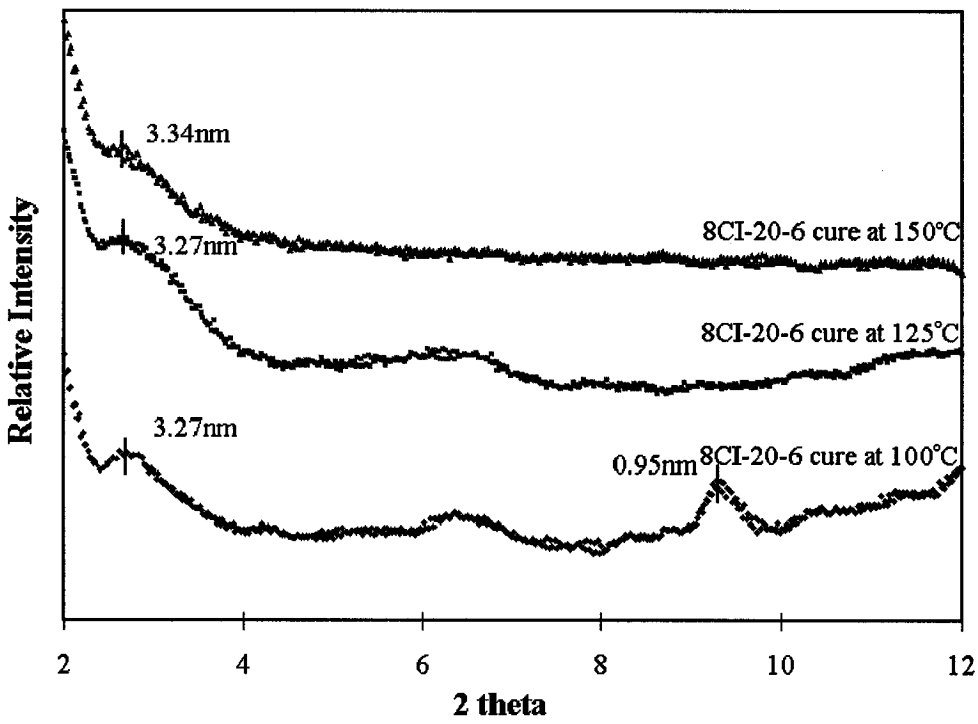

Figure 5-22: XRD patterns of 8CI-20-6 nanocomposites cured at different temperatures

5.3.6 Formation Mechanism and Proposed Models

The formation mechanism of nanocomposites made by the HPM method was validated on the DGEBA/BF_3.MEA epoxy system. Although I.30E has a strong catalytic effect on the homopolymerization of DGEBA, the reaction rate on the

DGEBA/BF_3.MEA epoxy system in the presence of I.30E (intergallery) is slower than in the pure resin system (extragallery). In addition, some alkylammonium ions were replaced by monoethylamine (MEA) from BF_3.MEA. As a result, the basal spacing did not increase, but rather decreased, during curing; to about 3.1 nm. Such nanocomposites should be intercalated if only chemical mechanisms pertain; however, by means of the HPM method, organoclay agglomerates are broken down to form tactoids consisting of 5 ~ 10 silicate layers, uniformly distributed in the epoxy system. The tactoids look like discs, with a diameter equal to that of clay layers, and a thickness of 15~30 nm. Therefore, real nanocomposites were synthesized.

CTBN rubber has an insignificant influence on the structures of organoclays in epoxy resin. Therefore, the changes of organoclay in hybrid nanocomposites (8CI-20-x) are the same as above. However, the organoclay exerts a significant effect on the formation of the rubber phase in the epoxy system. Figure 5-23 shows the development of a two-phase structure *via* spinodal decomposition in the absence of organoclay [121]: A) co-continuous structure; B) early development of spinodal decomposition, and growing self-similarity to yield a similar structure with longer periodic distance; C) phase connectively interrupted and converted into a fragmented structure; and D) further forming a spherical domain structure. As the organoclay is added into the uncured rubber-epoxy system, it could be possible that the organoclay enhances the compatibility between the CTBN rubber and the epoxy resin system, and accelerate the reaction at high temperature; this would result in phase separation becoming more difficult as the clay loading is increased. Therefore, at low clay loading, the rubber phase still retains spherical morphology. However, the co-continuous structure of early stage phase

separation would be fixed in the cured resin at 6-phr clay loading.

The schematic illustrations and parameters of organoclays in these nanocomposites are the same as in the nanocomposites based on the TGDDM/DDS/I.30E system, except that the basal spacing is 3.1 nm.

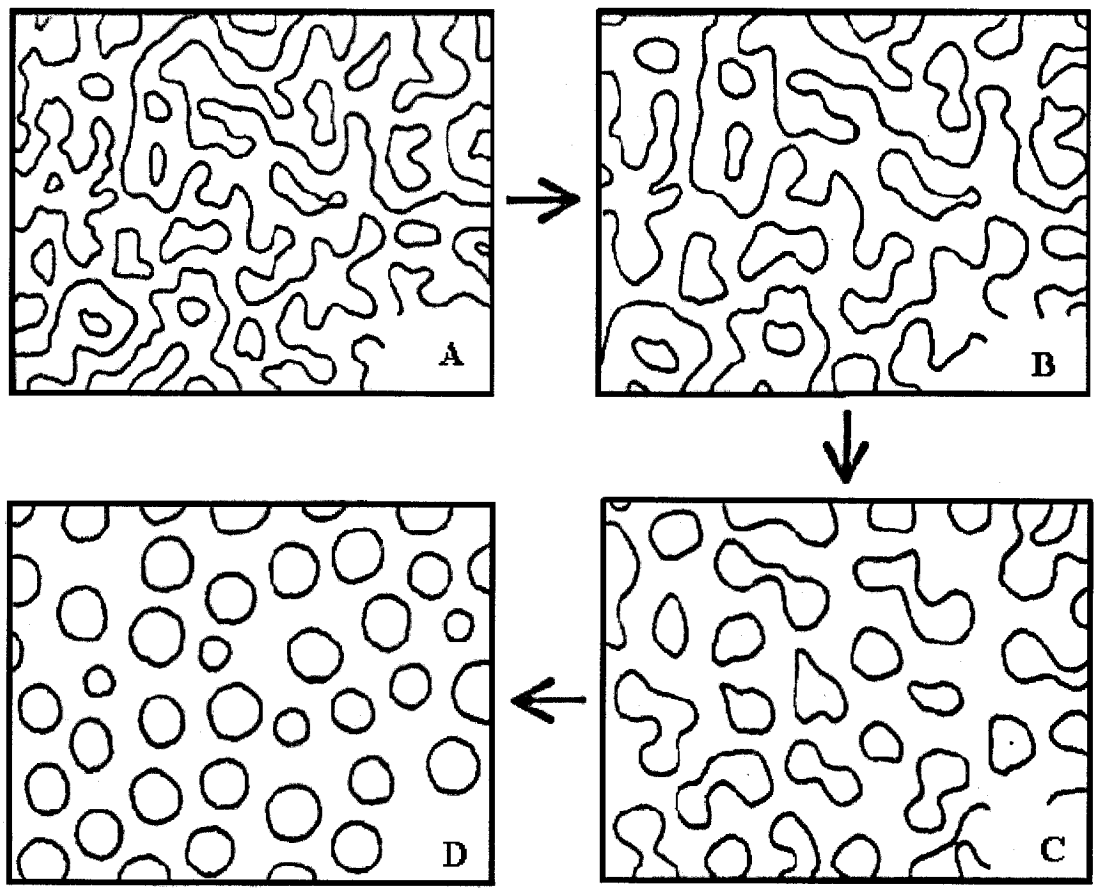

Figure 5-23: Schematic representation of phase separation scheme

5.4 Summary

Hybrid nanocomposites modified with rubber and organoclay were synthesized by the HPM method. Adding organoclay into rubber-modified epoxies not only increases

the degree of cure and T_g, but also changes the morphology of the rubber phase. The formation mechanism of nanocomposites made by the HPM method was validated on the DGEBA/BF_3.MEA epoxy system. The organoclay tactoids consist of 5 ~ 10 silicate layers, uniformly distributed in the epoxy system. The shape and size of tactoids are the same as those in nanocomposites based on the TGDDM/DDS/I.30E system, but the basal spacing of the organoclay is only 3.1 nm.

Chapter 6

Water Uptake of Epoxy-Clay Nanocomposites

The service temperature of advanced composites depends mainly on the glass transition temperature (T_g) of the matrix in wet conditions. However, epoxy resin matrices are very sensitive to moisture content; as a general rule, for most epoxy resin systems the T_g is reduced by 20°C/1% moisture content [6, 10].

Water uptake behavior of epoxy-clay nanocomposites is studied in this chapter. Diffusion models including Fick's Law, the Langmuir Model of Diffusion (LMD), Diffusion with Time-Varying Diffusivity (DTVD), and diffusion models for composites are reviewed; models for the diffusivities of exfoliated and intercalated nanocomposites are developed. Specimens of nanocomposites were immersed in distilled water at constant temperatures of 23°C, 50°C and 80°C for 5,000 hours. The equilibrium moisture content of the nanocomposites was measured, and diffusivities were determined by fitting Fick's Law, LMD and DTVD to the experimental data, employing a least-square approach. Diffusion models for nanocomposites are discussed, and confirmed by experimental data for different kinds of nanocomposites. The effects of materials, dispersion processes and morphology on water uptake behavior of nanocomposites are investigated.

6.1 Introduction

It is well known that mechanical and thermal properties of epoxy resins in advanced composites are more strongly affected by water uptake than those of other matrices, such as bismaleimide (BMI), polyetheretherketone (PEEK), cyanate ester, *etc.* [122]. Absorbed water acts as an efficient plasticizer for cured epoxy systems; as a consequence, the T_g's of the systems are greatly reduced. As a general rule, in most epoxy resin systems the T_g is reduced by 20°C/1% moisture [6, 10]. For example, the TGDDM/DDS epoxy resin system has a high T_g, about 260°C, but its service temperature is limited to 130°C due to its high water absorption, about 7 % [123-125].

Moisture effects on epoxy resin systems or their composites have been widely studied using various techniques [126-128]. Water transport is related to the existence of molecule-size holes in polymer structures, and the affinity between polar groups of polymers and water. Apicella, *et al.* [129] proposed three different modes for the water uptake of epoxy systems: (a) bulk dissolution of water in the polymer network; (b) moisture sorption onto the surface of holes that define the excess free volume of the glass structure; and (c) hydrogen bonding between hydrophilic groups of the polymer and water. Moy and Karasz [130] reported that water exists in two distinct forms in epoxy systems: free water that fills the micro-cavities, and bound water in strong interactions with polar groups.

The substantial decrease of permeability brought about by nanocomposite structures is a major advantage of polymer-clay nanocomposites, due to the tortuous path presented by high aspect ratio clay. The Toyota researchers reported that the rate of

water absorption in their polyamide 6-clay nanocomposite is reduced by 40% compared with the pristine polymer [22, 61]. Later, Messersmith, *et al.* [62] observed a dramatic decrease (up to 80 %) of water permeability in a poly (ε-caprolactone) layered silicate nanocomposite with only 5 vol % of clay.

However, there are contradictory reports of water absorption for epoxy–clay nanocomposites. Peter and Anne [67, 68] used I.30E to reinforce an epoxy system consisting of Shell Epon 828 cured with Jeffamine D 230 hardener; they found no obvious improvement in water absorption upon adding I.30E into the epoxy resin; the greatest moisture absorption rate was found at 6 wt% clay loading, the least at 3 wt%.

Massam and co-workers [32] investigated the resistance of epoxy nanocomposites towards organic solvents and water; the absorption of methanol, ethanol and propanol in nanocomposites is faster in neat epoxy systems, and properties of neat systems are much more affected by the absorbed solvent than nanocomposites. However, in the case of water, only the rate of absorption is reduced; the equilibrium water uptake is relatively unaffected. It was further observed that the barrier to solvent uptake is more significant in exfoliated composites than conventional or intercalated layered silicate composites.

Becker, *et al.* [65] studied the water uptake of nanocomposites made by the DM method, based on epoxy resins of three different functionalities with I.30E organoclay. The equilibrium water uptake at 80°C was reduced by 4.76 % for bi-functional (DGEBA) epoxy, 9.74% for tri-functional epoxy, and 4.76% for tetra-functional (TGDDM) epoxy at 10 % clay loading, compared to the neat epoxy system; however, the maximum increases of diffusivity for these three materials were 14%, 61% and 78% respectively.

The concentration of clay did not correlate proportionally with the reduction in equilibrium water uptake or the increase of diffusivity; this may depend on the type of epoxy systems.

The objective of the work presented in this chapter is to build a diffusion model for nanocomposites, and to study the effects of materials, synthesizing processes and structures on the water uptake behavior of nanocomposites.

6.2 Diffusion Models

Numerous models have been proposed for modeling water diffusion behavior in polymers and polymer composites. The most common approach is to apply Fick's law to simple single-free-phase diffusion, due to its simplicity and mathematical tractability [88]. However, it has been demonstrated that diffusion of water in some glassy polymers is anomalous (non-Fickian). Two main approaches are proposed to model the anomalous diffusion. One is the Langmuir-type model, assuming that absorbed water molecules consist of mobile and bound phases [131, 132]; the other is the time-varying diffusivity model, where a constant coefficient of diffusion is replaced by a decreasing function of time (by analogy with a relaxation modulus for a viscoelastic solid) [133, 134]. Several models have been proposed to predict the behavior of composites based on the analogy between thermal conductivity and diffusivity [135, 136]. The most extensively cited model in polymer/clay nanocomposites is the Nielsen model, which predicts that relative permeability is only a function of the aspect ratio at a given loading of clay, for all permeants [137].

6.2.1 Fick's Law

Moisture absorption is generally considered to be independent of moisture concentration. The diffusion of moisture into cured epoxy resin is generally considered to obey Fick's Law:

Fick's First Law: $$J = -D\left(\frac{\partial c}{\partial x}\right) \tag{6-1}$$

where $J(t, x)$ is the mass flux, D is the diffusivity, c is the moisture concentration, and x is the distance from the edge of the plate normal to the surface.

The moisture concentration, $c\ (t, x)$, is defined as:

$$c = \lim_{\Delta v \to 0} \frac{M_A}{M_D} \tag{6-2}$$

where M_A is the mass of water absorbed in volume Δv, and M_D is the mass of dry material in volume Δv.

Fick assumed that water is driven to penetrate the material by the water concentration gradient dc/dx, so that water uptake as a function of time is given by:

Fick's Second Law:

$$\frac{\partial c}{\partial t} = \frac{\partial}{\partial x}\left(D\frac{\partial c}{\partial x}\right) \tag{6-3}$$

where t is the time. As D is considered to be constant, the governing equation of moisture diffusion is:

$$\frac{\partial c}{\partial t} = D_x \frac{\partial^2 c}{\partial x^2} \qquad t \geq 0, -l \leq x \leq l \tag{6-4}$$

where D_x is the diffusivity in the direction normal to the surface.

Boundary conditions of the above equation are:

$$c(x,0) = c_0(x) \qquad \text{at } -l \leq x \leq l \tag{6-5}$$

$$c(\pm \ell, t) = c_\ell(t) \qquad t \geq 0 \tag{6-6}$$

Upon solving the above equations, moisture uptake M_t can be obtained [138]:

$$\frac{M_t}{M_\infty} = \left[1 - \sum_0^\infty \frac{8}{(2n+1)^2 \pi^2} \exp\left[\frac{-D(2n+1)^2 \pi^2 t}{4l^2}\right]\right] \tag{6-7}$$

where M_∞ is the maximum water uptake in the sample mass, and $2l$ is the sample thickness. The solution for Fick's Law at short times then reduces to the following equation for the initial stage of diffusion:

$$\frac{M_t}{M_\infty} = 2\left(\frac{Dt}{\pi l^2}\right)^{1/2} \tag{6-8}$$

6.2.2 Anomalous (Non-Fickian) Models

6.2.2.1 Langmuir Model of Diffusion (LMD)

Water is considered to occur in two categories: one free for diffusion, and the other trapped, not free to move in polymers. At a given time and place in a polymer, there are $c(t)$ mobile H_2O molecules per unit volume, which can diffuse with a diffusivity D and

become linked or trapped in the polymer with a probability γ. At a certain time and place there are $C(t)$ trapped molecules per unit volume, which become mobile with a probability α. According to the Langmuir theory of adsorption [131, 132], the concentrations of mobile and trapped molecules at equilibrium, c_∞ and C_∞ respectively, satisfy the relation:

$$\gamma c_\infty = \alpha C_\infty \tag{6-9}$$

Diffusion of water molecules through the matrix is described by the mass conservation law:

$$\frac{\partial c}{\partial t} = \frac{\partial J}{\partial x} - \frac{\partial C}{\partial t} \tag{6-10}$$

where $J(t, x)$ is the mass flux, which conforms to simple diffusion theory (Equation 6-1), and the diffusivity remains independent of water concentration, as in Fick's model. Thus, for the one-dimensional case, concentrations at position x and time t satisfy the coupled pair of equations:

$$D\frac{\partial^2 c}{\partial^2 x} = \frac{\partial c}{\partial t} + \frac{\partial C}{\partial t} \tag{6-11}$$

$$\frac{\partial C}{\partial t} = \gamma c - \alpha C \tag{6-12}$$

Boundary conditions of the above equation are:

$$C(x,0)=0 \text{ and } c(x, 0) = 0 \quad \text{at} \quad -l \leqslant x \leqslant l \tag{6-13}$$

$$c(\pm\ell,t) = c_\ell(t) \qquad t \geqslant 0 \tag{6-14}$$

An approximate moisture uptake M_t can be obtained [131]:

$$\frac{M_t}{M_\infty} = 1 - \frac{\gamma}{\gamma+\alpha} e^{-\alpha} - \frac{8}{\pi^2} \frac{\alpha}{\alpha+\gamma} \sum_0^\infty \frac{1}{(2n+1)^2} \exp\left\{ -\left[\frac{\pi(2n+1)}{2l} \right]^2 Dt \right\} \tag{6.15}$$

6.2.2.2 Diffusion with Time-Varying Diffusivity (DTVD)

For an unstressed isotropic viscoelastic polymer, time-varying effective diffusivity can be expressed in the form of a Prony series [133]:

$$D(T,t) = D_0(T) + \sum_{r=1}^{n} D_r(T)(1 - e^{-t/\tau_r}) \tag{6-16}$$

where D_0, D_r are the unknown temperature-dependent Prony coefficients, τ_r is the corresponding time, and n is the number of terms in the Prony series. As $D(T, t)$ is assumed to be uniform through the thickness of specimen, the governing equation (6-4) for one-dimensional diffusion is still effective:

$$\frac{\partial c}{\partial t} = D(t) \frac{\partial^2 c}{\partial x^2} \tag{6-17}$$

The concentration boundary conditions are

$$c(\pm\ell,t) = c_\ell(t) \tag{6-18}$$

Defining a change in variable:

$$dU = D(t)dt \tag{6-19}$$

giving $$U(t) = \int_0^t D(t')dt' \tag{6-20}$$

with this change of variable, Equation (6-17) reduces to

$$\frac{\partial c}{\partial U} = \frac{\partial^2 c}{\partial x^2} \tag{6-21}$$

The modified boundary conditions in terms of variable U take the form:

$$c(\pm \ell, U) = c_\ell(U) \tag{6-22}$$

Upon solving Equation 6-21, similar to Equation 6-4, moisture uptake M_t can be obtained [138]:

$$\frac{M_t}{M_\infty} = \left[1 - \sum_0^\infty \frac{8}{(2n+1)^2\pi^2} \exp\left[\frac{-(2n+1)^2\pi^2 U}{4l^2}\right]\right] \tag{6.23}$$

Substituting Equation (6-16) into (6-20):

$$U(t) = \int_0^t [D_0(T) + \sum_{r=1}^n D_r(T)(1 - e^{-t'/\tau_r})]dt' \tag{6-24}$$

$$U(t) = D_0(T)t + \sum_{r=1}^n D_r\left[t + \tau_r\left(e^{-t/\tau_r} - 1\right)\right] \tag{6-25}$$

Substituting Equation (6-25) into (6-23) gives [133]:

$$\frac{M_t}{M_\infty} = 1 - \sum_{n=0}^\infty \frac{8}{(2n+1)^2\pi^2} \exp\left\{\frac{-(2n+1)^2\pi^2}{4l^2}\left[D_0 t + \sum_{r=1}^m D_r\left[t + \tau_r\left(e^{-t/\tau_r} - 1\right)\right]\right]\right\} \tag{6-26}$$

6.2.3 Models for Composites

In studying the kinetics of diffusion, small molecule diffusion in polymers is often considered analogous to thermal conduction. Shen and Springer [135] proposed a theory of moisture diffusion in unidirectional composites, based on the analogy between thermal conductivity and diffusivity.

$$D_{11} = D_m(1-\upsilon_f)+D_f\upsilon_f \tag{6-27}$$

$$D_{22} = (1-2\sqrt{\upsilon_f/\pi})D_m + \frac{D_m}{B_D}\left[\pi - \frac{4}{\sqrt{1-(B_D^2\upsilon_f/\pi)}}\tan^{-1}\frac{\sqrt{1-(B_D^2\upsilon_f/\pi)}}{\sqrt{1+(B_D^2\upsilon_f/\pi)}}\right] \tag{6-28}$$

where D_{11} and D_{22} are diffusivities parallel and normal to the fibers (longitudinal and transverse directions), D_m and D_f are the diffusivities of matrix and fiber, υ_f is the volume fraction of the fibers, and B_D is defined as following equation:

$$B_D = 2\left(\frac{D_m}{D_f}-1\right) \tag{6-29}$$

As the diffusivity of fibers such as carbon or glass is small compared to the diffusivity of the matrix ($D_m \gg D_f$), and Equations (6.27) and (6.28) reduce to ($\upsilon_f < 0.785$)

$$D_{11} = D_m(1-\upsilon_f) \tag{6-30}$$

$$D_{22} = (1-2\sqrt{\upsilon_f/\pi})D_m \tag{6-31}$$

Shirrell and Halpin [139] derived the composite diffusivity based on the analogy between diffusivity and shear stiffness. The longitudinal diffusivity (D_{11}) is the same as Equation 6-30, but the transverse diffusivity (D_{22}) is obtained by the following equation:

$$D_{22} = D_m \frac{1+\zeta\eta v_f}{1-\eta v_f} \tag{6-32}$$

$$\eta = \frac{D_f / D_m - 1}{D_f / D_m + \zeta} \tag{6-33}$$

where ζ is the aspect ratio.

6.2.4 Barrier Model

Nielsen proposed a simple, two-dimensional model that assumes perfect registry of the fillers parallel to the surface of the film [137]. The model predicts that relative permeability is a function of the aspect ratio alone at a given clay loading for all permeants. A fairly simple equation was derived by Nielsen for a two-dimensional case, as follows:

$$P_f / P_u = v_p + (L/2W) v_f \tag{6-34}$$

Where P_f is the permeability of the composites, P_u is the permeability of the polymer, v_p is the volume fraction of the polymer, v_f is the volume fraction of the fillers, L is the average length of the filler face, and W is the average thickness of the filler.

The L/W ratio of clay is critical in contributing to the barrier in the model. Experimental data show that this model predicts the permeability behavior of

nanocomposites reasonably well at very low loadings of clay (less than 1 wt %); at higher clay loadings, the data deviate substantially from the model [1].

6.2.5 Model Development for Nanocomposites

As organoclay is used as a reinforcement in polymers, the clay platelets may play an important role in changing the diffusion path of diffusing molecules in an anisotropic fashion, by hindering them from straight diffusion. To study the effect of morphology of nanocomposites on diffusivity, the simplest case, exfoliated and ordered nanocomposites, was first considered. Organoclay platelets are assumed to do not absorb water molecules.

6.2.5.1 Diffusion Model for Exfoliated Nanocomposites (DMEN)

Clay platelets are assumed to be uniformly distributed, completely exfoliated and aligned in one direction in a polymer, as shown in Figure 6-1 A. The face of a clay platelet is a square with side length ℓ and thickness t. The representative volume element (RVE) of the exfoliated composite is cut from the nanocomposite, as shown in Figure 6-1 B. The volume fraction of clay is given by:

$$v_c = \frac{\ell^2 t}{a^2 h} \tag{6-35}$$

where a is the length of RVE, and h is the thickness of RVE

As clay platelets are impermeable, diffusing molecules must take a tortuous pathway during diffusion; therefore, results from diffusion in porous media may be used in epoxy-clay nanocomposites.

The tortuosity factor has two effects on the diffusion process: one is the effect on the cross-sectional area perpendicular to the direction of diffusion flow; the other is the effect on the driving force (concentration gradient), due to the long diffusion pathway rather than the effective pathway. The tortuosity factor (τ) is defined as:

$$\tau = \left(\frac{d}{d'}\right)^2 \tag{6-36}$$

where ***d'*** is the effective distance that diffusing molecules must travel, and ***d*** is the shortest distance these molecules would have traveled in the absence of the clay platelets.

The diffusivity is proportional to the tortuosity for diffusion in porous media [140, 141]. Therefore, the diffusivity (D_n) of a nanocomposite is obtained by the following equation:

$$\frac{D_n}{D_m} = \tau = \left(\frac{d}{d'}\right)^2 \tag{6-37}$$

where D_n and D_m are the diffusivities of a nanocomposite and a matrix, respectively.

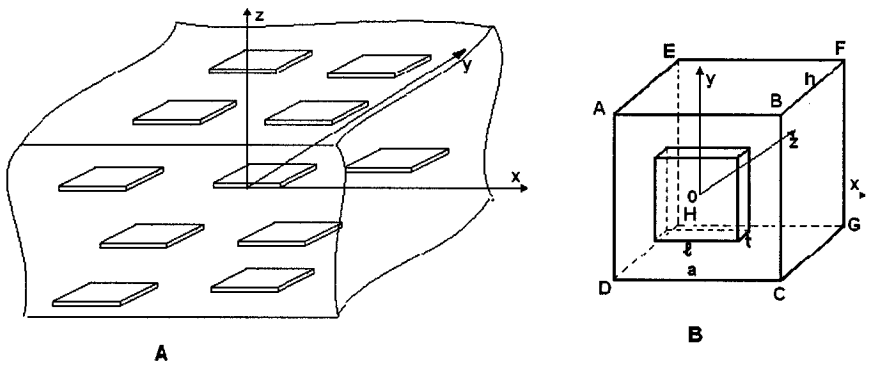

Figure 6-1: Schematic drawings of an exfoliated and ordered nanocomposite (A), and its square representative volume element (RVE) (B)

In order to obtain the effective distance (***d'***), the following assumptions are proposed:

(1) Diffusing molecules select the shortest distance to go around clay platelets;

(2) Diffusing molecules return to their original diffusion routes after going around clay platelets.

Diffusivity in the direction parallel to the face of the clay platelets ($D_{//}$)

From Figure 6-1B, it can be seen that the structure of clay platelets along the X- and Y-axes is the same; thus the same diffusivities pertain parallel to the face of clay platelets. If diffusing molecules diffuse along the Y-axis, as shown in Figure 6-2, the shortest distance (***d***) that diffuse molecules would have traveled in the absence of the clay platelets is ***a***. Because the length and width of clay platelets are much larger than their thickness, diffusing molecules go around the clay platelets along the thickness direction according to the assumption that diffusing molecules select the shortest distance to go around the clay platelets, as shown in Figure 6-2 B. The effective diffusion distance of a small strip ℓdz (shown in Figure 6-2A) is given by:

$$d_1' = a + 2(t/2 - z) \tag{6-38}$$

The average effective distance for traveling through the "AEFB" surface is given by

$$\bar{d}_1' = \frac{\int_{-t/2}^{t/2} (a + 2(t/2 - z))\ell dz + (ah - \ell t)a}{ah} \tag{6-39}$$

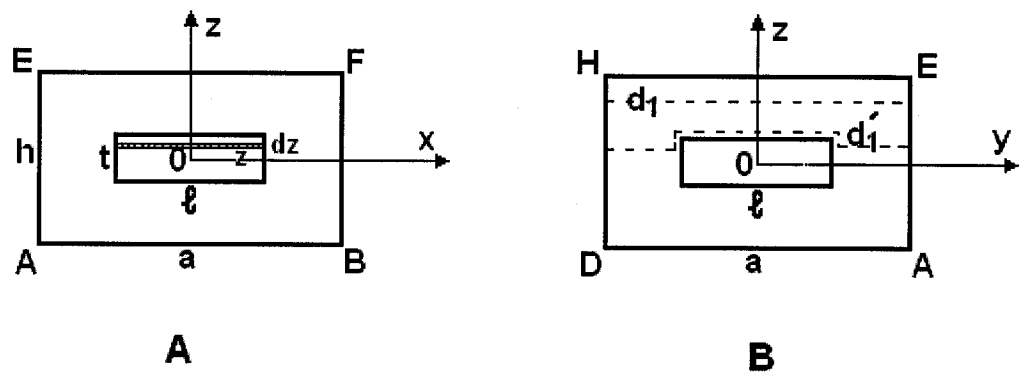

Figure 6-2: Schematic drawings of diffusion of diffusing molecules parallel to the face of clay platelets

Simplifying Equation 6-39, the average effective distance becomes:

$$\bar{d}_1' = \left(a + \frac{\ell t^2}{2ah} \right) \tag{6-40}$$

By substituting the shortest distance (***d***) and the average effective distance into Equation 6-37, the diffusivity in the direction parallel to the face of the clay platelets (D_{11}) is given by:

$$\frac{D_{11}}{D_m} = \left(\frac{a}{\bar{d}_1} \right)^2 = \left(\frac{a}{a + \frac{\ell t^2}{2ah}} \right)^2 = \frac{1}{\left(1 + \frac{\ell t^2}{2a^2 h} \right)^2} \tag{6-41}$$

The aspect ratio is defined as:

$$\zeta = \frac{\ell}{t} \tag{6-42}$$

By substituting the aspect ratio and the volume fraction of clay platelets into Equation 6-41, D_{11} is given by:

$$\frac{D_{11}}{D_m} = \frac{1}{\left(1+\frac{\upsilon_c}{2\zeta}\right)^2} \tag{6-43}$$

Diffusivity in the direction normal to the face of the clay platelets (D_{22})

If diffusing molecules diffuse in the direction normal to the face of the clay platelets, as shown in Figure 6-3, the shortest distance (***d***) that diffusing molecules would have traveled in the absence of the clay platelets is ***h***. In order to obtain the effective diffusion distance, the square ABCD is divided into four triangles, as shown in Figure 6-3A. These triangles have the same geometry, and thus diffusing molecules have the same diffusion behavior traveling through them. In each triangle, diffusing molecules go around the clay platelets along the same direction, according to the assumption that diffusing molecules select the shortest distance to go around the clay platelets. For example, as diffusing molecules travel through the triangle OBC, they are hindered by the triangle OB'C' of clay platelets, and go around the B'C' side of the clay platelets. The effective diffusion distance of a small strip ***2xdx*** (shown in Figure 6-3A) is given by:

$$d_2^{'} = h + 2(\ell/2 - x) \tag{6-44}$$

The average effective distance for traveling through the triangle "OBC" surface is given by:

$$\bar{d}_2' = \frac{\int_0^{\ell/2} (h + 2(\ell/2 - x)) \bullet 2x dx + \frac{(a+\ell)}{2}\frac{(a-\ell)}{2} \bullet h}{\frac{1}{4}a^2} \tag{6-45}$$

Simplifying Equation 6-45, the average effective distance becomes:

$$\bar{d}_2' = h + \frac{\ell^3}{3a^2} \tag{6-46}$$

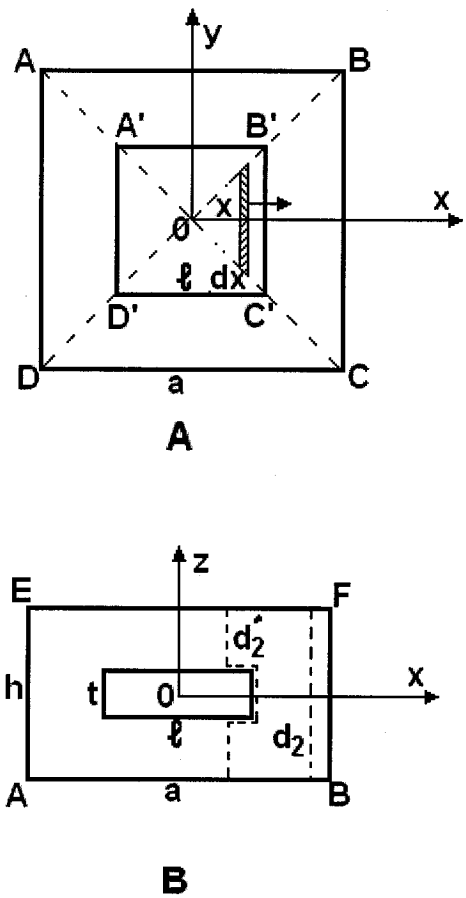

Figure 6-3: Schematic drawings of diffusion of diffusing molecules in the direction normal to the face of clay platelets

The same average effective distances pertain for the other three triangles, OAB, OAD and ODC, because ABCD is a square. Therefore, Equation 6-46 is effective throughout the ABCD square. By substituting the shortest distance (***d***) and the average effective distance into Equation 6-37, the diffusivity in the direction normal to the face of the clay platelets (D_{22}) is given by:

$$\frac{D_{22}}{D_m} = \left(\frac{h}{\bar{d}_2}\right)^2 = \left(\frac{h}{h + \frac{\ell^3}{3a^2}}\right)^2 = \frac{1}{\left(1 + \frac{\ell^3}{3a^2 h}\right)^2} \tag{6-47}$$

By substituting the aspect ratio and the volume fraction of clay platelets into Equation 6-47, D_{22} is given by

$$\frac{D_{22}}{D_m} = \frac{1}{\left(1 + \frac{\zeta v_c}{3}\right)^2} \tag{6-48}$$

Diffusivity of an exfoliated nanocomposite in random orientation (D_n)

In the case of completely random orientation in all three orthogonal directions, diffusivity in an exfoliated nanocomposite is complicated. First, the 2-D case for a platelet in random orientation in a polymer is considered, as shown in Figure 6-4.

The tortuosity factor has two effects on the diffusion process: the cross-sectional area and the long diffusion pathway. When the clay platelet has an angle θ with the X-axis, the effective diffusion distance of diffusing molecules at y position along x direction (shown in Figure 6-4 A) is given by:

$$d_x' = h + 2\left(\frac{\ell}{2} - \frac{y}{\cos\theta}\right) \tag{6-49}$$

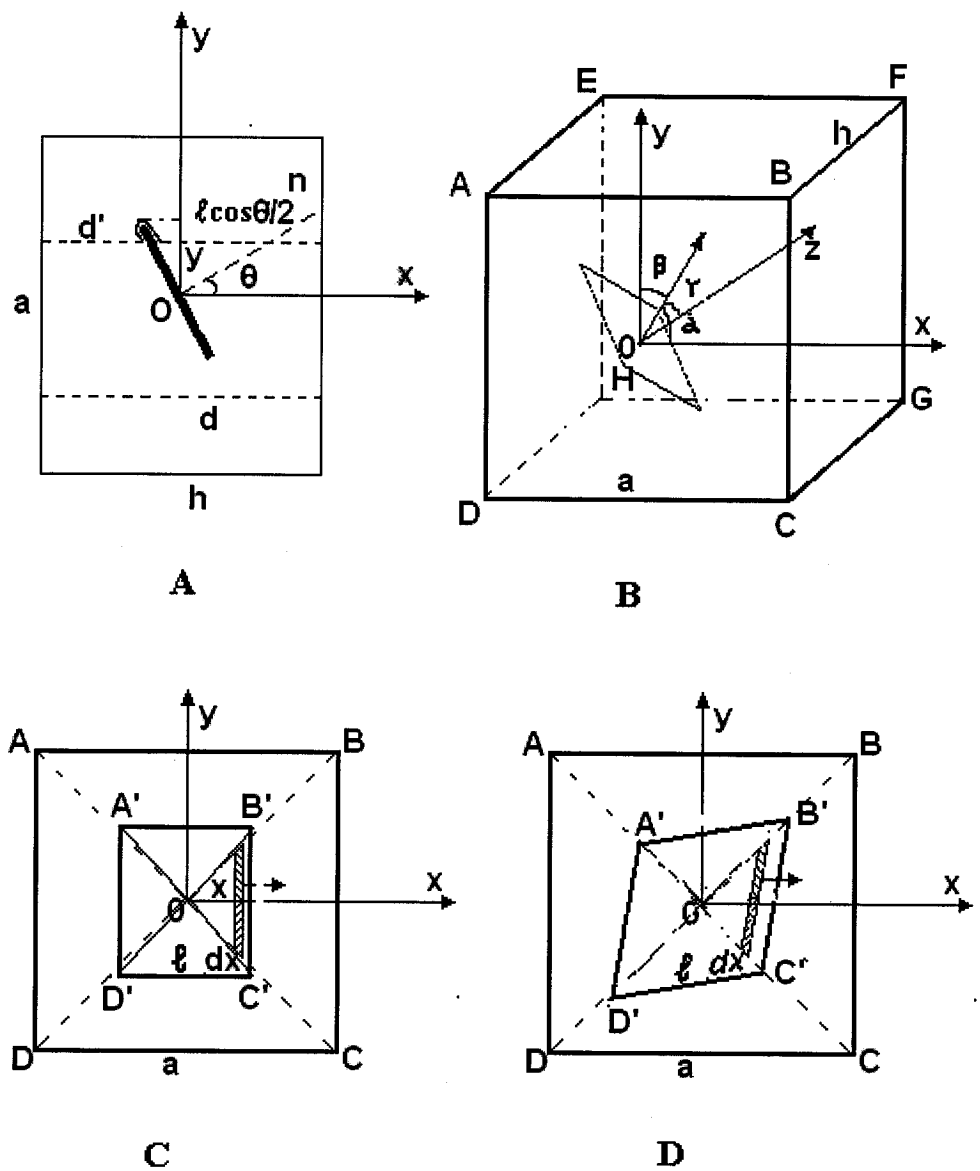

Figure 6-4: Schematic drawings of the 2-D and 3-D cases for diffusion of diffusing molecules in a nanocomposite at random orientation

The average effective distance for traveling along x direction is given by

$$\bar{d}_x' = \frac{\int_0^{\ell\cos\theta/2}(h+2(\ell/2-y/\cos\theta))dy+(a/2-\ell/2\cos\theta)h}{a/2} \tag{6-50}$$

Simplifying Equation 6-50, the average effective distance becomes:

$$\bar{d}_x' = h+\frac{\ell^2\cos\theta}{2a} \tag{6-51}$$

If the probability of platelets lying in any angle is the same, the average effective distance for platelets at random orientation is given by:

$$\bar{d}_x' = \frac{\int_0^{\pi/2}(h+\frac{\ell^2\cos\theta}{2a})d\theta}{\pi/2} = h+\frac{\ell^2}{2\pi a} \tag{6-52}$$

In the same way, for the 3-D case, it is assumed that a platelet is at random orientation in a polymer as shown in Figure 6-4 B. ***α, β, or γ*** is the angle between the clay platelet and the X, Y or Z-axis, respectively. If diffusing molecules diffuse in the Z-axis direction, the tortuosity factor depends on the projection area on the XY plane and the diffusion pathway. First, as the clay platelet revolves around the Y-axis in Figure 6-4 (***β=90°***), the projection shape of the clay platelet should be a rectangle in the XY plane, as shown in Figure 6-4 C. The effective diffusion distance of a small strip ***2xdx*** in the triangle OB'C' (shown in Figure 6-4C) is given by:

$$d_{z1}' = h+2\left(\frac{\ell}{2}-\frac{x}{\cos\gamma}\right) \tag{6-53}$$

The average effective distance for traveling through the triangle "OBC" surface is given by

$$\bar{d}'_{z1} = \frac{\int_0^{\ell\cos\gamma/2} (h + 2(\ell/2 - x/\cos\gamma)) \bullet 2x/\cos\gamma dx + \frac{(a+\ell)}{2}\frac{(a-\ell\cos\gamma)}{2} \bullet h}{\frac{1}{4}a^2} \tag{6-54}$$

Simplifying Equation 6-54, the average effective distance becomes:

$$\bar{d}'_{z1} = h + \frac{\ell^3\cos\gamma}{3a^2} + \frac{\ell h(1-\cos\gamma)}{a} \tag{6-55}$$

As the clay platelet revolves around the Y-axis, triangle OB'C' in Figure 6-4 C has the same cross-sectional area variation as triangle OA'D', and another pair of triangles, OD'C' and OA'B', have the same variation. Thus the effective diffusion distance of a small strip ***2ydy*** in the triangle OA'B' is given by:

$$d'_{Z2} = h + 2\left(\frac{\ell}{2} - y\right) \tag{6-56}$$

$$d'_{Z2} = h + 2\left(\frac{\ell}{2} - y\right) \tag{6-56}$$

The average effective distance for traveling through the triangle "OAB" surface is given by

$$\bar{d}'_{z2} = \frac{\int_0^{\ell/2} (h + 2(\ell/2 - y)) \bullet 2y\cos\gamma dy + \frac{(a+\ell\cos\gamma)}{2}\frac{(a-\ell)}{2} \bullet h}{\frac{1}{4}a^2} \tag{6-57}$$

Simplifying Equation 6-57, the average effective distance becomes:

$$\bar{d}'_{z2} = h + \frac{\ell^3 \cos\gamma}{3a^2} + \frac{\ell h(\cos\gamma - 1)}{a} \tag{6-58}$$

Thus, the average effective distance for traveling through the square ABCD surface is given by:

$$\bar{d}'_{z} = \frac{d'_{z1} + d'_{z2}}{2} = h + \frac{\ell^3 \cos\gamma}{3a^2} \tag{6-59}$$

In the same way, as the clay platelet revolves around X-axis (α=90°), the same average effective distance as Equation 6-59 pertains for traveling through the square ABCD surface.

If α, β, or γ is any angle, the projection area is a parallelogram, as shown in figure 6-4 D. It is very complicated to calculate the projection area and average effective distance. Thus, the above results for rectangles are used to approximate for the parallelograms.

If the probability of platelets lying at any angle is the same, the average effective distance for platelets at random orientation is given by:

$$\bar{d}'_{z} = \frac{\int_0^{\pi/2}\int_0^{\pi/2}\int_0^{\pi/2} (h + \frac{\ell^3 \cos\gamma}{3a^2}) d\gamma \cdot d\alpha \cdot d\beta}{(\pi/2)^3} = h + \frac{2\ell^3}{3\pi a^2} \tag{6-60}$$

By substituting the shortest distance (d) and the average effective distance into Equation 6-37, the diffusivity of a nanocomposite at random orientation (D_n) is given by:

$$\frac{D_n}{D_m} = \left(\frac{h}{\bar{d}_z}\right)^2 = \left(\frac{h}{h + \frac{2\ell^3}{3\pi a^2}}\right)^2 = \frac{1}{\left(1 + \frac{2\ell^3}{3\pi a^2 h}\right)^2} = \frac{1}{\left(1 + \frac{2\zeta v_c}{3\pi}\right)^2} \tag{6-61}$$

6.2.3.2 Diffusion Model for Intercalated Nanocomposites (DMIN)

In intercalated nanocomposites, agglomerates of organoclay are assumed to be uniformly distributed in a polymer. Each agglomerate consists of ***n*** platelets of clay, and all platelets of clay in agglomerates are aligned in one direction. If the basal spacing of clay is far smaller than the distance between two agglomerates, the square representative volume element (RVE) of an intercalated composite contains one agglomerate consisting of ***n*** platelets, as shown in Figure 6-5.

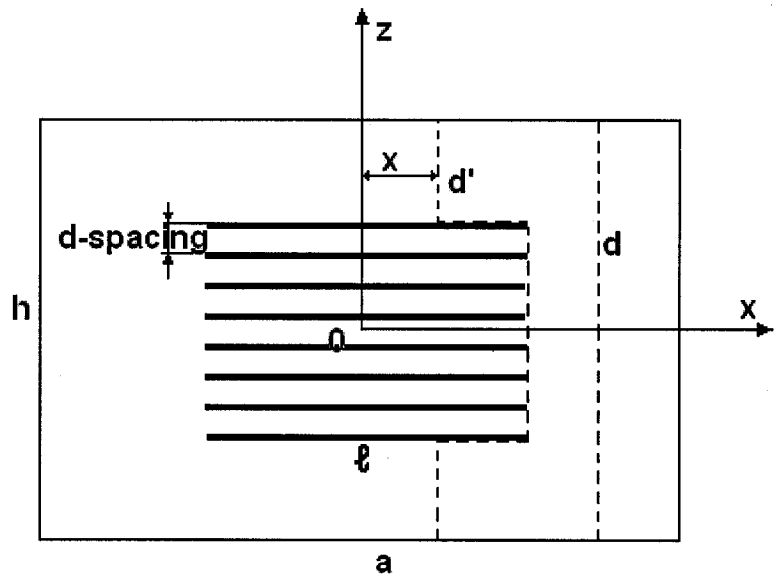

Figure 6-5: Schematic drawing of diffusion of diffusing molecules in the direction parallel to the face of the clay platelets in intercalated nanocomposites

The volume fraction of clay is given by:

$$\upsilon_c = \frac{n\ell^2 t}{a^2 h} \tag{6-62}$$

In the same way as above for exfoliated nanocomposites, the diffusivity of an intercalated nanocomposite in the direction parallel to the clay platelet is given by:

$$\frac{D_{11}}{D_m} = \frac{1}{\left(1+\frac{n\ell t^2}{2ah}\right)^2} = \frac{1}{\left(1+\frac{\upsilon_c}{2\zeta}\right)^2} \tag{6-63}$$

The diffusivity of an intercalated nanocomposite in the direction normal to the clay platelet is given by:

$$\frac{D_{22}}{D_m} = \frac{1}{\left(1+\frac{\ell^3}{3a^2 h}\right)^2} = \frac{1}{\left(1+\frac{\upsilon_c \zeta}{3n}\right)^2} \tag{6-64}$$

The diffusivity of an intercalated nanocomposite in random orientation (D_n) is given by:

$$\frac{D_n}{D_m} = \frac{1}{\left(1+\frac{2\ell^3}{3\pi a^2 h}\right)^2} = \frac{1}{\left(1+\frac{2\zeta\upsilon_c}{3n\pi}\right)^2} \tag{6-65}$$

6.3 Experimental Setup

6.3.1 Sample Preparation

The synthesis of epoxy resins, rubber-modified epoxies, conventional composites and nanocomposites is described in Chapters 4 and 5. These fully cured epoxy panels were cut into specimens of dimensions 50 × 24 × 1.75 mm for water absorption testing. Their thickness was deliberately controlled by polishing the specimens.

6.3.2 Physical Measurement

Water absorption measurement was performed according to ASTM D 570-98. At least 3 specimens of each composition were dried in vacuum at 120°C for 48 hrs. The initial weights and dimensions of all specimens were measured; then all specimens were immersed in distilled water at 23°C, 50°C or 80 °C, using constant temperature baths. Specimens were periodically removed, dried with filter paper, immediately weighed, and then returned to the water bath. However, specimens stored at high temperatures were dipped and cooled in water at room temperature for 10 min. prior to measuring, in order to suppress water desorption. All weights were measured on a digital analysis balance, with a resolution of 0.01mg.

Moisture content was determined using the following equation:

$$M_t(\%) = \left[\frac{W_t - W_0}{W_0}\right] \times 100 \qquad (6\text{-}66)$$

where W_t and W_0 are the weight of the sample at the time of the measurement and initial weight, respectively.

6.4 Results and Discussion

6.4.1 Moisture Content in Clay and Organoclays

Montmorillonite is naturally hydrophilic, and easily absorbs water from its environment during production and storage. An organoclay can still absorb water molecules after the montmorillonite has been organically treated. Figure 6-6 shows the weight loss of clay and organoclays with time at 120°C; commercial products I.30E and 30B organoclays contain about 2.2 and 2 wt% water, respectively. These water molecules may exist in two forms: hydrogen bonding with the hydroxyl groups (-OH) on the unmodified side surfaces of organoclay platelets, or bound to the modified surfaces in the galleries of organoclays.

X-ray diffraction (XRD) was used to inspect the basal spacing of these clays before and after drying, as listed in Table 6-1; the basal spacing of these organoclays decreases after drying. The reduction ratios of basal spacing for I.30E and 30B are 5.1% and 4.9 %, respectively, slightly larger than the volume reduction ratios (in Table 6-1) calculated from the weight loss due to experimental errors. This indicates that most water molecules in organoclays may be bound in the galleries. The important thing is that organoclays need to be dried prior to use, because water molecules may influence the cure processes of epoxy systems, and the final properties of the nanocomposites.

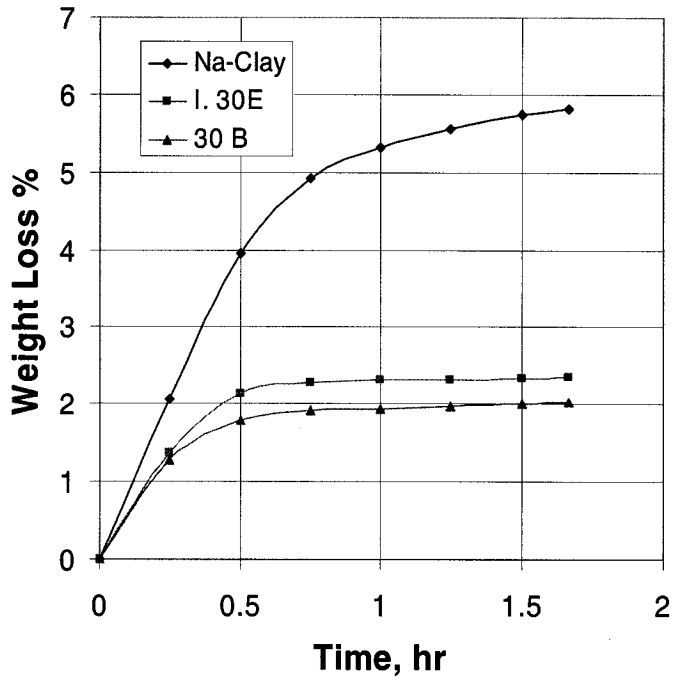

Figure 6-6: Weight loss of clay and organoclays over time at 120°C

Table 6-1: Basal spacing and volume reduction of clay and organoclays before and after drying

Materials	Na-clay	I.30E	30B
Basal spacing before drying (nm)	1.22	2.37	1.83
Basal spacing after drying (nm)	0.97	2.25	1.74
Reduction ratio in basal spacing (%)	20.5	5.1	4.9
Volume Reduction (%)	/	4.2	4.1

6.4.2 Water Uptake Behavior of Epoxy Resin Systems

Weight gain *vs.* square root of time curves were determined for two epoxy systems, DGEBA/BF_3.MEA and TGDDM/DDS, at 23°C, 50°C and 80°C, and are shown in Figures 6-7 and 6-8, respectively. As expected, these two epoxy systems have large difference in maximum water uptake. It can be seen in Figure 6-7 that DGEBA/BF_3.MEA reaches equilibrium at a lower moisture content of about 2.5 %, less than those of most epoxy systems. Furthermore, the maximum water uptake increases from 2.24% to 2.75% when environmental temperature increases from 23°C to 80°C. On the other hand, TGDDM/DDS has a higher maximum water uptake (about 7.7%, in Figure 6-8) than most epoxy resins; the maximum water uptake remains unaffected by changes of environmental temperature. Therefore, choosing these two resin systems with large differences in water absorption behavior can benefit the understanding of the mechanism of water diffusion in nanocomposites.

The Fickian numerical fits for two epoxy systems, DGEBA/BF_3.MEA and TGDDM/DDS at 23°C, 50°C and 80°C, are also plotted in Figures 6-7 and 6-8, respectively, given by Equation 6-7. The two epoxy resin systems appear to follow the Fickian numerical fits very closely at 23°C; but at 50°C and 80°C a two-stage diffusion process is observed. As a result, non-Fickian diffusion models are needed to describe diffusion behavior of water molecules in these materials.

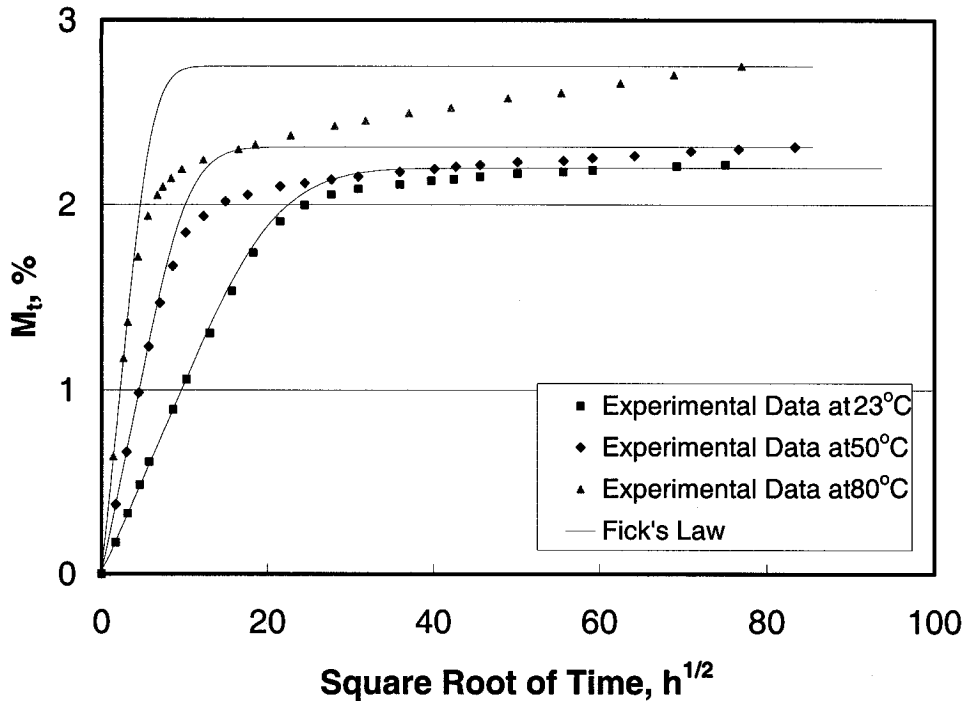

Figure 6-7: Water absorption profiles of DGEBA/BF_3.MEA epoxy system at different temperatures

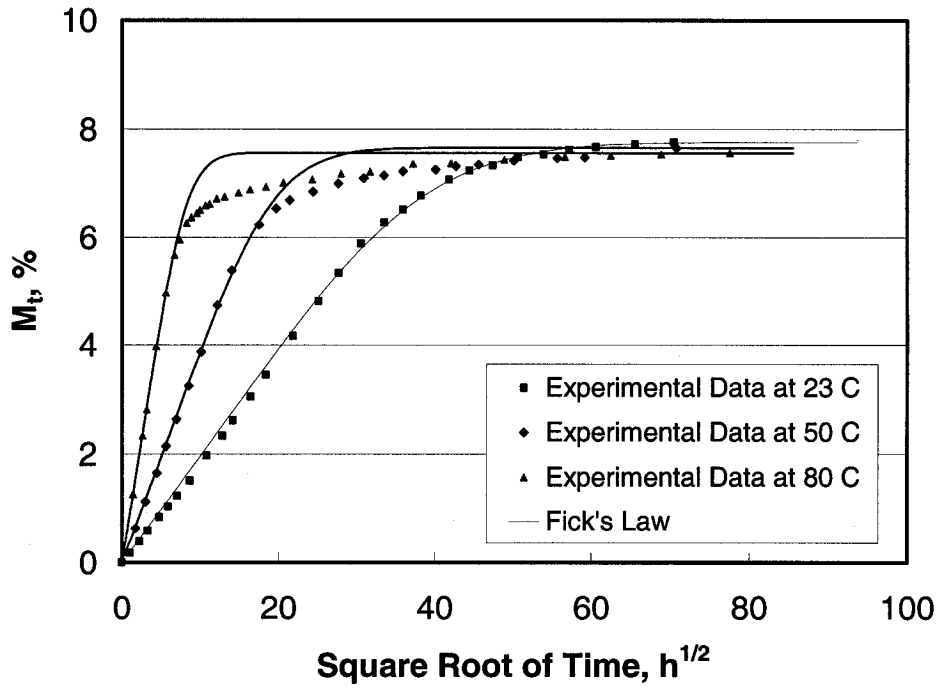

Figure 6-8: Water absorption profiles of TGDDM/DDS epoxy system at different temperatures

Although experimental data do not completely obey the Fickian law at higher environmental temperature, this law is often used to calculate diffusivities of polymers, because water uptake of polymers is linearly proportional to the square root of time at the initial stage [92]. As a result, the Fickian Law is the main method used here to calculate the diffusivities of all materials. The diffusivities ($\boldsymbol{D}$) of the two epoxy systems at different temperatures were calculated using Equation 6.8 from the initial slope of these plots for all sorption curves, and are listed in Table 6-2 for the DGEBA/BF_3.MEA system, and Table 6-3 for the TGDDM/DDS system. From Tables 6-2 and 6-3, it is clear that the DGEBA/BF_3.MEA system has a higher diffusivity (about 3.3-fold) than the TGDDM/DDS system, although the equilibrium moisture content of the TGDDM/DDS system is 3.2 times that of the DGEBA/BF_3.MEA system.

Non-Fickian diffusion models, including the Langmuir Model of Diffusion (LMD) and Diffusion with Time-Varying Diffusivity (DTVD), were used to describe the diffusion behavior of water molecules in these two resin systems. Using LMD, the values of probabilities of binding γ and unbinding α, and diffusivity ($\boldsymbol{D}$) at different temperatures were obtained by fitting Equation 6-15 to the experimental data employing a least-square approach, listed in Tables 6-2 and 6-3, respectively. The diffusivities obtained by LMD are higher than those from the Fickian law, due to the probabilities of binding and unbinding. The diffusivity of these two resin systems *versus* environmental temperature is shown in Figure 6-9; clearly the difference between the diffusivities obtained by the Fickian law and LMD increases with environmental temperature.

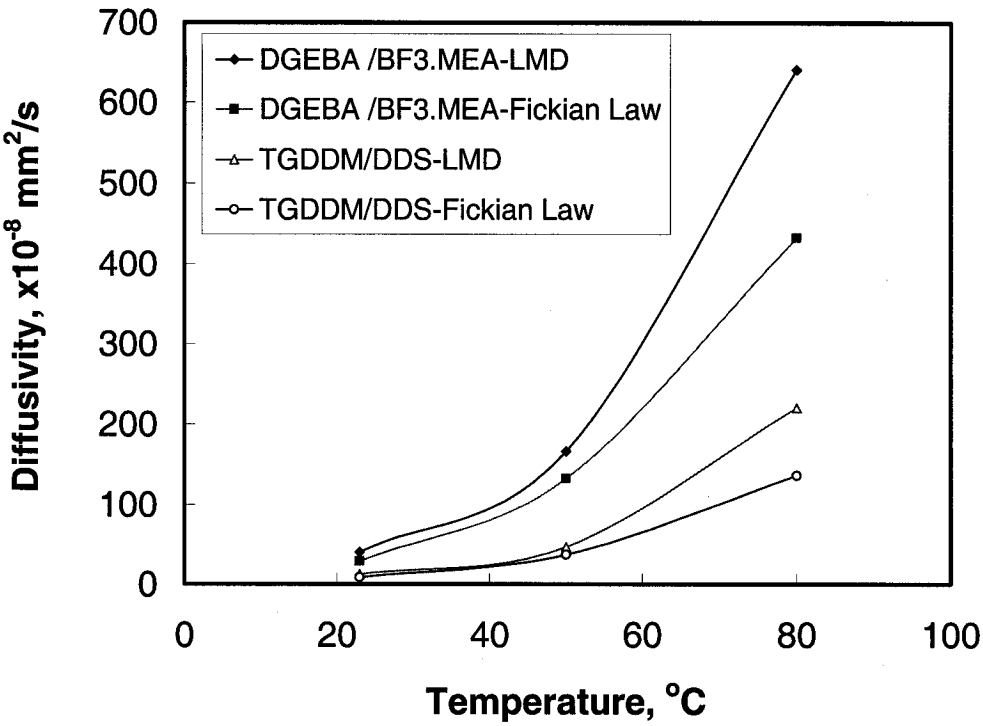

Figure 6-9: Diffusivity obtained with the Fickian law and LMD *versus* environmental temperature for DGEBA /BF_3.MEA and TGDDM/DDS

Table 6-2: Water uptake parameters of DGEBA /BF_3.MEA system

Model	Properties	Temperature		
		23°C	50°C	80°C
	M_∞	2.22 %	2.31 %	2.75 %
Fickian Law	D(mm^2/s)	$3.05x10^{-7}$	$1.32x10^{-6}$	$4.33x10^{-6}$
LMD	D(mm^2/s)	$4.05x10^{-7}$	$1.66x10^{-6}$	$6.41x10^{-6}$
	α	$2.01x10^{-7}$	$1.57x10^{-7}$	$1.68x10^{-7}$
	γ	$4.37x10^{-8}$	$2.38x10^{-8}$	$4.58x10^{-8}$

Table 6-3: Water uptake parameters of TGDDM/DDS system

Model	Properties	Temperature		
		23°C	50°C	80°C
	M_∞	7.76 %	7.65 %	7.56 %
Fick's Law	**D(mm^2/s)**	$8.80x10^{-8}$	$3.71x10^{-7}$	$1.36x10^{-6}$
LMD	**D(mm^2/s)**	$1.25x10^{-7}$	$4.66x10^{-7}$	$2.20x10^{-6}$
	α	$2.19x10^{-7}$	$1.15x10^{-7}$	$1.61x10^{-7}$
	γ	$1.15x10^{-7}$	$1.52x10^{-8}$	$4.22x10^{-8}$

The values of probabilities of unbinding α for these two systems are larger than those of binding γ. The LMD model is used here in order to determine the diffusivity of nanocomposites at high environmental temperatures, and examine whether the values of probabilities of binding γ and unbinding α can describe water uptake behaviors upon adding high-absorption-capability unmodified clay and low-absorption-capability organoclay into the epoxy system.

The same approach, fitting Equation 6-26 to the experimental data, has been performed to obtain a Prony series representation and retardation times of time-varying diffusivity for epoxy resin systems. As an example, Figure 6-10 shows the variation of diffusivity with time in the DGEBA/BF_3.MEA system at different temperatures. The exponential decay in diffusivity with time from an initial value toward a final threshold value is analogous to the change of the viscoelastic relaxation modulus of a polymer, at 80°C; however, the diffusivities at 23°C and 50°C remain almost invariable. Therefore,

the DVTD model is used in systems containing rubber at high environmental temperature, in order to describe water uptake behavior.

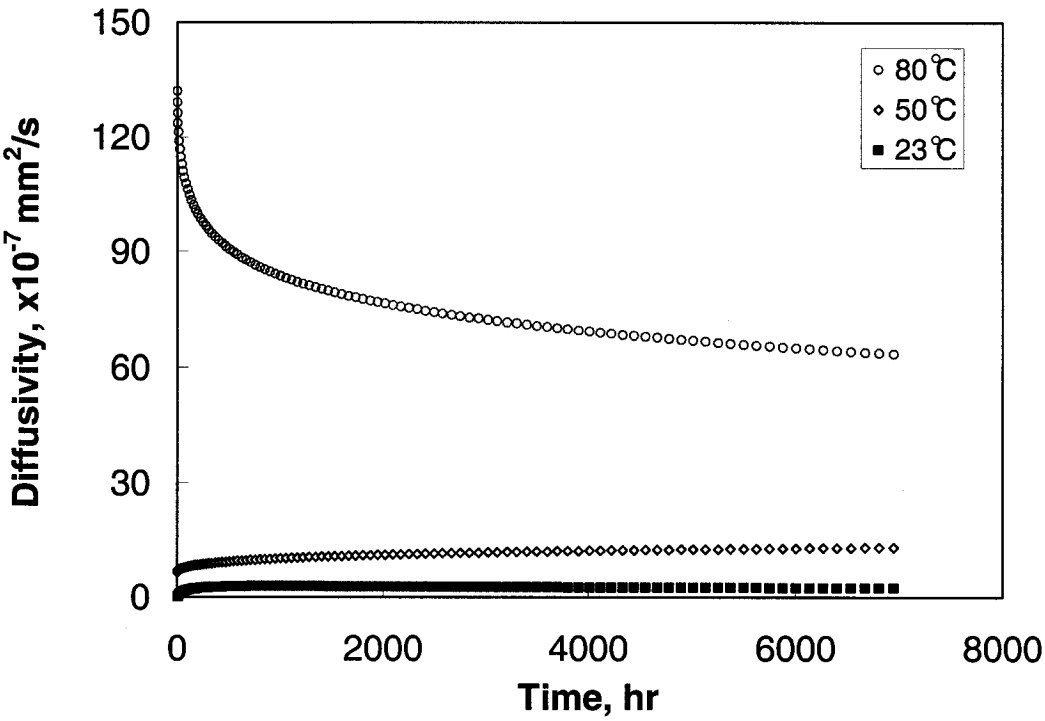

Figure 6-10: Diffusivity with time in DGEBA/BF_3.MEA system at different temperatures

For example, the LMD and DTVD numerical fits for two epoxy systems, DGEBA/BF_3.MEA and TGDDM/DDS at 80°C, are plotted in Figures 6-11 and 6-12, respectively. Clearly these anomalous diffusion models provide a better fit to the experimental data than the Fickian law, at higher environmental temperatures. Furthermore, the DTVD model has a better fit to the experimental data of systems containing rubber than the LMD.

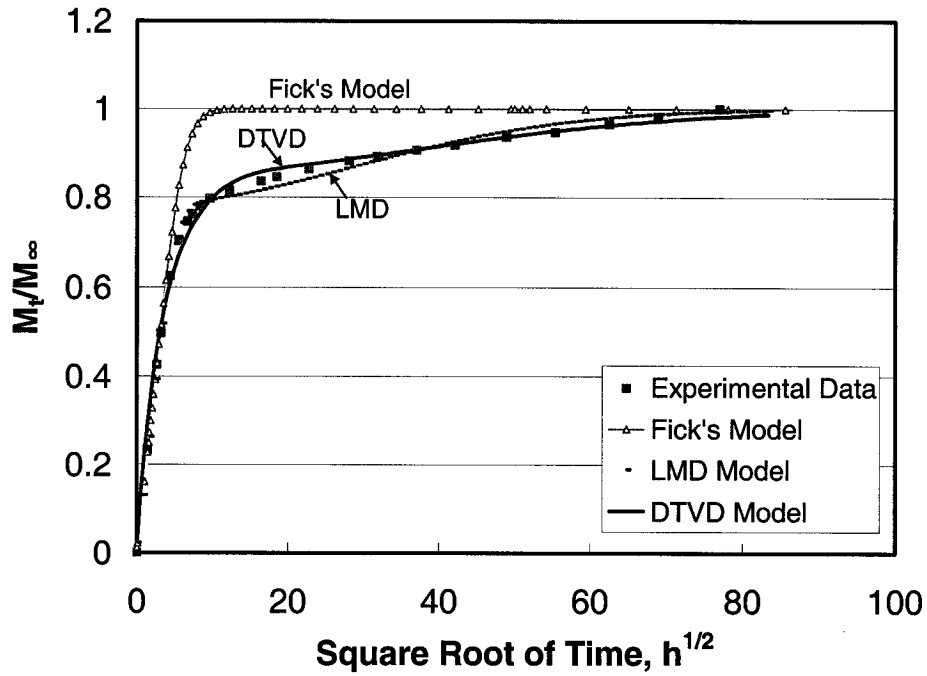

Figure 6-11: Different model profiles of DGEBA/BF_3.MEA system at 80°C

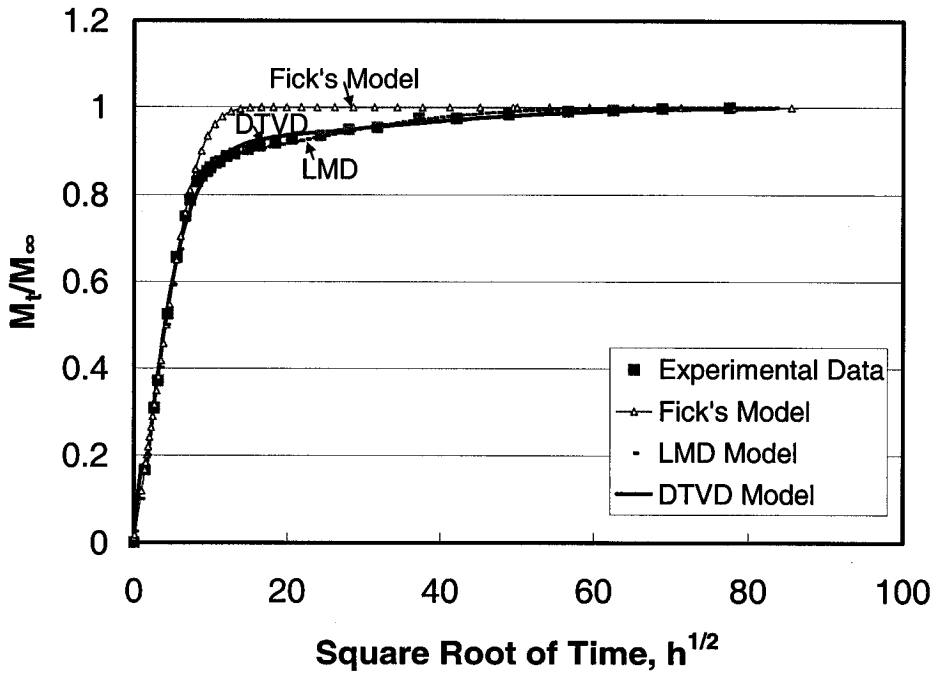

Figure 6-12: Different model profiles of TGDDM/DDS system at 80°C

6.4.3 Model Predictions

This section explains how aspect ratio, volume fraction and orientation of clay platelets influence the diffusivity of exfoliated and intercalated nanocomposites, and predicts the maximum improvements in diffusivity for these nanocomposites, based on the models proposed above.

6.4.3.1 Exfoliated Nanocomposites

Figure 6-13 shows the ratios of longitudinal diffusivity (D_{11}) of an exfoliated and ordered nanocomposite to pure resin (D_m) as a function of clay volume fraction, at different aspect ratios. In the direction parallel to the face of the clay platelets, clay platelets have an insignificant influence on the diffusivity of the nanocomposite, although the ratio (D_{11}/D_m) decreases slightly with both increasing volume fraction of clay and decreasing aspect ratio of clay platelets. For example, the ratio (D_{11}/D_m) decreases by only 0.2 % as 10 *vol %* clay is added into a polymer at low aspect ratio (50). Therefore, the longitudinal diffusivity (D_{11}) of the exfoliated and ordered nanocomposite depends largely on the resin matrix.

On the other hand, clay platelets have a great influence on the diffusivity of an exfoliated and ordered nanocomposite in the direction normal to the face of the clay platelets (D_{22}), as shown in Figure 6-14; transverse diffusivity declines rapidly with increasing clay content at low clay loading. As the volume content of clay reaches 2 %, the transverse diffusivity decreases by 96 % if the aspect ratio of clay platelets is 600;

after that, there is a small influence on transverse diffusivity from further increasing clay loading. The aspect ratio of the clay platelets is another important parameter for transverse diffusivity; the higher the aspect ratio, the greater the reduction of transverse diffusivity at the same clay loading. Therefore, transverse diffusivity in the exfoliated and ordered nanocomposites depends mainly on the volume fraction and aspect ratio of clay platelets.

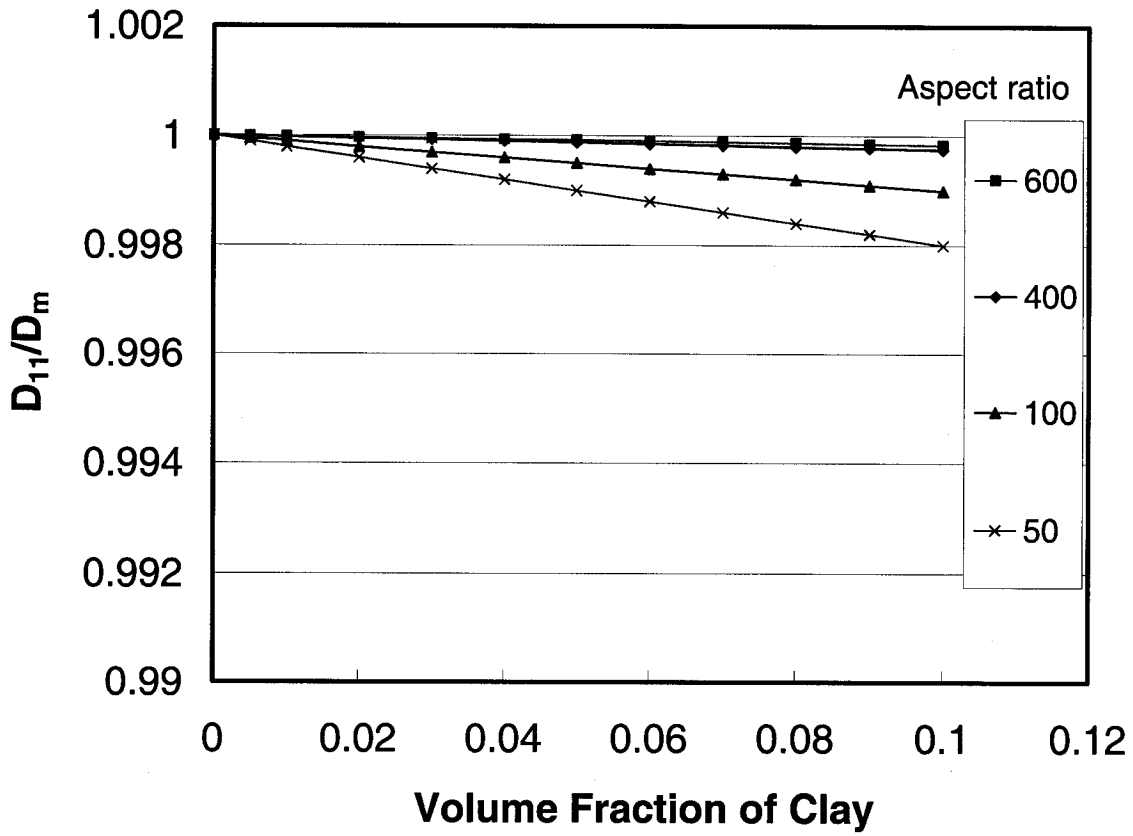

Figure 6-13: Ratio of longitudinal diffusivity (D_{11}) in an exfoliated and ordered nanocomposite to pure resin (D_m) *versus* volume fraction of clay, at different aspect ratios

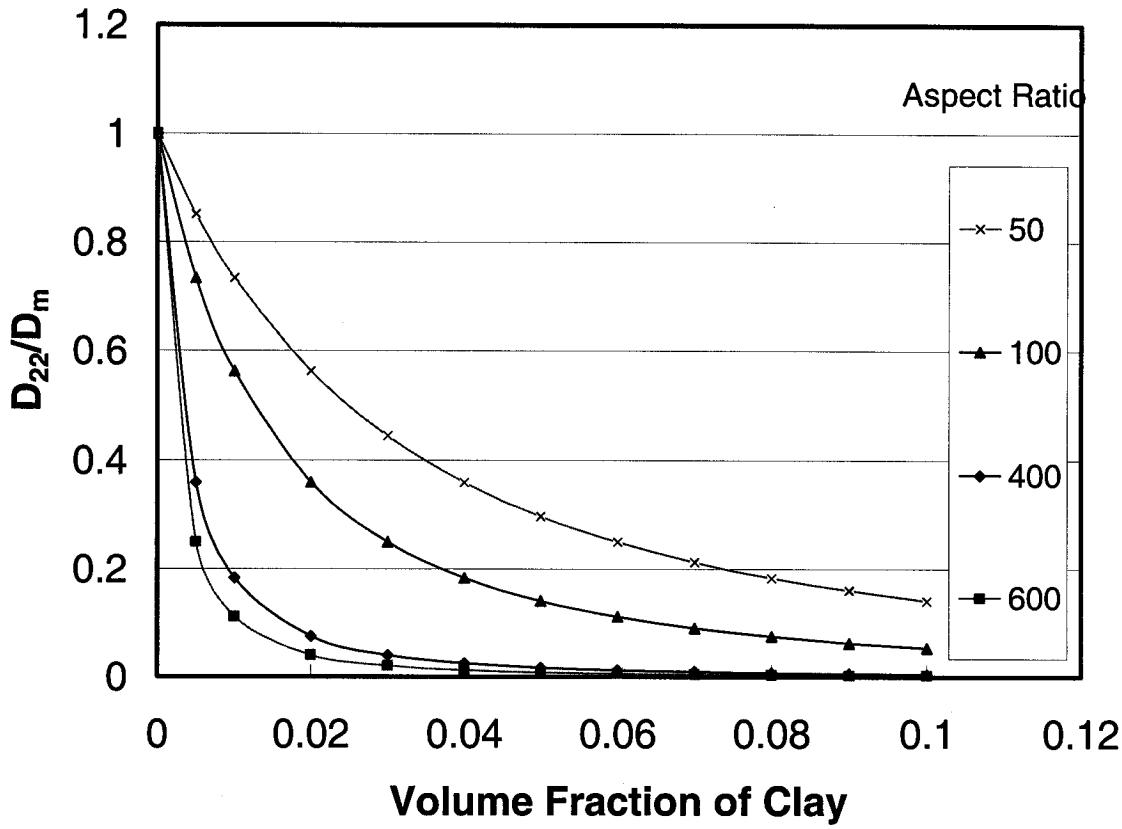

Figure 6-14: Ratio of transverse diffusivity (D_{22}) in an exfoliated and ordered nanocomposite to pure resin (D_m) *versus* volume fraction of clay, at different aspect ratios

In the case of completely random orientation in all three orthogonal directions, clay platelets also influence the diffusivity of an exfoliated nanocomposite, as shown in Figure 6-15. Diffusivity declines rapidly with increasing clay content at low clay loading; however, the reduction rate is smaller than that of the transverse diffusivity in the exfoliated and ordered nanocomposites. Similarly, at 2 % volume content of clay and high aspect ratio (600), diffusivity decreases by 92 %; after that, there is a small influence on diffusivity from further increasing clay loading.

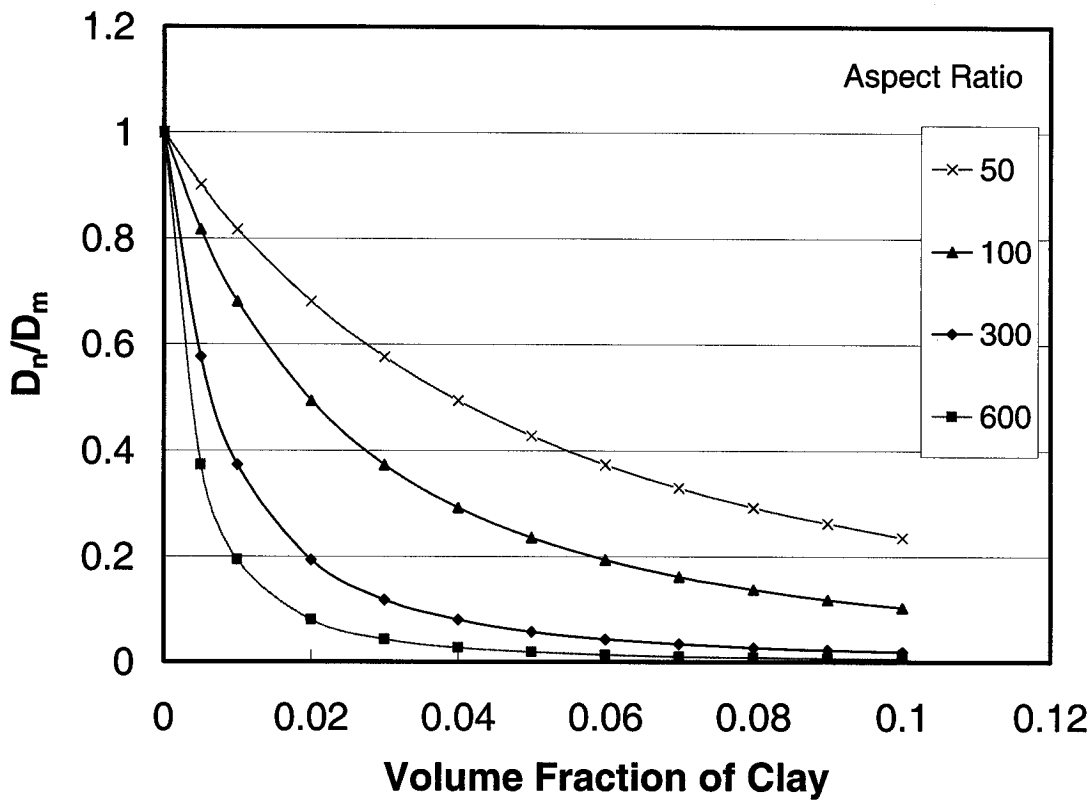

Figure 6-15: Ratio of diffusivity (D_n) in a randomly exfoliated nanocomposite to pure resin (D_m) *versus* volume fraction of clay, at different aspect ratios

6.4.3.2 Intercalated Nanocomposites

Clay platelets have the same effect on diffusion of water molecules in the direction parallel to the face of the clay platelets in an intercalated and ordered nanocomposite as in an exfoliated and ordered nanocomposite; as a result, the longitudinal diffusivity (D_{11}) of the intercalated and ordered nanocomposite is the same as that of an exfoliated and ordered nanocomposite.

On the other hand, the number of clay platelets in agglomerates has a great influence on the transverse diffusivity (D_{22}) of an intercalated and ordered nanocomposite, as shown in Figure 6-16. When the number of clay platelets (n) is equal to 1, this is the

exfoliated case; as the number increases, the reduction rate of the transverse diffusivity with clay content is rapidly reduced. Similarly, at 2 % volume content of clay and high aspect ratio (600), the transverse diffusivity decreases only by 49 % if the number of clay platelets is 10. Therefore, increasing the number of clay platelets in the agglomerates produces the same effect as decreasing the aspect ratio of clay platelets.

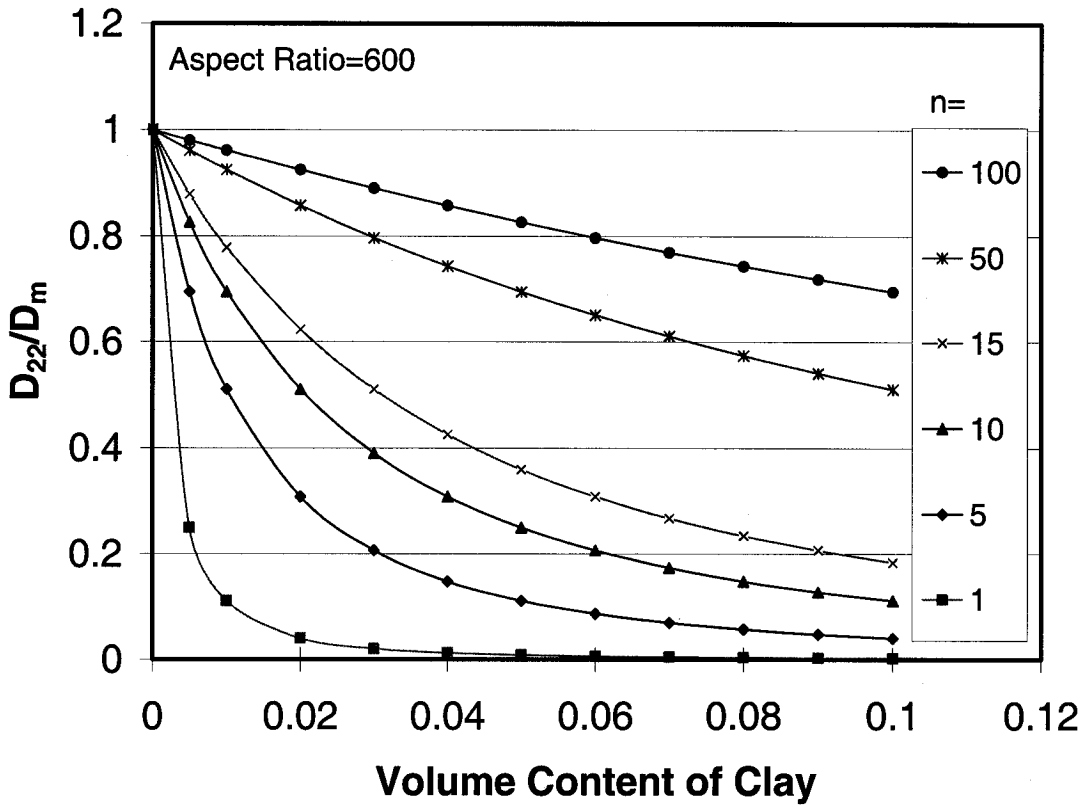

Figure 6-16: Ratio of transverse diffusivity (D_{22}) in an intercalated and ordered nanocomposite to pure resin (D_m) *versus* volume fraction of clay, at different numbers of clay platelets in agglomerates

Figure 6-17 shows the ratio of the diffusivity (D_n) in a random and intercalated nanocomposite to pure resin (D_m) as a function of clay volume fraction, at different numbers of clay platelets in agglomerates. Increasing the number of clay platelets in the

agglomerates can result in decreasing the reduction of the diffusivity with clay content. Similarly, at 2 % volume content of clay and high aspect ratio (600), diffusivity decreases only by 37 % if the number of clay platelets is 10. The reduction rate is smaller than that of the transverse diffusivity of the intercalated and ordered nanocomposite.

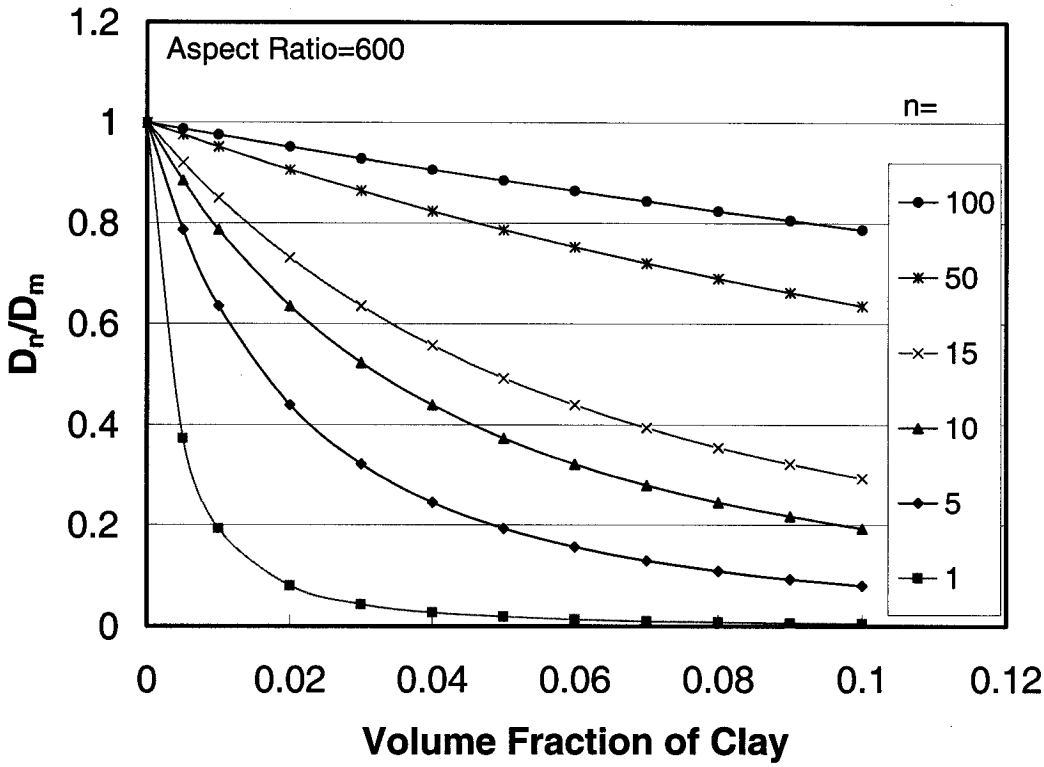

Figure 6-17: Ratio of diffusivity (D_n) in a randomly intercalated nanocomposite to pure resin (D_m) *versus* volume fraction of clay, at different numbers of clay platelets in agglomerates

6.4.4 Effect of Interface on Water Uptake of Composites

The effect of the interface between the clay surface and the epoxy resin on water uptake of composites was studied by adding unmodified (Na-clay) and modified clay

(I.30E organoclay) into the TGDDM/DDS epoxy system by the DM method. Water uptake behaviours of these materials were analyzed by Fick's Law and LMD.

The TGDDM/DDS epoxy resin system has a high equilibrium moisture content, which increases further upon adding Na-clay into this epoxy system. As an example, Figure 6-18 shows water uptake profiles of filler composites at 23°C. These filler composites also follow the Fickian numerical fit very closely at 23°C, but at higher environmental temperatures, all curves do not completely obey this law. The equilibrium moisture contents were measured, and the diffusivities (***D***) of the filler composites at different temperatures were calculated using Equation 6-8 (Fickian law).

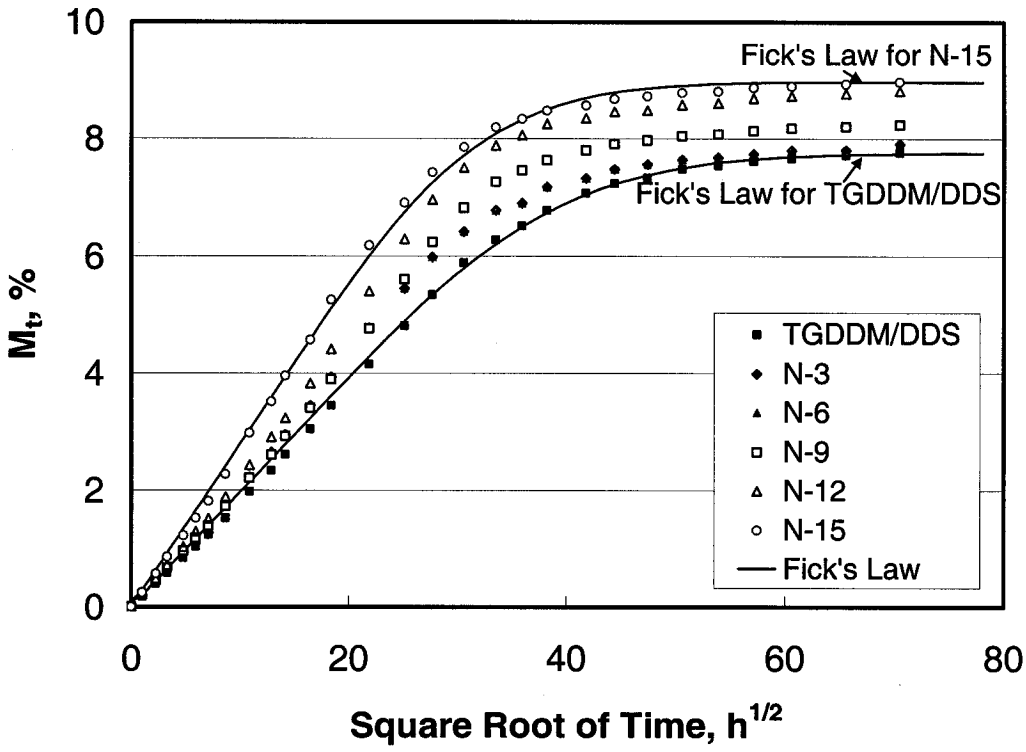

Figure 6-18: Water absorption profiles of filler composites at 23°C

Figures 6-19 and 6-20 show the ratio of diffusivities (D_c) in filler composites to pure resin (D_m), and the equilibrium moisture content ($M_{c\infty}$) of filler composites with clay loadings, at different temperatures. Clearly both the ratio (D_c/D_m) and the equilibrium moisture content increase with clay loading. As clay loading reaches 15-phr, diffusivity and equilibrium moisture content increase by 48% and 18%, respectively, indicating that adding high absorption-capability clay into the epoxy matrix enhances the water uptake behavior of the epoxy. Environmental temperature seems not to influence the ratio (D_c/D_m) or the equilibrium moisture contents.

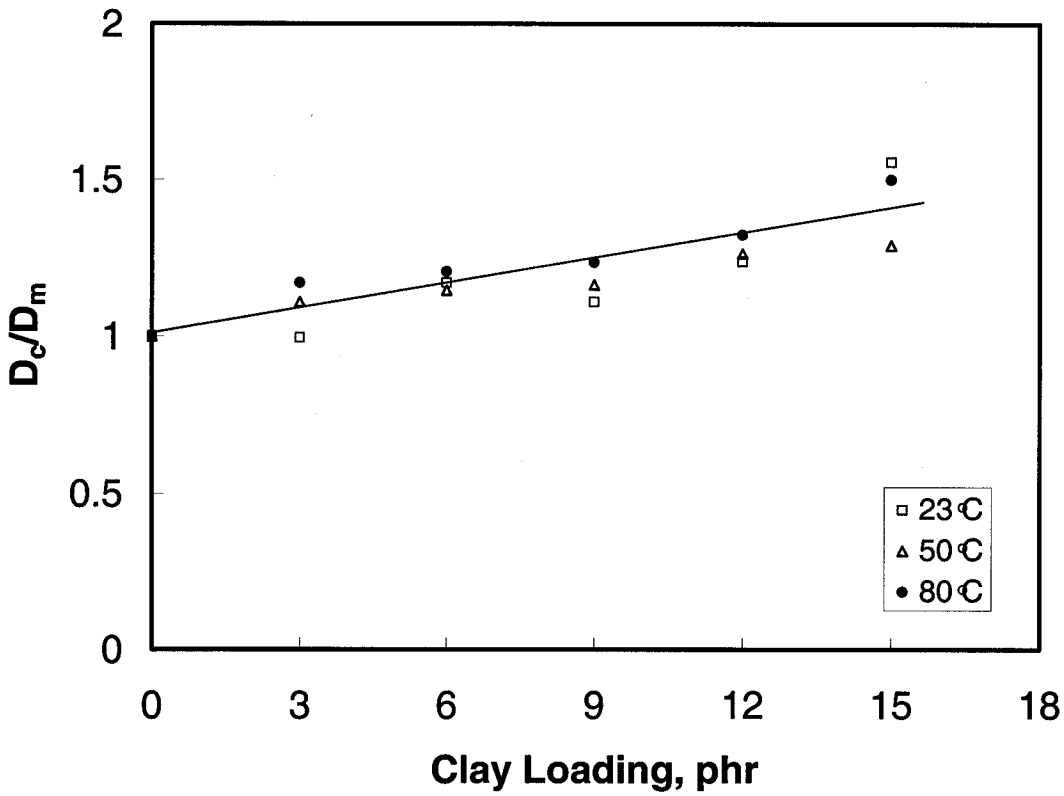

Figure 6-19: Ratio of diffusivity (D_c) in filler composites to pure resin (D_m), with clay loading with Fickian law

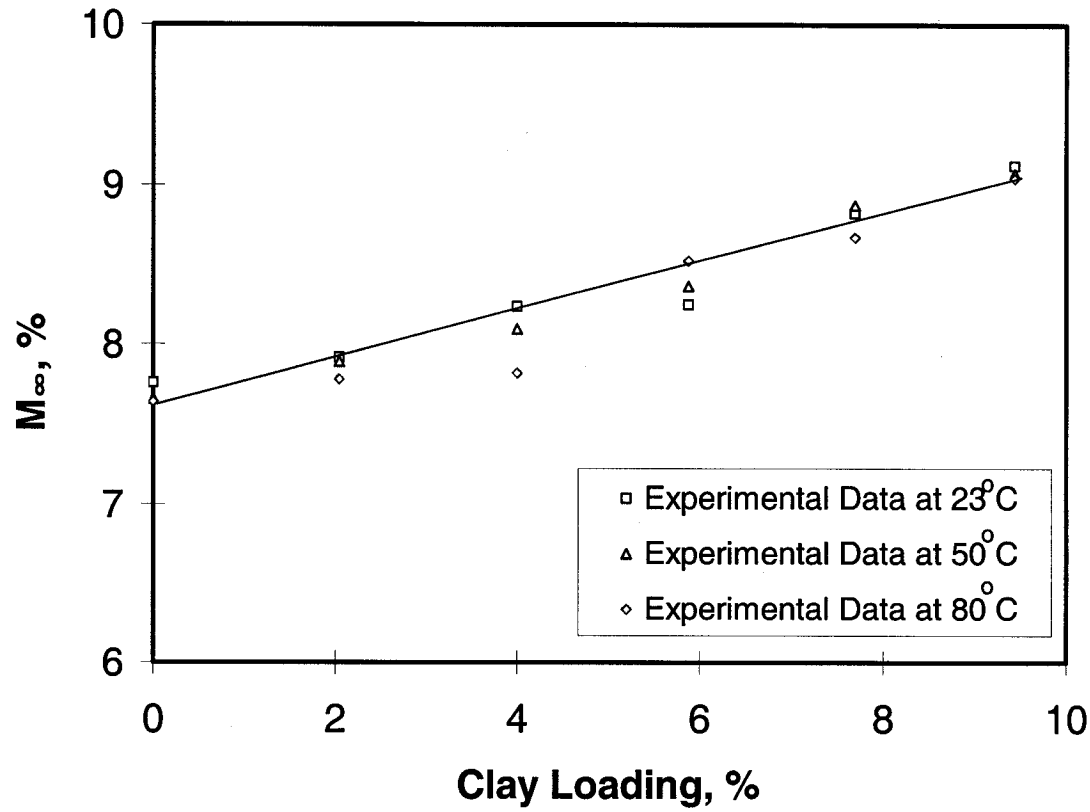

Figure 6-20: Equilibrium moisture content ($M_{c\infty}$) of filler composites with clay loading

On the other hand, the equilibrium moisture content and diffusivity decrease by adding I.30E organoclay into the TGDDM/DDS epoxy system by the DM method. As an example, Figure 6-21 shows water uptake profiles of nanocomposites made by the DM method at 23°C. These nanocomposites appear to follow the Fickian numerical fit very closely at 23°C, but they do not completely follow Fickian numerical fits at 50°C or 80°C, where a two-stage diffusion process is observed. Therefore, adding unmodified clay or organoclay into the TGDDM/DDS system does not greatly change the form of water uptake curves of this matrix.

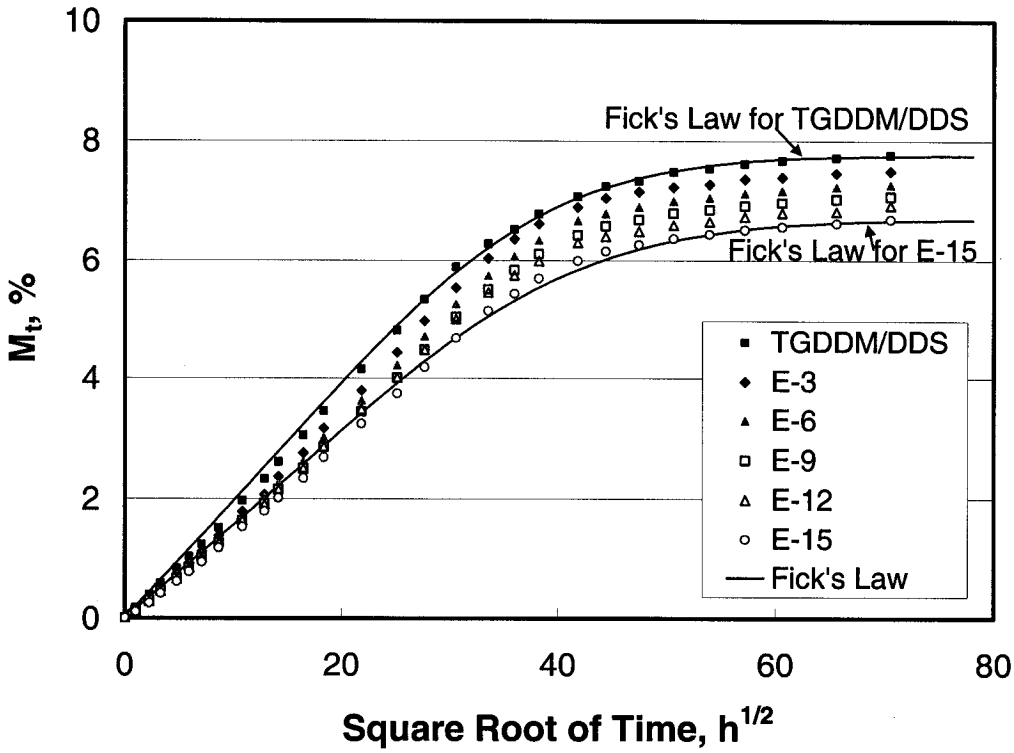

Figure 6-21: Water absorption profiles of nanocomposites made by the DM method at 23°C

Equilibrium moisture contents were measured, and diffusivities (D) of nanocomposites at different temperatures were calculated using Equation 6-8 from Fickian law. The equilibrium moisture content (M_∞) of the nanocomposites, and the ratio of diffusivities (D_n) in the nanocomposites to pure resin (D_m) with clay loadings at different temperatures, are shown in Figures 6-22 and 6-23, respectively.

Contrary to filler composites, nanocomposites reduce both diffusivity (D_n) and equilibrium moisture content (M_∞) with increasing clay loading; as clay loading reaches 15-phr, diffusivity and equilibrium moisture content decrease by 12.9% and 12.3%, respectively, indicating that adding organoclays into the epoxy matrix improves the water uptake resistance properties of the epoxy. Environmental temperature does not

influence greatly equilibrium moisture content with clay loading, but the reduction rate of ratio (D_n/D_m) at 80°C is smaller than at 23°C or 50°C.

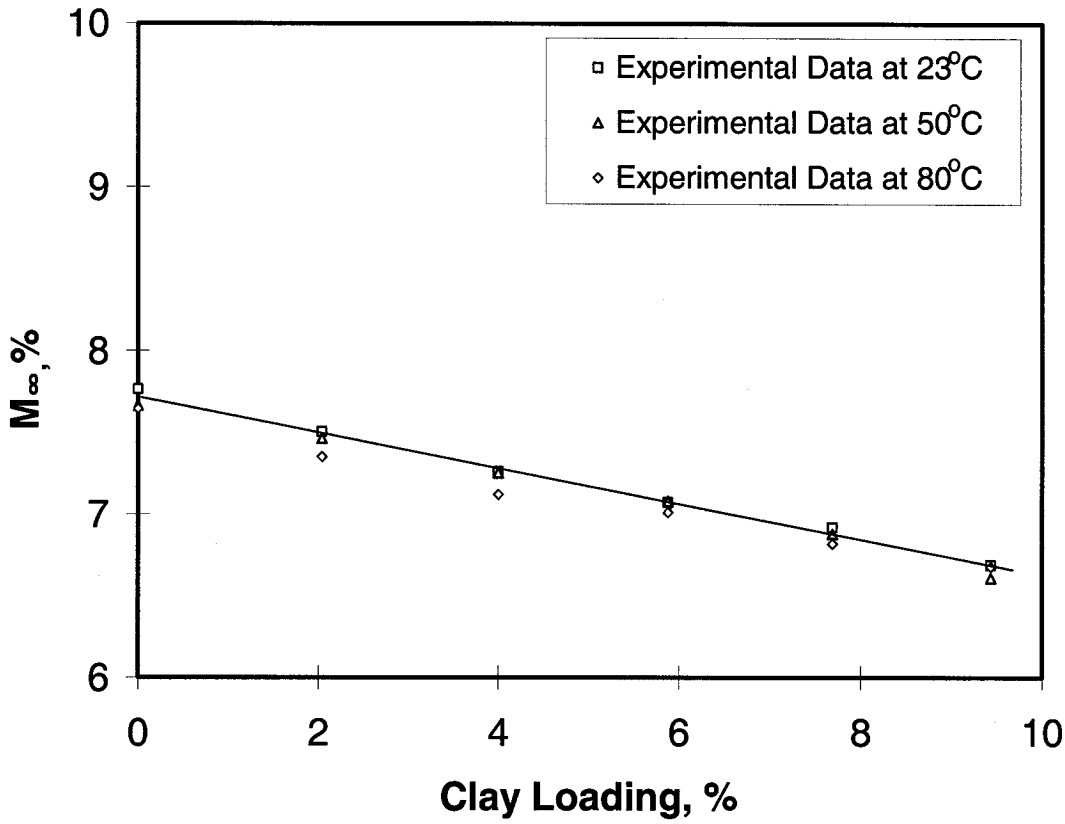

Figure 6-22: The equilibrium moisture content (M_∞) of nanocomposites made by DM method, as a function of clay loading

Because unmodified clay is hydrophilic, clay particles can absorb and bind more water molecules than can epoxy resin; however, organoclay particles have contrary absorption behaviors. The Langmuir Model of Diffusion (LMD) was applied to examine these different materials. The diffusivity (D) and values of probabilities of binding γ and unbinding α were obtained by fitting Equation 6-15 to the experimental data employing a least-square approach, listed in Table 6-4 for filler composites and Table 6-5 for nanocomposites, respectively.

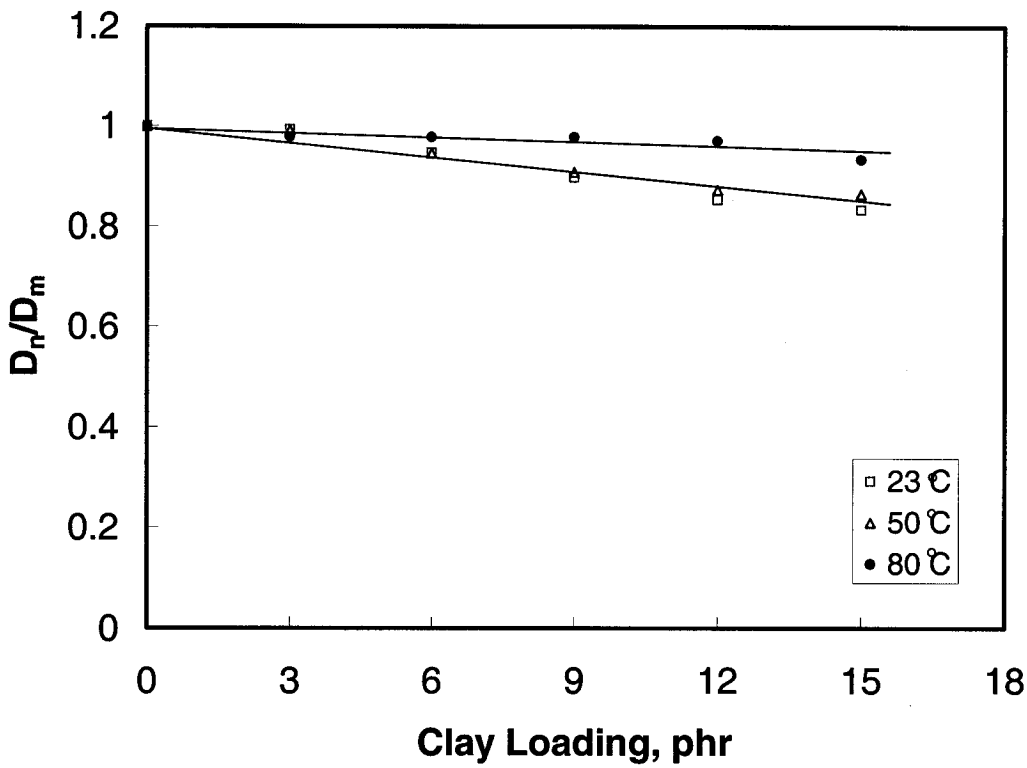

Figure 6-23: Ratio of diffusivity (D_n) in nanocomposites made by the DM method to pure resin (D_m), as a function of clay loading, by the Fickian law

The diffusivities obtained by LMD for all materials are higher than those from the Fickian law, due to the probabilities of binding and unbinding. However, the ratios of diffusivities (D) of the materials to pure resin (D_m) by the LMD method for filler composites and nanocomposites are very close to those with Fickian law at 23°C, as shown in Figures 6-24 and 6-25. At higher temperature, such as 80°C, they appear to be smaller than those from the Fickian law; this may be attributed to the fact that there is a big difference between Fickian numerical fit and experimental data at 80°C; therefore, the parameters obtained by LMD may approach more closely the measured values than those from the Fickian law at high temperatures.

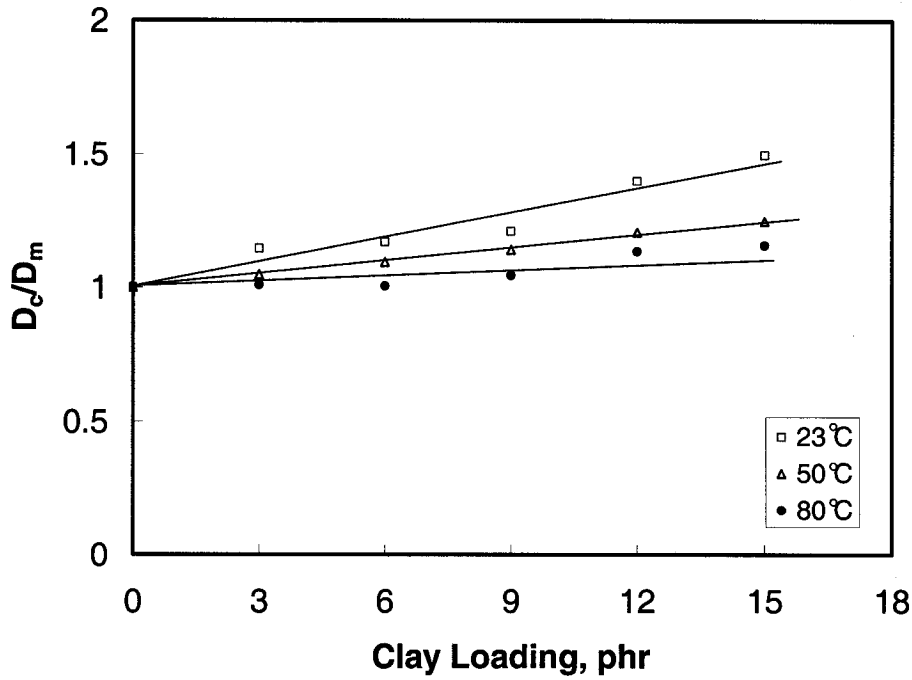

Figure 6-24: Ratio of diffusivity (D_c) in filler composites to pure resin (D_m) with clay loading with LMD model

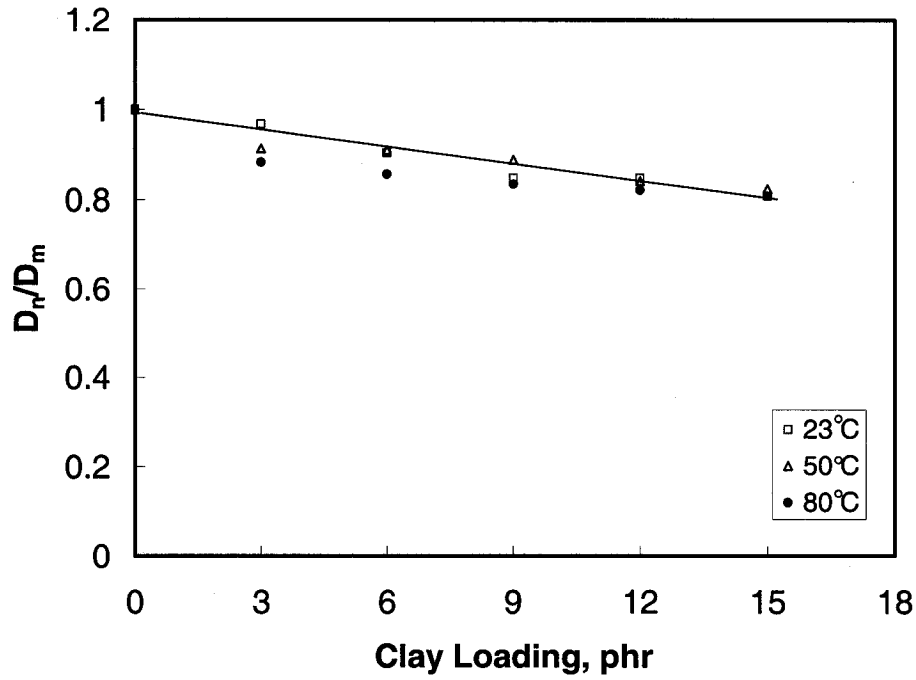

Figure 6-25: Ratio of diffusivity (D_n) in nanocomposites made by the DM method to pure resin (D_m), as a function of clay loading, by the LMD model

Table 6-4: Water uptake parameters obtained by LMD for filler composites

Clay Loading phr	23 °C			50 °C			80 °C		
	D, ($x10^{-8}$) mm^2/s	α ($x10^{-7}$)	γ ($x10^{-8}$)	D, ($x10^{-7}$) mm^2/s	α ($x10^{-7}$)	γ $x10^{-8}$	D, ($x10^{-6}$) mm^2/s	α $x10^{-7}$	γ $x10^{-8}$
0	12.5	2.19	11.5	4.66	1.15	1.52	2.24	2.94	4.24
3	14.3	2.43	14.7	4.88	1.04	1.25	2.26	4.28	6.08
6	14.6	2.56	15.7	5.10	1.06	1.25	2.25	4.88	6.19
9	15.1	2.95	20.2	5.31	1.10	1.39	2.34	4.88	6.28
12	17.5	3.12	24.2	5.62	1.05	1.25	2.54	4.78	5.80
15	18.7	3.65	25.0	5.81	1.04	1.26	2.59	3.39	4.80

Table 6-5: Water uptake parameters obtained by LMD for nanocomposites made by the DM method

Clay Loading phr	23 °C			50 °C			80 °C		
	D, ($x10^{-8}$) mm^2/s	α ($x10^{-7}$)	γ ($x10^{-8}$)	D, ($x10^{-7}$) mm^2/s	α ($x10^{-7}$)	γ $x10^{-8}$	D, ($x10^{-6}$) mm^2/s	α ($x10^{-7}$)	γ ($x10^{-8}$)
0	12.5	2.19	11.5	4.66	1.15	1.52	2.24	2.94	4.24
3	12.1	2.45	16.7	4.26	1.07	1.32	1.98	3.47	4.26
6	11.3	2.29	13.7	4.24	1.23	1.55	1.92	3.54	4.12
9	10.6	2.28	14.1	4.14	1.26	1.73	1.87	3.59	4.14
12	10.6	2.31	14.5	3.92	1.29	1.79	1.84	3.8	5.01
15	10.1	2.14	13.6	3.84	1.31	1.87	1.81	4.86	5.29

Comparing Table 6-4 with Table 6-5, no difference is found in the values of probabilities of binding γ and unbinding α between filler composites and nanocomposites, by the DM method. The ratio ($\alpha/\alpha+\gamma$) plotted with clay loading is shown in Figure 6-26. It is clear that TGDDM/DDS has a lower unbinding ratio at 23°C, indicating that more water molecules are bound to polar groups of this epoxy at lower environmental temperature. The unbinding ratio decreases slightly with increasing clay loading, in both unmodified clay and organoclay, at this temperature. As the environmental temperature rises, water molecules become more active, and thus the unbinding ratio increases; there is no obvious effect on the unbinding rate with increasing clay loading at high temperature. Therefore, probabilities of binding and unbinding of water molecules mainly depend on the epoxy matrix.

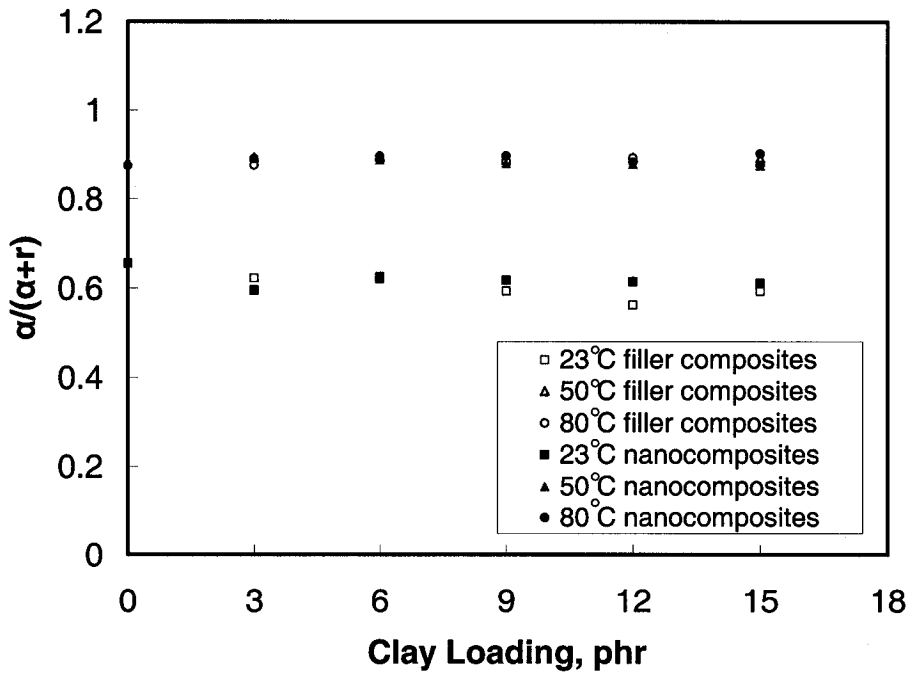

Figure 6-26: Ratio ($\alpha/\alpha+\gamma$) *versus* clay loading, for filler composites and nanocomposites made by the DM method

6.4.5 Water Uptake of Nanocomposites with Different Methods

As discussed in previous chapters, nanocomposites made with different dispersion methods have different structures. The previous section discusses water uptake of nanocomposites made by the DM method; this section presents experimental data for nanocomposites made by the HPM and GMM methods, and discusses the effect of different synthesis methods on water uptake of nanocomposites.

6.4.5.1 Water Uptake of Nanocomposites made by the HPM method

There are two routes to disperse I.30E organoclay into a TGDDM/DDS system by the HPM method: HPM-E and HPM-A, described in Chapter 3. For example, water uptake profiles of nanocomposites made by HPM-E and HPM-A methods at 23°C are shown in Figures 6-27 and 6-28, respectively. These nanocomposites appear to follow the Fickian numerical fit very closely at 23°C, but not completely at either 50°C or 80°C, where a two-stage diffusion process is observed. From Figures 6-27 and 6-28, it is clear that water uptake in HPM-A and HPM-E nanocomposites is still increasing after immersion in water for 5000 hours, although the pure resin system reaches equilibrium. Therefore, the moisture content of these nanocomposites at 5000 hours is not the equilibrium moisture content. Maximum water uptakes at 5000 hours were measured, and diffusivities (D) in HPM-E and HPM-A nanocomposites at different temperatures were calculated using Equation 6.8 (Fickian law).

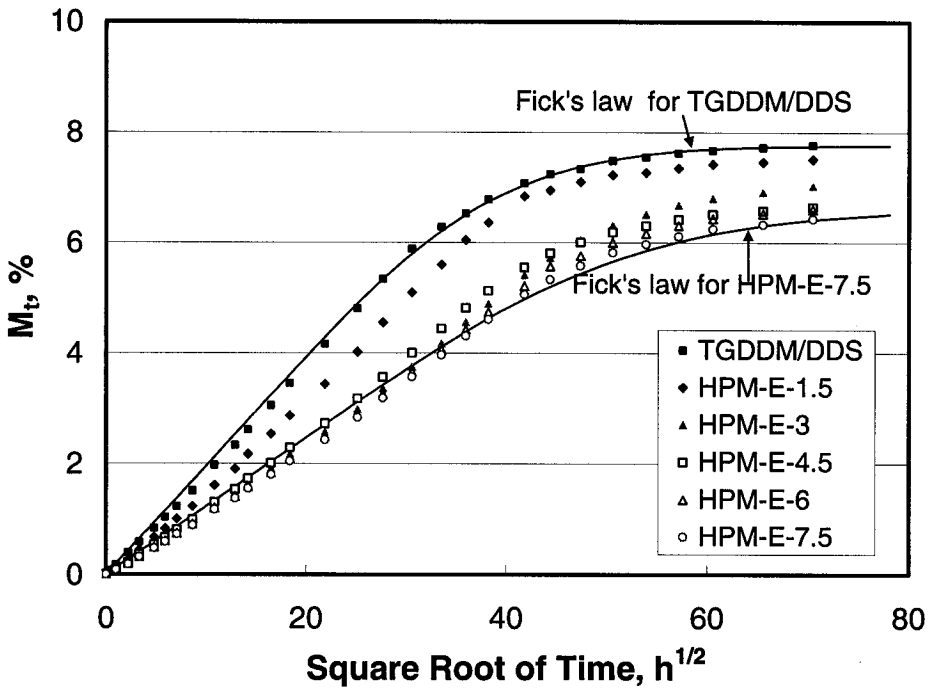

Figure 6-27: Water absorption profiles of HPM-E nanocomposites at 23°C

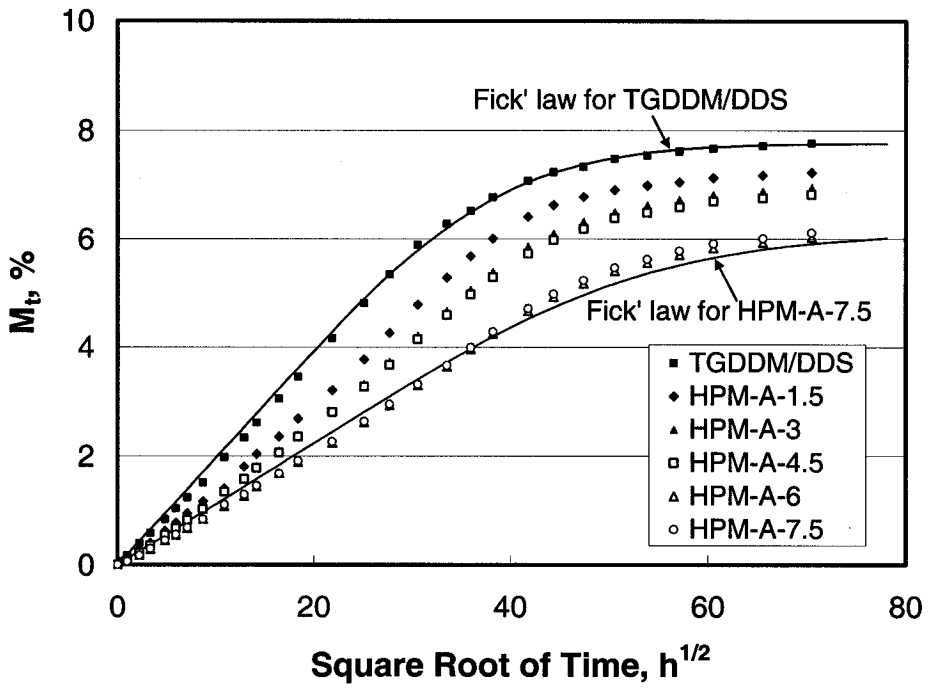

Figure 6-28: Water absorption profiles of HPM-A nanocomposites at 23°C

Figures 7-29 and 6-30 show that the ratio of maximum water uptakes of both HPM-E and HPM-A nanocomposites (M_{nm}) to pure resin ($M_{r\infty}$) decrease with increasing clay loading at all three environmental temperatures, because I.30E organoclay has lower maximum water absorption (about 2.5 wt%) than the TGDDM/DDS resin system (about 7.6 wt%).

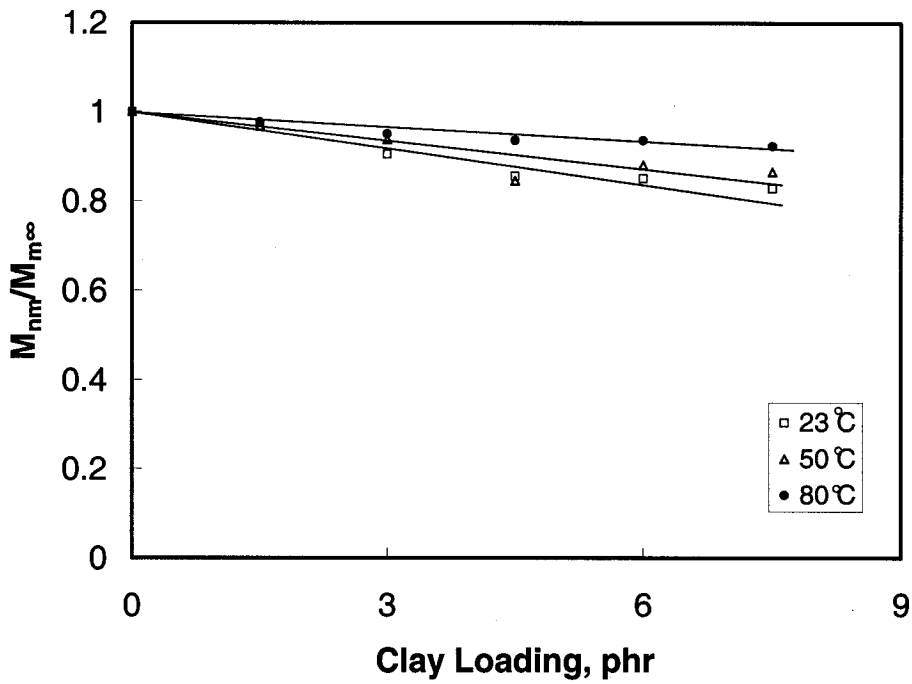

Figure 6-29: Ratio of maximum water uptake (M_{nm}) of HPM-E nanocomposites to pure resin ($M_{m\infty}$) *versus* clay loading, at different temperatures

HPM-A and HPM-E nanocomposites have almost the same maximum water absorption, lower than those of nanocomposites made by DM, but this difference decreases with increasing environmental temperature. This may be attributed to a tortuosity effect; that is, the impermeable clay platelets mandate a tortuous pathway for water to enter the nanocomposites; at lower environmental temperatures, the nanocomposites do not reach full saturation due to this effect. As a result,

nanocomposites have low values of maximum water absorption. Moreover, the value decreases further as tortuosity is enhanced by improving the dispersion of organoclay in the epoxy resin system. At higher environmental temperatures, all materials have higher diffusion coefficients than at lower temperature; therefore, nanocomposites at higher environmental temperature are nearer full saturation than at lower environmental temperature, for the same duration of immersion.

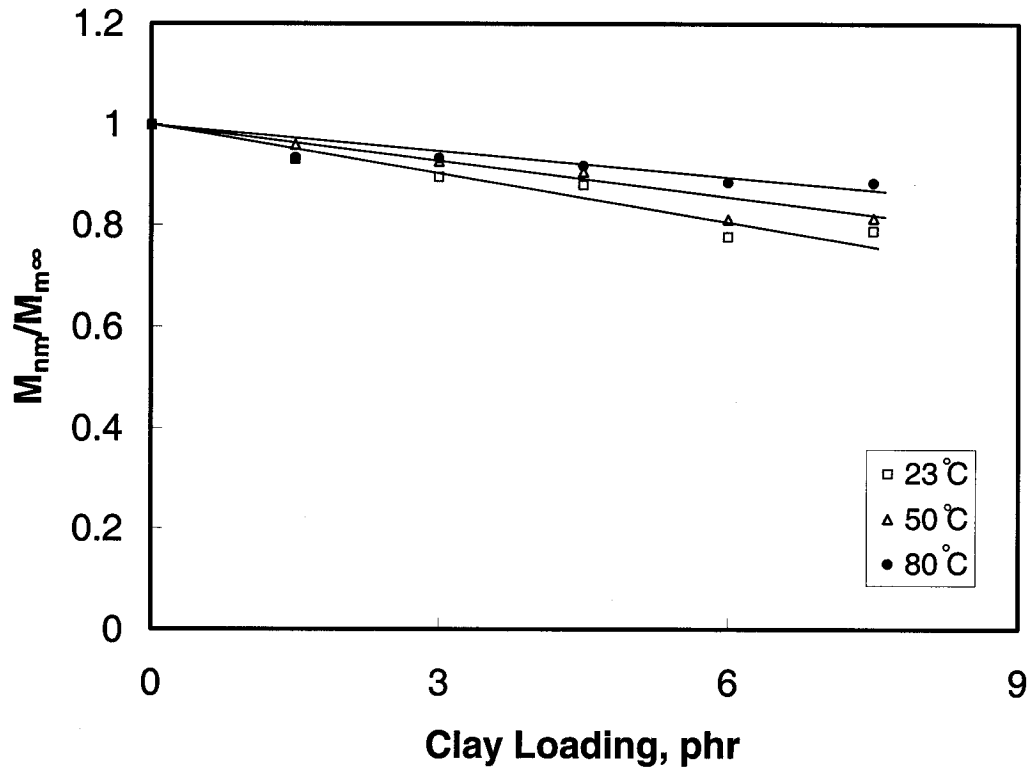

Figure 6-30: Ratio of maximum water uptake (M_{nm}) of HPM-A nanocomposites to pure resin ($M_{m\infty}$) *versus* clay loading, at different temperatures

The ratios of diffusivity in nanocomposites (D_n) to pure resin (D_r) at different temperatures also decrease with increasing clay loading, as seen in Figures 6-31 and 6-32; these diffusivities were obtained using Fickian law. HPM-A and HPM-E

nanocomposites have almost the same efficiency in decreasing diffusivity, higher than DM nanocomposites. Environmental temperature has little influence on diffusivity in HPM nanocomposites, attributed to the tortuosity effect. Therefore, according to these experimental and analytical results, nanocomposites made by HPM-A or HPM-E have almost the same water uptake behavior.

Curves based on the proposed Diffusivity Model for Intercalated Nanocomposites (DMIN) are also plotted in Figures 6-31 and 6-32. Most experimental data fall between the model prediction curves, for numbers of clay platelets in agglomerates of 12 or 20; the numbers are slightly larger than observed by TEM.

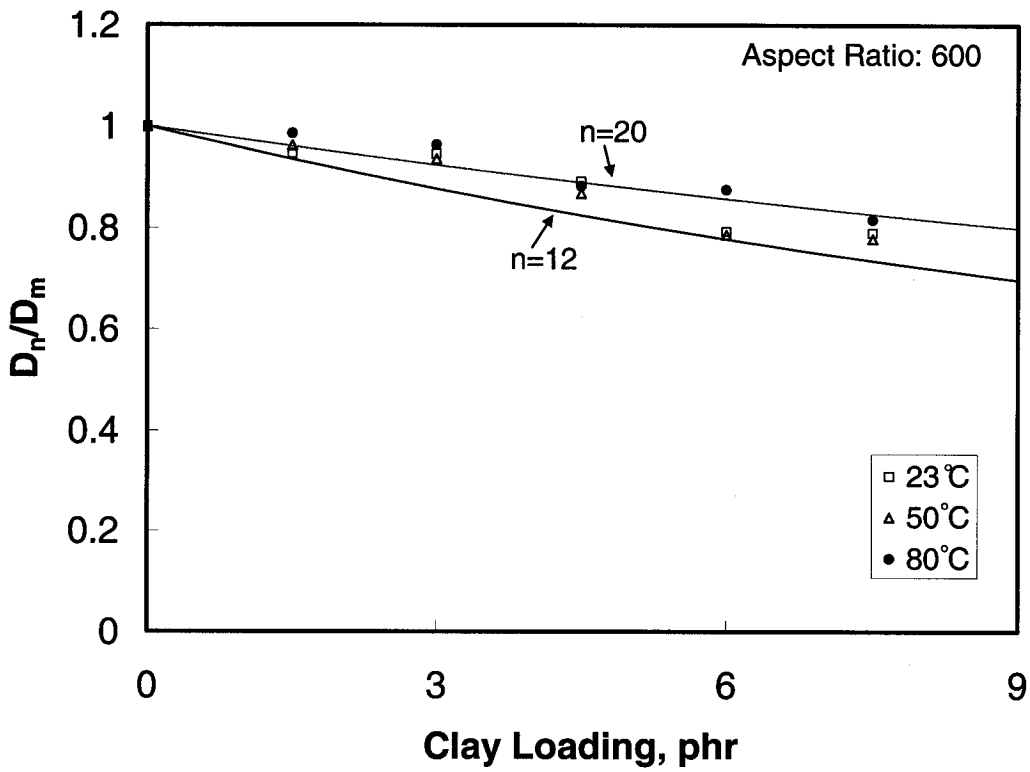

Figure 6-31: Ratio of diffusivity (D_n) obtained by Fickian law for HPM-E nanocomposites to pure resin (D_m) *versus* clay loading, at different temperatures

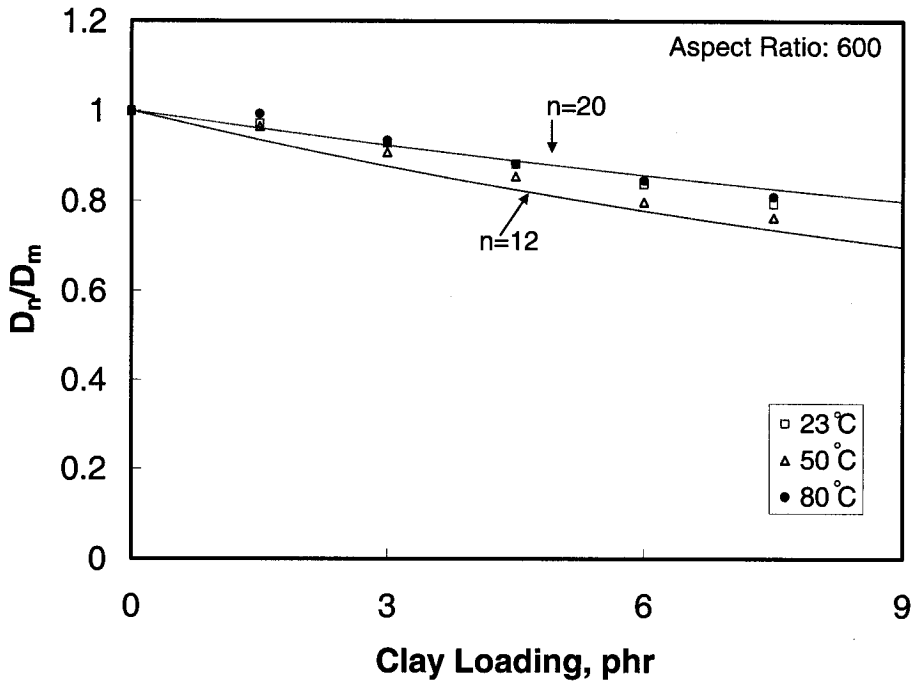

Figure 6-32: Ratio of diffusivity (D_n) obtained by Fickian law for HPM-A nanocomposites to pure resin (D_m) *versus* clay loading, at different temperatures

Because HPM-E and HPM-A nanocomposites do not reach full saturation at 5,000 hours, the maximum water uptakes of these nanocomposites at 5,000 hours are smaller than their equilibrium moisture contents. Using these values of maximum water uptake in Equation 6-8 to calculate diffusivities results in calculated diffusivities larger than the actual values. Moreover, the non-saturation extent increases with clay loading; as a result, the difference between calculated and factual values grows with increasing clay loading.

However, the LMD method can avoid this error; diffusivities of HPM-A nanocomposites obtained by the LMD method are shown in Figure 6-33. The data fall between the model prediction curves for 6 or 10 clay platelets in agglomerates; this result agrees with those observed by TEM.

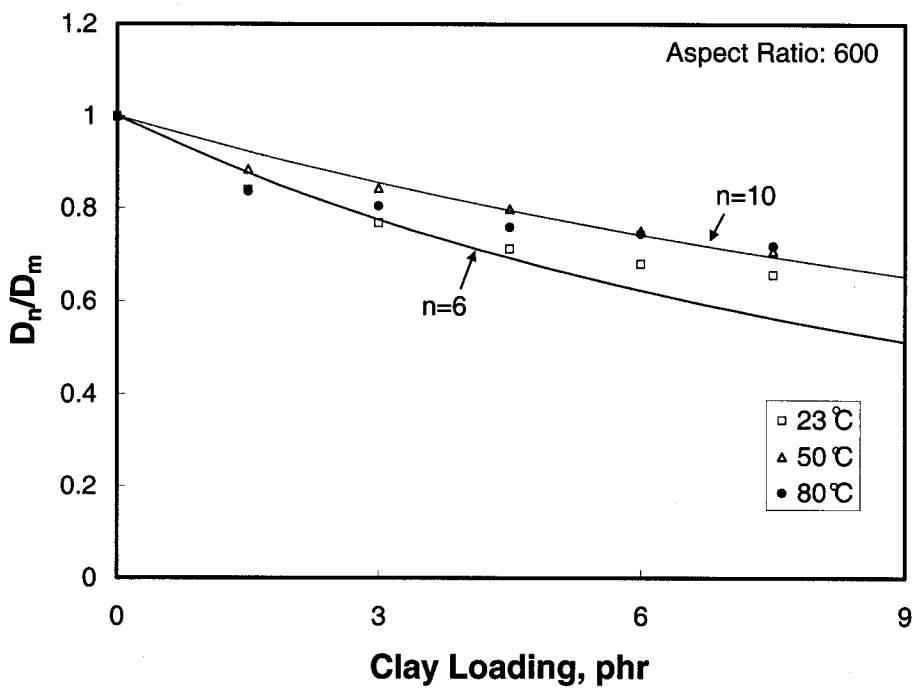

Figure 6-33: Ratio of diffusivity (D_n) obtained by LMD for HPM-A nanocomposite to pure resin (D_m) *versus* clay loading, at different temperatures

6.4.5.2 Water Uptake of Nanocomposites made by the GMM Method

After 6-phr I.30E organoclay was dispersed into a TGDDM/DDS system using the GMM method with different grinding times, nanocomposites were synthesized. These nanocomposites have similar water uptake behaviour to those made by the DM and HPM methods: They appear to follow the Fickian numerical fit very closely at 23°C, but not completely at 50°C or 80°C, where a two-stage diffusion process is observed.

Figures 6-34 and 6-35 show maximum water uptakes and diffusivities of GMM nanocomposites with different grinding times at 6-phr clay loading at 23°C; the diffusivities were obtained by the LMD method. In order to compare the effect of

different methods, data from nanocomposites made by DM and HPM methods at the same clay loading are also given in these figures.

The experimental results show that grinding time has an insignificant influence on water uptake behavior of GMM nanocomposites; they have almost the same maximum water uptake and diffusivity, lower than DM nanocomposites but larger than HPM nanocomposites. This may be attributed to a tortuosity effect; that is, the impermeable clay platelets mandate a tortuous pathway for water to enter the nanocomposites. GMM nanocomposites have better dispersion of clay platelets in epoxy than DM; therefore, they have higher tortuosity efficiency. On the other hand, HPM nanocomposites have the best dispersion, and thus the highest tortuosity efficiency.

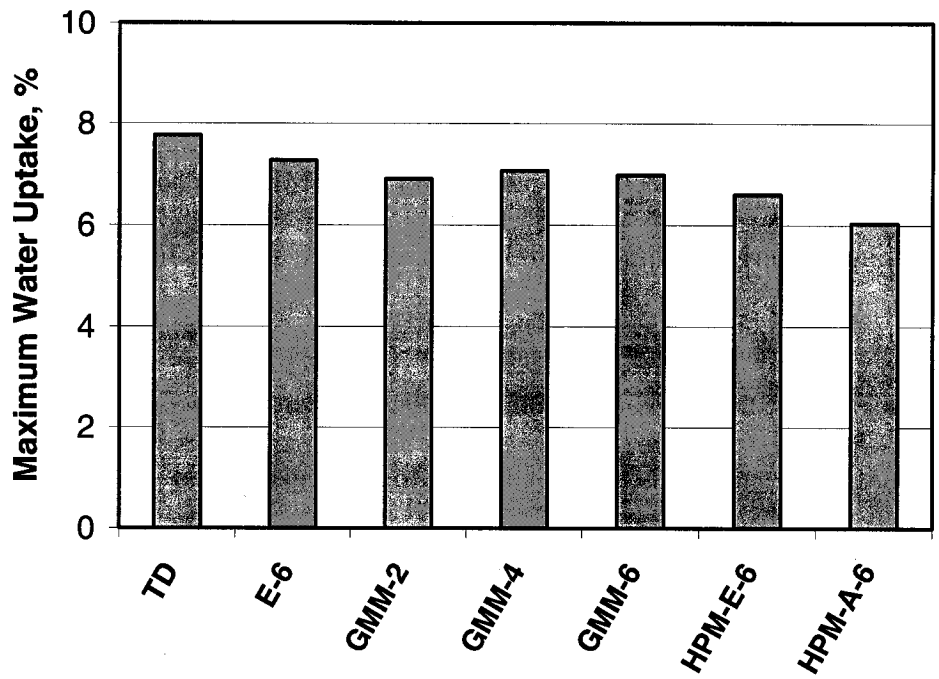

Figure 6-34: Maximum water uptakes of TGDDM/DDS and its nanocomposites made with different dispersion methods, at 6-phr clay loading for 5000 hours at 23°C

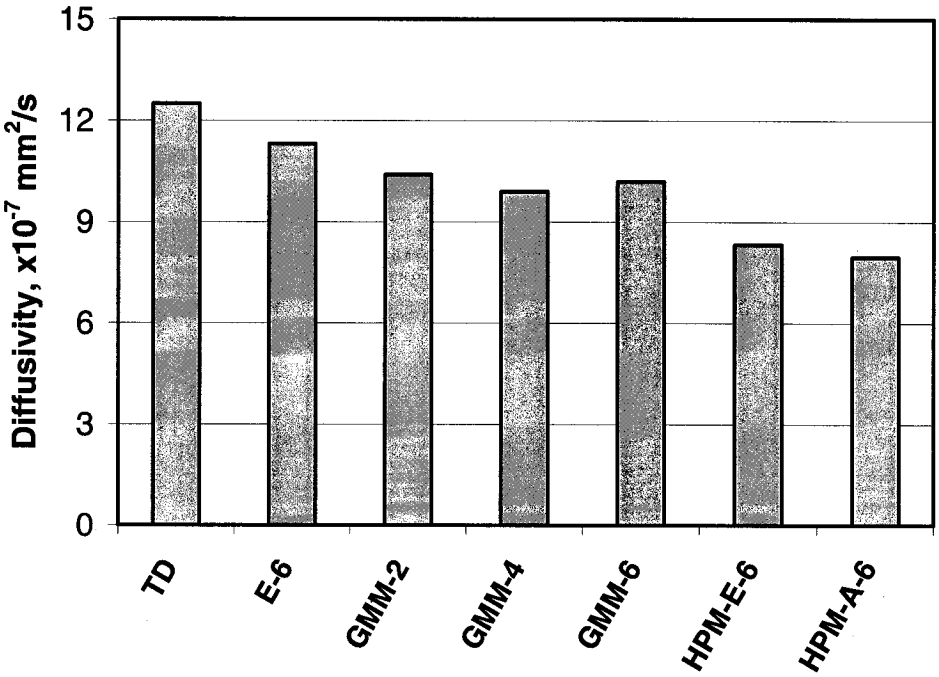

Figure 6-35: Diffusivities of TGDDM/DDS and its nanocomposites made with different dispersion methods, at 6-phr clay loading at 23°C

6.4.6 Water Uptake of Nanocomposites with Different Organoclays

Water uptake behaviour of nanocomposites made of I.30E organoclay is analyzed in previous sections. In this section, nanocomposites made of 30B organoclay and the TGDDM/DDS system are discussed, in order to understand the effect of different organoclays on water uptake of nanocomposites.

30B nanocomposites have similar water uptake behaviour to I.30E nanocomposites, whether 30B organoclay is dispersed in epoxy by the DM or HPM method: The nanocomposites follow the Fickian Law at 23°C, but not completely at 50°C or 80°C, where a two-stage diffusion process is observed.

Figures 6-36 and 3-37 show maximum water uptakes and diffusivities in 30B nanocomposites made by the DM method at 3-phr and 6-phr clay loadings at 23°C, respectively; the diffusivities were obtained by the LMD method. In order to compare the effect of different organoclays, those of I.30E nanocomposites at the same clay loadings are also given in these figures.

Like I.30E organoclay, 30B organoclay reduces both maximum water uptake and diffusivity of the TGDDM/DDS system with increasing clay loading. Moreover, at the same clay loading, 30B nanocomposites have lower maximum water uptake and diffusivity than I.30E nanocomposites, although 30B organoclay contains hydroxyl groups in its surface modifier; this may be because 30B nanocomposites have better dispersion of clay platelets in epoxy than I.30E nanocomposites made by the DM method. The morphologies of I.30E and 30B organoclays in DM nanocomposite were observed and introduced in Chapter 4.

On the other hand, when the nanocomposites were made by the HPM method, both I.30E and 30B nanocomposites have almost same dispersion quality of clay platelets in the epoxy. However, experimental results show that the maximum water uptake and diffusivity of 30B nanocomposites are slightly higher than those of I.30E nanocomposites, as shown in Figures 6-38 and 6-39, respectively; this may be because I.30E organoclay has a higher aspect ratio than 30B.

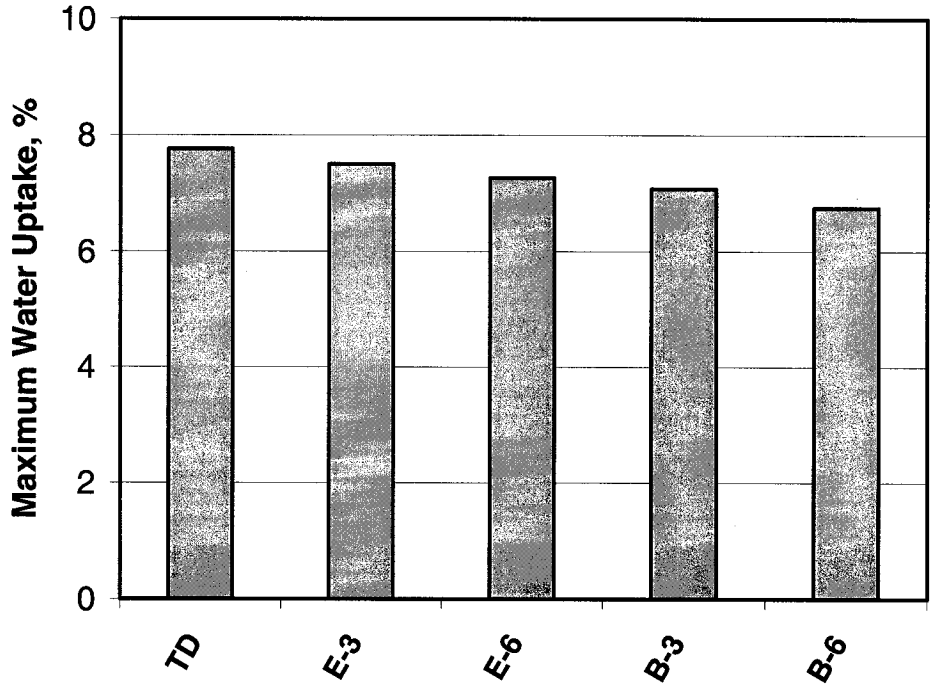

Figure 6-36: Maximum water uptakes of 30B and I.30E nanocomposites made by the DM method at 3-phr and 6-phr clay loading, for 5000 hours at 23°C

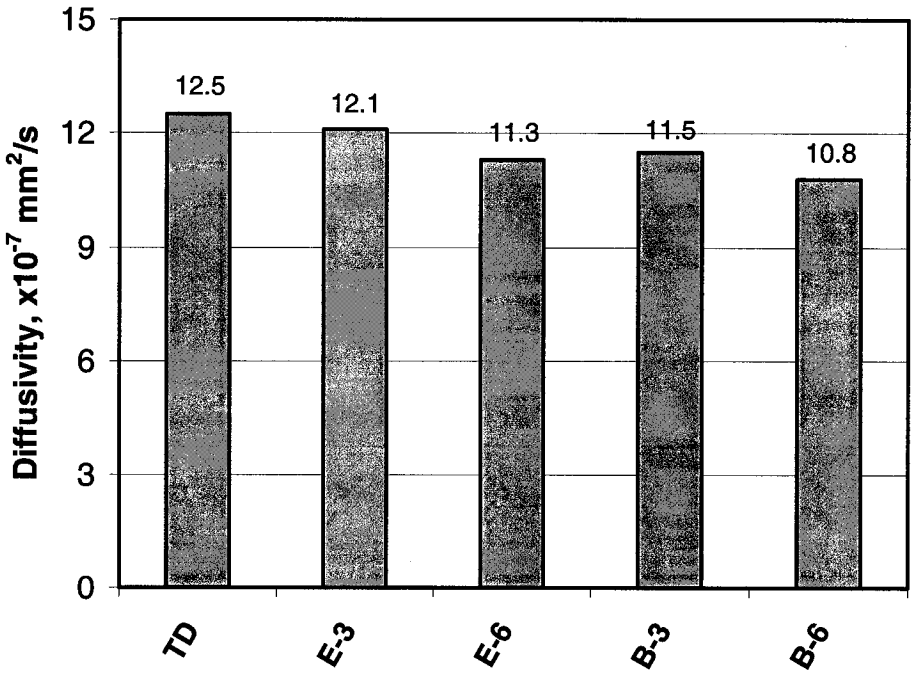

Figure 6-37: Diffusivities of 30B and I.30E nanocomposites made by the DM method at 3-phr and 6-phr clay loading, at 23°C

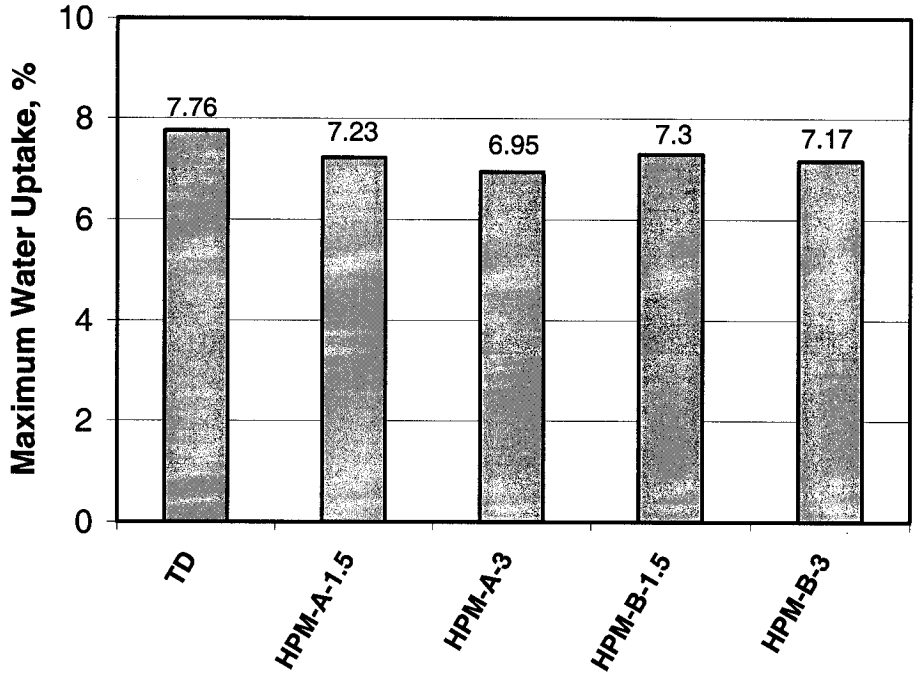

Figure 6-38: Maximum water uptakes of 30B and I.30E nanocomposites made by the HPM method at 1.5-phr and 3-phr clay loading, for 5000 hours at 23°C

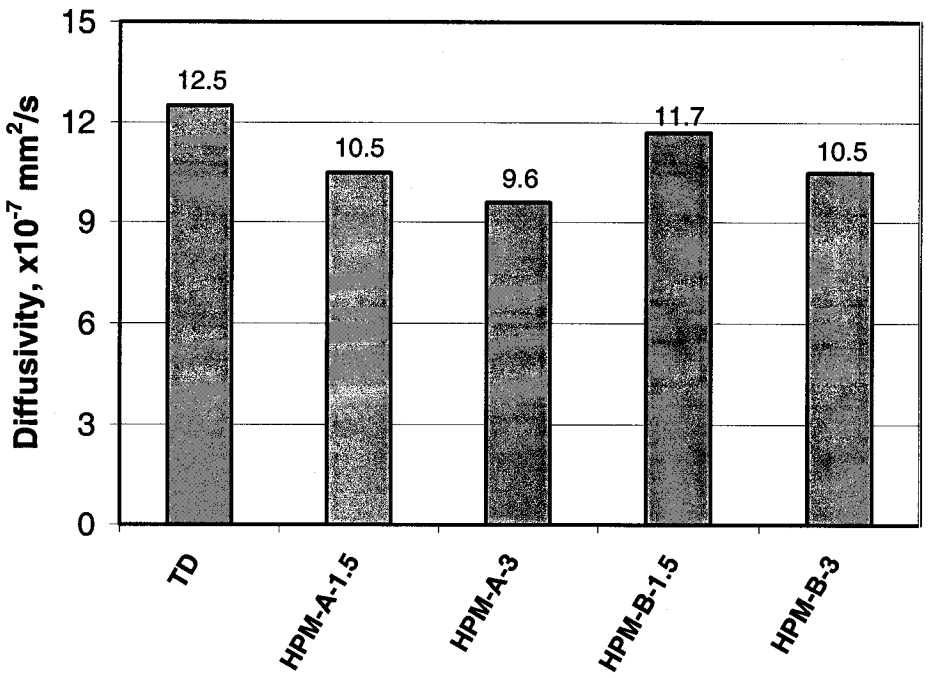

Figure 6-39: Diffusivities of 30B and I.30E nanocomposites made by the HPM method at 1.5-phr and 3-phr clay loading, at 23°C

6.4.7 Water Uptake of Nanocomposites with Different Matrices

Nanocomposites based on a high water-uptake epoxy TGDDM/DDS system are analyzed in previous sections. This section discusses nanocomposites based on the low water uptake epoxy DGEBA/BF_3.MEA system, made with I.30E organoclay by the HPM dispersion method.

For example, Figure 6-40 shows water uptake profiles of nanocomposites based on DGEBA/BF_3.MEA at 23°C. Compared with nanocomposites based on a TGDDM system, these nanocomposites do not completely follow the Fickian numerical fit even at 23°C; a two-stage diffusion process is observed.

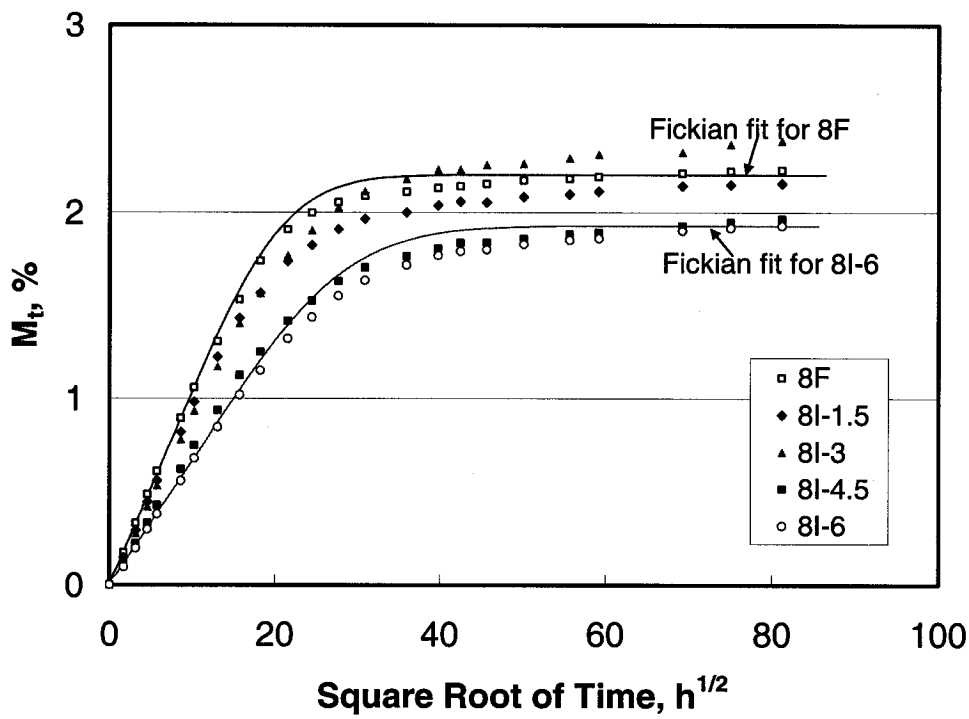

Figure 6-40: Water absorption profiles of I.30E/DGEBA/BF_3.MEA nanocomposites at 23°C

Contrary to nanocomposites based on a TGDDM/DDS system, nanocomposites based on DGEBA/BF_3.MEA have lower equilibrium moisture contents, which vary around the values of pure resin, and do not correlate proportionally with clay loading of organoclay, as shown in Figure 6-41; this may be because I.30E organoclay has a similar equilibrium moisture content to the DGEBA/BF_3.MEA resin system.

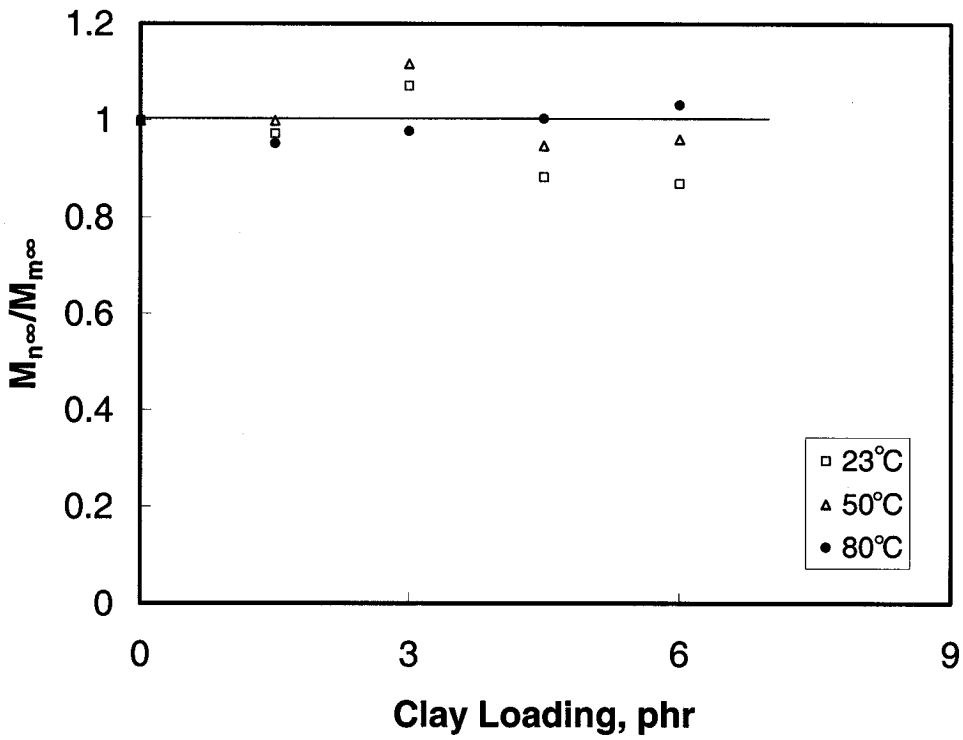

Figure 6-41: Ratio of maximum water uptake (M_{nm}) of 8I nanocomposites to pure resin ($M_{m\infty}$) *versus* clay loading, at different temperatures

On the other hand, DGEBA/BF_3.MEA nanocomposites have the same variational trend in diffusivity as TGDDM/DDS nanocomposites. The diffusivities were obtained only by using the LMD method, because the experimental data do not completely follow the Fickian numerical fit. The ratios of diffusivity of nanocomposites (D_n) to pure resin

(D_r) decrease with increasing clay loading at different temperatures, as shown in Figure 6-42.

Curves based on the proposed Diffusivity Model for Intercalated Nanocomposites (DMIN) are plotted in Figure 6-42. Most experimental data fall between the model prediction curves for 7 or 13 clay platelets in agglomerates. The numbers agree with those observed by TEM.

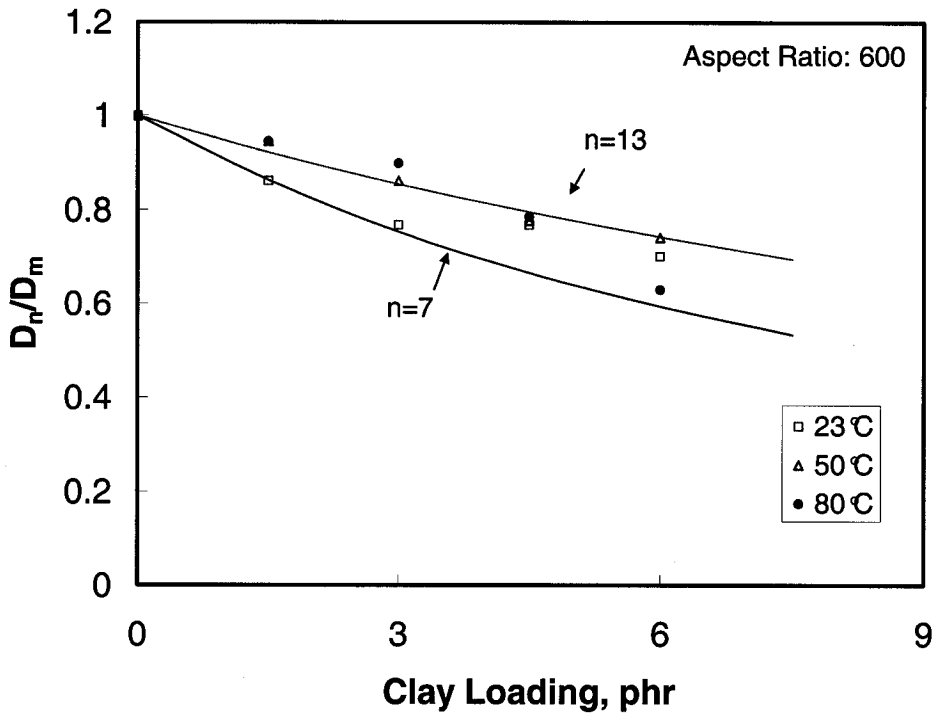

Figure 6-42: Ratio of diffusivity (D_n) obtained by the LMD method for 8I nanocomposite to pure resin (D_m) *versus* clay loading, at different temperatures

6.4.8 Water Uptake of Hybrid Nanocomposites

Water uptake behaviors of hybrid nanocomposites modified with CTBN rubber and I.30E organoclay depend on not only the clay loading, but also the concentration of

CTBN rubber. As a result, in this section, water uptake of rubber-modified DGEBA/BF_3.MEA epoxies is discussed first.

6.4.8.1 Water Uptake of Rubber-Modified Epoxies

Figure 6-43 shows water uptake profiles of rubber-modified epoxy at 20-phr CTBN concentration at different temperatures; in order to understand the effect of rubber, water uptake data of pure resin is also plotted in Figure 6-43. Clearly adding rubber into the epoxy system greatly changes the water uptake behavior of DGEBA/BF_3.MEA. At lower environmental temperatures such as 23°C or 50°C, the rubber-modified epoxy (8C-20) has lower water uptake than the pure resin (8F) at any time; however, at higher environmental temperatures such as 80°C, the opposite result is obtained.

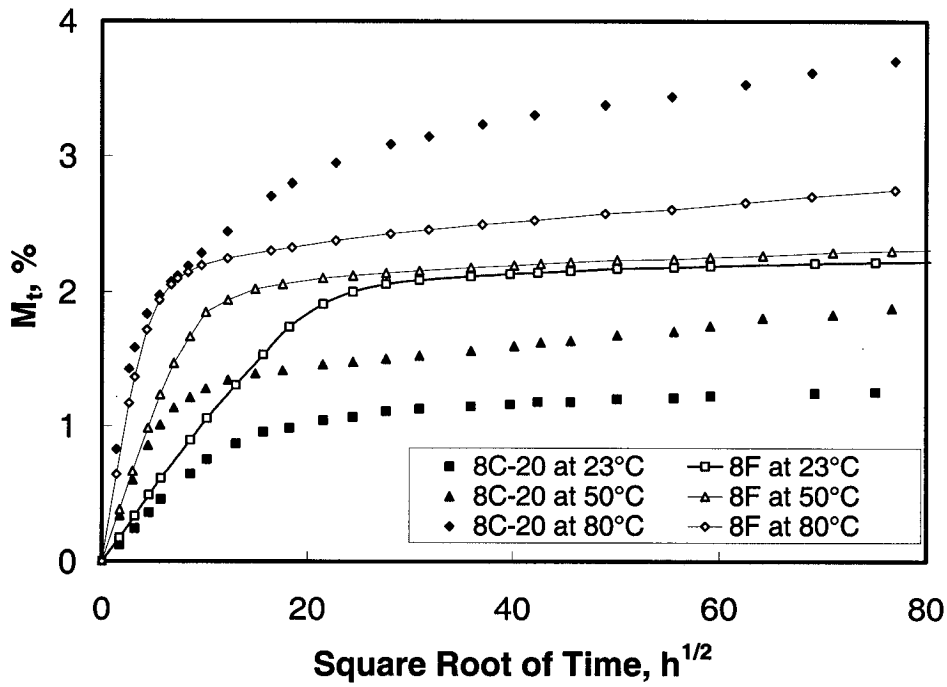

Figure 6-43: Water absorption profiles of DGEBA/BF3.MEA pure epoxy (8F) and rubber-modified epoxy (8C-20), at different temperatures

Figure 6-44 plots maximum water uptakes of rubber modified epoxies ($M_{r\infty}$) *versus* the concentration of CTBN rubber at different temperatures. At 23°C and 50°C, the maximum water uptake of the rubber-modified epoxy systems quickly decreases with increasing CTBN content up to 10-phr; any further addition of CTBN rubber has no significant influence on the maximum water uptake. On the other hand, it linearly increases with CTBN content at 80°C.

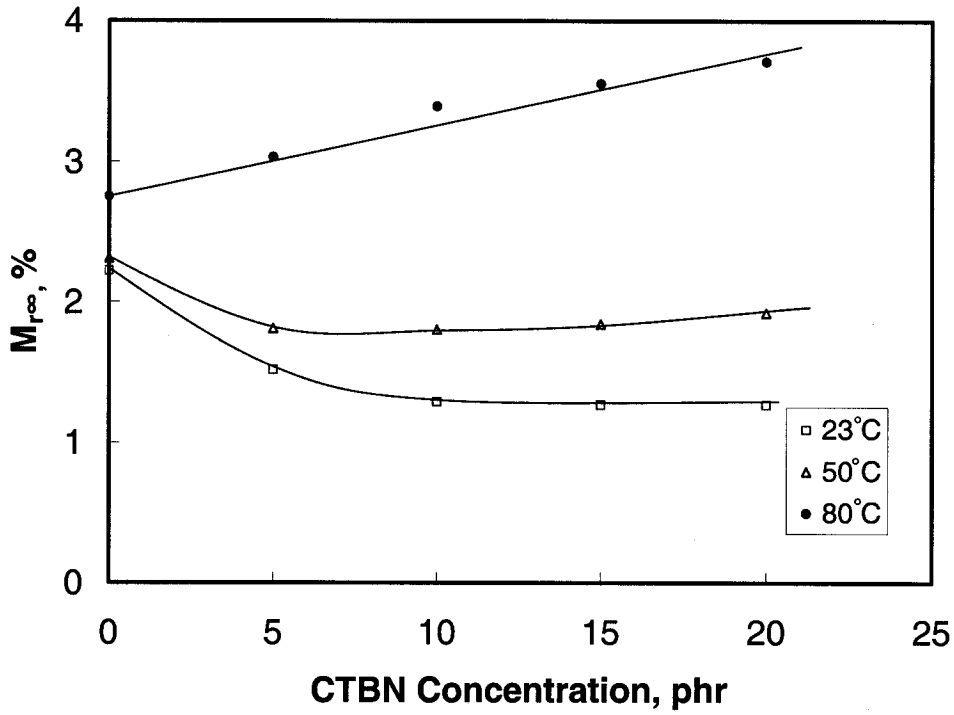

Figure 6-44: Maximum water uptake (M_{rm}) of rubber-modified epoxies *versus* CTBN concentration, at different temperatures

Figure 6-45 shows the Fickian, LMD and DTVD numerical fits for rubber-modified epoxy at 20-phr CTBN concentration at different temperatures. Clearly the experimental data do not completely follow the Fickian numerical fit at all temperatures; the anomalous diffusion models, LMD and DTVD, provide a better fit to

the experimental data than the Fickian law. Furthermore, the DTVD model has a better fit to the experimental data of rubber-modified epoxy systems than LMD at 80°C. However, the diffusivities obtained by the DTVD model for modified epoxies are not constant values, and decay exponentially with time; therefore, diffusivities were obtained only by using the LMD method. The ratios of diffusivity of rubber-modified epoxy (D_r) to pure resin (D_m) increase with increasing CTBN concentration at different temperatures, as shown in Figure 6-46; the slope of the ratio (D_r /D_m) decreases with increasing environmental temperature.

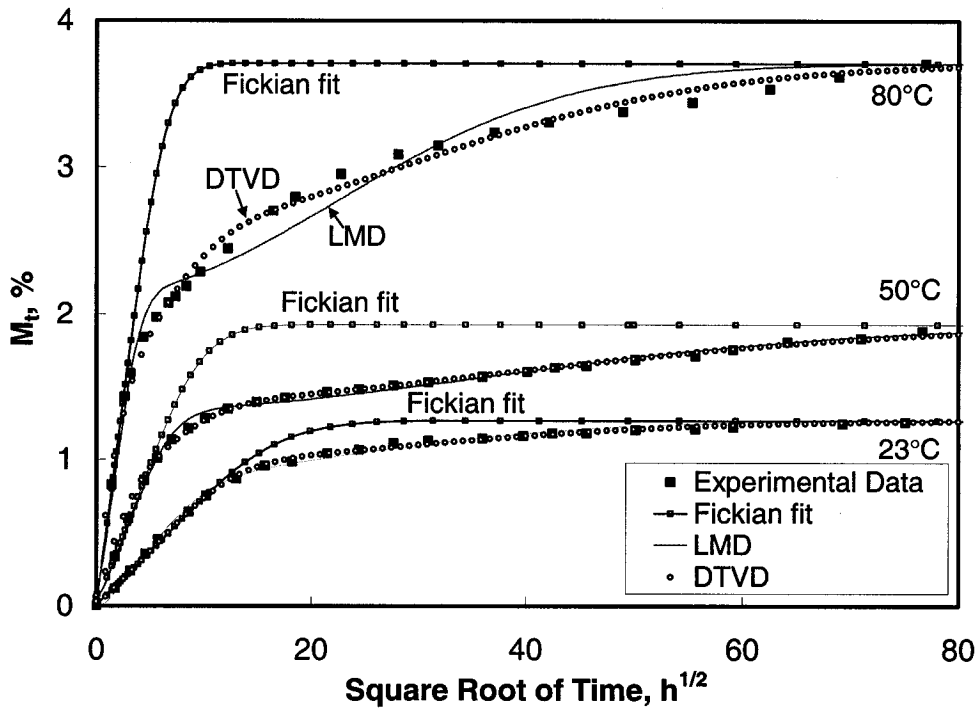

Figures 6-45: Fickian, LMD and DTVD numerical fits for rubber-modified epoxy at 20-phr CTBN concentration, at different temperatures

Therefore, incorporating CTBN rubber can improve water uptake behaviour of epoxy systems at lower environmental temperatures, but damages it at high

environmental temperatures. However, water uptake behaviour of resin matrices at high environment temperatures is a key factor in determining the service temperature.

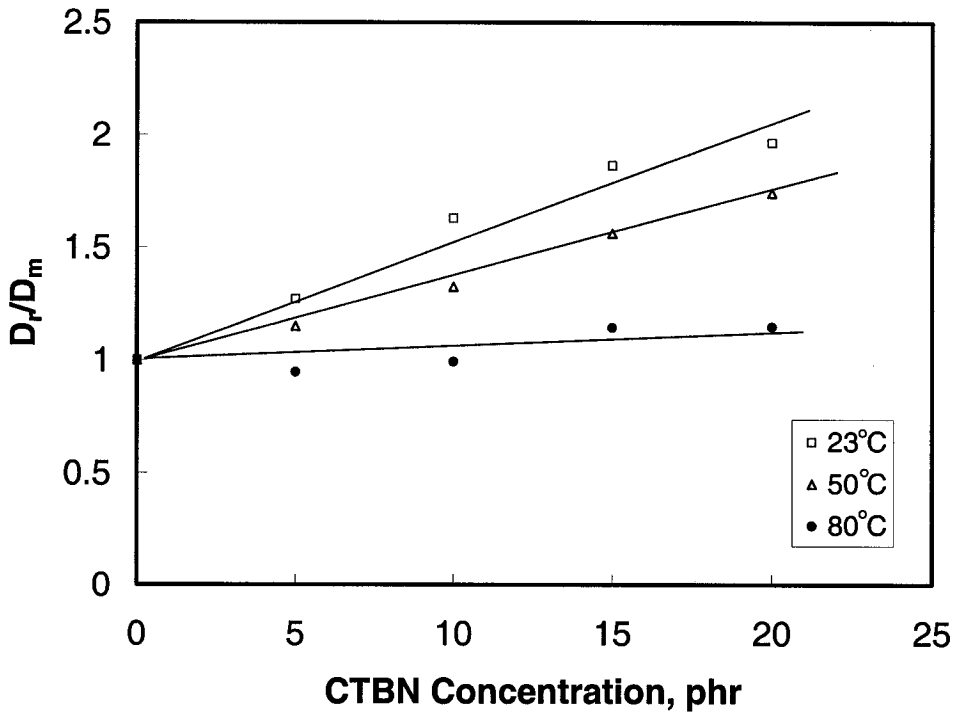

Figure 6-46: Ratio of diffusivity (D_r) obtained by the LMD method for rubber-modified epoxies to pure resin (D_m) *versus* CTBN concentration, at different temperatures

6.4.8.2 Water Uptake of Hybrid Nanocomposites

Because incorporating CTBN rubber increases water uptake of the epoxy system at high environmental temperature, water uptake behaviour of hybrid nanocomposites at high environmental temperature is more interesting. Figure 6-47 shows water absorption profiles of hybrid nanocomposites at 80°C. Clearly hybrid nanocomposites have lower water uptake than rubber-modified epoxy (8C-20), but higher than pure resin

(8F), at any time. Moreover, the water uptake content of nanocomposites decreases with increasing clay loading.

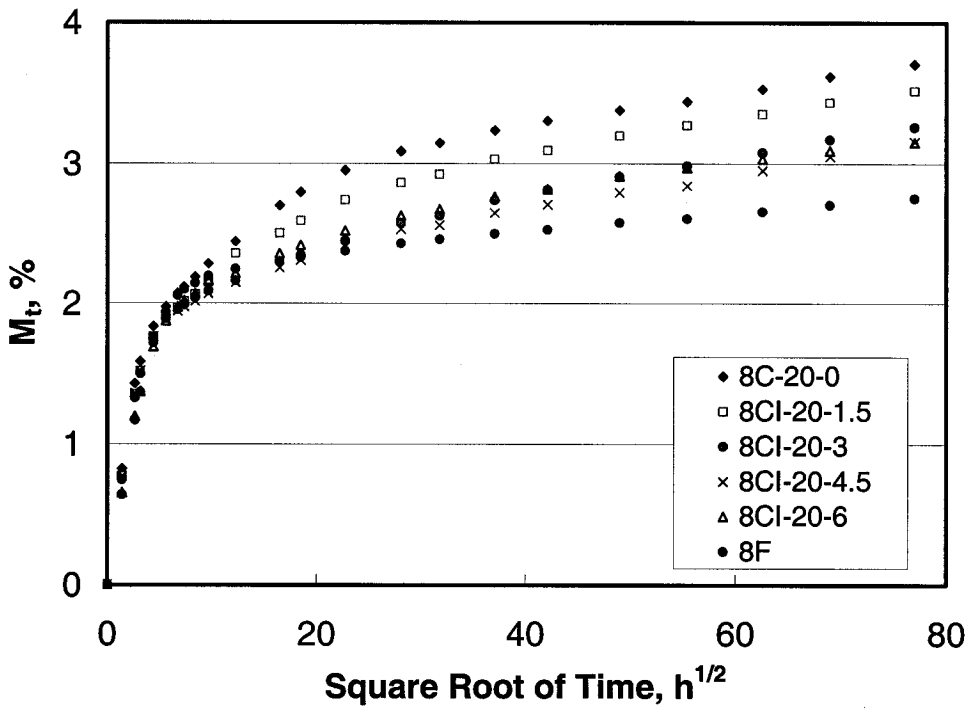

Figure 6-47: Water absorption profiles of hybrid nanocomposites modified with CTBN rubber and I.30E organoclay, at 80°C

Figure 6-48 plots the maximum water uptake of hybrid nanocomposites *versus* clay loading of organoclay at different temperatures. At 23°C and 50°C, the maximum water uptake of hybrid nanocomposites increases with clay loading, perhaps because I.30E organoclay has higher maximum water uptake than rubber-modified epoxy (8C-20) at these temperatures. On the other hand, the maximum water uptake of hybrid nanocomposites decreases with clay loading at 80°C; this may be because maximum water uptake of rubber-modified epoxy (8C-20) increases with environmental temperature, up to a value larger than that of I.30E organoclay.

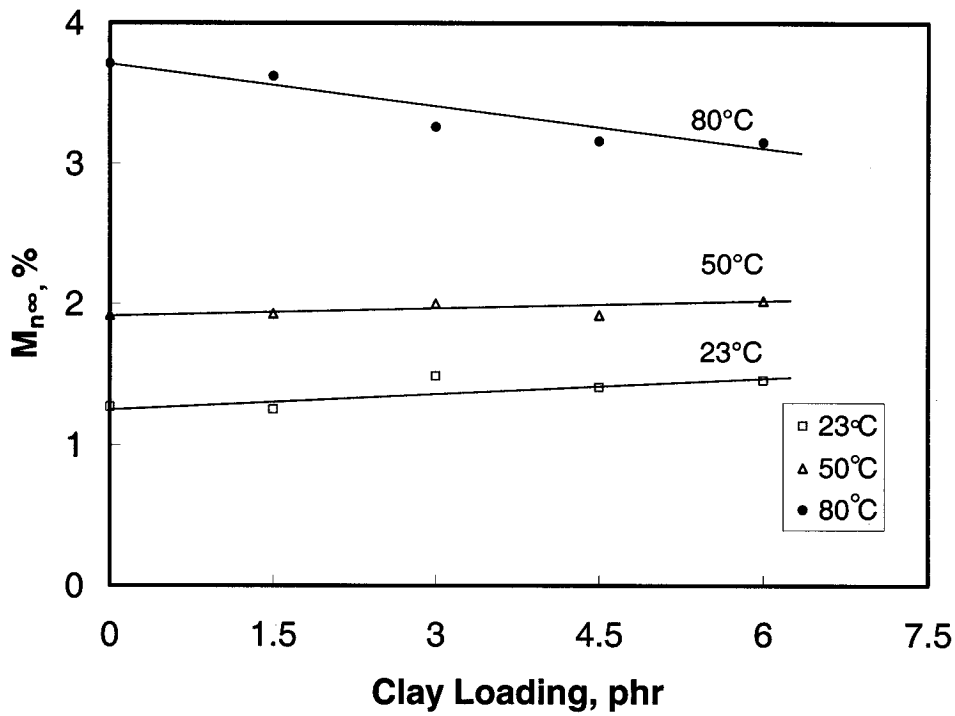

Figure 6-48: Maximum water uptake (M_{nm}) of hybrid nanocomposites *versus* clay loading, at different temperatures

Figure 6-49 shows the ratios of diffusivity in hybrid nanocomposites (D_n) to pure resin (D_r) *versus* clay loading, at different temperatures. The diffusivities were obtained by using the LMD method, because the experimental data do not completely follow the Fickian numerical fit. Hybrid nanocomposites have the same variational trend in diffusivity as DGEBA/BF_3.MEA and TGDDM/DDS nanocomposites at 23°C and 50°C, but hybrid nanocomposites have higher diffusivity than rubber-modified epoxy (8C-20).

Curves based on the proposed Diffusivity Model for Intercalated Nanocomposites (DMIN) are plotted in Figure 6-49. Most experimental data fall between the model prediction curves for 8 and 12 clay platelets in agglomerates.

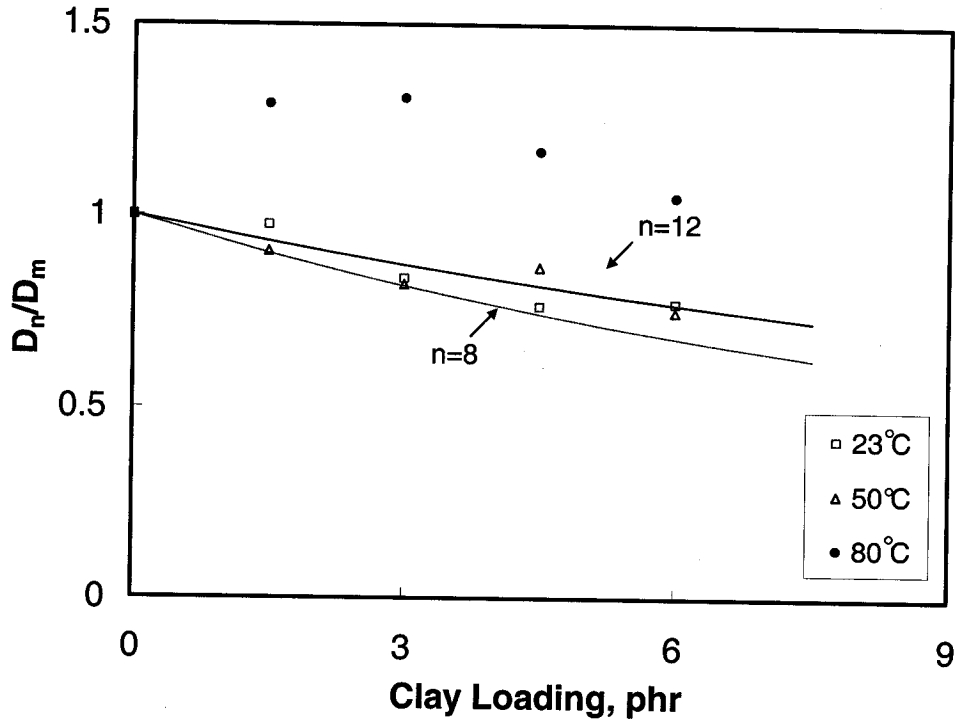

Figure 6-49: Ratio of diffusivity (D_n) obtained by the LMD method for hybrid nanocomposites to pure resin (D_m) *versus* clay loading, at different temperatures

6.5 Summary

Diffusion Models for both Exfoliated (DMEN) and Intercalated Nanocomposites (DMIN) were developed. The models predict that the diffusivity of nanocomposites strongly depends on the aspect ratio of clay platelets, volume fraction of clay and extent of dispersion; the predictions are in agreement with the experimental data.

Water uptake behavior of epoxy-clay nanocomposites based on DGEBA/BF_3.MEA and TGDDM/DDS epoxy systems has been systematically studied. The two epoxy resin systems appear to follow Fickian behavior very closely at 23°C, but not at 50°C or 80°C, where a two-stage diffusion process is observed. Non-Fickian diffusion models,

including the Langmuir Model of Diffusion (LMD) and Diffusion with Time-Varying Diffusivity (DTVD) are able to describe the diffusion behavior of water molecules in these two resin systems at higher environmental temperatures.

The TGDDM/DDS system has a higher maximum water uptake (about 7.7%) and lower diffusivity (about 8.80×10^{-8} mm^2/s at 23°C). The interface between clay surface and epoxy resin influences the water uptake of epoxy resin. Upon adding untreated clay into the epoxy system, maximum water uptake and diffusivity increase with clay loading. On the other hand, upon incorporating organoclay into the epoxy, maximum water uptake and diffusivity decrease with increasing clay loading, due to the tortuosity effect; the reduction ratio strongly depends on dispersion quality. GMM nanocomposites have better dispersion of clay platelets in epoxy than DM, and thus higher tortuosity efficiency; HPM nanocomposites have the best dispersion, and thus the highest tortuosity efficiency. As organoclay is dispersed by HPM, maximum water uptake and diffusivity decrease by about 20% at 7.5-phr clay loading.

The DGEBA/BF_3.MEA system has a lower maximum water uptake (from 2.24% to 2.75%) and higher diffusivity (about $3.05 \times 10^{-7} mm^2/s$ at 23°C). Contrary to nanocomposites based on the TGDDM/DDS system, those based on DGEBA/BF_3.MEA have lower maximum water uptake, varying around the value for pure resin, and do not correlate proportionally with clay loading of organoclay. However, DGEBA/BF_3.MEA nanocomposites have the same variational trend in diffusivity as TGDDM/DDS nanocomposites.

Incorporating rubber into the DGEBA/BF_3.MEA epoxy system greatly changes the water uptake behavior of the resin system; it reduces water uptake of the epoxy system at lower environmental temperatures, but increases it at high environmental temperatures. However, hybrid nanocomposites reduce the effect of rubber at high environmental temperatures.

Chapter 7

Fracture Toughness of Epoxy-Clay Nanocomposites

Fracture toughness is considered a key parameter for selecting the matrix of advanced composites for structural applications. A high toughness matrix reduces the damaged area of composites in response to impact. Effective toughening methods are being pursued.

The fracture toughness of epoxy-clay nanocomposites for structural applications is studied in this chapter. Toughening mechanisms of particle-filled and rubber-modified epoxies are reviewed; fracture surface areas of nanocomposites are analyzed. Both critical stress intensity factor (K_{IC}) and critical strain energy release rate (G_{IC}) of nanocomposites, filler composites and rubber-modified epoxies were measured by the single-edge, notch-bending (SENB) method. The influence of materials, surface modification, processing and morphology on fracture toughness is discussed. The fracture surfaces of specimens were observed using SEM to elucidate the toughening mechanisms in the materials. The crack pinning mechanism was applied to the toughening of exfoliated and intercalated nanocomposites.

7.1 Introduction

The fracture toughness of neat epoxy resins is extremely low, due to their highly crosslinked structure, which absorbs insignificant amounts of energy during the fracture process. Cured epoxy resins have fracture energies (G_{IC} about 100 J/m^2) two orders of magnitude lower than thermoplastics [6]. As a result, the applications of these materials are limited to situations where the stress is relatively low, and preferably static.

The basic goal in toughening cross-linked epoxy resins is to enhance fracture toughness without greatly decreasing other important inherent properties, such as modulus and mechanical properties in wet/hot conditions. Most work has focused on improving the relatively poor fracture properties of epoxy resins, either by reducing the cross-linked density of the epoxy network, or by incorporating a second phase component into the continuous matrix of epoxy resins, through physical blending or chemical reactions. Modifiers have been classified into four main groups: low molecular weight liquid rubbers [7], engineering thermoplastics [8], reactive ductile diluents [142], and inorganic particles [9].

Recently, nanocomposite technology using organoclay as a nanoscale reinforcement offers an interesting alternative for modifying epoxy resins. Like fillers, it simultaneously improves the toughness and modulus of resins, and it provides higher efficiency than fillers [52-55].

Zerda, *et al.* [54] proposed that toughening occurs over a specific particle size range, generally greater than 0.1μm. In an intercalated system, where polymers have

entered into the galleries between silicates but have not fully delaminated them into a completely exfoliated structure, there is considerable interaction between silicate layers, which might improve toughness. The fracture energy of intercalated nanocomposites increases by 100% at 5wt% organoclay loading [54].

Kornmann, *et al.* [55] showed a 112% increase in fracture toughness of a TGDDM-DDS matrix reinforced by 4.2 vol % organoclay, as well as a large improvement (nearly 80~90%) in fracture toughness for untreated clay.

Recently, Zhao and Hoa [143] reported that the stress concentration around particles decreases until the particles are partitioned to 0.95 μm and that increase of fracture area is a main factor in improving toughness of the material.

The purpose of this chapter is to study the effect of material, process and morphology on toughness of nanocomposites, and explore the toughening mechanism.

7.2 Background

7.2.1 Fracture Toughness

The fracture toughness of a material may be defined as energy per unit volume required for fracture. However, this definition of toughness does not indicate the criterion that fracture has occurred. In general, the two terms are widely used for fracture toughness: critical strain energy release rate (G_C), and critical stress intensity factor (K_C).

7.2.1.1 Critical Strain Release Rate

Critical strain energy release rate (G_C) is defined as the critical energy required for propagating a crack per unit area. If work done on an area exceeds this critical energy, fracture occurs. Critical strain energy release rate is based on the energy criterion arising from Griffith's early work, which proposed that critical failure occurs when the growth of the crack releases sufficient energy to overcome the increase in free energy by creating two new surfaces, which are generated by crack propagation [144]. For an infinitesimal increase of crack length, ∂a, it may be written

$$\frac{\partial(F-U)}{\partial a} \geq \frac{\partial 2A\gamma}{\partial a} = 2b\gamma \tag{7-1}$$

where F is the external work done on the system, U is the internal energy of the system, A is the new surface area created by the crack growth, and γ is the surface free energy. b is the thickness, and thus $A = ab$. However, the energy required for fracture of a material is sometimes much greater, even a thousand times, more than twice its surface free energy. One reason for this discrepancy is that fracture of a material includes breaking covalent bonding, in addition to rupturing secondary bonds, for which energy per unit area corresponds to 2γ. The energy required for bond rupture per unit area is referred to as the intrinsic fracture energy (G_o). Therefore, the critical strain energy release rate is defined to include the intrinsic fracture energy (G_o) and the energy dissipated by the viscoelastic or plastic deformation in the vicinity of the crack tip. The term 2γ in Equation 7-1 is replaced with G_C [144]:

$$\frac{1}{b}\frac{\partial(F-U)}{\partial a} \geq G_c \tag{7-2}$$

There are three fundamental modes of crack propagation, as illustrated in Figure 7-1; they may be superimposed in the practical case of crack loading. However, cracks are usually controlled experimentally to follow only one of the three modes. The most frequently used mode is tensile crack opening, *i.e.* mode I. Therefore, G_{IC} indicates the critical strain energy release rate measured in mode I.

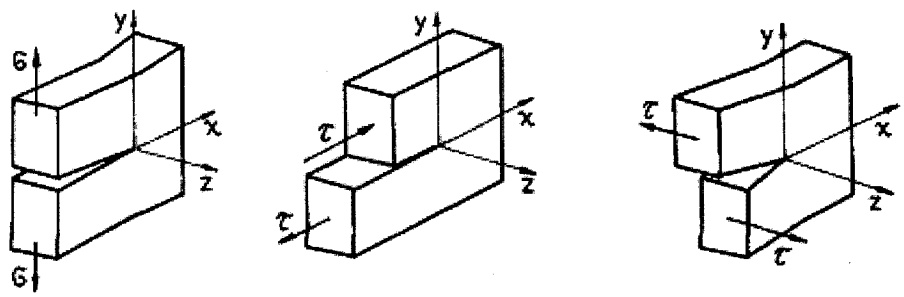

Figure 7-1: Three basic modes for crack propagation: Mode I, tensile opening model; Mode II, sliding or in-plane shear mode; Mode III, tearing or anti-plane shear mode

7.2.1.2 The critical stress intensity factor

The critical stress intensity factor (K_C) is defined as the value of stress intensity which causes fracture in that material. Irwin found that the stress field around a sharp crack in a linear elastic material can be defined by a parameter called the stress intensity factor (K_C) [145]. When an isotropic, elastic, and infinitely thin plate containing a infinitely sharp crack size of a is deformed uniaxially with stress σ_0, the components of

the stress tensor in a volume element at distance r and angle θ from the crack tip, as shown in Figure 7-2, are given by:

$$\sigma_x = \sigma_0 \frac{\sqrt{\pi a}}{\sqrt{2\pi r}} \cos\frac{\theta}{2}\left(1 - \sin\frac{\theta}{2}\sin\frac{3\theta}{2}\right) \tag{7-3}$$

$$\sigma_y = \sigma_0 \frac{\sqrt{\pi a}}{\sqrt{2\pi r}} \cos\frac{\theta}{2}\left(1 + \sin\frac{\theta}{2}\sin\frac{3\theta}{2}\right) \tag{7-4}$$

$$\tau_{xy} = \sigma_0 \frac{\sqrt{\pi a}}{\sqrt{2\pi r}} \sin\frac{\theta}{2}\cos\frac{\theta}{2}\cos\frac{3\theta}{2} \tag{7-5}$$

where σ and τ are tensile and shear stresses, respectively. Equations (7-3~7-5) indicate that the stress at the crack tip ($r = 0$) goes to infinity; thus a reasonable criterion for fracture cannot be made using this stress. Therefore, Irwin introduced the stress intensity factor K_I, to define the criterion for fracture in mode I; he set the stress intensity factor as:

$$K_I = \sigma_0 \sqrt{\pi a} Q \tag{7-6}$$

where Q is the geometry factor that corrects the assumption of an infinite thin plate in the derivation of Equations (7-3~7-5). Similarly the critical stress intensity factor can be defined as:

$$K_{IC} = \sigma_C \sqrt{\pi a} Q \tag{7-7}$$

Therefore, the criterion for fracture is

$$K_I \geq K_{IC} \tag{7-8}$$

The critical stress intensity factor is a material property that characterizes the intensity of the stress field ahead of the crack tip. The geometry factor can be found in several handbooks.

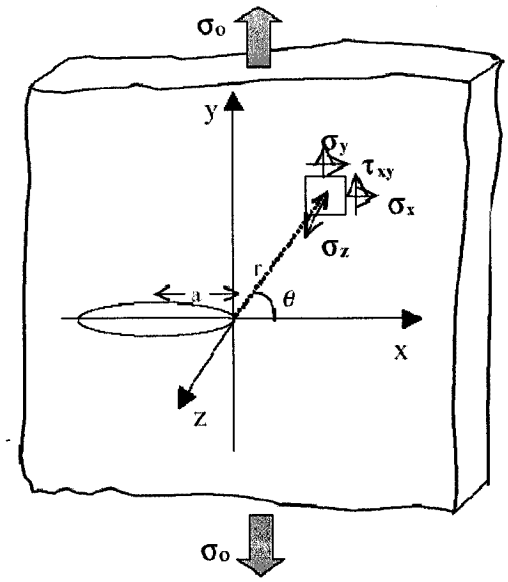

Figure 7-2: Stress analysis near a sharp crack tip of an isotropic and elastic plate [ref. 144]

7.2.2 Toughening Mechanisms

It is well known that some materials, such as liquid reactive rubbers, are able to significantly improve the fracture toughness of epoxies. Therefore, questions such as how to explain increased fracture toughness, and how to predict the extent of toughness improvement, have resulted in several theories or models for rubber, thermoplastic and filler-toughened epoxies. Moreover, some theories offer quantitative descriptions

between microstructures and fracture behavior of toughened epoxies; some important toughening mechanisms are summarized here.

7.2.2.1 Crack Pinning Mechanism

The crack pinning mechanism was first proposed by Lange [146], then modified and extended by Evans [147] and Green, *et al.* [148, 149]. It assumes that propagating cracks can be impeded by rigid, impenetrable and well-bonded particles. When a propagating crack encounters such obstacles, it becomes temporarily pinned and tends to bow out between the particles, forming secondary cracks; thus it results in increasing absorption of energy, including not only the creation of the new fracture surface, but also the formation of a new non-linear crack front, which is assumed to possess a line energy.

Lange [146] gave a quantitative expression for the fracture energy, G_{IC}, of composites, by assuming that the crack front breaks away from the pinning positions when it attains a radius $D_s/2$:

$$G_{1C} = G_{1CM} + 2T_L / D_S \tag{7-9}$$

where G_{ICM} is the fracture energy of the matrix, T_L is the line energy per unit length of bowed crack front, and D_s is the interparticle spacing.

However, this equation has been found to be inadequate to describe the crack pinning mechanism. More satisfactory theoretical models have been derived by several groups of workers, who have calculated from first principles the stresses required to propagate a crack through a matrix reinforced by an array of rigid particles [147, 149]. Evans first demonstrated that the line-energy contribution is a major mechanism for rigid,

impenetrable and well-bonded particles, and the value of T_L is a function of particle size and shape [147]. Evans' analysis also enables the fracture strength of filler composites to be predicted. The results are given in Table 7-1, where the ratio of the stress required to propagate a crack in a composite to the stress required for a crack in pure matrix, σ_c/σ_m, is given in terms of the ratio of particle diameter to interparticle separation, d_p/D_s. Values are given for elliptical secondary crack fronts, and for both cases of (1) no interactions between elliptical secondary cracks, and (2) crack interactions. Green, *et al.* modified Evans' analysis and, in particular, have taken into account the exact position of the secondary crack front when it breaks away from the pinning positions [148,149]. They obtained a similar dependence of σ_c/σ_m upon d_p/D_s as Evans, as may be seen from Table 7-1, but their analysis yields somewhat higher values of σ_c/σ_m. For a filler composite and unfilled polymer containing primary cracks of the same length, the ratio σ_c/σ_m is equivalent to the ratio K_{IC}(composite)/K_{IC}(matrix) [150].

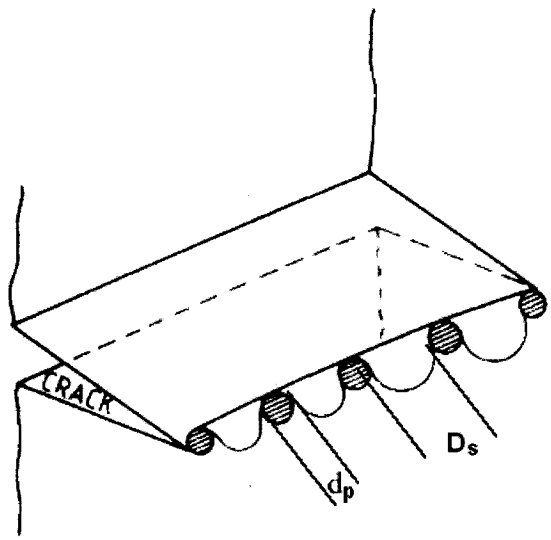

Figure 7-3: Schematic illustration of crack pinning [ref. 146]

Table 7-1: Predicted values of σ_c/σ_m as a function of d_p/D_s for particle-filled composites

d_p/D_s	Non-interacting elliptical cracks		Interacting elliptical cracks	
	Evans	Green	Evans	Green
0	1.00	1.00	1.00	1.00
0.25	1.85	2.02	1.19	1.19
0.5	2.18	2.52	1.65	1.80
1.0	2.55	3.05	2.23	2.52
1.25	2.7	3.25	2.40	2.86
2.0	2.90	3.75	2.75	3.52

7.2.2.2 Crack Tip Blunting

Crack tip blunting may take place due to localized shear yielding [151] or damage zones [152], such as debonding of the particle/matrix interface and fracture of particles. Rigid particles act as stress concentrators, because they have different elastic properties compared to pristine epoxy. When the local stress exceeds the yield stress of the pristine epoxy or the adhesive strength of the particle/matrix interface, shear yielding or debonding of the particle/matrix interface occurs. Therefore, the material is able to absorb large quantities of energy upon fracture.

7.2.2.3 Crack-Path Deflection Mechanism

When a propagating crack encounters a particle, the crack is diverted by the particle and results in an increase of the crack surface area [153]. The crack-path deflection may explain the increase in fracture energy, given by:

$$\Delta G_{1C} = \frac{2}{3} r_m \upsilon_f \tag{7-10}$$

where r_m is the specific fracture energy of the matrix. This relationship is derived on the assumption that the increase in the fracture surface area created by the deviation of the crack is equivalent to half the surface area of the particle ($2\pi r^2$), minus the matrix area (πr^2) in the absence of the particle.

7.2.2.4 Crack Bridging Mechanism

Crack bridging is considered to be a toughening mechanism of rubber- or glass filler-modified epoxy [154]. The increase in fracture toughness is considered to be due to the dissipation of energy stored during stretching the particles by the crack opening, by tearing or debonding particles from the matrix.

7.2.2.5 Rubber Tear-Energy Toughening Theory

Kuna-Douglass, *et al.* proposed the rubber tear-energy toughening theory, and defined the quantitative model equation for toughened thermosets [155]. Their model is based upon energy dissipation during the stretching and bridging of the crack surfaces by rubber particles, that is, the rubber bridging mechanism. The increase of fracture energy can be expressed as:

$$\Delta G_{1C} = 4\Gamma_t(T)\upsilon_{f_r} \tag{7-11}$$

Where Γ_t(T) is the tearing energy of the rubber particles, and υ_{fr} is the volume fraction of rubber particles. However, this model fails to explain the phenomenon of stress whitening, observed in most relatively tough rubber-modified epoxies. Kinloch, *et al.* [156] suggested that the rubber-tear mechanism does not represent the major toughening mechanism, but only provides a secondary contribution to toughening.

7.2.2.6 Localized Shear Yielding (or Shear Banding) Mechanism

Kinloch, *et al.* [156, 157] proposed a mechanism involving dilatational deformation of the matrix, and cavitation of rubber particles in response to triaxial stresses near the crack tip, combined with shear yielding between the holes formed by the cavitated rubber particles. Stress-whitening is attributed to light scattering by these holes, and the major energy absorption mechanism is suggested to be the plastic deformation of the matrix. Plastic deformation blunts the crack tip, which reduces the local stress concentration and allows the material to support higher loads before failure occurs.

Kinloch [156, 157] calculated the increase in fracture toughness due to localized shear yielding inside the plastic zone. The fracture energy is expressed by:

$$G_{IC} = G_{ICM} + \psi \tag{7-12}$$

where ψ is the toughening contribution based on localized shear yield.

The main toughening mechanisms are introduced above; it seems that a single theory cannot explain every experimental result and phenomenon of toughening. One

reason may be discrepancies of raw materials and manufacturing processes among different researchers because the initial properties of raw materials and the quality of specimens significantly influence the final fracture properties of epoxy matrices. Another reason is that the fracture itself is a complex phenomenon, and a single theory cannot represent every detail; so the toughening mechanism may be a combination of two or more mechanisms.

Concerning fracture toughness of particle-filled epoxies, possible toughening mechanisms include: crack deflection, localized shear banding and yielding in the matrix around particles, crack tip blunting by the particles, and crack pinning. It is believed that crack tip blunting and crack pinning mechanisms are primarily responsible for enhanced toughness in particulate composites [150].

For rubber-modified epoxies, based on the works of Kuna-Douglass, *et al.* and Kinloch, Huang [158] developed a model involving three main energy-dissipating toughening mechanisms: (1) localized shear yielding or shear banding occurs between rubbery particles in the epoxy matrix; (2) plastic void growth is initiated by cavitation or debonding of rubbery particles in the epoxy matrix; and (3) the rubber-bridge mechanism exists in the crack tip zone. The total increase in fracture energy is the sum of the respective contributions from these three mechanisms.

7.2.3 Fracture Surface Area Analysis

In this section, the fracture surface area of different nanocomposites is analyzed. It is assumed that facture occurs at the interface between the clay platelets and the matrix.

7.2.3.1 Fracture Surface Area of Exfoliated Nanocomposites

Because the volume content of clay in nanocomposites is very low (about 5%) and clay platelets are very small, clay platelets do not change the propagating direction of fracture surface, but result in local tortuosity in the vicinity of clay platelets, that is, crack-trajectory tortuosity occurs around the clay platelets or the shorter end of a clay platelet is pulled out from the epoxy resin, as shown in Figure 7-4.

It is assumed that clay platelets are uniformly distributed, completely exfoliated and aligned in one direction in a polymer. The face of clay platelets is a square with side length ℓ and thickness t. The square representative volume element (RVE) of the exfoliated composite is cut from the nanocomposite. The volume fraction of clay is given by:

$$v_c = \frac{\ell^2 t}{a^2 h} \tag{7-13}$$

where a is the length of RVE, and h is its thickness.

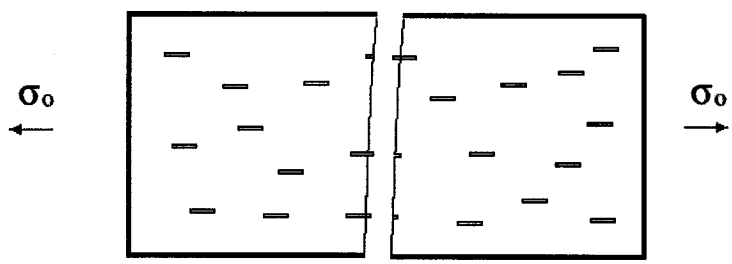

Figure 7-4: Schematic drawing of pull-out of clay platelets

For any fracture surface at x position ($x \geqslant 0$), as shown in Figure 7-5, the fracture surface area (S_{n22}) is given by:

$$S_{n22} = S_{m22} + 2(\ell/2 - x) \bullet \ell/2 + 2(\ell/2 - x)t \tag{7-14}$$

where S_{m22} is the fracture surface area of the resin matrix in the absence of clay platelets. S_{m22} is given by:

$$S_{m22} = ah \tag{7-15}$$

Therefore, the maximum fracture surface occurs at $x = 0$, and the fracture surface area is:

$$S_{n22} = S_{m22} + \ell^2/2 + \ell t = ah + \ell^2/2 + \ell t \tag{7-16}$$

The minimum fracture surface occurs at $x = \ell/2$, and the fracture surface area is:

$$S_{n22} = S_{m22} = ah \tag{7-17}$$

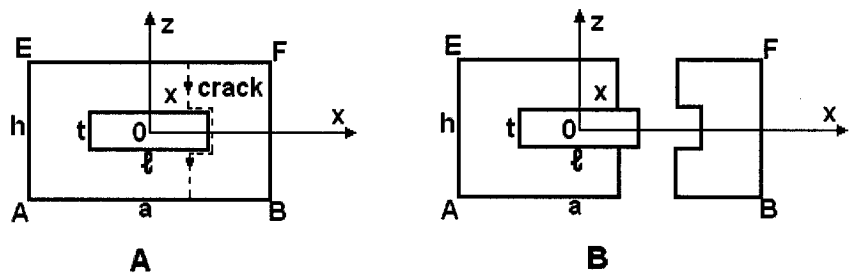

Figure 7-5: Schematic drawings of pull-out of clay platelets in the direction normal to the face of the clay platelets in an exfoliated nanocomposite

If the probability of fracture along side EF is the same, the average fracture surface area is given by:

$$\bar{S}_{n22} = \frac{S_{m22}(a/2-\ell/2) + \int_0^{\ell/2}[S_m + 2(\ell/2-x)\ell + 2(\ell/2-x)t]dx}{a/2} \tag{7-18}$$

Simplifying Equation 7-18, the average fracture surface area becomes:

$$\bar{S}_{n22} = ah + \frac{\ell^2(\ell+t)}{2a} \tag{7-19}$$

The ratio of the average fracture surface area to the fracture surface area of the resin matrix in the absence of the clay platelets is given by:

$$\frac{\bar{S}_{n22}}{S_{m22}} = \frac{ah + \ell^2(\ell+t)/2a}{ah} = 1 + \frac{\ell^2}{2a^2h}(\ell+t) \tag{7-20}$$

By substituting the aspect ratio and the volume fraction of clay platelets into Equation 7-20, the ratio is given by:

$$\frac{\bar{S}_{n22}}{S_{m22}} = 1 + \frac{\ell^2}{2a^2h}(\ell+t) = 1 + \frac{1}{2}\upsilon_c(\zeta+1) \tag{7-21}$$

According to Griffith's theory, the energy release for crack propagation is:

$$U = 2A\gamma \tag{7-22}$$

The ratio of the energy release of an exfoliated nanocomposite (U_{n22}) to that of resin matrix (U_m) is given by:

$$\frac{U_{n22}}{U_{m22}} = \frac{2\bar{S}_{n22}\gamma_m}{2S_{m22}\gamma_m} = \frac{\bar{S}_{n22}}{S_{m22}} = 1 + \frac{\upsilon_C}{2}(\zeta + 1) \tag{7-23}$$

As a crack propagates in the direction parallel to the face of the clay platelets and encounters the clay platelets, the thickness of a single clay platelet is too small to provide toughening through crack-trajectory tortuosity.

In the case of completely random orientation in all three orthogonal directions, the fracture surfaces of an exfoliated nanocomposite are complicated. As a result, some simplified fracture modes in 2-D are shown in Figure 7-6. Figure 7-6 A shows a platelet in a polymer at any orientation. As a crack encounters the clay platelet, the shorter end of the clay platelet is pulled out, as shown in Figure 7-6 B. In this case, the fracture surface area is the same as that for crack propagation in the direction normal to the face of the clay platelets. However, two other cases have smaller fracture surface areas.

7.2.3.2 Fracture Surface Area Analysis of Intercalated Nanocomposites

In intercalated nanocomposites, agglomerates of organoclay are assumed to be uniformly distributed in a polymer. Each agglomerate consists of ***n*** platelets of clay, and all platelets of clay in agglomerates are aligned in one direction. If the basal spacing of the clay is smaller than the distance between two agglomerates, the square representative volume element (RVE) of an intercalated composite contains one agglomerate. The volume fraction of clay is given by:

$$\upsilon_c = \frac{n\ell^2 t}{a^2 h} \tag{7-24}$$

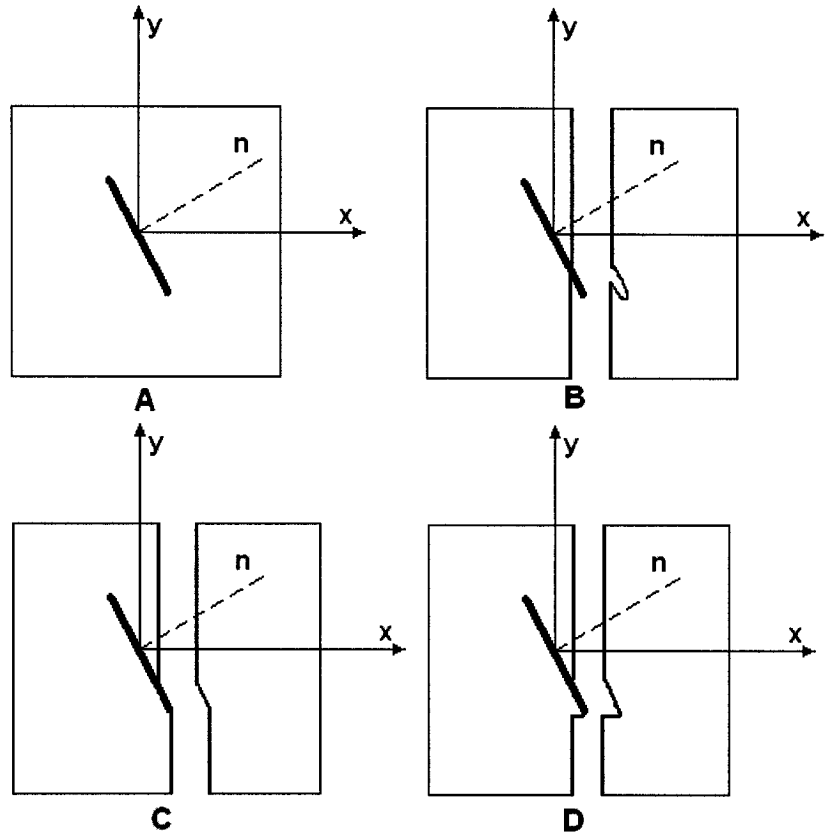

Figure 7-6: Schematic drawings of crack propagation and fracture modes of clay platelets in the completely random orientation in an exfoliated nanocomposite

As a crack propagates in the direction normal to the face of the clay platelets and encounters an agglomerate, as shown in Figure 7-7, in the same way as above for exfoliated nanocomposites, the average fracture surface area is given by:

$$\bar{S}_{n22} = \frac{S_{m22}(a/2-\ell/2)+\int_0^{\ell/2}[S_{m22}+2(\ell/2-x)\ell+2(\ell/2-x)nd]dx}{a/2} \qquad (7\text{-}25)$$

where ***d*** is the basal spacing in intercalated nanocomposites.

Simplifying Equation 7-25, the average fracture surface area becomes:

$$\bar{S}_{n22} = ah + \frac{\ell^2(\ell + nd)}{2a} \tag{7-26}$$

The ratio of the average fracture surface area to the fracture surface area of resin matrix in the absence of the clay platelets is given by:

$$\frac{\bar{S}_{n22}}{S_{m22}} = \frac{ah + \ell^2(\ell + nd)/2a}{ah} = 1 + \frac{\ell^2}{2a^2h}(\ell + nd) \tag{7-27}$$

By substituting the aspect ratio and the volume fraction of clay platelets into Equation 7-27, the ratio is given by:

$$\frac{\bar{S}_{n22}}{S_{m22}} = 1 + \frac{\ell^2}{2a^2h}(\ell + nd) = 1 + \frac{v_c}{2}\left(\frac{\ell}{nt} + \frac{nd}{nt}\right) = 1 + \frac{v_c}{2}\left(\frac{\zeta}{n} + \frac{d}{t}\right) \tag{7-28}$$

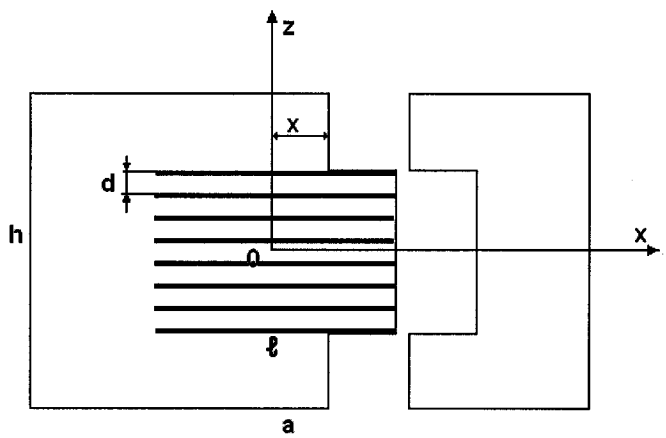

Figure 7-7: Schematic drawing of pull-out of clay platelets in the direction normal to the face of the clay platelets in the intercalated nanocomposite

The ratio of the energy release of an intercalated nanocomposite (U_{n22}) to that of resin matrix (U_m) is given by:

$$\frac{U_{n22}}{U_{m22}} = \frac{\bar{S}_{n22}}{S_{m22}} = 1 + \frac{\upsilon_c}{2}\left(\frac{\zeta}{n} + \frac{d}{t}\right) \tag{7-29}$$

As a crack propagates in the direction parallel to the face of clay platelets and encounters an agglomerate, as shown in Figure 7-8, in the same way, the average fracture surface area is given by:

$$\bar{S}_{n11} = \frac{S_{m11}(h/2 - nd/2) + \int_0^{nd/2}[S_m + 4(nd/2 - z)\ell]dz}{h/2} \tag{7-30}$$

Simplifying Equation 7-30, the average fracture surface area becomes:

$$\bar{S}_{n11} = a^2 + \frac{\ell n^2 d^2}{h} \tag{7-31}$$

The ratio of the average fracture surface area to the fracture surface area of resin matrix in the absence of the clay platelets is given by:

$$\frac{\bar{S}_{n11}}{S_{m11}} = \frac{a^2 + \ell n^2 d^2 / h}{a^2} = 1 + \frac{\ell n^2 d^2}{a^2 h} \tag{7-32}$$

By substituting the aspect ratio and the volume fraction of clay platelets into Equation 7-32, the ratio is given by:

$$\frac{\bar{S}_{n11}}{S_{m11}} = 1 + \frac{\ell n^2 d^2}{a^2 h} = 1 + \frac{\upsilon_c n d^2}{\ell t} = 1 + \frac{\upsilon_c n}{\zeta}\left(\frac{d^2}{t^2}\right) \tag{7-33}$$

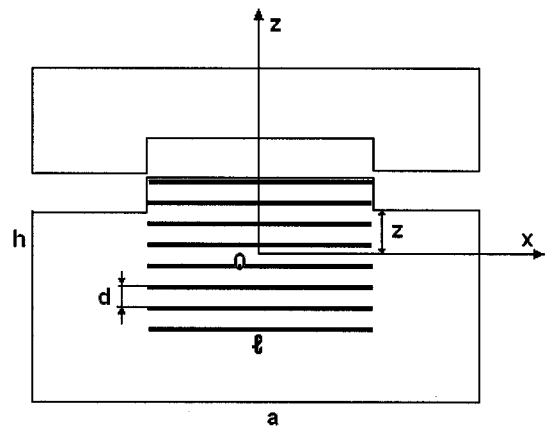

Figure 7-8: Schematic drawing of pull-out of clay platelets in the direction parallel to the face of the clay platelets in the intercalated nanocomposite

The ratio of the energy release of an intercalated nanocomposite (U_{n11}) to that of resin matrix (U_m) is given by:

$$\frac{U_{n11}}{U_m} = \frac{\bar{S}_{n11}}{S_{m11}} = 1 + \frac{\upsilon_c n}{\zeta}\left(\frac{d^2}{t^2}\right) \tag{7-34}$$

If agglomerates of organoclays are spheres, uniformly distributed in epoxy resins, the cube representative volume element (RVE) of an intercalated composite contains one agglomerate, as shown in Figure 7-9. The volume fraction of the agglomerate is given by:

$$\upsilon_a = \frac{4\pi R^3}{3a^3} \tag{7-35}$$

where R is the radius of the sphere and a is the side length of the cube. Because the resin matrix is intercalated into the agglomerate, the volume fraction of clay platelets has the following relationship with the volume fraction of the agglomerate:

$$v_c = \frac{t}{d} v_a \tag{7-36}$$

The fracture surface area (S_n) for any fracture surface at x position, as shown in Figure 7-9 B, is given by:

$$S_n = (a^2 - \pi(R^2 - x^2)) + 2\pi R(R - x) \tag{7-37}$$

If the possibility of fracture along the side of the cube is the same, the average fracture surface area is given by:

$$\bar{S}_n = \frac{a^2(a/2 - R) + \int_0^R [a^2 - \pi(R^2 - x^2) + 2\pi R(R - x)]dx}{a/2} \tag{7-38}$$

Simplifying Equation 7-38, the average fracture surface area becomes:

$$\bar{S}_n = a^2 + \frac{2\pi R^3}{3a} \tag{7-39}$$

The ratio of the average fracture surface area to the fracture surface area of resin matrix is given by:

$$\frac{\bar{S}_n}{S_m} = \frac{a^2 + 2\pi R^3/3a}{a^2} = 1 + \frac{2\pi R^3}{3a^3} \tag{7-40}$$

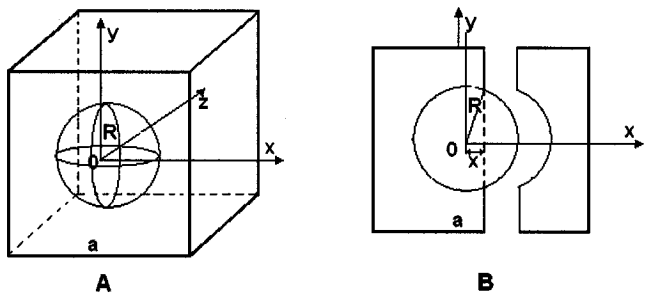

Figure 7-9: Schematic drawings of a cube representative volume element (RVE) and crack propagation and fracture mode in intercalated nanocomposite

By substituting the aspect ratio and the volume fraction of clay platelets into Equation 7-40, the ratio is given by:

$$\frac{\bar{S}_n}{S_m} = 1 + \frac{2\pi R^3}{3a^3} = 1 + \frac{\upsilon_a}{2} = 1 + \frac{d\upsilon_c}{2t} \tag{7-41}$$

The ratio of the energy release of an intercalated nanocomposite (U_n) to that of resin matrix (U_m) is given by:

$$\frac{U_n}{U_m} = \frac{\bar{S}_n}{S_m} = 1 + \frac{d\upsilon_c}{2t} \tag{7-42}$$

7.3 Experimental

7.3.1 Sample Preparation

The synthesis of epoxy resins, rubber-modified epoxies, conventional composites and nanocomposites is described in Chapters 4 and 5. The notation of nanocomposites and filler composites corresponding to the concentrations of various materials and

dispersion methods is listed in Tables 4-1 and 5-1. Single edge notch bending (SENB) specimens, including notch, were cast from a rubber mold, their upper surfaces were machined, and the specimens were pre-cracked by tapping a fresh razor blade frozen in liquid nitrogen into the notch. Specimen size is shown in Figure 7-10; at least 4 specimens of each composition were tested. The support span is 4 times the width of the specimen.

7.3.2 Mechanical Measurement

Fracture tests were performed on an MTS Servo Hydraulic Testing Machine at a crosshead speed of 10 mm/min, according to ASTM D 5045-99.

The critical stress intensity factor (K_{IC}) can be calculated from the following formula in units of MPa.m$^{1/2}$:

$$K_{1C} = \sqrt{1000} \bullet \left(\frac{P_{\max}}{BW^{1/2}} \right) f(x) \tag{7-43}$$

where $$f(x) = 6x^{1/2} \frac{\left[1.99 - x(1-x)(2.15 - 3.93x + 2.7x^2)\right]}{(1+2x)(1-x)^{3/2}} \tag{7-44}$$

$$x = a/W \tag{7-45}$$

P_{max} is the maximum load (N); B is the specimen thickness (about 7.3 mm, shown in Figure 7-10);W is the specimen width (about 22 mm, shown in Figure 7-10); and a is the crack length (about 11 mm).

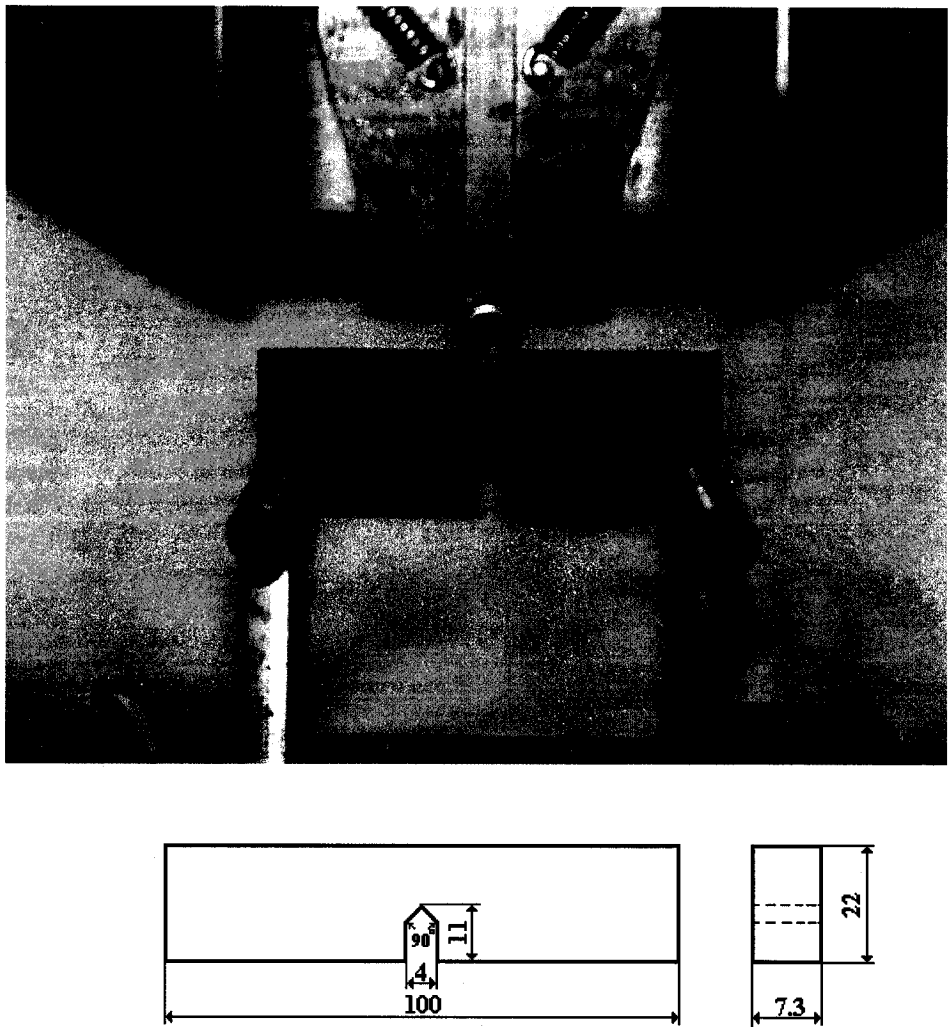

Figure 7-10: Specimen dimensions of SENB.

The critical strain energy release rate (G_{IC}) can be calculated from the following formula, in units of J/m^2:

$$G_{1C} = U / BW\Phi \tag{7-46}$$

where: $U = 1/2 P_{max}(u_{\max} - u_i)$ (7-47)

$$\Phi = \frac{A + 18.64}{dA/dx} \tag{7-48}$$

$$A = \left[16x^2/(1-x^2)\right]\left(8.9 - 33.717x + 79.616x^2 - 112.952x^3 + 84.815x^4 - 25.672x^5\right) \tag{7-49}$$

u_{max} is the maximum displacement; and u_i is the indentation displacement.

7.4 Results and Discussion

Fracture toughness was measured using three-point single-edge notched bending (SENB) specimens of pure epoxy resin, rubber-modified epoxies, filler composites and nanocomposites. Effects of surface modification of clay, dispersion methods, different epoxy resins and organoclays, and hybrid modification with organoclay and rubber on toughness are discussed.

7.4.1 Effect of Surface Modification of Clay on Toughness

The effects of the interface between clay surface and epoxy resins on toughness were studied by adding unmodified (Na-clay) and modified clay (I.30E organoclay) into a TGDDM/DDS epoxy system by the DM method. Both critical stress intensity factor (K_{IC}) and critical strain energy release rate (G_{IC}) of filler composites and nanocomposites, as a function of clay loading are shown in Figures 7-11 and 7-12, respectively. The toughness of filler composites and nanocomposites increases with increasing clay loading. Nanocomposites show a higher increase in both K_{IC} and G_{IC} than filler composites at the same clay loading; 170% and 257% increase respectively, in K_{IC} and G_{IC} of TGDDM-DDS with 15-phr organoclay loading, but only 144% and 185% increase for untreated clay. These results are similar to those reported by Kornmann [55].

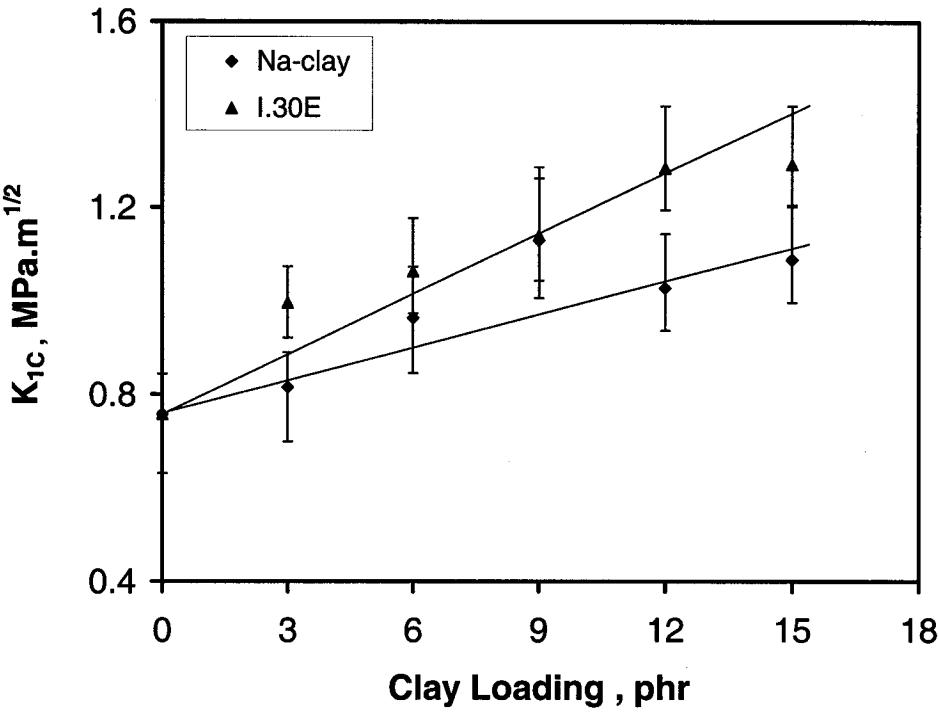

Figure 7-11: K_{IC} **of nanocomposites and filler composites made by the DM method.**

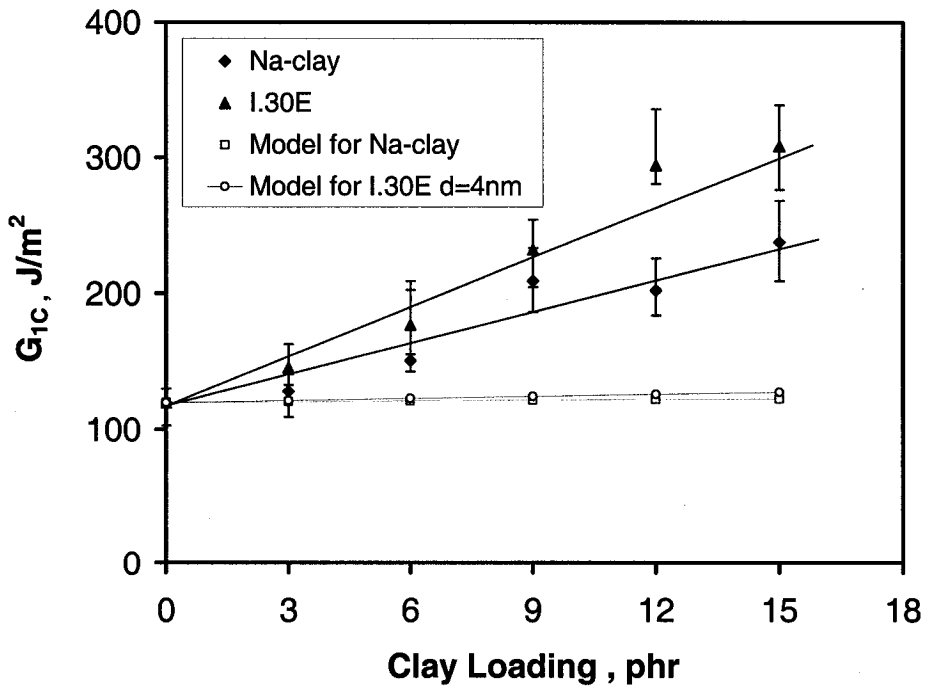

Figure 7-12: G_{IC} **of nanocomposites and filler composites made by the DM method.**

G_{IC} values calculated according to Equation 7-42 are also plotted in Figure 7-12. For the nanocomposites, the basal spacing and clay platelet thickness used in calculation are 4nm and 1nm, respectively. Clearly the experimental data are much higher than the calculated values, for both filler composites and nanocomposites, indicating that the increased fracture surface area contributes little to enhancing toughness for these two materials.

According to the crack-pinning mechanism, the ratio σ_c/σ_m is equivalent to the ratio K_{IC} (composite)/K_{IC} (matrix), as a filler composite and unfilled polymer contain primary cracks of the same length. From Figure 7-9, the ratio of particle diameter to interparticle separation (d_p/D_s) of nanocomposites is given by:

$$\frac{d_p}{D_s} = \frac{2R}{a-2R} = \frac{2}{\sqrt[3]{\frac{4\pi}{3d\upsilon_c}} - 2} \tag{7-50}$$

Measured values of the ratio K_{IC} (nanocomposite)/K_{IC} (matrix) are plotted against the ratio (d_p/D_s) in Figure 7-13. The basal spacing used in calculation are 4nm. It is clear that DM nanocomposites follow the theoretical predictions quite closely, indicating that the crack pinning mechanism may be the main reason for enhancing the fracture toughness of nanocomposites made by the DM method.

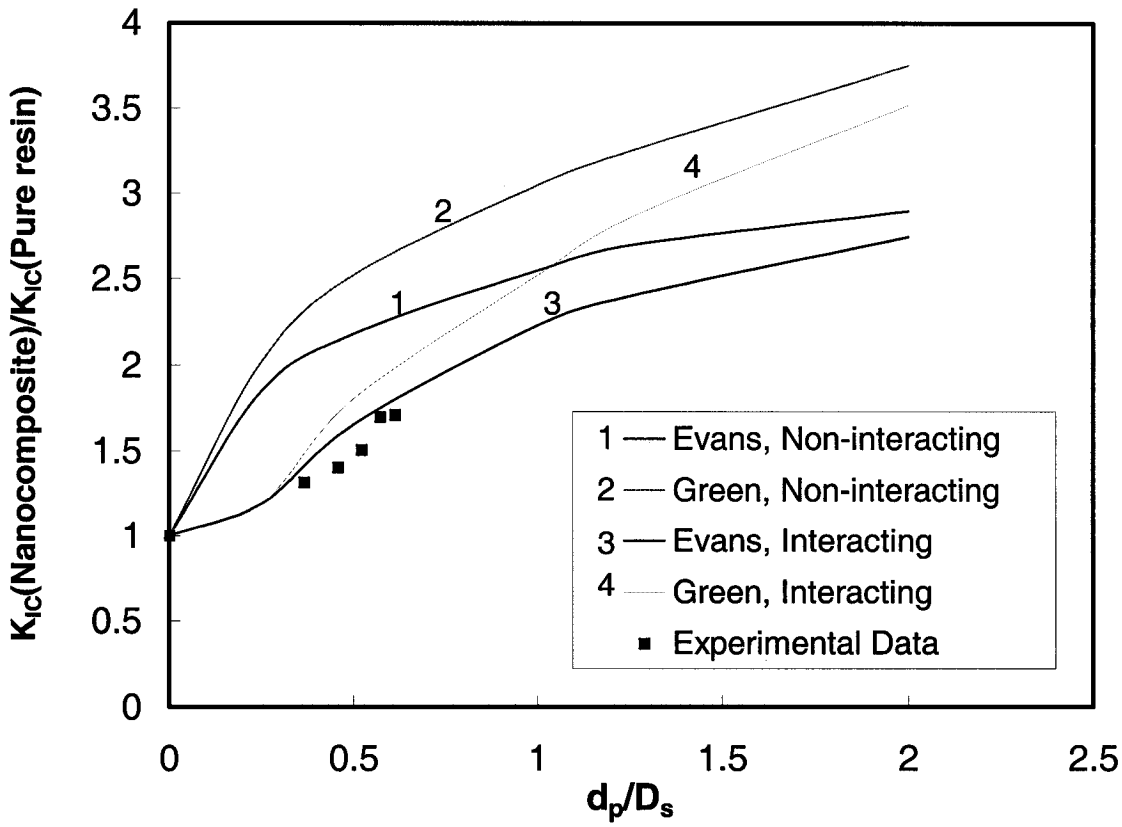

Figure 7-13: Ratio K_{IC} (nanocomposite)/K_{IC} (matrix) *versus* ratio (d_p/D_s), for nanocomposites made by the DM method

SEM was used to elucidate the toughening of these filler composites and nanocomposites. The pristine resin samples show smooth and featureless surfaces, representing brittle failure in a homogenous material, even at high magnification (shown in Figures 7-14 A and B). The arrows above the figures indicate the direction of crack propagation.

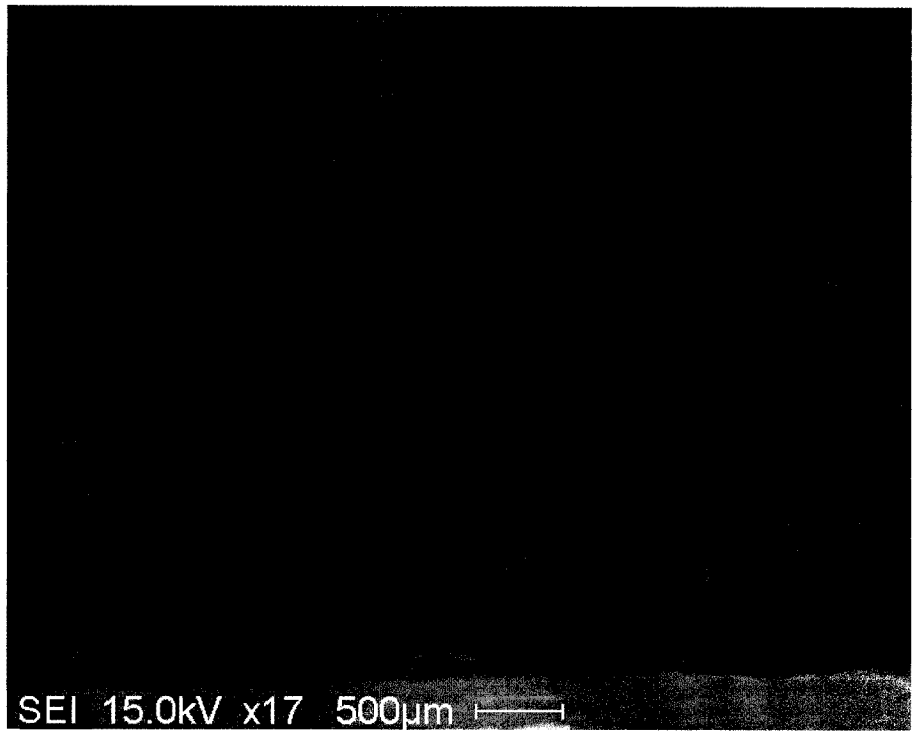

A

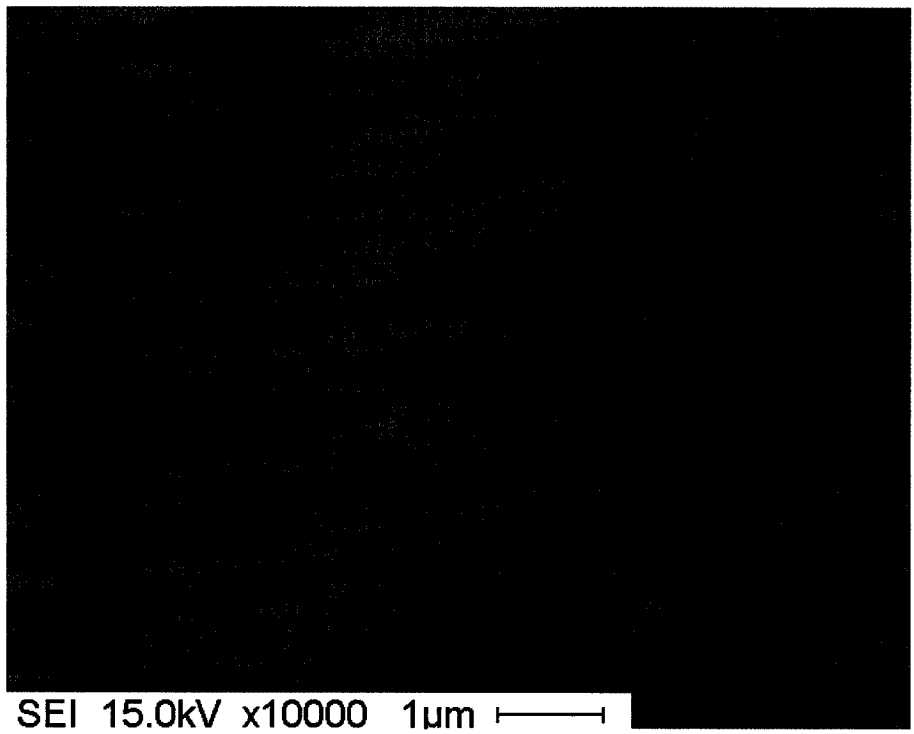

B

Figure 7-14: SEM micrographs of TGDDM/DDS epoxy systems.

Figures 7-15 A and B show typical fracture topology of filler composites (6-phr clay loading). Agglomerates are visible in different sizes, with a maximum diameter of about 20 μm. The particles are debonded from the resin, and voids are formed around the particles due to the poor compatibility and low adhesive strength of interface between the epoxy and the untreated clay. Thus toughness improvement may mainly be attributed to crack tip blunting due to local energy absorption from these features. A few shallow 'river-markings' are observed around the particles, running in the direction of crack propagation. These 'river-markings' occurred as a result of crack deflection and subsequent propagation on two slightly different fracture planes.

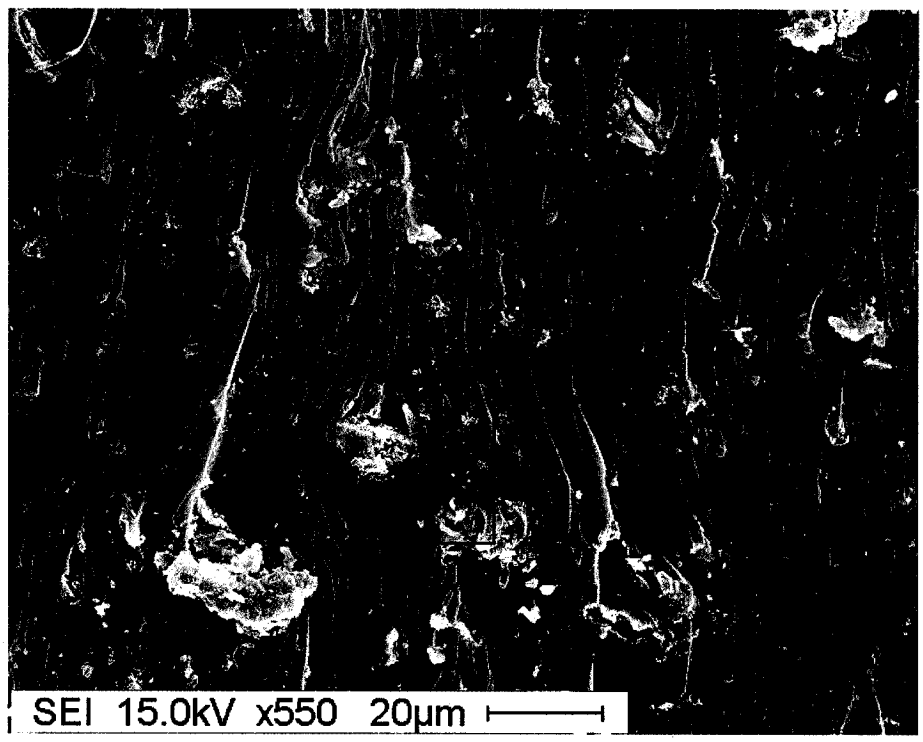

A

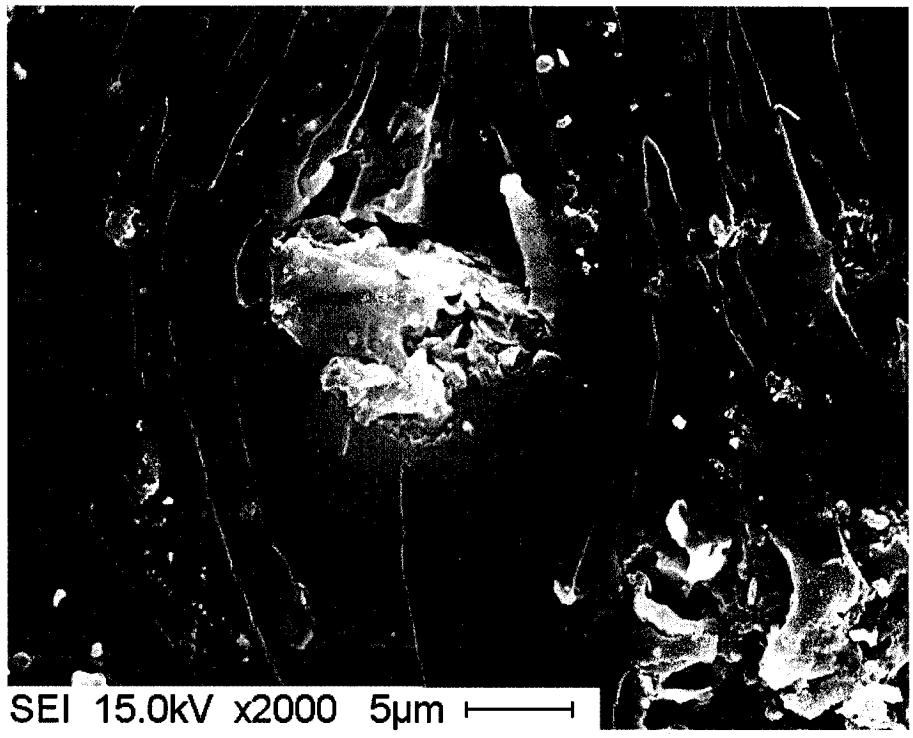

B

Figure 7-15: SEM micrographs of filler composite at 6-phr clay loading.

However, nanocomposites made by the DM method exhibit very different fracture surfaces, as shown in Figures 7-16 A (3-phr I.30E) and B (6-phr I.30E). Agglomerates are also visible, with maximum diameter of about 30 μm for these nanocomposites, larger than in filler composites. More agglomerates and deeper river-markings are observed with increasing clay loading; but only a few interface sections are debonded from the resin, and fewer voids are seen in the high magnification image (shown in Figure 7-16 C). This is attributed to the fact that epoxy molecules are intercalated into the organoclay and have a good interface with the platelets of organoclay, resulting in the formation of rigid and well-bonded agglomerates. These particles impede the propagation of cracks; as a propagating crack becomes temporarily pinned, and starts to bow out between the particles, forming secondary cracks; more and deeper river-markings are formed around

agglomerates. When the local stress exceeds the strength of the agglomerates or the adhesive strength of the particle/matrix interface, fracture of agglomerates or debonding of the particle/matrix interface occurs. Therefore, in contrast to filler composites, the pinning effect may be more dominant than the crack tip blunting effect in enhancing the facture toughness of nanocomposites made by the DM method. Further, increasing the quantity of agglomerates results in enhancing resistance to the propagation of cracks, and thus improving fracture toughness with increasing clay loading.

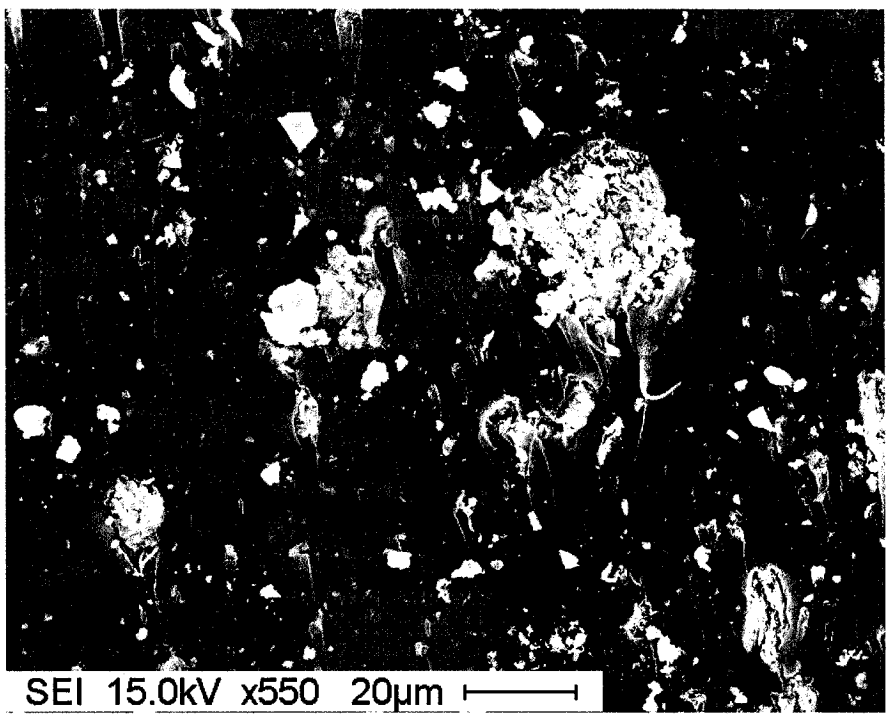

A (3-phr I.30E)

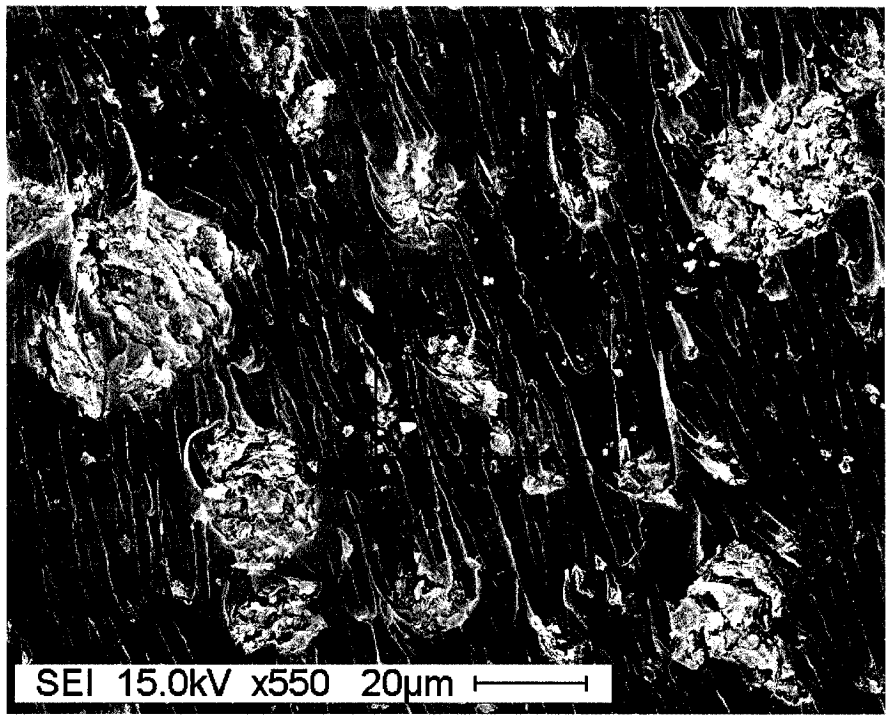

B (6-phr I.30E)

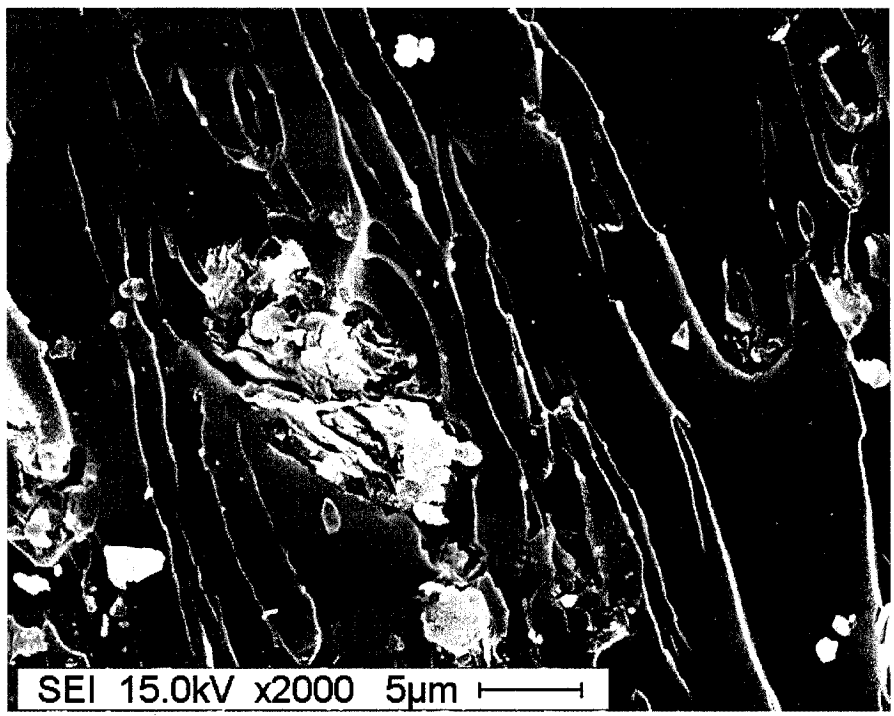

C (6-phr I.30E)

Figure 7-16: SEM micrographs of a nanocomposite made by the DM method.

7.4.2 Toughness of Nanocomposites with Different Dispersion Methods

As discussed in previous chapters, nanocomposites made by different dispersion methods have different structures. The previous section discusses toughness of nanocomposites made by the DM method; in this section, the results from nanocomposites made by the HPM and GMM methods are presented, and the effect of different methods on toughness of nanocomposites is discussed.

7.4.2.1 Nanocomposites Made by the HPM Method

Two groups of nanocomposites based on a TGDDM/DDS epoxy system were synthesized by the HPM method: I.30E organoclay dispersed in acetone, and I.30E dispersed in TGDDM epoxy/acetone solution, both introduced in Chapter 3. The former is symbolized as HPM-A, and the latter as HPM-E.

The critical stress intensity factor (K_{IC}) and critical stain energy release rate (G_{IC}) of HPM-E and HPM-A nanocomposites as a function of clay loading are shown in Figures 7-17 and 7-18, respectively. In these figures, the fracture toughness of nanocomposites made by the DM method is also given as a reference. For HPM-E nanocomposites, K_{IC} and G_{IC} increase almost linearly with increasing clay loading up to 4.5-phr clay loading; after that they increase slowly. K_{IC} and G_{IC} increase by 2.1 and 4.9 fold respectively, at 4.5-phr clay loading compared with pristine epoxy resin.

On the other hand, for nanocomposites made by HPM-A, K_{IC} and G_{IC} also increase linearly below 4.5-phr clay loading, but they decrease with further increase in clay loading. The maximum enhancement ratios of nanocomposites made by HPM-A are 2.2 in K_{IC} and 5.8 in G_{IC} at 4.5-phr clay loading. Therefore, nanocomposites made by HPM-A have higher toughness, but their data is more scattered than HPM-E. However, both have similar trends, that is dramatic improvement in fracture toughness below 4.5-phr clay loading due to better dispersion, whether nanocomposites were made by HPM-E or HPM-A.

G_{IC} values calculated according to Equation 7-29 are plotted in Figure 7-18. For the HPM nanocomposites, the basal spacing ***(d),*** clay platelet thickness ***(t),*** aspect ratio ***(ζ)*** and number of clay platelet ***(n)*** used in calculation are 6nm, 1nm, 600 and 5 respectively. Clearly the experimental data are much higher than the calculated values for either HPM-E or HPM-A nanocomposites; however, the calculated values for HPM nanocomposites are higher than those for DM nanocomposites. For example, the fracture surface increases by 2 fold at 7.5-phr clay loading compared with pristine epoxy resin. Therefore, the fracture surface of nanocomposites by the HPM method is greatly increased and the increase of fracture surface area is one reason for enhancing fracture toughness of epoxy resins.

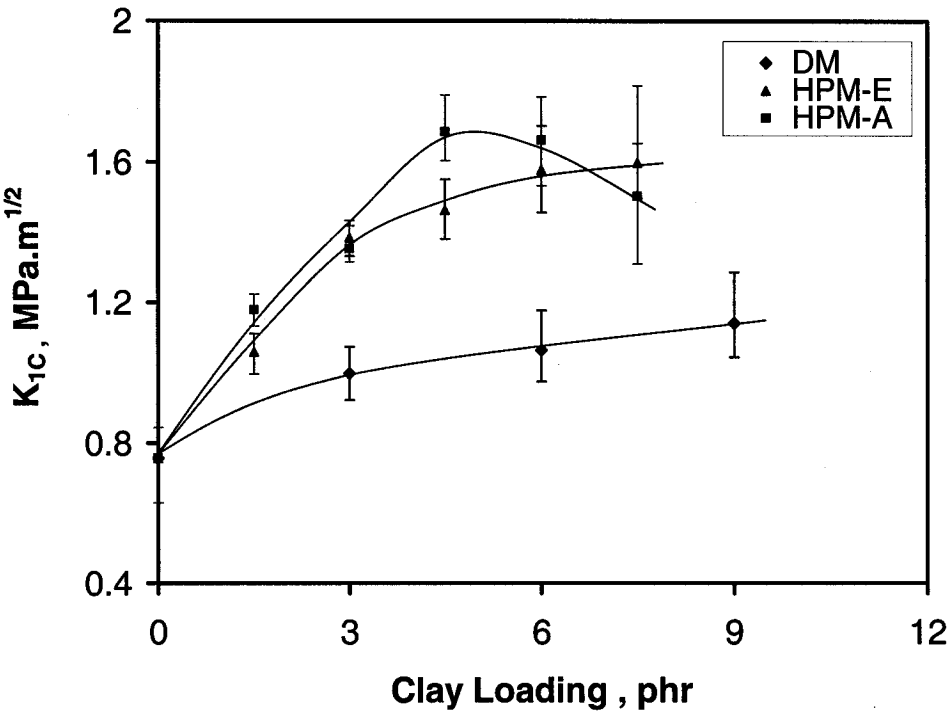

Figure 7-17: K_{IC} **of nanocomposites made by different methods.**

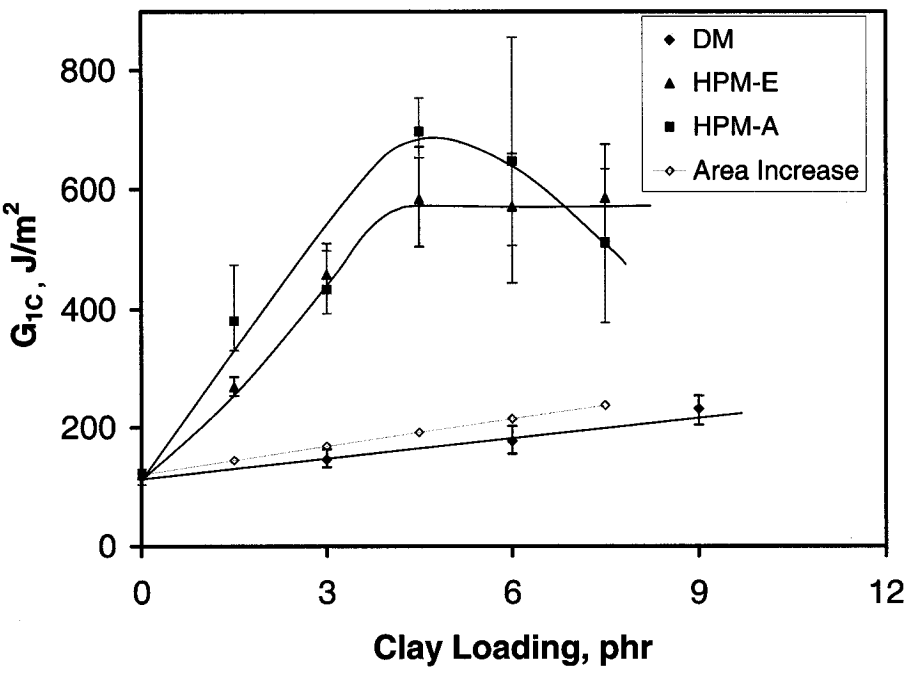

Figure 7-18: G_{IC} **of nanocomposites made by different methods.**

As organoclay is dispersed in the epoxy system by the HPM method, one spherical agglomerate (6 μm in diameter, if made by the DM method) can be broken down to 7000~10000 tactoids consisting of 5 ~ 10 silicate layers. Therefore, the interparticle separation (D_s) is greatly reduced.

Green, *et al.* have studied rectangular obstacles, and obtained the relationship between the ratio σ_c/σ_m and the ratio (d_p/D_s) of nanocomposites [148, 149]. If the face of clay platelets is a square with side length ℓ, and tactoids are placed as shown in Figure 7-13, the maximum possible interparticle separation is given by:

$$D_s = \left(\frac{nt}{v_c} - nt - (n-1)d \right) \tag{7-51}$$

The ratio of the side length to the interparticle separation (ℓ / D_s) of nanocomposites is given by:

$$\frac{\ell}{D_s} = \frac{\ell}{\left(\frac{nt}{v_c} - nt - (n-1)d \right)} \tag{7-52}$$

Measured values of the ratio (K_{IC}(nanocomposite)/K_{IC}(matrix)) are plotted against the ratio (ℓ/D_s) in Figure 7-19. For the HPM nanocomposites, the basal spacing *(d),* clay platelet thickness *(t),* side length *(l)* and number of clay platelet *(n)* used in calculation are 6nm, 1nm, 600 and 5 respectively. Clearly the measured values of HPM nanocomposites follow the theoretical predictions quite closely at clay loading below 4.5-phr, for either HPM-E or HPM-A nanocomposites, but they are less than the theoretical predictions beyond that. Therefore, the crack pinning mechanism may still

be the main factor in enhancing the fracture toughness of nanocomposites made by the HPM method.

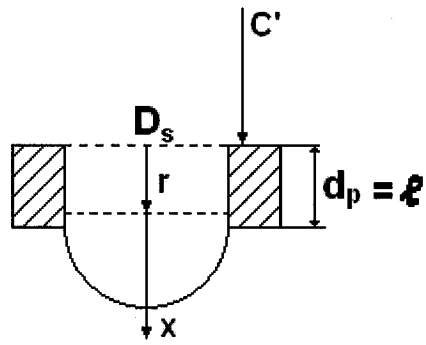

Figure 7-19: Schematic illustration of rectangular obstacles.

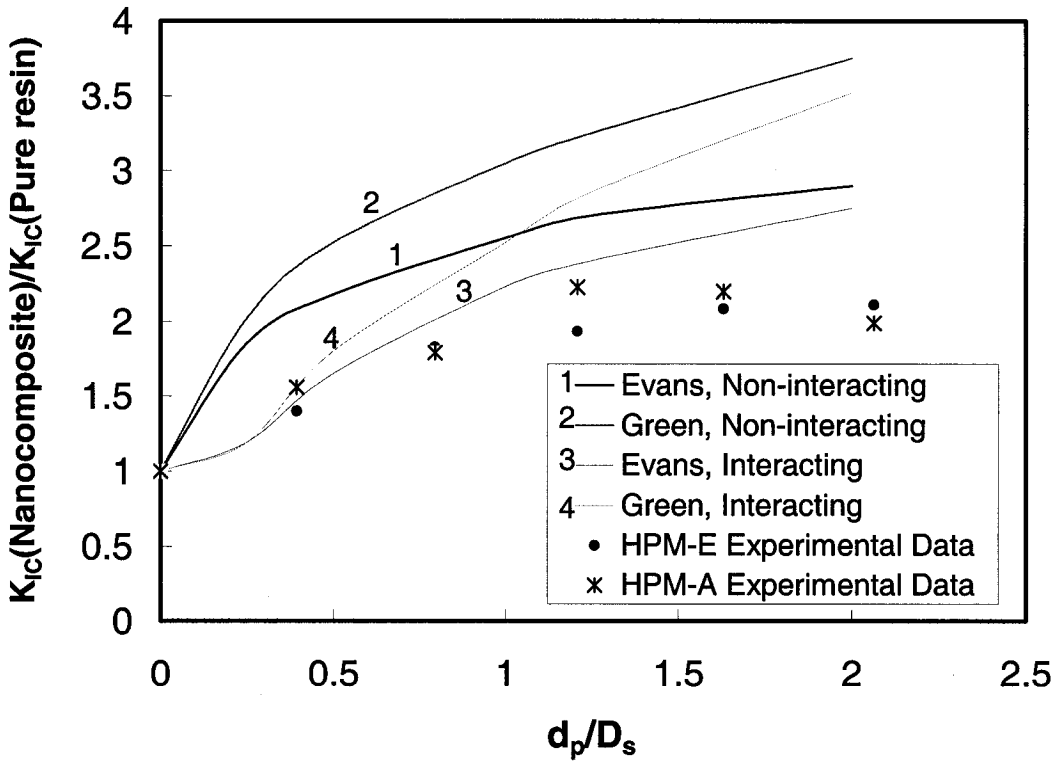

Figure 7-20: Ratio K_{IC} (nanocomposite)/K_{IC} (matrix) *versus* ratio (ℓ/D_s) for nanocomposites made by the HPM method

Figures 7-21 (A and B) and 7-22 (A and B) show fracture surfaces of nanocomposites at 6-phr clay loading made by HPM-E and HPM-A, respectively; they have very similar topology. The fracture surface of nanocomposites made by HPM-E or HPM-A is rougher than those made by DM. No distinct agglomerates are observed on this micrograph, even at relatively high magnification. Crack bifurcation is quite evident, associated with the presence of very small particles that are assumed to be dispersed clay. Therefore, the pinning effect may be still the main factor enhancing the fracture toughness of nanocomposites made by HPM. But there are some holes on the surface of the latter, which may be attributed to small particles pulled out during testing.

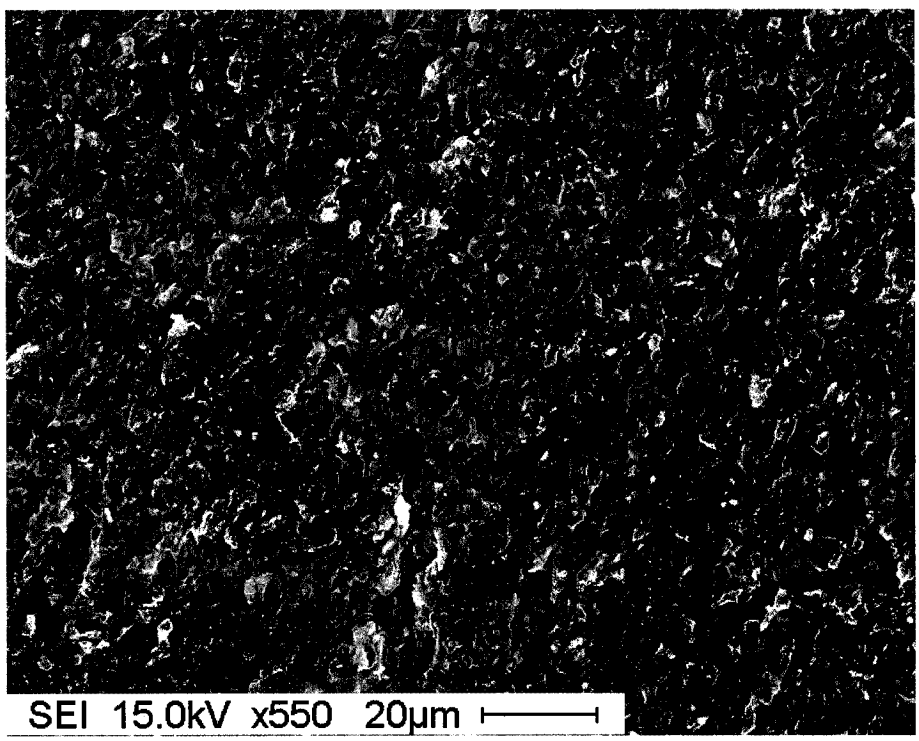

A

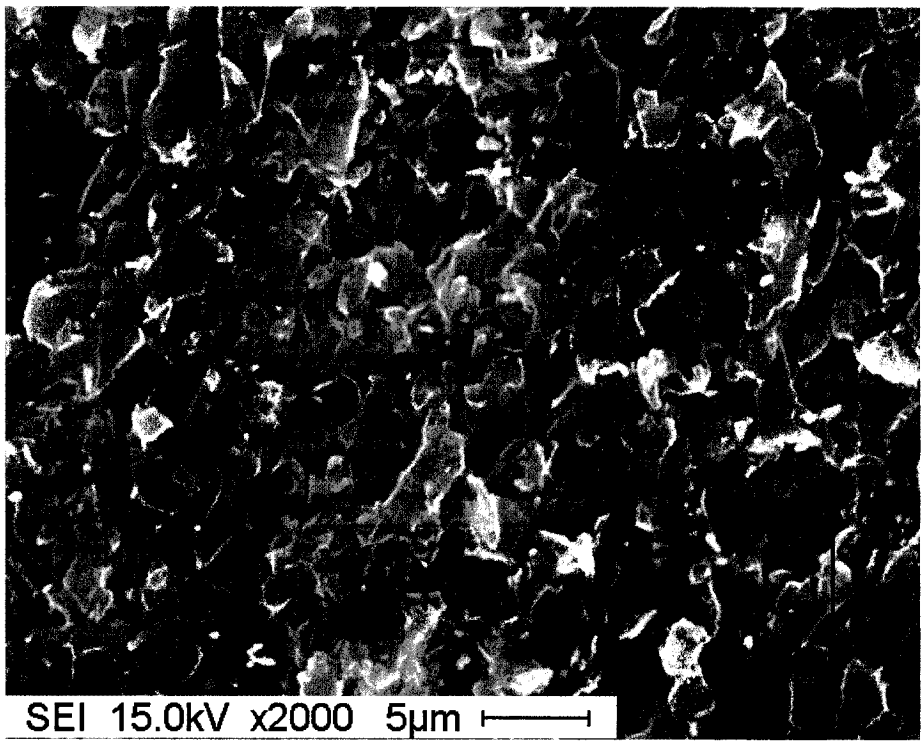

B

Figure 7-21: SEM micrographs of HPM-E nanocomposite at 6-phr clay loading.

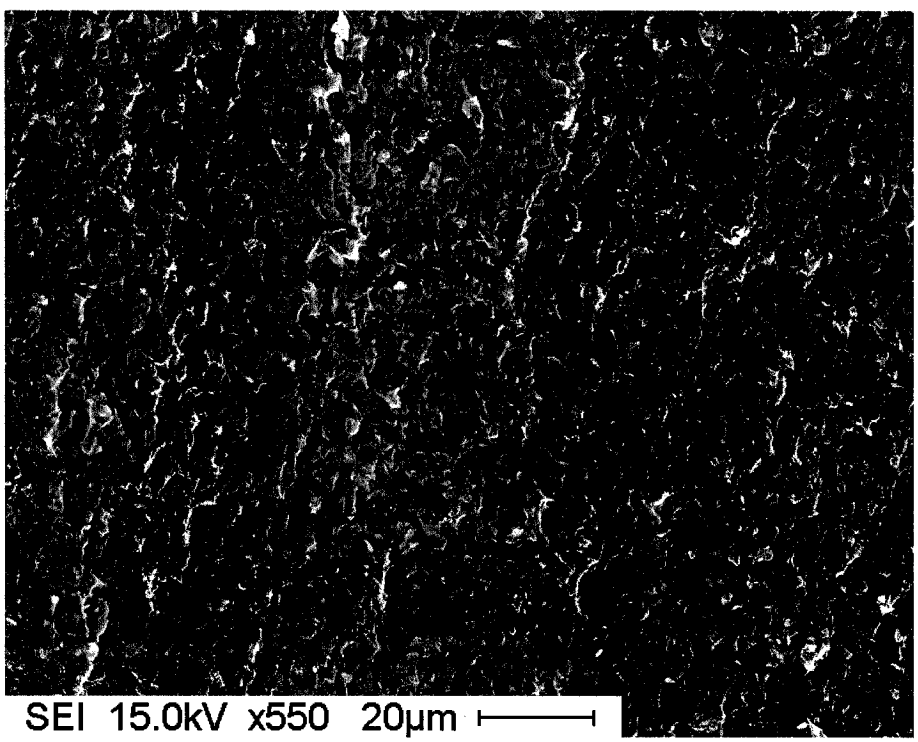

A

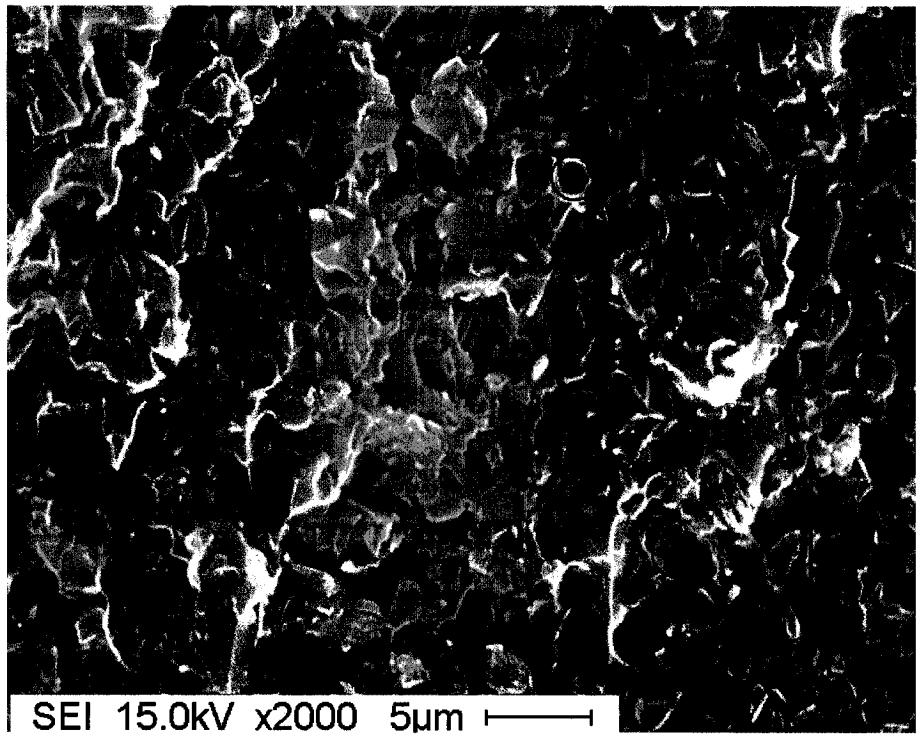

B

Figure 7-22: SEM micrographs of HPM-A nanocomposite at 6-phr clay loading.

7.4.2.2 Nanocomposites Made with the GMM Method

GMM nanocomposites were synthesized by dispersing 6-phr I.30E organoclay into a TGDDM/DDS system, using the GMM method with different grinding times. Figures 7-23 and 7-24 show the critical stress intensity factor (K_{IC}) and critical strain energy release rate (G_{IC}) of the GMM nanocomposites with different grinding times at 6-phr clay loading, respectively. In order to compare the effect of different methods, those of nanocomposites made with the DM and HPM methods at the same clay loading are also given in these figures.

Figure 7-23 shows that the critical stress intensity factor (K_{IC}) of the GMM nanocomposites increases with grinding time. However, the critical stain energy release

rate (G_{IC}) of the GMM nanocomposites increases with grinding time below 4 hours, but it does not change with further increase in grinding time, as shown in Figure 7-24. The K_{IC} and G_{IC} of GMM nanocomposites are higher than those of DM, but lower than those of HPM, nanocomposites. This may be attributed to the fact that the GMM nanocomposites have better dispersion of clay platelets in the epoxy than DM, but worse dispersion than the HPM nanocomposites.

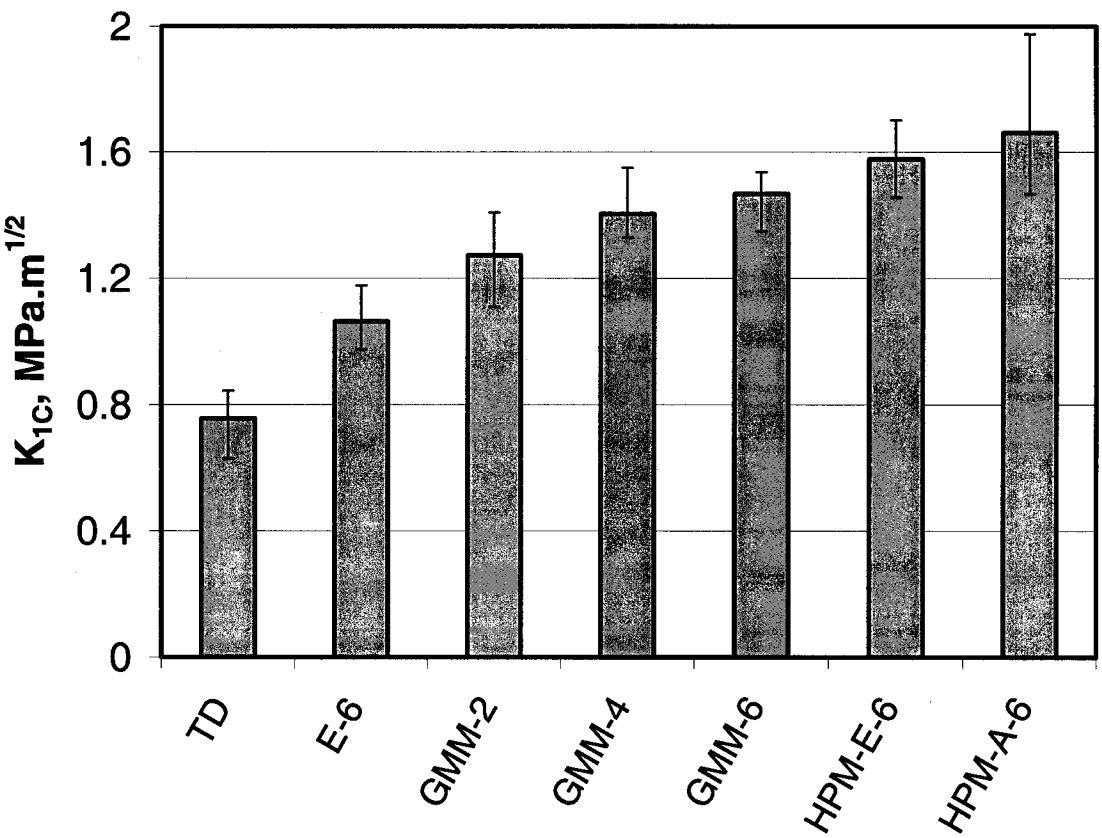

Figure 7-23: K_{IC} of nanocomposites with different methods at 6-phr clay loading

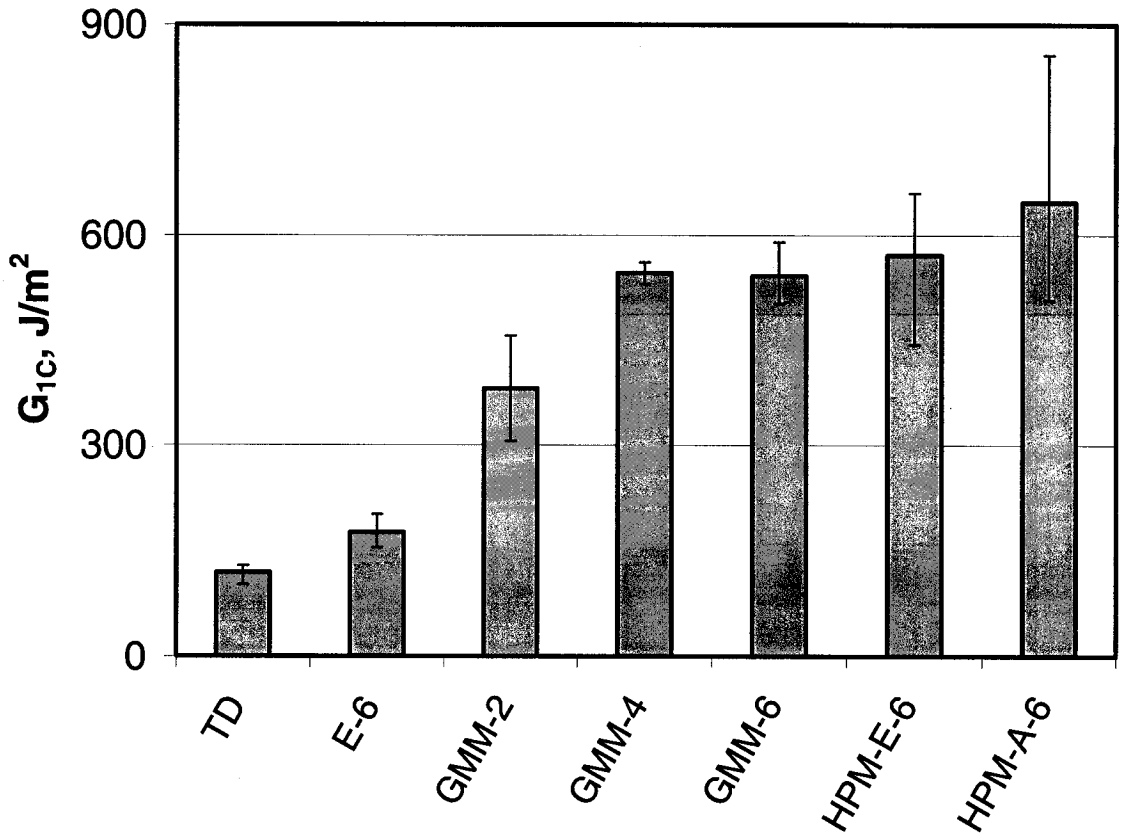

Figure 7-24: G_{IC} of nanocomposites with different methods at 6-phr clay loading

Figures 7-25 (A and B), 7-26 (A and B) and 7-27 (A and B) show fracture surfaces of GMM nanocomposites at 6-phr clay loading for 2, 4 and 6 hours, respectively. They have very similar topology, containing both agglomerates and evident crack bifurcations.

Compared with the DM nanocomposite (E-6, Figure 7-16 B and C), the GMM-2 (grinding time of 2 hours) nanocomposite shows that the number and size of agglomerates are greatly reduced on the fracture surface (Figures 7-25 A and B). The maximum diameter of agglomerates is about 10 μm. The crack bifurcation of GMM-2 nanocomposites is more evident than that of DM nanocomposites. On the other hand, compared with HPM nanocomposites (Figure 7-20 and 7-21), the GMM-2

nanocomposite still contains some agglomerates, and the crack bifurcation is less evident than those of HPM nanocomposites.

As grinding time increases to 4 hours, the number and size of agglomerates reduces, and crack bifurcation is stronger. When we further increase the grinding time to 6 hours, the maximum size of agglomerates is further decreased to 5 μm, but the number increases (shown in Figure 7-27 A and B) due to different batches and lack of control of the amount of energy applied.

Therefore, the pinning effect in GMM nanocomposites may be still the main reason for enhancing the facture toughness of nanocomposites with the GMM method.

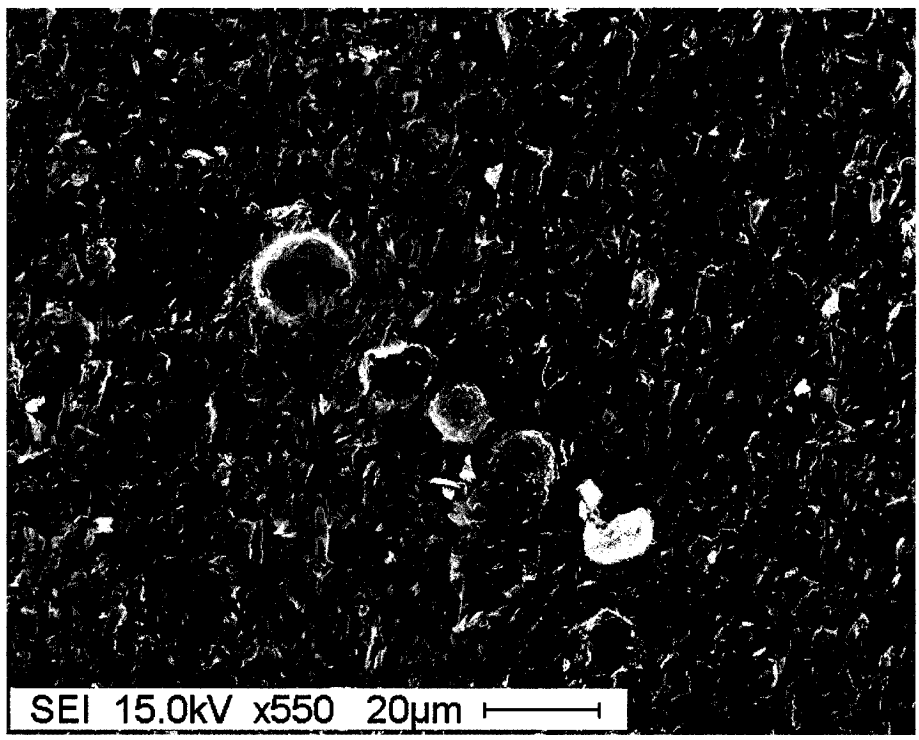

A

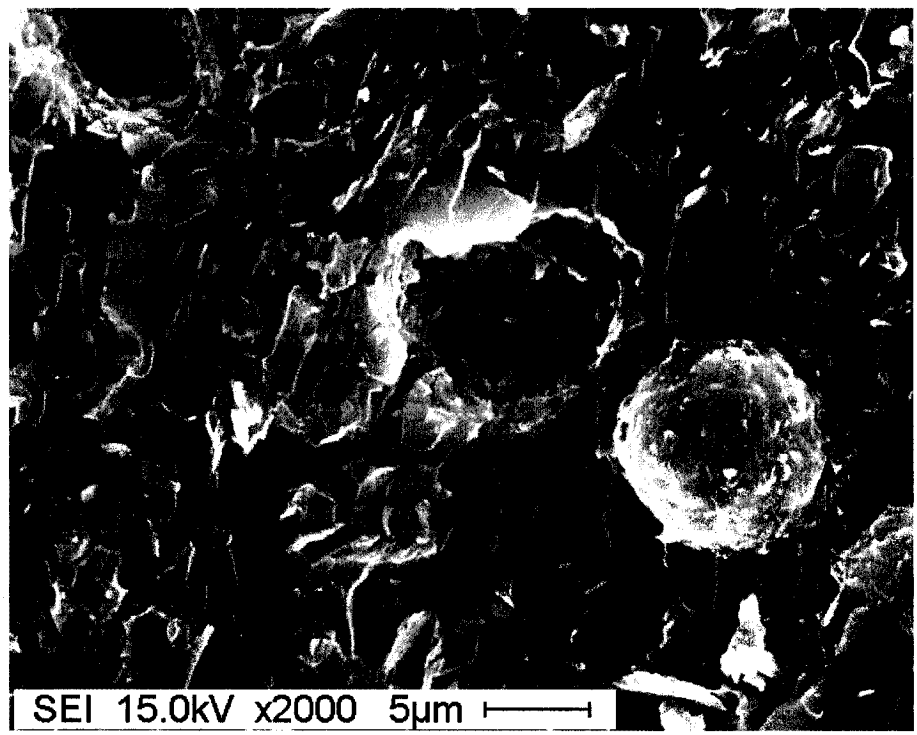

B

Figure 7-25: SEM micrographs of the GMM-2 nanocomposite at 6-phr clay loading

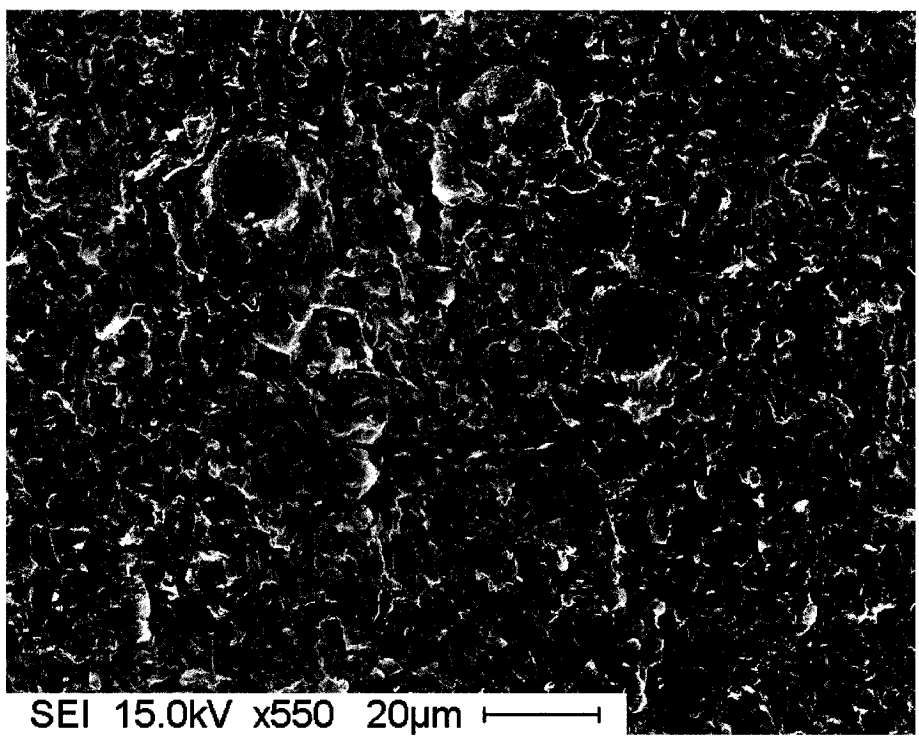

A

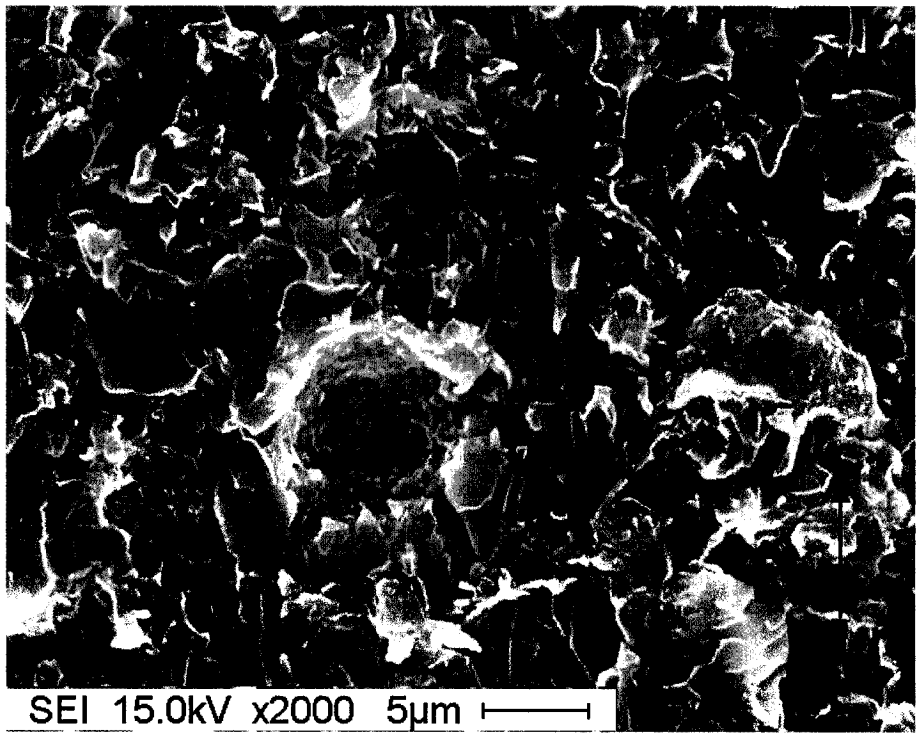

B

Figure 7-26: SEM micrographs of the GMM-4 nanocomposite at 6-phr clay loading

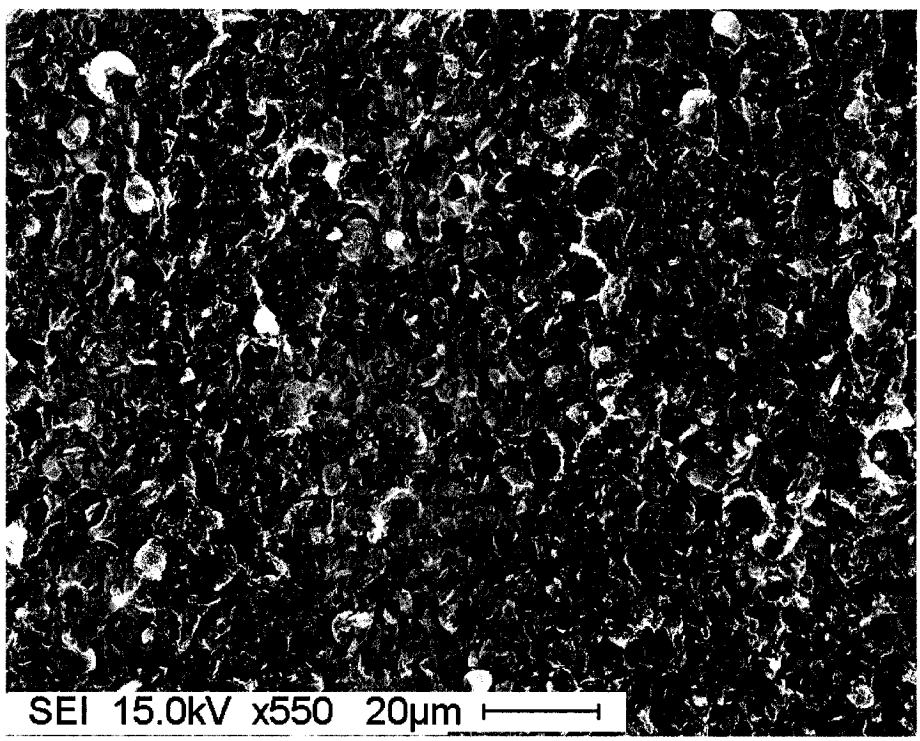

A

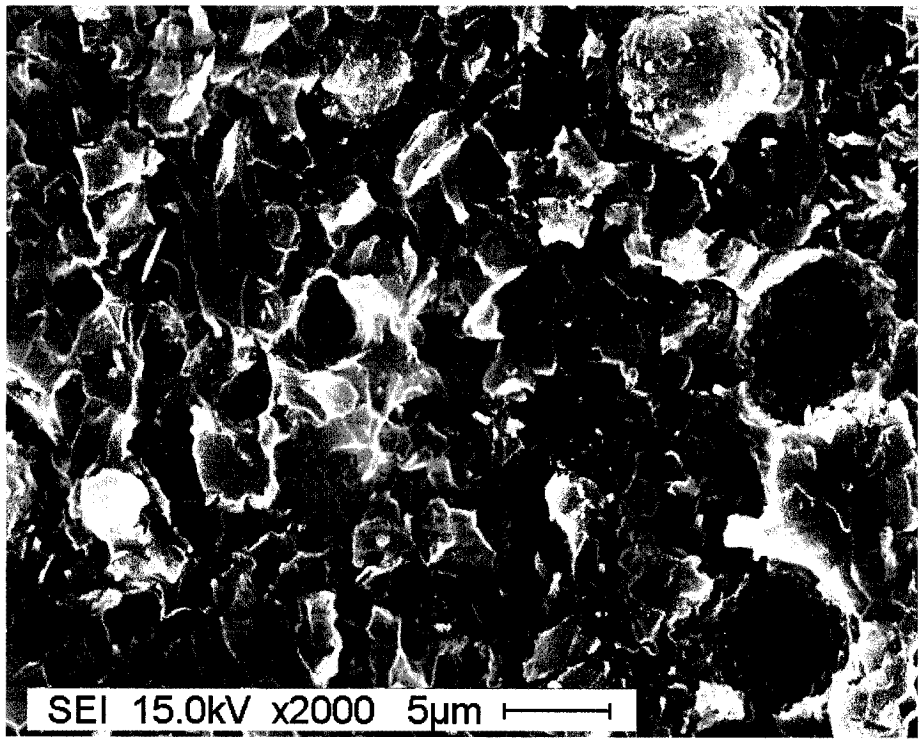

B

Figure 7-27: SEM micrographs of the GMM-6 nanocomposite at 6-phr clay loading

7.4.3 Nanocomposites with Different Epoxy Systems

The fracture toughness of nanocomposites based on the TGDDM/DDS system has been studied in previous sections. In this section, nanocomposites based on a DGEBA/BF_3.MEA epoxy system are discussed. These nanocomposites were only made of DGEBA/BF_3.MEA system and I.30E organoclay, with the HPM-E dispersion method.

Figures 7-28 and 7-29 show the critical stress intensity factor (K_{IC}) and critical stain energy release rate (G_{IC}) of nanocomposites based on DGEBA/BF_3.MEA epoxy as a function of clay loading, respectively. In these figures, the fracture toughness of nanocomposites based on the TGDDM/DDS system is also given as a reference.

In nanocomposites based on DGEBA/BF_3.MEA, K_{1C} almost linearly increases with increasing clay loading; however, there is a significant jump of G_{IC} upon adding 1.5-phr clay, and after that it increases slowly. The K_{IC} and G_{IC} of the nanocomposite at 6-phr clay loading are increased by 1.84 and 2.97 times those of the pristine resin system, respectively. Therefore, nanocomposites based on DGEBA/BF_3.MEA have a similar increasing trend in fracture toughness with clay loading as nanocomposites based on TGDDM/DDS system. However, enhancing efficiency in toughness for nanocomposites based on DGEBA/BF_3.MEA is lower than that of nanocomposites based on TGDDM/DDS system, indicating that the matrix resin also has an effect on the toughness enhancement of nanocomposites.

Figure 7-30 shows a smooth and featureless fracture surface of a DGEBA/BF_3.MEA pure resin system, similar to that of TGDDM/DDS, and representing brittle failure in a homogenous material. Figure 7-31 exhibits a fracture surface of a nanocomposite based on DGEBA/BF_3.MEA at 6-phr clay loading. Compared with a nanocomposite based on the TGDDM/DDS system (Figures 7-21 A and B), the fracture surface of the nanocomposite based on DGEBA/BF_3.MEA has less evident crack bifurcation than the nanocomposite based on TGDDM/DDS system. Some small agglomerates can be detected on the fracture surface of the nanocomposite based on DGEBA/BF_3.MEA. These surface features make it clear that nanocomposites based on this resin have lower toughening enhancement than those based on the TGDDM/DDS system.

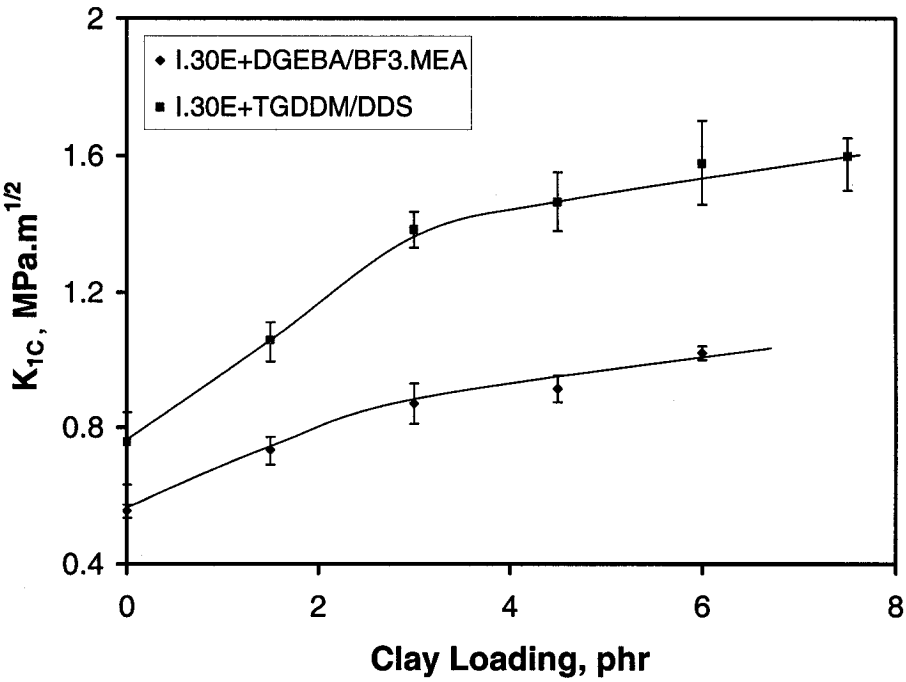

Figure 7-28: K_{IC} **of nanocomposites based on different epoxy systems with the HPM method**

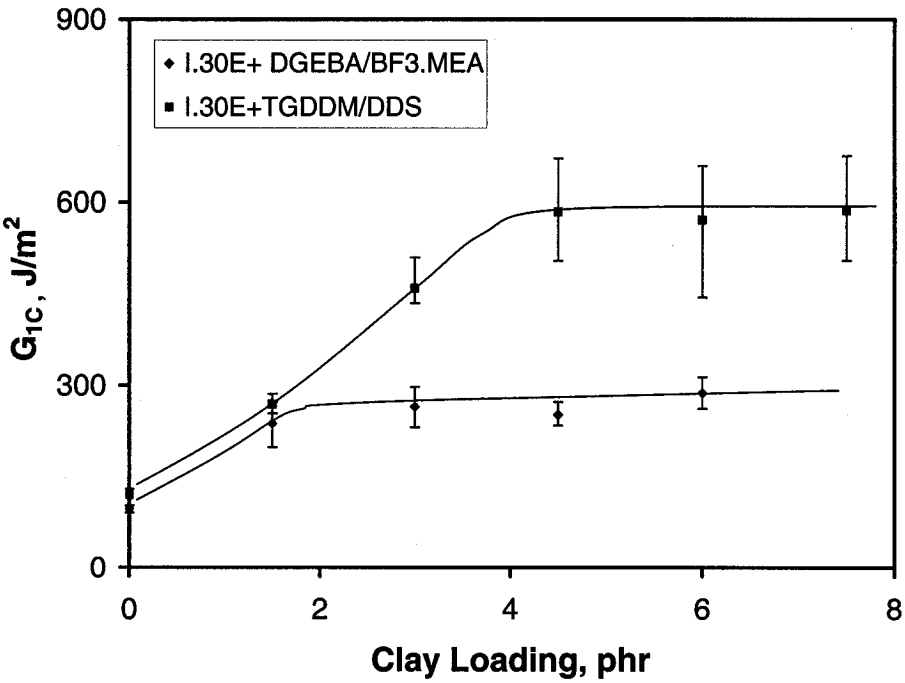

Figure 7-29: G_{IC} **of nanocomposites based on different epoxy systems with the HPM method**

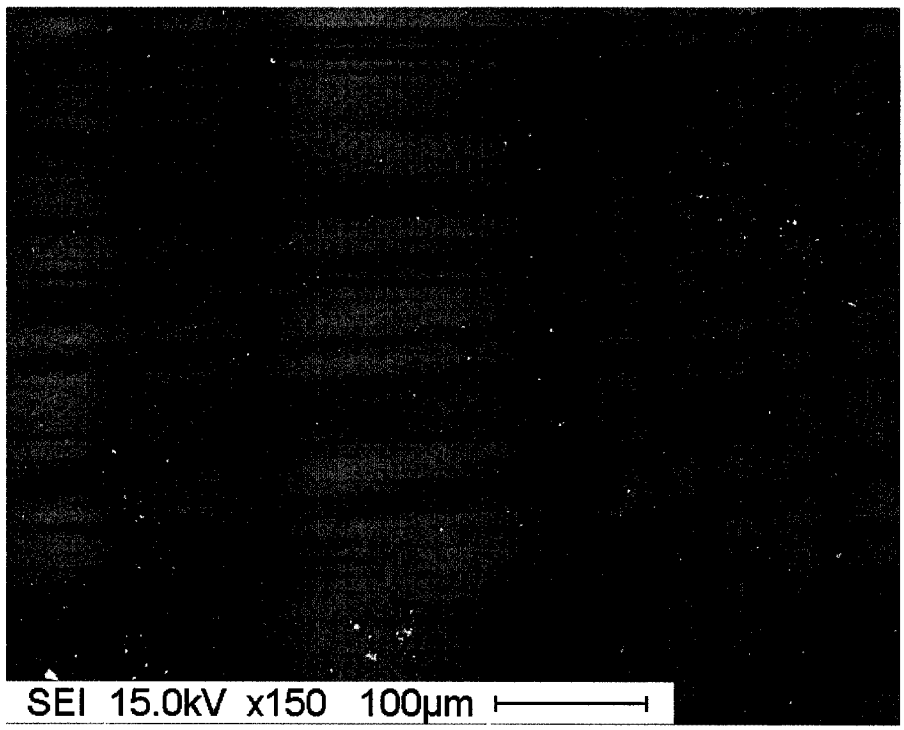

Figure **7-30: SEM micrograph of BF_3.MEA/DGEBA epoxy system**

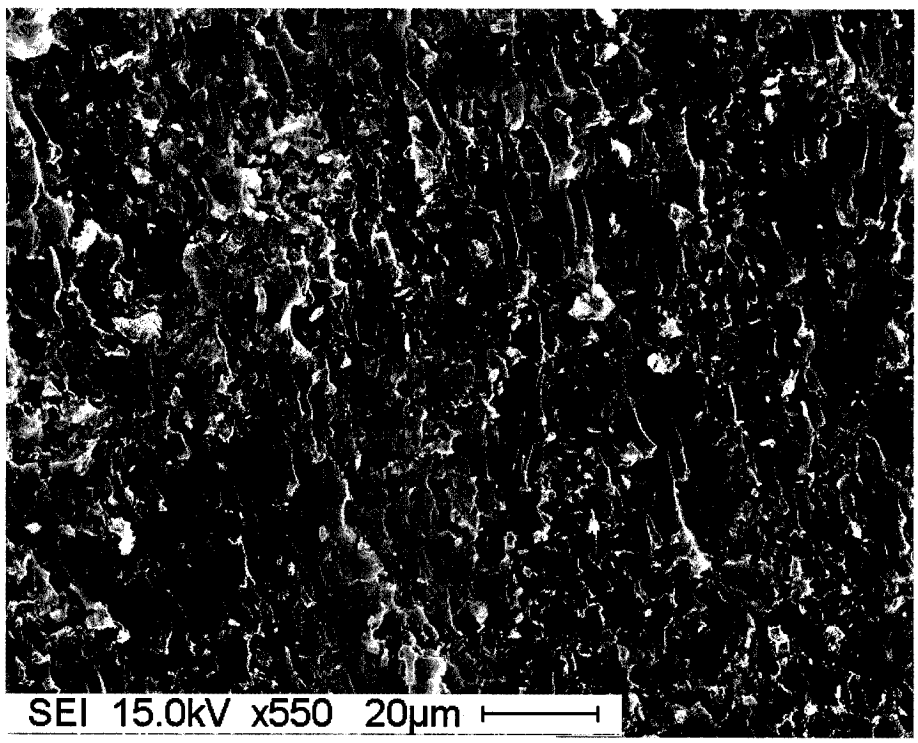

Figure 7-31: SEM micrograph of I.30E/BF_3.MEA/DGEBA nanocomposite at 6-phr clay loading

7.4.4 Fracture Toughness of Hybrid Nanocomposites

Fracture toughness of hybrid nanocomposites modified with CTBN rubber and I.30E organoclay depend on not only the clay loading but also the concentration of CTBN rubber. As a result, in this section, fracture toughness of the rubber-modified DGEBA/BF_3.MEA epoxies is first discussed.

7.4.4.1 Fracture Toughness of Modified Epoxies

The K_{IC} and G_{IC} of rubber-modified DGEBA/BF_3.MEA epoxies increase with increasing concentrations of CTBN, as shown in Figures 7-32 and 7-33, respectively. However, at lower CTBN content, such as 5-phr and 10-phr, fracture toughness increases slowly, due to only a small quantity of rubber phase separated from the epoxy resin. On the other hand, as CTBN content goes over 15-phr, K_{IC} decreases and G_{IC} increases slightly only because of the great reduction of strength. Compared with the pure resin system, K_{IC} and G_{IC} are increased by 1.7 and 3.7 times, respectively, at 20-phr concentration of CTBN.

Figures 7-34 A, B and C show fracture surfaces of the modified epoxy at 5, 15 and 20-phr CTBN rubber content. A two–phase microstructure with the rubber spheres dispersed in the continuous epoxy phase is observed. The number of rubber spheres increases with the concentration of CTBN. The white lines are due to tearing of the material between two crack planes, causing a surface step. Some cavities are observed in the rubber particles and the epoxy resin, because of the cohesive failure of rubber particles.

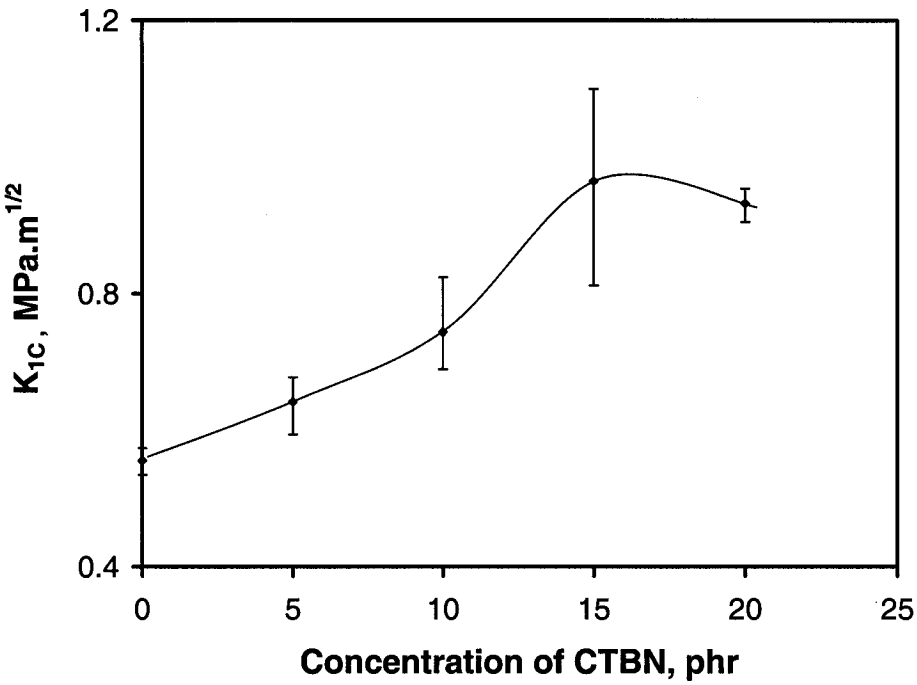

Figure 7-32: K_{IC} **of rubber modified epoxies with concentration of CTBN**

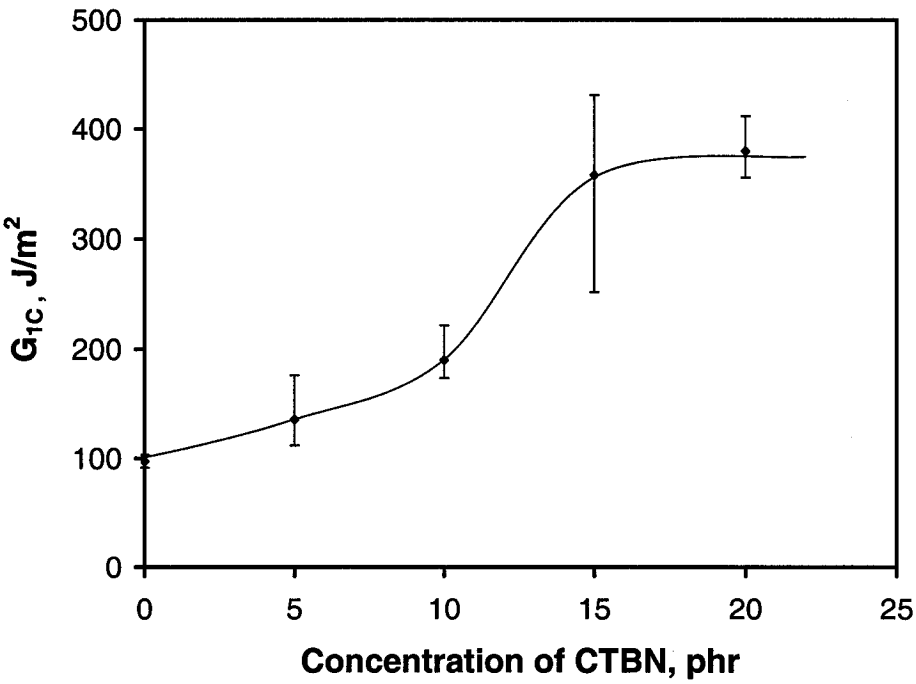

Figure 7-33: G_{IC} **of rubber modified epoxies with concentration of CTBN**

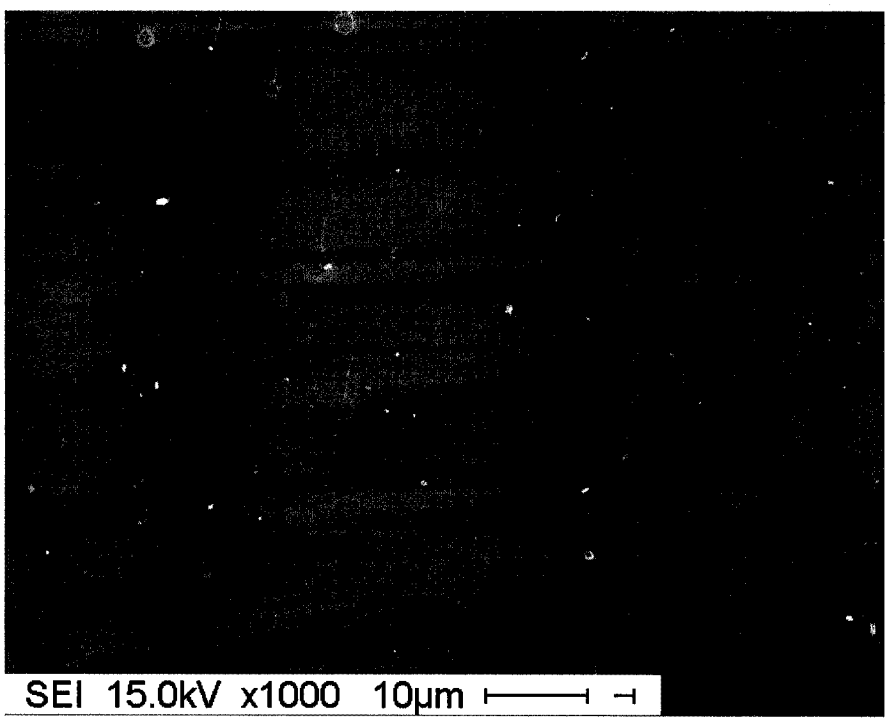

A (8C-5)

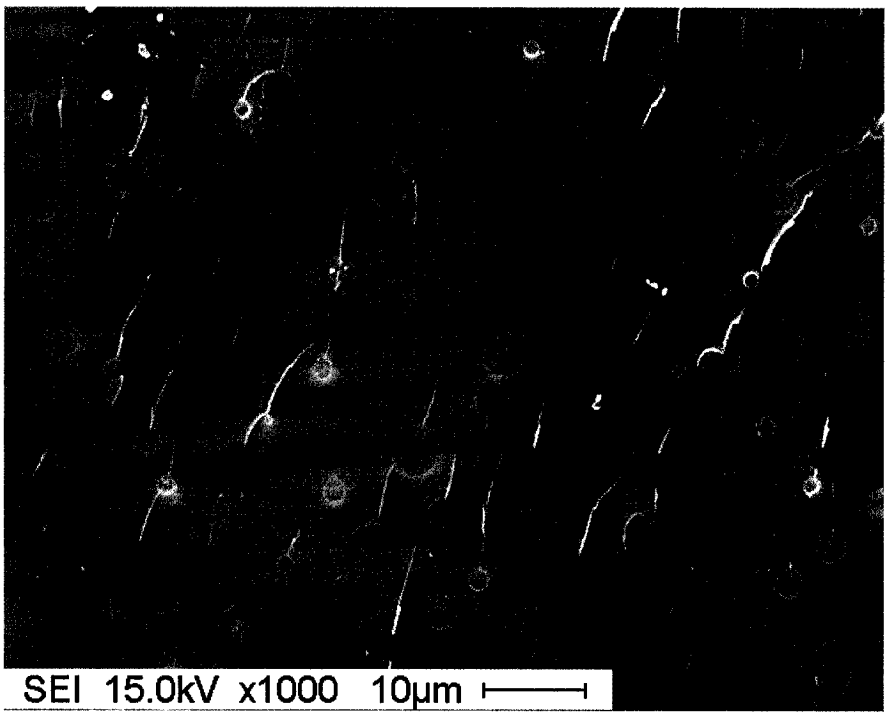

B (8C-15)

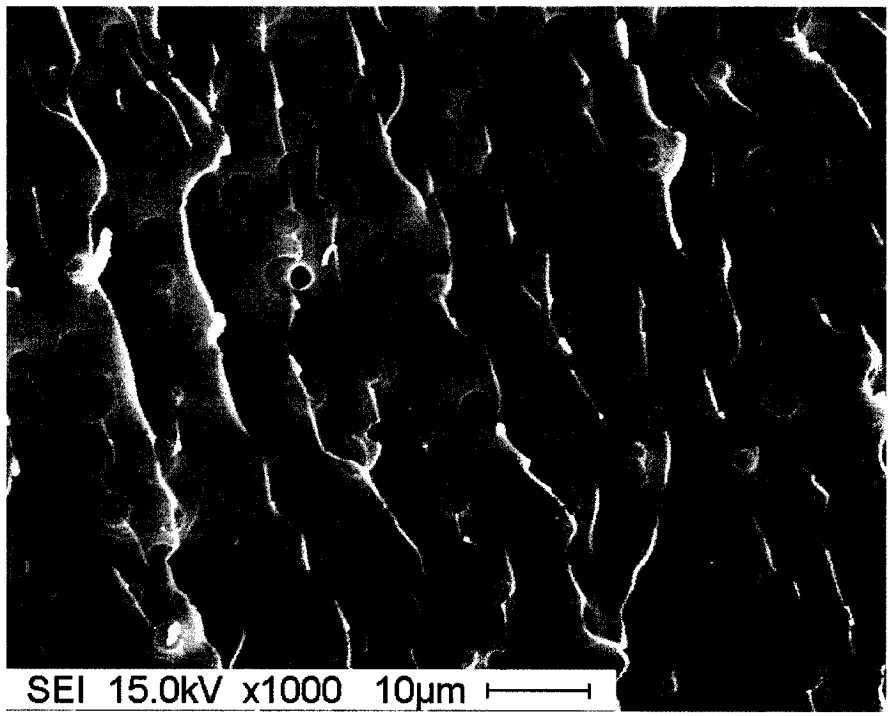

C (8C-20)

Figure 7-34: SEM micrographs of rubber modified epoxies

7.4.4.2 Fracture Toughness of Hybrid Nanocomposites

Both critical stress intensity factor (K_{IC}) and critical strain energy release rate (G_{IC}) of hybrid nanocomposites as a function of clay loading are shown in Figures 7-35 and 7-36. In these figures, the fracture toughness of nanocomposites based on DGEBA/BF_3.MEA without CTBN is also given as a reference.

Hybrid nanocomposites modified with rubber and organoclay show a further increase in both K_{IC} and G_{IC} (over the rubber-modified epoxies) as the clay loading increases. All the nanocomposites contain the same content of CTBN (20-phr), but with different organoclay contents ranging from 0 to 6-phr. While clay loading is less than

3-phr, fracture toughness increases slowly; but beyond this value, there is a dramatic improvement in fracture toughness. K_{IC} and G_{IC} are increased by 2.2 and 7.7 times respectively, at 6-phr organoclay loading and 20-phr CTBN, compared with the pristine epoxy system. Therefore, there is a superposition effect on fracture toughness of the hybrid epoxy nanocomposites modified with rubber and organoclay.

When the epoxy is modified with both rubber and organoclay at low clay loading (8CI-20-3), the fracture surface shows both features of fracture surfaces described above: rubber modified epoxies and nanocomposites (Figure 7-37A). Rubber particles are observed with diameters of 14~ 20 μm, larger than those in the rubber-modified epoxy. The crack bifurcations are smaller and of lower degree, indicating that toughening by rubber dominates the toughness of this material at lower clay loading. Upon increasing clay loading to 4.5-phr, the fracture surface exhibits a stronger three-dimensional appearance (Figure 37B). The rubber particles are difficult to detect, and the crack bifurcation is stronger. Upon further increasing the clay loading to 6-phr, the three-dimensional appearance is further strengthened, and rubber particles are not found (Figure 37C). The cracks bifurcate, creating multiple fracture surfaces and causing greater energy dissipation.

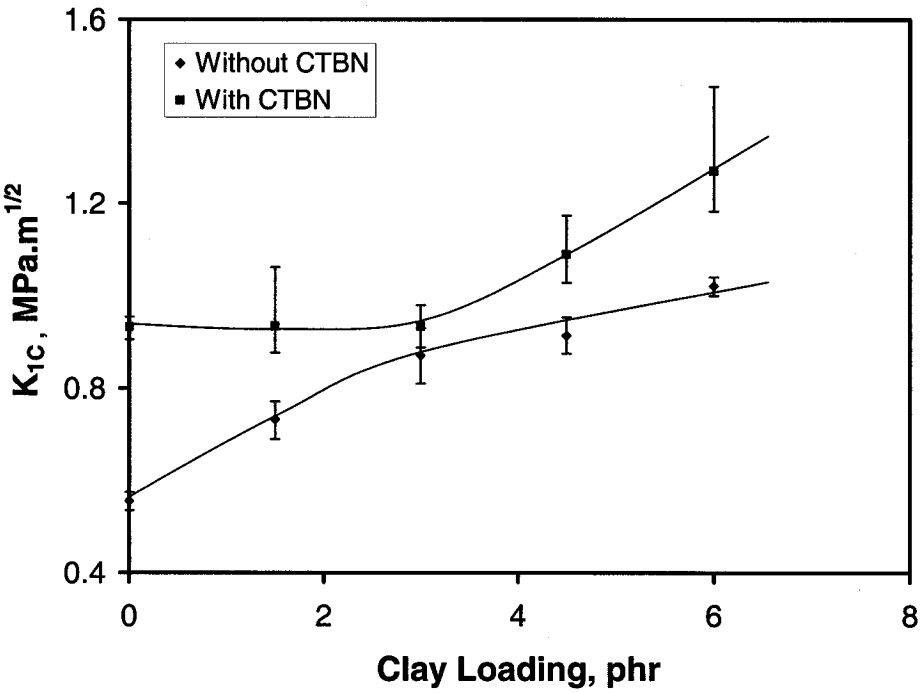

Figure 7-35: The critical stress intensity factor (K_{IC}) of nanocomposites with clay loading

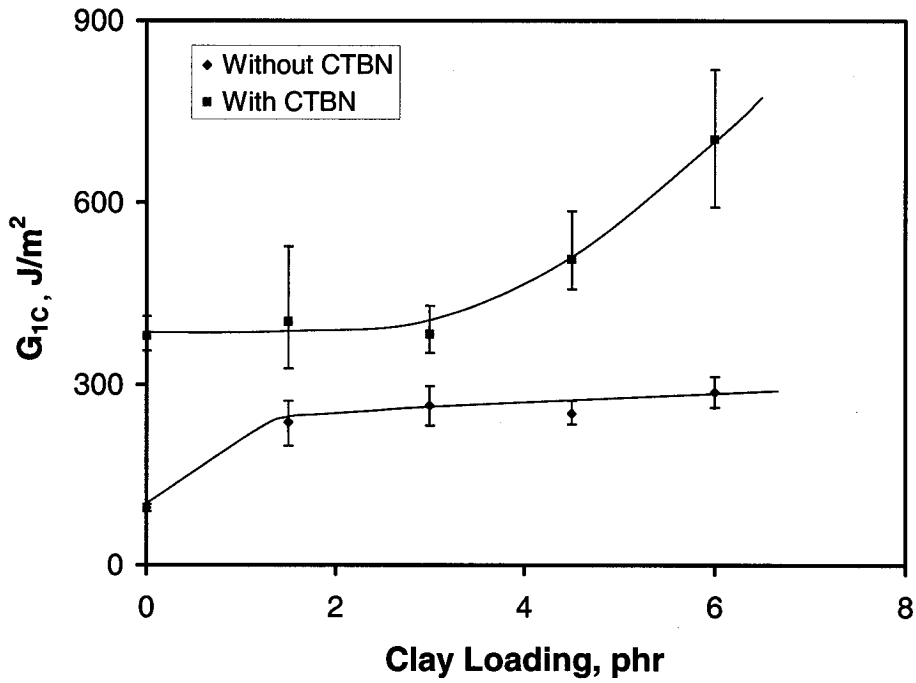

Figure 7-36: The critical strain energy release rate (G_{IC}) of nanocomposites with clay loading

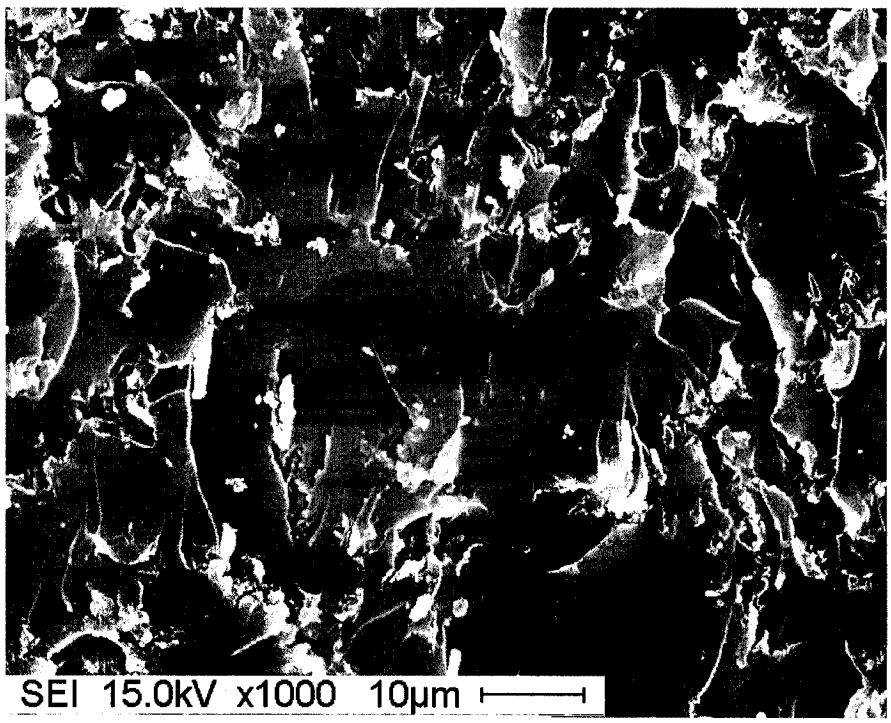

A (8CI-20-3)

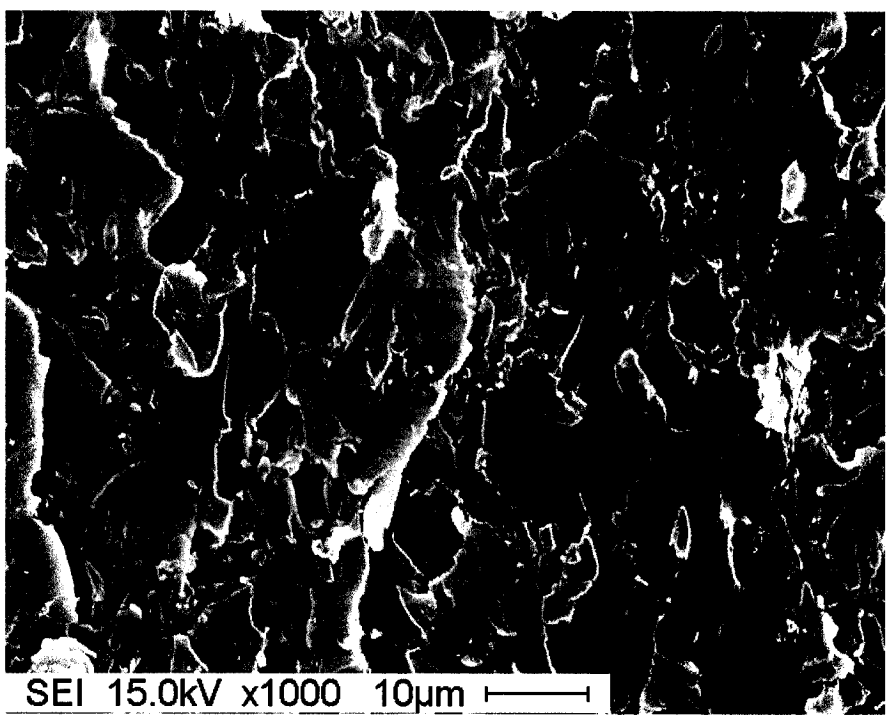

B (8CI-20-4.5)

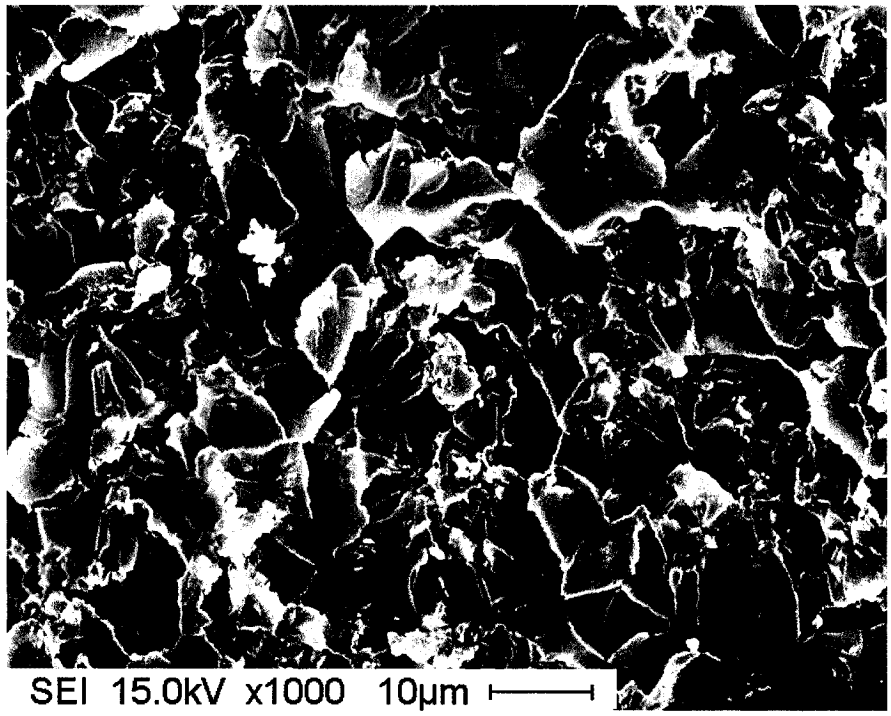

Figure 7-37: SEM micrographs of hybrid nanocomposites

7.5 Summary

The fracture toughness of epoxy-clay nanocomposites based on DGEBA/BF_3.MEA and TGDDM/DDS epoxy systems has been systematically studied. Epoxy resin systems have low toughness; adding untreated clay and organoclay into the epoxy system with the DM method increases toughness with clay loading. The DM nanocomposite shows a higher increase in both K_{IC} and G_{IC} than filler composites at the same clay loading. The experimental data on DM nanocomposites follow the theoretical predictions of crack pinning mechanism quite closely. The fracture surfaces show that the toughness improvement is mainly attributed to crack tip blunting for filler composites, and the crack pinning effect for nanocomposites with the DM method.

The increasing fracture toughness of nanocomposites strongly depends on dispersion quality. Although the fracture surface area of nanocomposites is greatly increased with improving dispersion, the main reason for enhancing fracture toughness of epoxy resins is not the increase of fracture surface area, but the crack pinning mechanism. The better dispersion a nanocomposite has, the higher the crack pinning effect is. When the organoclay is dispersed with HPM-A, the maximum enhancement ratios are 2.2 in K_{IC} and 5.8 in G_{IC}, at 4.5-phr clay loading. The experimental data on HPM nanocomposites also follow the theoretical predictions of the crack pinning mechanism.

SEM images show that GMM nanocomposites have better dispersion of clay platelets (fewer agglomerates and stronger crack bifurcation) in TGDDM/DDS epoxy than DM composites, and thus have higher fracture toughness. HPM nanocomposites have the best dispersion, and thus the highest toughening efficiency.

The matrix resin has an effect on the toughness enhancement of nanocomposites. Nanocomposites based on DGEBA/BF_3.MEA have a similar increasing trend in fracture toughness with clay loading as the nanocomposites based on the TGDDM/DDS system. However, the improvement in toughness of nanocomposites based on DGEBA/ BF_3.MEA is lower than that of nanocomposites based on the TGDDM/DDS system.

Incorporating CTBN rubber into the DGEBA/BF_3.MEA epoxy system increases the toughness of the epoxy. There is a superposition effect on fracture toughness of the hybrid epoxy nanocomposites modified with rubber and organoclay. K_{IC} and G_{IC} are increased by 2.2 and 7.7 times respectively, at 6-phr organoclay loading and 20-phr CTBN, compared with the pristine epoxy system. The fracture surface of hybrid

nanocomposites shows both features of fracture surfaces of rubber-modified epoxies and nanocomposites.

Chapter 8

Conclusions, Contribution and Future Work

8.1 Conclusions

High-performance epoxy-clay nanocomposites and hybrid nanocomposites with rubber and organoclay were synthesized. The effects of materials and dispersion methods on the morphology and properties of these epoxy-clay nanocomposites were investigated. These experimental results can be summarized as the following.

8.1.1 Organoclay Suspensions with Different Dispersion Methods

When organoclays are dispersed in acetone by the HPM method, the agglomerates of organoclays are broken down into very small particles, and the swelling factor, viscosity and shear–thinning behavior of organoclay suspensions greatly increase with process pressure. However, the basal spacing of organoclay in suspensions does not change with process pressure. The experimental results show that high shear forces in the HPM method do not break the clay platelets, or wash out the modifiers on the surfaces of the organoclays.

The organoclays still remain as very small particles in epoxy resins, after suspensions made by the HPM method are mixed with epoxy resins by stirring.

Suspensions made by the HPM method have higher viscosity and much stronger shear-thinning behavior than those made by the DM method. However, the basal spacing of organoclays in epoxy resins is independent of dispersion methods.

8.1.2 Nanocomposites Based on TGDDM/DDS Epoxy System

High-performance epoxy-clay nanocomposites based on TGDDM epoxy cured with DDS were synthesized by three mixing methods: DM, GMM and HPM. With the conventional mixing method DM, organoclay exists in the epoxy matrix in the form of agglomerates, whose size is on a micro-scale (maximum about 30 μm), although the basal spacing is increased to 5~7 nm. However, these agglomerates may be broken down to tactoids consisting of 5 ~ 10 silicate layers, uniformly distributed in the epoxy system made by the HPM method. The tactoids look like discs, with diameter equal to that of clay layers, and thickness of 30~60 nm. The basal spacing of nanocomposites made by the HPM is the same as those made by the DM method. The dispersion quality of clay platelets in the epoxy made by the GMM method is between those of the DM and HPM methods.

The TGDDM/DDS system has high maximum water uptake (about 7.7%) and low diffusivity (about 8.80×10^{-8} mm^2/s at 23 °C). While adding untreated clay into the epoxy system, maximum water uptake and diffusivity increase with clay loading. On the other hand, upon incorporating organoclay into the epoxy, maximum water uptake and diffusivity decrease with increasing clay loading, due to the tortuosity effect; the reduction ratio strongly depends on the dispersion quality. GMM nanocomposites have higher tortuosity efficiency than DM, but lower than HPM. When organoclay is dispersed

by HPM, maximum water uptake and diffusivity decrease by about 20% at 7.5-phr clay loading.

Diffusion Models for Exfoliated Nanocomposites (DMEN) and Intercalated Nanocomposites (DMIN) were developed. The models predict that the diffusivity of nanocomposites strongly depends on the aspect ratio of clay platelets, volume fraction of clay, and extent of dispersion. The predictions agree with the experimental data.

The TGDDM/DDS epoxy system is not very tough. Upon adding untreated clay and organoclay into the epoxy system by the DM method, toughness increases with clay loading. The DM nanocomposite shows a higher increase in both K_{IC} and G_{IC} than filler composites at the same clay loading; the increase in fracture toughness for nanocomposites strongly depends on dispersion quality. GMM nanocomposites have better dispersion of clay platelets in epoxy than DM, and thus higher fracture toughness. HPM nanocomposites have the best dispersion, and thus the highest toughening efficiency. When organoclay is dispersed by HPM-A, the maximum enhancement ratios are 2.2 in K_{IC} and 5.8 in G_{IC} at 4.5-phr clay loading. These experimental data of DM and HPM nanocomposites follow the theoretical predictions for the crack pinning mechanism.

Although the fracture surface area of nanocomposites is greatly increased with improving dispersion, the main reason for enhancing fracture toughness of epoxy resins is not the increase of fracture surface area, but the crack pinning mechanism. The better dispersion a nanocomposite has, the higher the crack pinning effect.

8.1.3 Hybrid Nanocomposites Modified with Rubber and Organoclay

As I.30E organoclay is added into BF_3.MEA/acetone solution, ammonium ions in the galleries of I.30E organoclay may be replaced by the monoethylamine (MEA) of the BF_3.MEA, and the long alkyl chains are expelled out of the galleries, resulting in reducing the basal spacing of the organoclay.

Hybrid nanocomposites modified with rubber and organoclay were synthesized by the HPM method. Adding organoclay into rubber-modified epoxies not only increases the degree of cure and T_g, but also changes the morphology of the rubber phase. The formation mechanism of nanocomposites made by the HPM method was validated on the DGEBA/BF_3.MEA epoxy system. Organoclay tactoids consist of 5 ~ 10 silicate layers, uniformly distributed in the epoxy system. The shape and size of tactoids are the same as in nanocomposites based on TGDDM/DDS/I.30E system, but the basal spacing of the organoclay is only 3.1 nm.

The DGEBA/BF_3.MEA system has low maximum water uptake (from 2.24% to 2.75%), and high diffusivity (about $3.05 \times 10^{-7} mm^2/s$ at 23°C). Contrary to nanocomposites based on the TGDDM/DDS system, those based on DGEBA/BF_3.MEA have lower maximum water uptake, varying around the value for pure resin, and not correlated proportionally with clay loading of organoclay. However, DGEBA/ BF_3.MEA nanocomposites have the same variational trend in diffusivity as TGDDM/ DDS nanocomposites.

Incorporating rubber into the DGEBA/BF_3.MEA epoxy system greatly changes the water uptake behavior of the resin system; it improves water uptake behaviour at lower

environmental temperatures, but increases uptake at high temperatures. However, hybrid nanocomposites decrease this effect of rubber at high environment temperatures.

The matrix resin has an effect on the toughness enhancement of nanocomposites. Nanocomposites based on DGEBA/BF_3.MEA have a similar increasing trend in fracture toughness with clay loading as those based on TGDDM/DDS. However, the improvement in toughness for the nanocomposites based on DGEBA/BF_3.MEA is lower than that for the nanocomposites based on the TGDDM/DDS system.

Incorporating CTBN rubber into the DGEBA/BF_3.MEA epoxy system increases the toughness of the epoxy. Organoclay not only enhances the T_g of rubber-modified epoxies, but also further improves their fracture toughness. There is a superimposition effect on fracture toughness of hybrid epoxy nanocomposites modified with rubber and organoclay; K_{IC} and G_{IC} are increased by 2.2 and 7.7 fold respectively at 6-phr organoclay loading and 20-phr CTBN, compared with the pristine epoxy system. Fracture surfaces of hybrid nanocomposites show both features of fracture surfaces of rubber modified epoxies and nanocomposites.

8. 2 Claims of Originality

The original contributions of this thesis have been mentioned in various locations within each chapter. However, for the convenience of the reader, they are outlined below:

In Chapter 3:

(1) A new method to disperse organoclays into organic media, high pressure mixing (HPM), is proposed. Agglomerates of organoclays are broken down into very small particles in organic media by the HPM method.

(2) The basal spacing of organoclay in suspensions is independent of dispersion method or process pressure.

(3) Ammonium ions in the galleries of I.30E organoclay may be substituted by the monoethylamine (MEA) of BF_3.MEA; the long alkyl chains are expelled out of the galleries of the organoclay, as I.30E organoclay is added to the BF_3.MEA/acetone solution.

In Chapter 4:

(1) High-performance epoxy-clay nanocomposites based on tetraglycidyl-4,4' diaminodiphenylmethane (TGDDM) cured with diaminodiphenyl sulphone (DDS) were synthesized by the HPM method. Agglomerates of organoclays may be broken down to tactoids consisting of 5 ~10 silicate layers, uniformly distributed in the epoxy system.

In Chapter 5:

(1) Hybrid epoxy nanocomposites modified with carboxyl-terminated butadiene acrylonitrile (CTBN) rubber and I. 30E organoclay were synthesized.

In Chapter 6:

(1) Diffusion Models for Exfoliated Nanocomposites (DMEN) and Intercalated Nanocomposites (DMIN) were developed. The predictions are in agreement with the experimental data.

(2) The correlation between the materials, process, morphology and water uptake behavior of epoxy-clay nanocomposites is systematically developed.

(3) The correlation between the materials, process, morphology and water uptake behavior of hybrid epoxy-clay nanocomposites modified with rubber and organoclay is systematically developed.

In Chapter 7:

(1) The correlation between the materials, process, morphology and fracture toughness of epoxy-clay nanocomposites is systematically developed.

(2) The correlation between the materials, process, morphology and fracture toughness of hybrid epoxy-clay nanocomposites modified with rubber and organoclay is systematically developed.

8.3 Suggested Future Work

Our preliminary experimental research has attracted attention from three Canadian Companies (ADS Composites, GYF Plastique and Forintek); on the basis of wide investigation and discussion, our near future work will be the following:

(1) To transfer the present dispersion technology from the laboratory bench to the factory environment;

(2) To study water uptake and fracture toughness of composites where the matrices are based on epoxy-clay nanocomposites dispersed by the HPM method;

(3) To study water uptake and fracture toughness of structural adhesives based on epoxy-clay nanocomposites dispersed by the HPM method;

(4) To study morphology and properties of nanocomposites based on the rubbery epoxy system by the HPM method;

(5) To further increase the clay loading in nanocomposites made by the HPM method.

8.4 List of Publications

1. Liu W. P., Hoa S. V. and Pugh M. "Fracture Toughness and Water Uptake of High-Performance Epoxy /Nanoclay Nanocomposites" *Composites Science and Technology*, 65 (2005), 2364-2373

2. Liu W. P., Hoa S. V. and Pugh M. "Organoclay-Modified High Performance Epoxy Nanocomposites" *Composites Science and Technology*, 65 (2005), 307-316

3. Liu W. P., Hoa S. V. and Pugh M. "Morphology and Performance of Epoxy Nanocomposites Modified with Organoclay and CTBN Rubber", *Polymer Science and Engineering*, June 2004 *Vol 44 No 6* P1179-1186

4. Liu W. P., Hoa S. V. and Pugh M. "Fracture Toughness and Hydrothermal Properties of High Performance Epoxy-Clay Nanocomposites" *the American Society for Composites Conference in Philadelphia,* September, (2005)

5. Liu W. P., Hoa S. V. and Pugh M. "Epoxy-Clay Nanocomposites: Dispersion, Morphology and Performance", TNT 2004 " *Trends in Nanotechnology"* Segovia, Spain, Sept 13-17, 2004

6. Liu W. P., Hoa S. V. and Pugh M. "Fracture Toughness and Hydrothermal Properties of Epoxy Nanocomposites Modified with Nanoclay and Rubber" *Nanocomposites 2004*, San Francisco, California, Sept. 1-4, 2004

7. Liu W. P., Hoa S. V. and Pugh M. "Augmentation of Fracture Toughness of Modified Epoxy Using Nanoclay" *Canada-Japan Workshop*, August 2004

8. Liu W. P., Hoa S. V. and Pugh M. "Organoclay-Modified High Performance Epoxy for Advanced Composites" *SAMPE,* Long Beach, May 2003

9. Liu W. P., Hoa S. V. and Pugh M. "Effects of Morphology of Organoclay-Modified Epoxy Nanocomposites on Mechanical Performance" *ICCM-14*, 2003

10. Liu W. P., Hoa S. V. and Pugh M. "Hybrid Epoxy Nanocomposites Modified With Organoclay and Rubber" *CANCOM-3*, 2003 August

8.5 Patent

1. Hoa S. V., Liu W. P., Pugh M. and Ton-That M.T "Process for the development of epoxy nanocomposites and products" U. S. Patent, in process

References

1. Pinnavaia T. J. and Beall G. W., **Polymer-Clay Nanocomposites**, John Wiley & Sons, New York, (2000).
2. Biswas M. and Ray S. S. "Recent Progress in Synthesis and Evaluation of Polymer-Montmorillonite Nanocomposites", *Advance in Polymer Science*, 155 Springer, pp167-221, (2001).
3. Giannelis E. P., Krishnamoorti R., and Manias E., "Polymer–Silicate Nanocomposites: Model Systems for Confined Polymers and Polymer Brushes", *Advance in Polymer Science*, 138, Springer, pp107-147, (1999).
4. Morgan R. J., "Structure–Property Relations of Epoxies Used as Composite Matrices", *Advance in Polymer Science*, 72, Springer, pp1-45. (1985).
5. Gutowski T.G., **A Brief Introduction to Composite Materials and Manufacturing Processes, In Advanced Composites Manufacturing**, John Wilney & Sons, New York, 1997.
6. Ellis B., **Chemistry and Technology of Epoxy Resins**, Blackie A & P, Chapman & Hall, London, (1993).
7. Kunz S.C., Sayre J. A. and Assink R. A. "Morphology and toughness characterization of epoxy resins modified with amine and carboxyl terminated rubbers" *Polymer*, Vol. 23, 1897-1906, (1982).
8. Pasquale G. D., Motto O., Carter A. R. T., Acierno P. T. M. "New high-performance thermoplastic toughened epoxy thermosets " *Polymer*, Vol. 38, 4345-4348, (1997).

9. Lee J. and Yee A. F. "Inorganic particle toughening I: micro-mechanical deformations in the fracture of glass bead filled epoxies" *Polymer*, 42, 577-588, 2001
10. Wright W. W. " The effect of diffusion of water into epoxy resins and their carbon-fibre reinforced composites" *Composites*,12, 201-205, (1981)
11. Joshi OM K., "The effect of moisture on the shear properties of carbon fiber composites" *Composites*, Vol. 14, No.3, 196-200, (1983).
12. Lan T. and Pinnavaia T. J., "Clay-reinforced epoxy nanocomposites", *Chem. Mater.*, 6, 2216-2219, (1994).
13. Hoa S.V., Oliver A., and Ton-That M.T. "Enhancing properties of epoxy resin using nanoclay", *Proc. 3rd Canadian International Conference on Composites*, Montreal, August (2001).
14. Kelly P., Akelah A., Qutubuddin S., and Moet A., "Reduction of residual stress in montmorillonite /epoxy compounds", *J. Mater. Sci.*, 29, 2274-2280 (1994).
15. Gillman J.W. "Flammability and thermal stability studies of polymer layered-silicate (clay) nanocomposites", *J. Applied Clay Science*, 15, 31-49, (1999).
16. Wang M. S. and Pinnavaia T. J., "Clay-polymer Nanocomposites Formed from Acidic Derivatives of Montmorillonite and an Epoxy Resin" *Chem. Mater.*, 6, 568-474 (1994).
17. Lan T., Kaviratna P. D., and Pinnavaia T. J., "Mechanism of clay tactoid exfoliation in epoxy-clay nanocomposites", *Chem. Mater.*, 7, 2144-2150 (1995).
18. Pinnavaia T. J., Lan T., Wang Z., Shi H., and Kaviratna P. D., "Clay-reinforced epoxy nanocomposites: synthesis, properties, and mechanism of formation", *ACS Polym. Mat. Sci. Eng. Proc.*, 73, 250-261 (1995).

19. Kornmann X., Lindberg H. and Berglund L. A. "Synthesis of epoxy-clay nanocomposites: influence of the nature of the clay on structure" *Polymer* 42 1303-1310, (2001).

20. Kornmann X., Lindberg H. and Berglund L. A. "Synthesis of epoxy-clay nanocomposites: influence of the nature of the curing agent on structure" *Polymer* 42 4493-4499, (2001).

21. Seymour R. B. and Deanin R. D., **History of Polymeric Composites**, VNU Science Press, Utrecht, The Netherlands (1987).

22. Okada A., Kawasumi M., Usuki A., Kojima Y., Kurauchi T., and Kamigaito O., "Nylon 6-clay hybrid", *Mater. Res. Soc. Proc.*, 171, 45-50 (1990).

23. Kojima Y., Usuki A., Kawasumi M., Okada A., Fukushima Y., Kurauchi T., and Kamigaito O., "Mechanical properties of nylon 6-clay hybrid", *J. Mater. Res.*, 8, 1185-1189 (1993).

24. Velde B. **Introduction to clay minerals: chemistry, origins, uses, and environmental significance,** London; New York: Chapman & Hall, (1992).

25. Weaver C. E. and Pollard L. D. **The chemistry of clay minerals**, Amsterdam, New York, Elsevier Scientific Pub. Co., (1973).

26. Hoffman U., Endell K., and Wilm D., "Kristallstruktur and Quellung von Montmorillonit", *Z. Krist.*, 86, 340-348 (1933).

27. Pluart L. L., Duchet J., Sautereau H., Halley P., and Gerard J.F. "Rheological properties of organoclay suspensions in epoxy network precursors" *Applied Clay Science*, 25, 207-219 (2004).

28. Olphen H. van " An Introduction to Clay Colloid Chemistry" A Wiley-Interscience Publication, John Wiley& Sons, Now York (1977)

29. Jordan J. W. " Organophilic bentonites" *J. Phys. Colloid Chem.* , 53, 294-306 (1949)

30. http://www.nanocor.com/

31. http://www.scprod.com/

32. Massam J. and Pinnavaia T. J. "Clay nanolayer reinforcement of a glassy epoxy polymer" *Mater. Res. Soc. Symp. Proc.* 520, 223-232, (1998).

33. Becker O., Varley R., and Simon G. "Morphology, thermal relaxations and mechanical properties of layered silicate nanocomposites based upon high-functionality epoxy resins" *Polymer* 43, 4365-4373, (2002).

34. Tolle T. B. and Anderson D. P. "Morphology development in layered silicate thermoset nanocomposites" *Composites Science and Technology*, 62 1033-1041, (2002).

35. Miyagawa H. Rich M. J. and Drzal L. T. "Amine-cured epoxy/clay nanocomposites. I. processing and chemical characterization" *J. of Polymer Science: Part B Polymer Physics*, vol. 42, 4384-4390, (2004).

36. Chen C. and Curliss D. "Resin Matrix Composites: Organoclay-Aerospace epoxy Nanocomposites Part II", *SAMPE Journal*, vol.37 No.5, 11-18 September/October (2001).

37. Karger-Kocsis J., Gryshchuk O., Frohlich J. and Mulhaupt R. "Interpenetrating vinylester/epoxy resins modfied with organophilic layered silicates" *Composites Science and Technology* 63 2045-2054, (2003).

38. Varma I. K. and Gupta V. B. "Thermosetting Resin-Properties" in **Polymer Matrix Composites, Vol. 2, Comprehensive Composite Materials**, Elsevier Science Ltd, (2000).

39. Li Y. S., Li M. S. and Chang F. C. "Kinetics and curing mechanism of epoxy and boron trifluoride monoethyl amine complex system", *J. of Polym. Sci.: Part A: Polym. Chem.*, vol 37, 3614-24, (1999).

40. Diamant J. and Moulton R. J. "Constituent property-composite property relationships in thermoset matrices" in **Tough Composite Materials**, Recent Development, NASA Langley research Center, 145-156, (1985).

41. Hedrick J. C., Patel N.M. and J.E. McGrath "Toughening of Epoxy Resin Networks with Functionalized Engineering Thermoplastics," in **Toughened Plastics I**, Science and Engineering Edited by Riew C. K. and Kinloch A. J., Oxford, (1993).

42. Wang Z. and Pinnavaia T. J. "Hybrid organic-inorganic nanocomposites: exfoliation of magadiite nanolayers in an elastomeric epoxy polymer", *Chem. Mater.*, 10, 1820-1826 (1998).

43. Usuki, A, Mizutani, T, Fukushima Y., Kojima Y., Usuki A., Kawasumi M., Kurauchi T., and Kamigaito O. *U. S. Patent* 4889885, (1989).

44. Chen C. and Tolle T. B. "Fully exfoliated layered silicate epoxy nanocomposites" *J. Polym. Sci. : Part B: Polymer Physics*, vol.42, 3981-86, (2004).

45. T. Lan, P. D. Kaviratna, and T. J. Pinnavaia, "Epoxy self-polymerization in smectite clays", *J. Phys. Chem. Solids*, 57, 1005-1010, (1996).

46. Wang Z. and Pinnavaia T. J. "Nanolayer reinforcement of elastomeric polyurethane", *Chem. Mater.*, 10, 3769-3771 (1998).

47. LeBaron P. C. and Pinnavaia T. J. "Clay Nanolayer Reinforcement of a Silicone Elastomer", *Chem. Mater.*,13, 3760-3765, (2001).

48. H. P. Klug and L. E. Alexander, **X-ray diffraction procedures for Polycrystalline and Amorphous Materials**, Wiley & Sons (1974).

49. D. B. Williams and C. B. Carter, **Transmission Electron Microscopy**, Plenum Press, New York (1996).

50. P. J. Goodhew and F. J. Humphreys, **Electron Microscopy and Analysis**, Taylor & Francis, London (1988).

51. X. Kornmann, H. Lindberg, and L. A. Berglund, "Epoxy-Clay Nanocomposites: Synthesis, Structure and Mechanical Properties", *EUROFILLERS'99*, CD ROM (1999).

52. J. P. Harcup and A. F. Yee, "Deformation and fracture of polymer silicate layer nanocomposites", *ANTEC'99 Conf. Proc.*, 3, 3396-98, (1999).

53. Zilg C. R. Mulhaupt and J. Finter "Morphology and toughness/stiffness balance of nanocomposites based upon anhydride-cured epoxy resins and layered silicates" *Macromol. Chem. Phys.* 200, 661-670, (1999).

54. Zerda A. S. and A. J. Lesser "Intercalated Clay Nanocomposites: Morphology, Mechanics and Fracture Behavior" *Journal of Polymer Science: Part B Polymer Physics*, Vol. 39, 1127-46, (2001).

55. Kornmann, X. Thomann, R. Mulhaupt, R. Finter, J. Berglund, L.A., " High performance epoxy-layered silicate nanocomposites" *Polymer Engineering and Science*, 42(9), 1815-26, (2002).

56. Wang L., Zhang K. L., Feing W., Wang F. and Li Z. B., "Preparation and Characterization of Modified Montmorillonite Reinforced and Toughened Epoxy

Resin Nanocomposites" *International Symposium on Polymer Nanocomposites, Science and Technology*, Montreal, (2001).

57. Ratna D., Manoj N.R. , Varley R., Raman R. K. S. and Simon G. P. "Clay–reinforced epoxy nanocomposites" *Polym. Int.* 52, 1403-07, (2003).
58. Gam K. T.; Lu J. J., Sue H. J., and Miyamoto M. "mechanical property and toughening of epoxy nanocomposites" *Annual Technical Conference-Society of Plastics Engineers*, 60th, Vol 2, 1524-1529, (2002).
59. D. Ratna, O. Becker, R. Krishnamurthy, G.P. Simon, R.J. Varley "Nanocomposites based on a combination of epoxy resin, hyperbranched epoxy and a layered silicate" *Polymer,* 44, 7449–7457, (2003).
60. Liu T., Tjiu W. C., Tong Y., He C., Goh S. S., and Chung T. S. "Morphology and Fracture Behavior of Intercalated Epoxy/Clay Nanocomposites" *Journal of Applied Polymer Science*, Vol. 94, 1236–1244 (2004).
61. Kojima Y., Usuki A., Kawashmi M., Okada A., Kurauchi T., and Kamigalto O. "Sorption of Water in Nylon 6-Clay Hybrid" *Journal of Applied Polymer Science*, Vol. 49, 1259-1264, (1993).
62. Messersmith P. B. and Giannelis E. P., "Synthesis and barrier properties of poly(e-caprolactone)-layered silicate nanocomposites", *J. Appl. Polym. Sci. Part* A, **3**3, 1047-1057 (1995).
63. Bharadwaj R. K. "Modelling the Barrier Properties of Polymer-Layered silicate Nanocomposites" *Macromolecules*, 34, 9189-9192, (2001).
64. Yano K., Usuki A., and Okada A., "Synthesis and properties of polyimide-clay hybrid films", *J. Polym. Sci. Part* A, **3**5, 2289-2294, (1997).

65. Becker O., Varley R. J. and Simon G. P. " Thermal stability and water uptake of high performance epoxy layered silicate nanocomposites" *European Polymer Journal*, 40, 187-195, (2004).

66. Peter B. and Anne D. N. A., "Epoxy + Montmorillonite Nanocomposite: Dynamic Mechanical Analysis", *Annual Technical Conference of the Society of Plastics Engineers*, p. 1527, (2000).

67. Peter B. and Anne D. N. A "Epoxy + Montmorillonite Nanocomposite: Effect of composition on catalyzed reaction rate", *Annual Technical Conference of the Society of Plastics Engineers*, p. 1531, (2000).

68. Hoa S. V., Oliver. A. and Ton-That M.T. "Adhesive Properties of Nanoclay Reinforced Epoxy for Graphite/Epoxy", *International Symposium on Polymer Nanocomposites,* Science and Technology, Montreal, (2001).

69. Messersmith P. B. and Giannelis E. P., "Synthesis and characterisation of layered silicate-epoxy nanocomposites", *Chem. Mate*r., 6, 1719-1725, (1994).

70. Brown J. M., David C. and Richard A. V. "Thermoset-Layered Silicate Nanocomposites. Quaternary Ammonium Montmorillonite with Primary Diamine Cured Epoxies", *Chem. Mater.*; *12*(11) pp 3376 - 3384; (2000).

71. Gilman J. W., Kashiwagi T., and Lichtenhan J. D. "Nanocomposites: A revolutionary new flame retardant approach", *SAMPE* J., **33**, 40-46 (1997).

72. Gilman J. W., Kashiwagi T., Nyden M. Brown J. E. T., Jackson C. L., Lomakin S., Giannelis E. P. and Manias E. "Flammability studies of polymer layered silicate nanocomposites: polyolefin, epoxy, and vinyl ester resins," in **Chemistry and Technology of Polymer Additives**, Malden M., Al-Malaika S., Golovoy A., and

Wilkie C. A., Eds , Oxford, Blackwell Science Inc., Chapter 14. pp 249-265, (1999)

73. Boyd, S. A., Lee J. F. and Mortland M. M. "Attenuating organic contaminant mobility by soil modification" *Nature* 333:345-347, (1988).
74. Theng B. K. G., The Chemistry of Clay-Organic Reactions, Wiley, New York, (1987).
75. Fu X. A. and Qutubuddin S. "Swelling behavior of organoclays in styrene and exfoliation in nanocomposites" *Journal of Colloid and Interface Science*, Vol. 283, 2, 373-379, (2005)>
76. Lagaly G. and Malberg R. "Disaggregation of Alkylammonium Montmorillonites in Organic Solvents", *Colloids and Surfaces*, 49, 11-27, (1990).
77. Yasmin A., Abot J. L. and Daniel I. M. "Processing of clay/epoxy nanocomposites by shear mixing" *Scripta Materialia* 49 81-86, (2003).
78. Yasmin A., Abot J. L. and Daniel I. M. "Compounding of nanoclay/epoxy composites with a three-roll mill" Materials Research Society Symposium-Proceedings 740: 75-80, (2002).
79. Knudson, M. I. and Jones T. R. "Process for manufacturing organoclays having enhanced gelling properties" *U. S. Patent 4664842*, (1987).
80. Liu W. P., Hoa S. V. and Pugh M. "Organoclay-modified high performance epoxy nanocomposites" *Composites Science and Technology*, Vol. 65, 2, 307-316, (2005).
81. Liu W. P., Hoa S. V. and Pugh M. "Fracture toughness and water uptake of high-performance epoxy/nanoclay nanocomposites" *Composites Science and Technology*, In Press, Corrected Proof, Available online (2005).

82. Liu W. P., Hoa S. V. and Pugh M. "Process for the development of epoxy nanocomposites and products" *U. S. Patent*, in process.

83. Krishnamoorti R. and Giannelis E. P. " Rheology of end-tethered polymer layered silicate nanocomposites" *Macromolecules*, 30, 4097-4102, (1997).

84. Gouy, G. Sur la constitution de la charge electrique a la surface d'un electrolyte. *J. Phys. Radium. (Paris)* **9:**457–468; (1910).

85. Chapman, D. L. "A contribution to the theory of electrocapillarity" *Phylos. Mag.* 25:475–481; (1913).

86. O. Stern "Zur Theorie der electrolytischen doppelschicht" *Z. Electrochem* 30, 508, (1924).

87. Derjaguin B. V. and Landau L. D. "Theory and stability of strongly charged lyophobic sols and of the adhesion of strongly charged particles in solutions of electrolytes" *Acta Physicochim*, USSR 14, 633, (1941).

88. Verwey, E. J. W., and Overbeek J. T. G. **Theory of the stability of lyophobic colloids**. Elsevier, Amsterdam, The Netherlands, (1948).

89. Luckham P. F. and Rossi S. "The colloidal and rheological properties of bentonite suspensions" *Advances in colloid and Interface Science*, 82, 43-92, (1999).

90. Hunter R. J. and White L. R. **Foundations of colloid science,** Oxford: Clarendon Press; New York: Oxford University Press, (1987).

91. Kissa E., **Dispersions: characterization, testing, and measurement**, New York : Marcel Dekker, (1999).

92. Stein H.N., **The preparation of dispersions in liquids,** New York: Marcel Dekker, (1996).

93. Schilling R. E. and Yang M. "Attritor grinding mills and new development" *Panamerican Coatings 2000*, World Trade Center, Mexico city, Mexico, July 2000.

94. Cook E. J. and Lagace A. P. "Apparatus for forming emulsions" *U. S. Patent 4533254*, Aug 1985

95. User manual, Model M-110EH XP Microfludizer Processor, *Microfluidics*,

96. Einstein, A. "On the theory of Brownian movement". *Ann. Phys. (Leipz.)* 19, 371–381, (1906).

97. Simha, R. "The influence of Brownian movement on the viscosity of solutions." *J. Phys. Chem.* 44:25–34. (1940)

98. Maron S. H. and Pierce P. E. "Application of Ree-Eyring Generalized Flow Theory to Suspensions of Spherical Particles," *J. Colloid Science*, 11, 80-95, (1956).

99. Product bulletin " Epon Resin 828", *Shell Resin, Shell chemical company*

100. Data Sheet "Araldite MY 720, a medium viscosity multifunctional epoxy resin" *Vantico Inc*

101. Data Sheet "Boron trifluoride monoethylamine (BF_3.MEA, $BF_3.NH_2CH_2CH_3$)", *Sigma-Aldrich Fine Chemicals*

102. Data Sheet "Aradur 976-1," *Vantico Inc*

103. Slabaugh W. H. and Hiltner P. A. "The swelling of alkylammonium montmorillonites" *J. Phys. Chem.* 72, 12, 4295-4298, (1968).

104. Burgentzlé D., Duchet J., Gérard J. F., Jupin A., and Fillon B. "Solvent-based nanocomposite coatings I. Dispersion of organophilic montmorillonite in organic solvents" *Journal of Colloid and Interface Science* 278, 26–39, (2004).

105. Page S. A., Mezzenga R. and Manson J. A. "Surface energetics evolution during

processing of epoxy resins", *J. of Colloid and Interface Sci.,* 222, 55-62, (2000).

106. Polinski A. J., Ryan M. E., Gupta R. K., Seshadri S. G., and Frechette F. J. " Rheological behavior of filled polymeric systems. I. yield stress and shear-thinning effects." *J. Rheol.* 32, 703-735, (1988).

107. Fessenden R. J. and fessenden J. S. **Organic Chemistry**, Brooks/Cole Publishing Company, California, (1986).

108. Wu Q. and L. A. Berglund " FT-IR spectroscopic study of hydrogen bonding in PA6/clay nanocomposites" *Polymer,* 43, 2445-2449, (2002)

109. Deimede V. A., Fragou K. V., Koulouri E. G., Kallitsis J. K. and Voyiatzis G. A. "Miscibility behavior of polyamide 11/sulfonated polysulfone blends using thermal and spectroscopic techniques" *Polymer*, 41, 9095-9101, (2000).

110. Tackie M. and martin G. C. "The polymerization mechanism and kinetics of DGEBA with BF_3-MEA," *J. Applied Polym. Sci.*, Vol. 48, 793-808, (1993).

111. Raghava R. S. Soc Adv Mat. Pro Eng. 28th Nat. Symp., 367, (1983).

112. Bucknall C. B. and Gilbert A. H. "Toughening tetrafunctional epoxy resins using polyetherimide" *Polymer*, 30 213, (1989).

113. D. C. Lee and L. W. Jang, "Characterization of epoxy-clay hybrid composite prepared by emulsion polymerization", *J. Appl. Polym. Sci.*, 68, 1997-2005 (1998).

114. Becker O., Varley R., and Simon G. "Layered silicate nanocomposites based on various high-functionality epoxy resins. Part I: the influence of an organoclay on resin cure" *Polymer Engineering and Science*, Vol. 43, No. 4, (2003).

115. Brown J. M., Curliss D., and Vaia R. A. "Thermoset-Layered Silicate Nanocomposites. Quaternary Ammonium Montmorillonite with Primary Diamine

Cured Epoxies" *Chem. Mater*, 12, 3376-3384, (2000).

116. Chan L. C., Gillham J. K., Kinloch A. J. and Shaw S. J. in **Rubber-Modified Thermoset Resins**, Eds., Riew C. K. and Gillham J. K., adv. Chem. Ser. 208, Am. Chem/ Soc. Washington, (1984).

117. Yee A. F. and Pearson R. A. "toughening mechanism in elastomer-modified epoxies" *J. of Mater. Sci.*, 21, 2462-74, (1986).

118. Lee J. and Yee A. F. "Fracture of glass bead /epoxy composites: on micro-mechanical deformations", *Polymer*, 41, 8363-73, (2000).

119. Young R. J., Maxwell d. L. and Kinloch A. J. "The deformation of hybrid-particulate composites" *J. of Mater. Sci.*, 21, 380-388, (1986).

120. Kinloch A. J, Maxwell d. L. and Young R. J. "Micromechanisms of crack propagation in hybrid-particulate composites" *J. of Mater. Sci. Letters*, 4 1276-1279, (1985).

121. Yamanaka K. Takagi Y. and Inoue T. "Reaction-induced phase separation in rubber-modified epoxy resins" *Polymer*, Vol 60, 1839-1844, (1989).

122. Ernest G. Wolff "Moisture Effects of Polymer Matrix Composites" *SAMPE Journal,* Vol. 29, No.3, 11-19, (1993).

123. Jovan Mijovic and King-Fu Lin, "The Effect of Hygrothermal Fatigue on Physical/Mechanical Properties and Morphology of Neat Epoxy Resin and Graphite/Epoxy composite" *Journal of Applied Polymer science*, vol.30, 2527-2549 (1985).

124. Jiming Zhou and James P. Lucas, "Hygrothermal effects of epoxy resin. Part I: the nature of water in epoxy" *Polymer*, 40, 5505-5512, (1999)

125. Jiming Zhou and James P. Lucas, "Hygrothermal effects of epoxy resin. Part II: variations of glass transition temperature" *Polymer*, 40, 5513-5522, (1999).

126. Grave C., Mcewan I. and Pethrick R. A. "Influence of Stoichiometric Ratio on Water Absorption in Epoxy Resins" *Journal of Applied Polymer Science*, Vol. 69, 2369-2376 , (1998).

127. Soles C. L. and Yee A. F. "A Discussion of the Molecular Mechanisms of Moisture Transport in Epoxy Resins" *Journal of Polymer Science: Part B: Polymer Physics*, Vol. 38, 792–802, (2000).

128. Richard A. Pethrick et al "Effect of Cure Temperature on the Structure and Water Absorption of Epoxy/ Amine Thermosets" *Polymer International,* 39, 275-288, (1996).

129. Apicella A., Nicolais L., Nobile M. R. Castiglione-Morelli M. A., "Effect of processing variables on the durability of epoxy resins for composite systems", *Comp. Sci. and Tech.*, 24, 101-121, (1985).

130. Moy, P.; Karasz, F.E. *Polym. Eng. Sci.*, **20**, 315, (1980).

131. Carter H. G. and Kibler K. G. "Langmuir-Type Model for Anomalous Moisture Diffusion in Composite Resins" *J. composite Materials*, Vol. 12, 118-131, (1978).

132. Gurtin M. E. and Yatomi C. "On a Model for Two Phase Diffusion in Composite Materials" *J. Composite Materials*, Vol.13, 126-130, (1979).

133. Roy S., Xu W. X., Park S. J. and Liechti K. M. "Anomalous Moisture Diffusion in Viscoelastic Polymers: Modeling and Testing" *Journal of Applied Mechanics*, Vol. 67, 391-396, (2000).

134. Cai L. W. and Weitsman Y. "Non-Fickian Moisture Diffusion in Polymeric Composites" *Journal of Composite Materials*, Vol. 28, No.2, 130-154, (1994).

135. Shen, C. H. and Springer, G. S. " Moisture Absorption and Desorption of Composite materials", *Journal of Composite Materials*, Vol.10, 2-20, (1976).

136. Dewimille B. and Bunsell **A** R "The modelling of hydrothermal aging in glass fibre reinforced epoxy composites" *J. Phys. D: Appl. Phys.*, 15, 2079-2091, (1982).

137. Nielsen L.E. "Models for the permeability of filled polymer systems." *J. Macromol. Sci.*, **5**(A1), p 929-942. (1967).

138. Crank J., **The Mathematics of Diffusion**, Oxford, Clarendon, (1956).

139. Shirrell C. D. and Halpin J. In: "Composite materials: testing and design [Fourth Conference]. *ASTM STP 617, American Society of Testing and Materials*, 514-528, (1977).

140. Grathwohl P. **Diffusion in natural porous media-contaminant transport, sorption/desorption and dissolution kinetics**, Kluwer Academic Publishers, 1998

141. Choi H. S., Ahn K. J. Nam J. D. and Chun H. J. "Hygroscopic aspects of epoxy/carbon fiber composite laminates in aircraft environments" *Composites: Part A* 32, 709-720, (2001).

142. Alvey, F. B., "Selectivity of the epoxide phenol reaction" *J. Appl. Polym. Sci*, 13, 1473, (1969).

143. Zhao Q. and Hoa S. V. "Toughening mechanism of epoxy resins with micro/nano particles" in Materials for Safety and Health , Mesoscopic and Multiscale Consideration in modern Science and Engineering, Eds Sih G. S. Vu-Khanh T., Proceedings of the seventh International Conference on Mesomechanics, Monteral Canada, pp201-208 (2005).

144. Hellan K., **Introduction to fracture mechanics**, New York: McGraw-Hill, (1984).

145. Irwin G. R. *Appl. Mats. Res.*, 3, 65, (1964).

146. Lange F. F. "The interaction of a crack front with a second-phase dispersion" *Philos. Mag*, 22: 983-992, (1970).

147. Evans A G. "The strength of brittle materials containing second phase dispersions" *Philos. Mag*; 26:1327-1344, (1972).

148. Green D. G., Nicholson P. S. and Embrury J. D. "Fracture of a brittle particulate composite, part 1: experimental aspects" *J Mater Sci*; 14: 1413-1420 (1979).

149. Green D. G., Nicholson P. S. and Embrury J. D. "Fracture of a brittle particulate composite, part 2: theoretical aspects" *J Mater Sci*; 14: 1657-1661(1979).

150. Kinloch A. J., Maxwell D. L. and Young R. J. "The fracture of hybrid-particulate composites" *J. Mat. Sci.*, 20 4169-4184, (1985).

151. Imanaka M. et al "Fracture Toughness of spherical silica-filled epoxy adhesive" *International Journal of Adhesion & adhesives* 21,389-398 (2001).

152. Evans AG, Williams S, Beaumont PWR. "On the toughness of particulate filled polymers" *J Mater Sci*; 20:3668-3674 (1985).

153. Faber K. T. and Evans A. G. "Crack Growth Resistance of Microcracking Brittle Materials," *J. Am. Cerom.* Soc. 67, 255, (1984).

154. Sigl, L. S., Mataga, P. A., Dalgleish, B. J., McMeeking, R. M., and Evans, A. G. "On the toughness of brittle materials reinforced with a ductile phase". *Acta Metall.* 36 (4), 945–953. (1988).

155. Kunz-Douglass, S.; Beaumont, W. R.; Ashby, M. F. "A model for the toughness of epoxy-rubber particulate composites" *J. Mater. Sci.,* 15, 1109-23, (1980).

156. Kinloch A. J., Shaw S. J., Tod D. A. and Hunston D. L. "Deformation and fracture behaviour of a rubber-toughened epoxy: 1. Microstructure and fracture studies," *Polymer*, 24, 1341-54, (1983).

157. Kinloch A. J., Shaw S. J. and Hunston D. L. "Deformation and fracture behaviour of a rubber-toughened epoxy: 2. Failure criteria" *Polymer*, 24, 1354-63, (1983).

158. Huang Y. and Kinloch A. J. "Modelling of toughening mechanisms in rubber modified epoxy polymer, Part I: finite element analysis studies" *J. Mater. Sci.*, 27, 2763-2769, (1992).